UNIVERSITY OF SOUTHAMPTON

PRECISION MEASUREMENT OF CARBON ISOTOPE RATIO IN EXHALED BREATH FOR THE DETECTION OF HELICOBACTER PYLORI

by

Arun Kannath

A thesis submitted in partial fulfillment for the degree of Doctor of Philosophy

in the

Faculty of Engineering and Applied Science
School of Electronics and Computer Science

August 2009

UNIVERSITY OF SOUTHAMPTON

ABSTRACT

FACULTY OF ENGINEERING AND APPLIED SCIENCE
SCHOOL OF ELECTRONICS AND COMPUTER SCIENCE

Doctor of Philosophy

by Arun Kannath

The utility of breath trace compounds as bio-markers for various physiological conditions has long been exploited for the diagnosis of various diseases. Urea breath tests have been adopted as the gold standard for the detection of *Helicobacter pylori* which is a primary cause for acute gastritis and peptic ulcers. In these tests, small changes in the ratio of stable CO_2 isotopomers, $^{13}CO_2$ and $^{12}CO_2$, present in exhaled breath are measured precisely and this is conventionally done by using an Isotope Ratio Mass Spectrometer. However, the huge cost and complexity involved in operating these instruments has restricted their widespread use. A viable and low cost alternative is offered by instruments employing non-dispersive infrared absorption techniques. The feasibility of such an instrument has been explored in this work.

The instrument presented here is a two channel isotope ratiometer that performs whole band integrated absorption measurements. Detection is based on a novel feedback mechanism whereby an imbalance in the channel absorptions causes the pathlength along one of the channels to be altered in order to bring the system back to balance. This change in ratio of pathlengths is directly related to the change in the $^{13}CO_2/^{12}CO_2$ concentration. Significant amount of work has already been done to investigate the effects of interferences from coincident absorption bands and other spectral effects that can lead to spurious results.

A comprehensive description of the overall system design, development and performance evaluation of the first prototype instrument has been presented here. This involved significant computer modeling and simulations and the results were verified experimentally. These results provided sufficient evidence to suggest the feasibility of such an instrument as a diagnostic tool. It was also concluded that some design improvements were required to circumvent issues related to pathlength variation and a list of recommendations has been provided for this purpose. On the basis of the results obtained as part of this research endeavour, it was concluded that the non-dispersive instrument design presented here can form the basis for a low cost commercial alternative for performing carbon isotope ratio breath tests.

Contents

List of Figures

List of Tables

Acknowledgements

This research work would not have been possible without the support and guidance offered by a number of people around me. First and foremost, I would like to express my profound gratitude to Prof. Harvey N. Rutt for offering me the opportunity to work on this project. His supervision, endless patience and unstinted support helped me to see through difficult times when faced with seemingly irresolvable problems. Thanks are also due to my group members Angela Swift, Chong Yew Lee, Paul Hoy, Everardo and Andrew with whom I have shared wonderful moments during the course of this project. Special thanks to all the technicians for helping me out when I needed it the most.

The past four years have seen many ups and downs and had it not been for my wonderful set of friends and flat mates and the help and encouragement they offered, I would have found it difficult to achieve this. Let me take this opportunity to offer all of them my heartfelt gratitude. My parents have been a pillar of strength for me all throughout my life and it was no different during this project work. I would like to thank them and my wife, who joined me towards the end of this thesis preparation, for their endless love, patience and constant backing that helped me continue during moments of difficulties.

Finally, to the One, who invisibly aided and guided me through the most arduous of times. This would not have been possible without the Almighty’s blessings.

Abbreviations

B	Rotational constant
BTC	Breath Trace Compound
C626	$^{12}CO_2$
C636	$^{13}CO_2$
D	Centrifugal dissociation constant
D*	Specific detectivity
DFB	Distributed Feed Back laser
ENBW	Equivalent Noise Bandwidth
F/V	Frequency to Voltage
FFT	Fast Fourier Transform
FSR	Free Spectral Range
FTIR	Fourier Transfer Infrared Spectrometer
FWHM	Full Width Half Maximum
G_r	Grashof number
h	Planck's constant
ICF	Isotope Correlation Filter
IF	Interference Filter
IR	Infrared
IRMS	Isotope Ratio Mass Spectrometry
ISFET	Ion-Sensitive Field Effect Transistor
J	Rotational quantum number
k	Boltzmann's constant
n	Refractive index
NDIRS	Non-Dispersive Infrared Spectroscopy
NEP	Noise Equivalent Power
nsp	non-sample pathlength
v	Vibrational frequency
PFA	Perfluoroalkoxy plastic
PLL	Phase Locked Loop
ppm	Parts per million
P_r	Prandtl number

PSD	Phase Sensitive Detector
psi	pound per square inch
PVF	Polyvinylfluoride
PWM	Pulse Width Modulation
R_a	Rayleigh number
$\sigma(v)$	Absorption cross-section
S/N	Signal to Noise ratio
STP	Standard Temperature and Pressure
T	Temperature
TDLAS	Tunable Diode Laser Absorption Spectroscopy
UBT	Urea Breath Test
V	Vibrational quantum number

Chapter 1

Introduction

1.1 Carbon Isotope Ratio Measurements

Isotopes are atoms of the same element having the same atomic number but different mass numbers owing to the difference in the number of neutrons. They result in isotopomers which are molecules of the same species where one atom has been replaced by its isotopic variant, creating molecules that have different physical properties and behaviour. It is this difference in behaviour that is exploited in their detection and concentration measurement which forms the basis of isotope ratio tests.

In the field of isotopic studies, carbon deserves a special mention because of its significance in various ecological, geophysical and physiological processes. The stable isotopes of carbon, ^{12}C and ^{13}C, have found applications in diverse areas such as measurement of atmospheric methane[4], age determination[5], global climate change research[6, 7], volcanic gas monitoring[8, 9] and detection of trace sources of petroleum and natural gases[10] to name a few. Another major area of application is in the field of medical diagnostics for the detection of various health conditions. This is done by performing different kinds of tests, the most popular among them being breath tests.

1.2 Breath Tests

Exhaled human breath has been known for many years to be an excellent indicator of health conditions. The popular alcohol breath test for drivers traces its origin

to Stubbs[11] who in 1964 realised that detection of certain trace compounds in exhaled breath indicated alcohol consumption by the individual. Numerous other studies were carried out independently and it was soon discovered that the detection of certain breath trace compounds (BTC) could act as bio-markers to various conditions such as diabetes[12], cellular damage[13], lung cancer[14, 15], liver cirrhosis[16], schizophrenia[17], kidney failure[18] and exposure to pollutants[19] among others.

The presence of isotopes of a BTC provides another useful means of performing diagnostic tests called isotope tracer tests. Here the ratio of concentration of isotopomers of a particular BTC is determined before and after a deliberate increase in the concentration of the rarer isotopomer. This increase in concentration is achieved by the intake of a suitable substrate labelled with the isotopic variant of the target molecule. This substrate is then metabolised by a biochemical reaction into a labelled byproduct that is eventually expired via the lungs. Therefore, by analysing a sample of the exhaled breath, the change in ratio of concentration can be determined which is then used as an indicator of some prevailing health condition.

The major constituents of human expired breath are shown in table 1.1[20].

Gases	*Dry Air*		*Alveolar Air*		*Expired Air*	
	mm Hg	%	mm Hg	%	mm Hg	%
N_2(plus inert gases)	600.2	78.98	569.0	74.9	566.0	74.5
O_2	159.2	20.98	149.3	13.6	120.0	15.7
CO_2	0.3	0.04	40.0	5.3	27.0	3.6
H_2O	0.0	0.0	47.0	6.2	47.0	6.2

TABLE 1.1: Partial pressure of gases at sea level

The table above shows that there is a significant difference in the composition of dry, alveolar and expired air. Dry air mainly constitutes nitrogen and oxygen. During inspiration exchange of gases take place across the blood-alveolar membrane whereby oxygen diffuses into the blood stream. Carbon dioxide, on the other hand, diffuses from the blood into the alveoli and is released out during expiration.

Initially breath tests were carried out using radioactive isotopes. Nitrogen and oxygen are two major constituents of expired breath. However, their radioisotopes have very short half life periods and hence not suitable for the tests. Carbon has two radioisotopes, ^{14}C and ^{11}C with half lives of 5715 years and 20.3 minutes respectively. $^{14}CO_2$ was initially used for carrying out breath tests for

the diagnosis of fat malabsorption[21]. But the associated health hazards posed by these radioisotopes made them unpopular and focus was shifted to the use of stable isotopes. $^{12}CO_2$ and $^{13}CO_2$ are two stable isotopomers having relative natural abundances of 98.9% and 1.1% respectively. Although these stable isotopes necessitate expensive measurement techniques and substrate preparation, their high cost is offset by the inherent safety they offer. This allowed the opportunity to conduct safe breath tests even on pregnant women and young children which otherwise would not have been possible with radioisotopes. Hence from a safety perspective, these isotopomers are ideal for performing breath tests.

The change in the ratio of concentration of the isotopomers is expressed as a delta value, δ‰ which is expressed mathematically by Craig's formula 1.1. Here Rs refers to the ratio of concentration of the isotopes in the breath sample after administration of the test dose and Rr refers to the concentration in the reference sample prior to it.

$$\delta = \frac{Rs - Rr}{Rr} 1000 \tag{1.1}$$

This value of Rr is taken as the standard reference or baseline measurement against which an increase in ^{13}C concentration is ratioed thereby resulting in positive delta values. A measurement process of this nature gives high resolution which enables a more convenient representation of the very small changes in ^{13}C concentration when compared to other forms of enrichment representation such as atom%. This is because atom% gives the absolute number of atoms of a given isotope in 100 atoms of the element and hence very small enrichment levels will appear only in the third or fourth decimal position. As this delta measure is not in wide use other than in this field, we give a detailed example of its usage. For instance, a value of 1‰ implies a change in ratio of $^{13}C/^{12}C$ of 1.1×10^{-5} which is equivalent to a ^{13}C enrichment of 0.001 atom%. This can be illustrated mathematically as follows:

1‰= $[(Rs\text{-}Rr)/Rr]1000$
$Rr/1000 = Rs\text{-}Rr$
Now, $Rr = [^{13}C]/[^{12}C] = 1.1/98.9 = 0.011$
Therefore, $0.011/1000 = Rs\text{-}Rr$
i.e. $\Delta[^{13}C]/[^{12}C] = 1.1\times10^{-5}$
$\therefore \Delta[^{13}C] = 1.0879\times10^{-3}$

This is equivalent to a ^{13}C enrichment of 0.001 atom%. Estimation of a delta value thus offers a useful means of representing very small changes in ^{13}C concentration.

1.3 Detection of *Helicobacter Pylori*

Helicobacter pylori is a spiral shaped bacterium that lives in the stomach and duodenum. It was first discovered in 1982 by two Australian physicians, Barry J. Marshall and J. Robin Warren, for which they were awarded the Nobel Prize for Physiology or Medicine in 2005. The inside of the stomach has a highly acidic environment composed of many digestive enzymes and concentrated hydrochloric acid (2-3 molar concentration) which would make it impossible for bacteria and other microorganisms to survive. However, the stomach walls are protected from these gastric juices and enzymes by a layer of mucus lining and it is here that *H.pylori* dwells safely. In order to repel any gastric juices that do reach it, *H.pylori* secretes an enzyme, urease, that converts the abundant urea in the stomach to bicarbonates and ammonia as per the reaction given in equation 1.2.

$$NH_2 - CO - NH_2 + H^+ + 2H_2O \longrightarrow HCO_3^- + 2NH_4^+ \tag{1.2}$$

The ammonia and bicarbonates form solutions that are basic and form a protective "cloud" around *H.pylori* thereby neutralising the effect of stomach acids. This is shown graphically in figure 1.1. It is this urea hydrolysis reaction that is subsequently used for *H.pylori* detection. The body's natural defense mechanisms such as killer T-cells and other white cells cannot reach the area of infection caused by *H.pylori* since they cannot pierce the mucus lining. As a result, *H.pylori* gradually colonizes the gastric mucosa leading to acute gastritis and chronic conditions which finally result in further complications such as peptic ulcer and mucosa associated lymphoid tissue lymphoma (MALT)[22]. It is also associated with heart diseases[23] and gastric cancer and has been classified as a class one carcinogen by the International Agency for Research on Cancer. *H.pylori* can be detected in about 30% of the population of developed countries. It is believed to be transmitted orally mainly through ingestion of fecal matter from waste tainted food or water. It may also be thrown up to the mouth from the stomach during gastro-esophageal reflux from where it could be transmitted to other people through oral contact. Strong evidence of intrafamilial spread of *H.pylori* has also been reported[24].

The detection of this bacterium is based on the fact that it produces the enzyme, urease, that dissociates urea molecule (NH_2-CO-NH_2) producing ammonia and carbon dioxide. Hence if an infected person consumes isotopically labelled ^{13}C-urea (NH_2-^{13}CO-NH_2), the urease produced by *H.pylori* will break it down producing

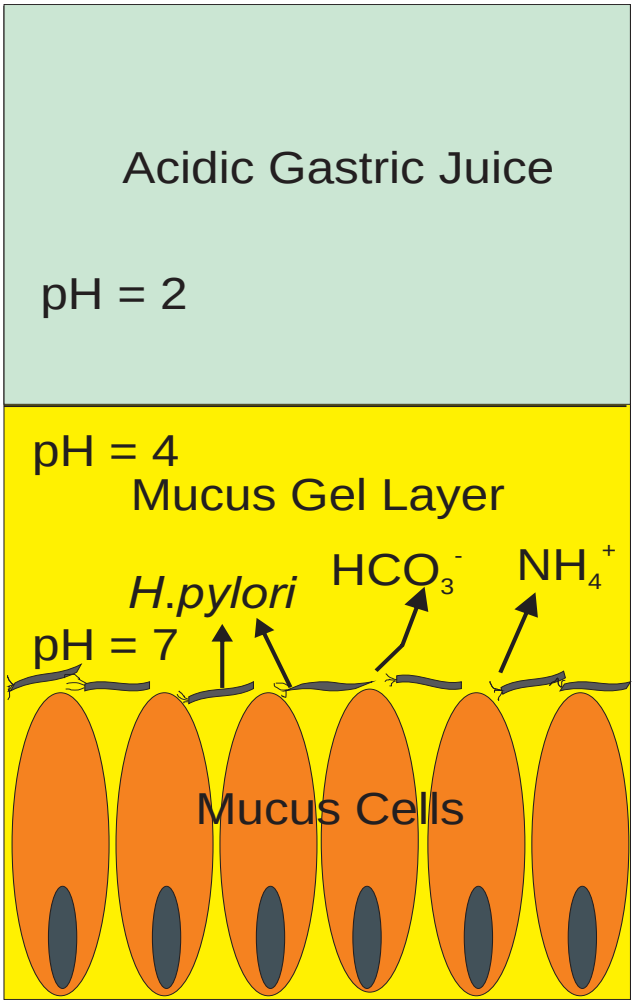

FIGURE 1.1: Figure showing how *H.pylori* is able to survive in the harsh acidic conditions present in stomach by urea hydrolysis

isotopically labelled CO_2. This excess $^{13}CO_2$ will then be released through the exhaled breath. A breath sample analysis will indicate a change in the concentration ratio of the two isotopomers relative to its initial ratio that existed prior to the administration of isotopically labelled urea. The associated delta value can then be used as a definite indicator of *H.pylori* infection and serves as a completely non-invasive diagnostic tool. This is the principle involved in Urea Breath Tests (UBT). Detection of *H.pylori* by UBT has been adopted as the gold standard because it determines the global presence of the bacterium in the stomach and quickly shows negative results in case of eradication of the bacterium following treatment. For UBTs, *Rr* refers to the ratio $[^{13}CO_2]/[^{12}CO_2]$ in the baseline measurement obtained from the breath sample prior to urea administration and *Rs* is the ratio $[^{13}CO_2]/[^{12}CO_2]$ obtained after urea intake. A pictorial representation of the UBT process is shown in figure 1.2 [25].

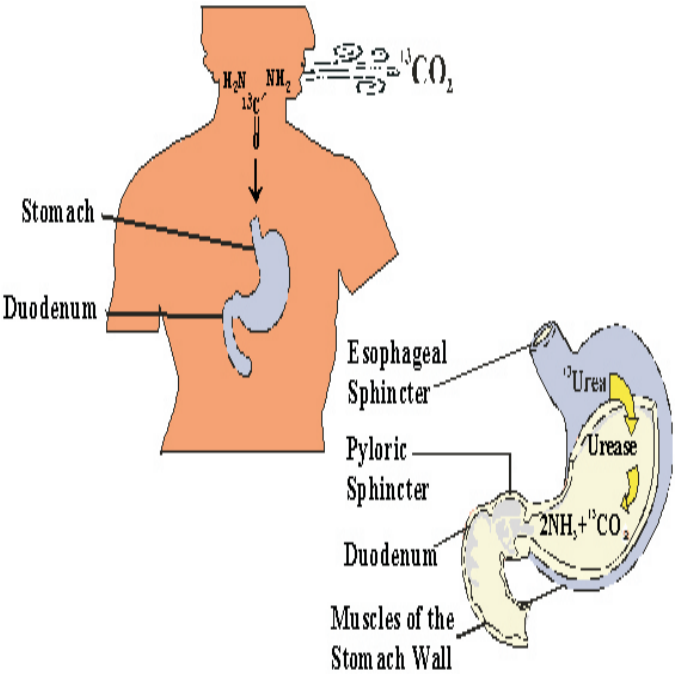

FIGURE 1.2: Principle of UBT which is used as a gold standard for *H.pylori* detection

1.4 Objective

Several analytical techniques are available for precise isotopic ratio measurements, the most important of which is Isotope Ratio Mass Spectrometry (IRMS). This is a highly reliable and accurate measurement technique that can detect $^{13}CO_2$ enrichment of the order of 0.1‰[26]. But the high cost of the instrument, its requirement for high quality vacuum, specialised technicians and careful sample preparation has restricted its use to large research establishments and laboratories. The most suitable alternative techniques for detection are the ones that employ infrared spectroscopy. These instruments are basically infrared ratiometers that detect the absorption of infrared radiation over a specified wavenumber region. Isotopic ratio measurement is made possible due to the isotopic shift in their absorption spectrum which is a direct consequence of their different mass numbers.

The objective of this research endeavour is to design, develop and evaluate the performance of a compact and low cost infrared spectroscopic instrument based on a novel detection technique that can perform isotopic ratio measurements for *H.pylori* detection with a precision of 1‰. This will make it a very pragmatic and commercial solution for non-invasive diagnosis. The proposed instrument will be very simple to use requiring minimum maintenance. The design will not involve expensive components thereby reducing the overall cost. It will also be portable

and will require minimum human intervention. The targeted end user is a doctor or a clinical technician who need not have any background information about the physics involved. This will be a big step forward in bringing isotope measurement instruments out from the confines of big research establishments to normal clinics within the reach of common man. The following chapters in this thesis explore the feasibility and development of such a spectroscopic instrument and describes in detail the performance evaluation of the first prototype instrument. Chapter 2 gives a concise overview of the science of spectroscopy and the theory involved. This is followed by chapter 3 which briefly describes some of the analytical techniques that exist today and attempts to critically evaluate each one of them. The proposed instrument design details and specifications are also included. Chapter 4 gives details of the computational work and simulations that were carried out for an indepth analysis of various interfering factors that might influence the measurement process. Chapter 5 provides an insight into the development of various sub systems and their testing. The initial experimental results followed by actual gas phase measurements are dealt with in chapter 6. Finally, chapter 7 discusses the results achieved so far and provides further guidelines and recommendations for improved instrument performance.

Chapter 2

Infrared Spectroscopy

2.1 Introduction

Spectroscopy deals with the interaction between matter and electromagnetic radiation. When a sample of some substance is placed in the path of light radiation having frequencies that match with the natural vibrational and rotational frequencies of the molecules, they absorb these radiations and this causes certain energy level transitions in them (not applicable for homonuclear diatomic molecules such as N_2 and O_2 as there is no net change in dipole moment). The unabsorbed part of the radiation is of course transmitted. By analysing this transmitted spectrum, it is possible to identify the portion of the incoming radiation that has been absorbed by the molecules which in turn tells us about the nature of the substance under investigation and also its concentration. This is due to the fact that different molecules or functional groups absorb characteristic frequencies of radiation. In other words, the absorption spectrum acts as a fingerprint for identifying the various molecules that we see around us. This is the governing principle of absorption spectroscopy. Infrared (IR) spectroscopy utilises the infrared part of the electromagnetic spectrum which extends beyond the visible from around 700 nm. It can be broadly divided into near infrared (750 nm-3 μm), mid infrared (3-50 μm) and far infrared (50-1000 μm). Absorption of monochromatic radiation is governed by the Beer-Lambert law as given in equation 2.1

$$I = I_0 \exp(-\sigma(\nu)cl) \tag{2.1}$$

where I is the transmitted radiation intensity, I_0 is the incident monochromatic radiation intensity, $\sigma(\nu)$ is the absorptivity or absorption cross-section, c is the

concentration and l the pathlength. The product cl is the effective concentration which is a measure of the the number of absorbing molecules in the infrared beam path with units of molecules/cm^2. Absorbance is given by equation 2.2

$$A = -\log(T) = \sigma(\nu)cl \tag{2.2}$$

where T is transmittance, I/I_0.

Two conditions are assumed for the Beer-Lambert law to hold true. Firstly, this law applies only to monochromatic incident radiations. Actually, the intensity of a region of the electromagnetic spectrum that has a small spread of frequencies is being measured. Hence absorptivity, $\sigma(\nu)$ is expressed as a frequency dependant function. Secondly, it is also assumed that the concentration of the absorbing species is low. At low concentrations, the absorbing component will be surrounded by solvent molecules whereas at higher concentrations (saturated absorption), the absorbing species will be surrounded by other similar molecules. This change in environment will cause a change in the absorptivity, $\sigma(\nu)$ by, for instance, changing the hydrogen bonding. Hence at lower concentrations, absorbance will exhibit a linear dependance on concentration but at higher concentrations this linearity ceases to exist as other higher order terms of the exponential function need to be considered. The absorption of incident radiation by a molecule results in transitions between the vibrational levels producing vibrational spectra. The classical vibrational frequency for a diatomic molecule is given by equation 2.3

$$\nu = (1/2\pi)\sqrt{\frac{k}{\mu}} \tag{2.3}$$

where k is the force constant and μ is the reduced mass. This shows the effect of mass on molecular vibrational frequency.

2.2 Modes of Vibration

Each atom has three degrees of freedom to specify its motion along the three coordinates. So a molecule with n atoms will have 3n degrees of freedom. However, three of these are required for the translational motion of the molecule through space. In the case of non-linear molecules, three other degrees of freedom are required to specify the rotation of the molecule around its centre of gravity. A linear molecule requires only two. Hence a non-linear molecule has 3n-6 internal

degrees of freedom whereas a linear molecule has 3n-5 degrees of freedom. These degrees of freedom correspond to the various vibrational modes of the molecule. However, not all of them may be IR active. Only those vibrations that produce a change in the dipole moment are IR active. CO_2 is a linear triatomic molecule and thus has 4 modes of vibration, namely the symmetric stretch, asymmetric stretch and two degenerate bending modes, one out of plane and the other in plane. These are shown in figure 2.1. Out of these, the symmetric stretching mode is not IR active as there is no change in the dipole moment of the molecule.

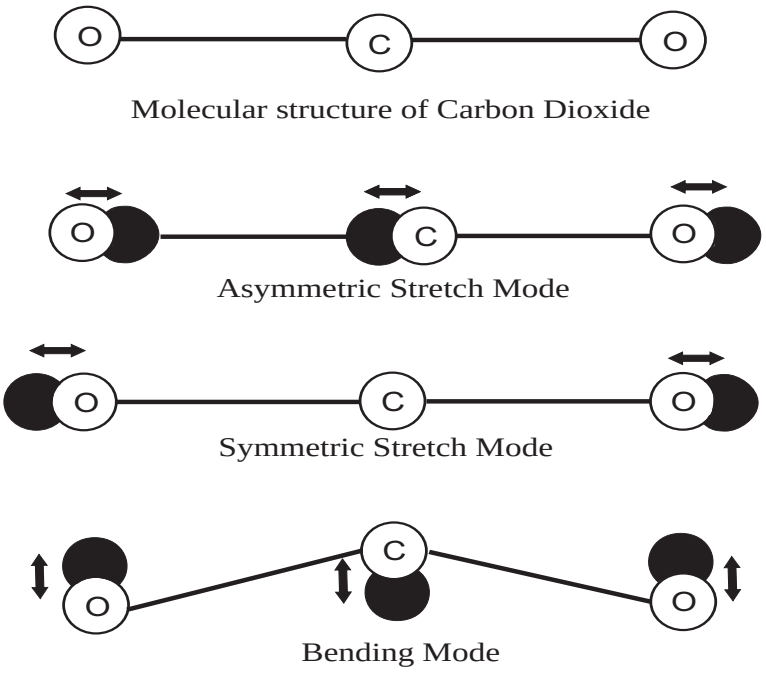

FIGURE 2.1: Vibrational modes of carbon dioxide

2.3 Rotational Vibrational Spectra of CO_2

Vibrational energy is quantized and has discrete values called energy levels given to a first approximation by equation 2.4

$$E_{vib} = (V + 1/2)h\nu \tag{2.4}$$

where V is the vibrational quantum number, h is Planck's constant and ν is the vibrational frequency. In order to interact with the incident electromagnetic radiation, the molecule should also have an oscillating dipole moment associated with the molecular vibration. This oscillating dipole moment leads to an exchange

of energy between the radiation and the molecule. As a result of this stipulation, homonuclear diatomic molecules, which do not produce a net change in their dipole moment, will not absorb the incident radiation and hence will have no vibrational spectra. Equation 2.4 is true for harmonic oscillators where the force holding the molecule is a linear function of the displacement of the atoms. A plot of displacement v/s time for such an oscillator will be sinusoidal. In anharmonic oscillators, the restoring force is not a linear function of displacement coordinates. Also the vibrational frequency is not completely independent of amplitude. For optical transitions in harmonic oscillators, V can vary by ± 1. Transitions where V changes from 0 to 1 are dominant and are called fundamental transitions. In anharmonic oscillators however, V can vary by ± 2, ± 3....giving rise to overtone transitions whose intensities depend on the anharmonicity of the molecule. These overtone transitions are generally weaker than their corresponding fundamentals (except for degenerate vibrations such as the bending mode in CO_2). The expression for vibrational energy in the case of anharmonic oscillators is given by equation 2.5 where x_e is the anharmonicity constant.

$$E_{vib} = (V + 1/2)h\nu - (V + 1/2)^2 h\nu x_e + ... \tag{2.5}$$

During IR absorption, rotational transitions also occur and these produce the rotational structure of absorption bands. In rotational transitions, absorption of a photon causes a change in the rotational frequency of the molecule unlike in vibrational transitions. Rotational energy levels are also quantized as expressed to a first approximation by equation 2.6

$$E_{rot} = BhcJ(J + 1) \tag{2.6}$$

where J is the rotational quantum number and B is the rotational constant derived from the moment of inertia I and is given by equation 2.7.

$$B = \frac{h}{8\pi^2 cI} \tag{2.7}$$

Since moment of inertia depends on molecular mass as shown in equation 2.8

$$I = \mu r_o^2 \tag{2.8}$$

where μ is the reduced mass of the molecule, it can be deduced that the rotational constant B also has a dependency on mass. This rotational constant has a slightly

different value for different vibrational levels. The is because the moment of inertia changes during a vibration in such a way that the average value of 1/I is not exactly the same as it is at the equilibrium position. A pure rotational IR spectra is produced only by those molecules that have a permanent dipole moment. Due to symmetry conditions, CO_2 belongs to the $D_{\infty h}$ point group. These do not have a permanent dipole moment and hence CO_2 does not have a pure rotational IR spectra. It produces ro-vibrational spectra due to the combined absorption by rotation and vibration. From equation 2.6, we expect to see rotational lines at equally spaced intervals of 2B cm^{-1}. This is based on the assumption that the molecule under consideration is a rigid rotor whose dimensions do not change with the rotation or vibration of the molecule. However, molecules are flexible and hence rotation causes a change in the bond length due to the effect of centrifugal distortion. The rotational energy expression for a non-rigid rotor is given by equation 2.9 where D is the centrifugal dissociation constant.

$$E_{rot} = BhcJ(J+1) - Dhc[J(J+1)]^2 \tag{2.9}$$

Consider a CO_2 molecule that is vibrating along the molecular axis and also rotating at the same time. The dipole moment is also oscillating and is given by

$$\mu = a\cos 2\pi\nu_v t \tag{2.10}$$

where ν_v denotes vibrational frequency. Suppose there is a plane polarised IR ray approaching this molecule oscillating along the X axis. At any given time, the molecular axis makes an angle θ with the X axis given by

$$\theta = 2\pi\nu_r t \tag{2.11}$$

where ν_r denotes rotational frequency. Therefore, the component of μ along the X axis is

$$\mu_x = \mu\cos\theta \tag{2.12}$$

$$\therefore \mu_x = a\cos 2\pi\nu_v t.\cos 2\pi\nu_r t \tag{2.13}$$

$$\mu_x = a/2[\cos 2\pi(\nu_v+\nu_r)t + \cos 2\pi(\nu_v-\nu_r)t] \tag{2.14}$$

Hence, this component of the dipole moment interacts with the IR rays of two frequencies (ν_v+ν_r) and (ν_v-ν_r). If we consider a large number of identical molecules, all of them will have the same ν_v but different values for ν_r which are quantized.

By plotting a distribution function of ν_r against the number of molecules, a peak value for ν_r can be obtained. This leads to the formation of a broad spectrum band spread across a range of frequencies. The asymmetric stretch in CO_2 causes the oscillating dipole moment to change along the molecular axis resulting, at low resolution, in a broad doublet band called a parallel band as shown in figure 2.2. The

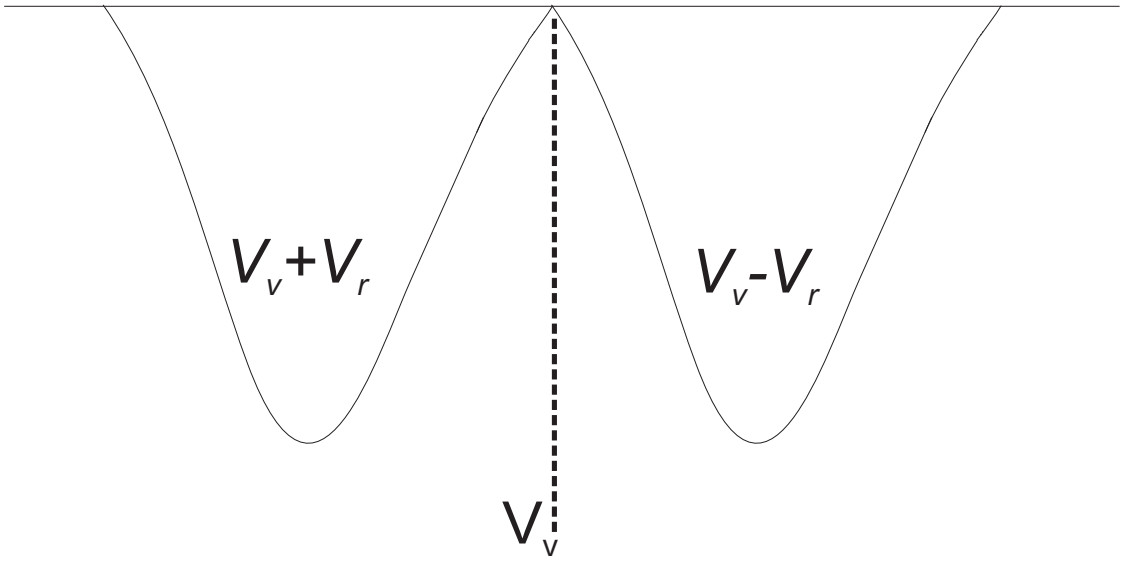

FIGURE 2.2: A parallel band formed from the asymmetric stretch mode resulting in a broad doublet at low resolutions with no central peak

bending mode on the other hand has two possible planes of bending. The molecule can rotate with equal probability about two mutually perpendicular axes. If the rotational axis is perpendicular to the plane of bending, then the dipole moment orientation changes along the molecular axis resulting in a broad doublet (parallel band). But if the rotational axis is parallel to the plane of bending, the dipole moment orientation does not change resulting in a central peak. Since both have equal probabilities, the total band is a combination of the two and is called a perpendicular band (broad doublet with a central peak) as shown below in figure 2.3.

On the basis of molecular symmetry, CO_2 belongs to the $D_\infty h$ point group. This defines certain selection rules that determine the allowed and forbidden transitions. Combining equations 2.4 and 2.6, the total ro-vibrational energy is given by equation 2.15

$$E_{v+r} = (V + 1/2)h\nu + BhcJ(J + 1) \tag{2.15}$$

Consider J'' is the rotational quantum number for the ground vibrational state, V=0 and J' is the rotational quantum number for the first excited vibrational state, V=1. Rotational selection rules permit parallel bands to have ΔJ=$\pm$1 and

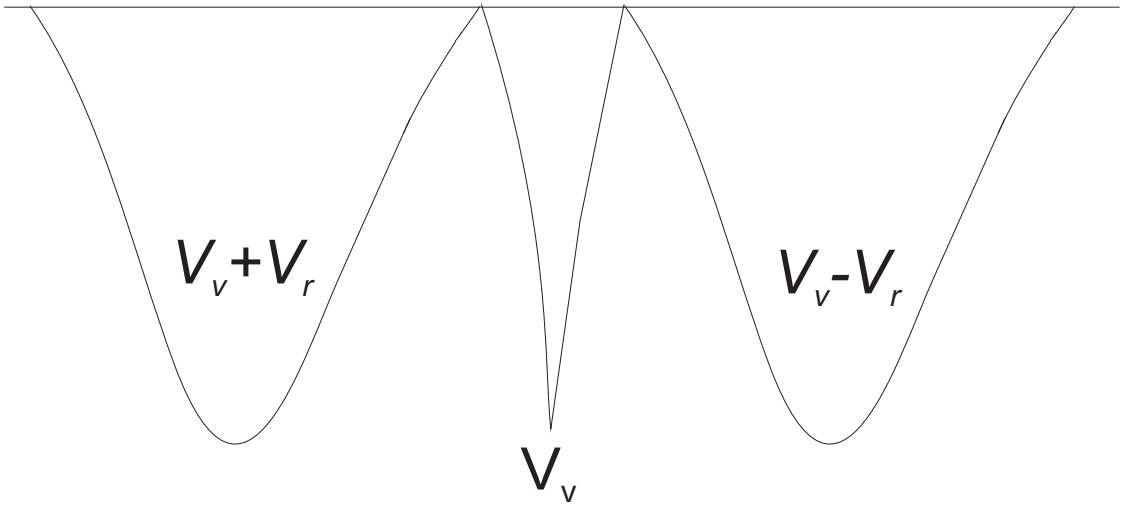

FIGURE 2.3: A perpendicular band formed from the bending mode resulting in a broad doublet at low resolution and a central peak

for perpendicular bands ΔJ=0,±1. Hence three different branches are produced depending upon the transitions of the rotational levels:

when ΔJ=-1 ie $J'=J''$-1 $\Longrightarrow$ P branch
when ΔJ=+1 ie $J'=J''+1$ $\Longrightarrow$ R branch
when ΔJ=0 ie $J'=J''$ $\Longrightarrow$ Q branch

Now equation 2.15 can also be expressed as

$$E_{v+r} = (V + 1/2)hc\bar{\nu_o} + BhcJ(J + 1) \tag{2.16}$$

where $\bar{\nu_o}$ is the band centre expressed in wavenumbers, cm^{-1}.

Hence, the energy change during a ro-vibrational transition for a rigid harmonic oscillator is given by

$$\frac{\Delta E_{v+r}}{hc} = \bar{\nu_o} + B[J'(J' + 1) - J''(J'' + 1)] \tag{2.17}$$

Hence, for a P branch

$$\frac{\Delta E_{v+r}}{hc} = \bar{\nu_o} - 2BJ'' \tag{2.18}$$

where J'' = 1,2,3...

For an R branch

$$\frac{\Delta E_{v+r}}{hc} = \bar{\nu_o} + 2B(J'' + 1) \tag{2.19}$$

where J'' = 0,1,2...

And for a Q branch

$$\frac{\Delta E_{v+r}}{hc} = \bar{\nu_o} \tag{2.20}$$

CO_2 has two strong IR absorption bands. The fundamental at 667.3 cm^{-1} is the perpendicular bending mode with P, Q and R branches and is designated as the ν_2 mode. The other strong fundamental absorption band occurs in the mid-infrared region of 2349 cm^{-1} which is the asymmetric stretch mode or the ν_3 mode. This is a parallel band and has no central maximum i.e., no Q branch. Apart from this, CO_2 also has a Raman active band or the ν_1 mode at 1340 cm^{-1}. This is a combination of two bands at 1288 cm^{-1} and 1388 cm^{-1} which are formed as a result of Fermi Resonance. This happens in anharmonic oscillators when the frequency of an overtone or a combination band may be nearly as same as that of a fundamental band. The resonance leads to perturbation of the energy levels and one of the level is pushed up and the other is pushed down due to repulsion. Only those vibrational levels that belong to the same species in terms of their symmetry can perturb each other. In such cases, two relatively strong absorption bands may be seen instead of a single band for the fundamental.

Chapter 3

Spectroscopic Methods

As discussed in section 1.3, UBTs have become the universally accepted method for the diagnosis of *H.pylori*. But there are different ways in which these tests can be performed. Almost all of these methods are based on infrared (IR) spectroscopy and several spectroscopic instruments have been designed in the past, each exhibiting varying degrees of accuracy and precision. Some of the prominently used techniques and their salient features are described briefly in the following sections.

3.1 Non-Dispersive Techniques

Instruments based on non-dispersive infrared spectroscopy (NDIRS) do not make use of any dispersive elements such as prisms or gratings and hence whole band absorption measurements are carried out. They offer a cheap and reliable alternative to IRMS. Optical filters can be used to restrict the IR window to a particular region of interest.

Non-dispersive infrared heterodyne spectrometry is a non-dispersive technique that was employed for the measurement of isotope ratios[27]. This spectrometer detects a heterodyne signal that is generated by the partial absorption of amplitude modulated radiation in pressure modulated gas samples. The modulation of the infrared radiation is achieved by passing it through gas samples whose density is modulated by a sinusoidal wave.

The radiation, ν_o, from the source is passed through a cell which contains a gas with density ρ_1 that is density modulated to $\Delta\rho_1$ at frequency ω_1 by means of a pneumatic modulator. This results in the generation of a fundamental F_1 at ω_1.

When this amplitude modulated signal is absorbed by a second gas at density ρ_2 and frequency ω_2, it generates not only another fundamental F_2 at ω_2 but also a heterodyne signal $H_{1,2}$ at $\omega_1 \pm \omega_2$. This signal is proportional to the concentration of absorbing species in the second cell and is given by equation 3.1 shown below.

$$H_{1,2} = [(1/2)\mu_1\mu_2 l_1 l_2 \Delta\rho_1 \Delta\rho_2 cos(\omega_1 - \omega_2)t]e^{-\Delta_o} \tag{3.1}$$

where Δ_o is a static component given by

$$\Delta_o = \mu_1 l_1 \rho_1 + \mu_2 l_2 \rho_2 \tag{3.2}$$

This principle can be used for the measurement of carbon isotopes by first passing the radiation through two optical cells containing a known amount of $^{12}CO_2$ and $^{13}CO_2$ respectively. The modulated radiation is then passed through a third cell containing the sample gas having both ^{12}C and ^{13}C. As a result, two additional heterodyne signals, $H_{12,S}$ and $H_{13,S}$, will be generated as shown in equation 3.3. Here ΔP_S is the pressure change of the sample gas and C_S^{12} and C_S^{13} are the concentrations of ^{12}C and ^{13}C in the sample gas.

$$\begin{aligned} H_{12,S} &= \mu_{12}^2 l_{12} l_S \Delta\rho_{12} \Delta P_S C_S^{12} \\ H_{13,S} &= \mu_{13}^2 l_{13} l_S \Delta\rho_{13} \Delta P_S C_S^{13} \end{aligned} \tag{3.3}$$

$$R_S = C_S^{13}/C_S^{12} = K H_{13,S}/H_{12,S} \tag{3.4}$$

where $K = (\mu_{12}^2 l_{12} \Delta\rho_{12})/(\mu_{13}^2 l_{13} \Delta\rho_{13})$

From equation 3.4 it is clear that the isotopic concentrations can be determined from the heterodyne signal. This instrument was reported to have achieved a precision of 0.4‰ and an accuracy of 1.3‰ within 120s on a sample of 3% CO_2. However, this method also has its drawback in the form of a liquid N_2 cooled InSb detector. This adds to the cost and complexity of the design. It takes about 5 minutes from start for the detector to be cooled. In addition, this technique requires larger breath samples than the IRMS. The use of pneumatic systems for pressure modulation is also inconvenient. Several comparisons between the IRMS and NDIRS were carried out[28, 29, 30] to evaluate the performance, reliability and accuracy of NDIRS. The results have shown that with proper collection protocols and test procedures, NDIRS can be used as a cheaper and viable clinical alternative to the IRMS although it may exhibit lower precision and accuracy.

3.2 Narrowband Techniques

These techniques make use of dispersive elements to achieve a high degree of wavelength selectivity when broadband sources are used. This makes it possible to resolve the individual absorption lines and hence the chances of coincident absorption bands are greatly reduced. The use of dispersive elements can be avoided by using lasers. However, this adds to the total cost of the system.

Photoacoustic (PA) spectroscopy is one such technique that has been employed for isotopic studies[5, 31, 1]. This method made use of a continuously tunable CO_2 laser with a bandwidth of 0.017 cm^{-1}. Studies were carried out on multicomponent CO_2 mixtures in the 9 μm to 11 μm region. The continuous tunability was achieved by operating the laser at a higher pressure of 11.5 bar resulting in a strong overlap of the pressure broadened transitions. The laser can be tuned between the 9R, 9P, 10R and 10P branches between 9.2 μm and 10.8 μm with a pulse duration of about 100 ns. The beam is allowed to pass through a non-resonant PA cell containing the gas mixtures. This beam excites the ro-vibrational energy levels of the gas molecules. A pressure wave is produced inside the cell by means of radiationless decay which is detected using a microphone. The experimental setup is shown in figure 3.1.

By using a fitting procedure to superimpose the spectra of individual compounds, concentration of the individual compounds were determined. However, this method achieved poor sensitivity because CO_2 absorption was not optimum in this wavelength region. Greater sensitivity can be achieved in the 4.3 μm region provided an adequate tunable source exists. The technique requires small gas quantities and is relatively easy to handle. However, from a purely commercial point of view, it still does not fulfill the needs of a low cost clinical instrument. The use of laser sources itself contributes to the design complexity and costs.

Laser analysis of isotope ratio based on the optogalvanic effect has also been employed for carbon isotope ratio measurement[32]. The optogalvanic effect is based on the detection of an electrical signal in response to a stimulation of resonant transition in a discharge species. In this particular case, the change in discharge impedance was detected. A CO_2 laser was used and the laser transitions were identical to the probing transitions. The transitions used were P(22) $^{12}CO_2$ line at 10.6 μm and the corresponding $^{13}CO_2$ line at 11.2 μm. This resonant laser transition induces a change in the molecular excited state population which in turn causes a change in the ionization rate. This finally produces a change in the

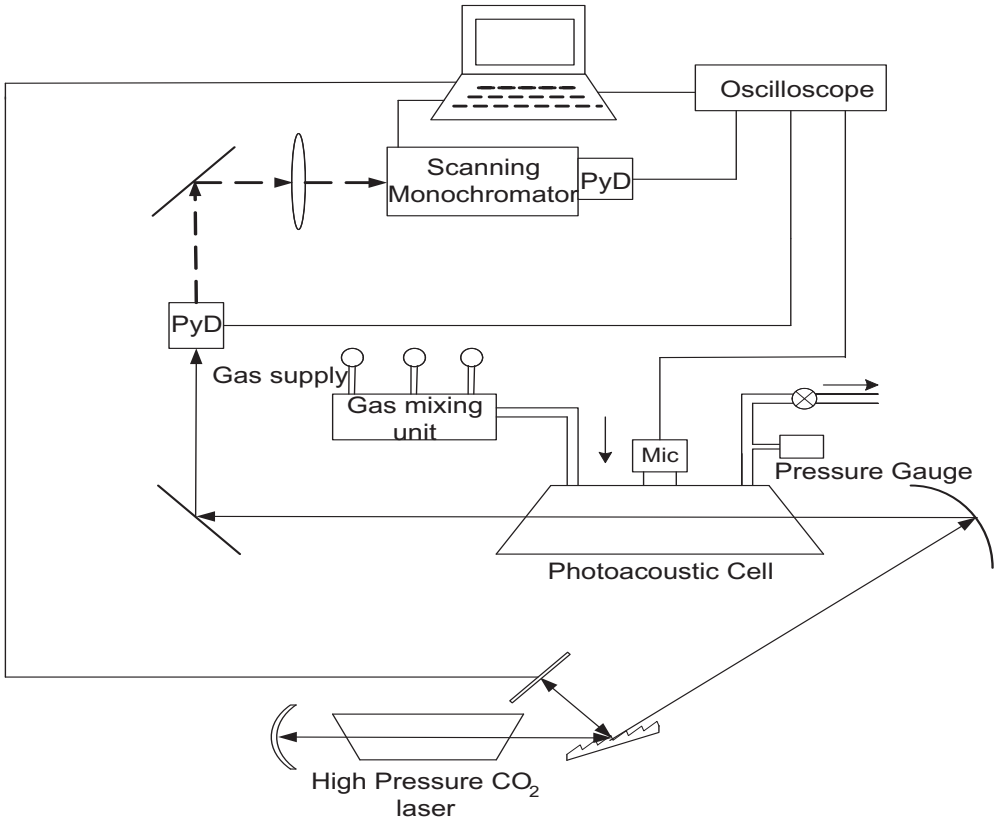

FIGURE 3.1: Experimental setup for PA investigations with continuously tunable CO_2 laser, redrawn from [1]. PyD's, pyrolectric detectors; Mic, microphone

electrical impedance of the discharge which is detected. Tests were conducted on an exhaled breath sample and the results were impressive. The system reported a precision of 10 ppm with a sensitivity and accuracy comparable to that of IRMS. This method has several advantages such as total elimination of any optical components and elimination of background optical noise. The only sample preparation was that the subject's breath was passed through a desiccator before entering the discharge cell. However, the use of gas lasers does not make it a cost effective solution and that explains why this technique has not been accepted as a clinically viable solution.

3.3 Tunable Diode Laser Systems

Another major technique that has been successfully employed for UBTs is the tunable diode laser absorption spectroscopy (TDLAS). A TDLAS system based on wavelength modulation spectroscopy with first harmonic detection was developed

for isotope ratio studies at 2.008 μm[2]. The schematic of the experimental setup is shown in figure 3.2. In this case a distributed feedback (DFB) diode laser was used. The isotope ratio in the sample cell is determined by comparing its spectra with that obtained from the reference cell. The laser frequency is scanned over the absorption regions by means of a triangular wave at 0.045 Hz. Tuning is achieved by varying the injection current by using a modulating signal at 10 Hz. Lock-in amplifiers were used for first harmonic detection for better S/N ratio. Line pairs were chosen taking into account their temperature effects and relative abundances. The system, however, displayed lower long term precision and drifts from zero value when both the cells had the same gas composition. This was attributed to certain non-linear absorption effects. Operating pressures were reduced and a better precision of 0.7‰ was obtained with reduced drift. However, further work needs to be done to achieve greater temperature stabilisation. A similar procedure was also followed for isotopic studies at 1.6 μm[33] and an accuracy of 0.5% was reported. An external Fabry-Perot interferometer was used for frequency stabilisation. A major problem with these systems is the poor S/N ratio due to the low absorption strengths and line intensities. This is particularly the case for the rarer isotope of ^{13}C. A logical solution is to perform these tests at a longer wavelength of 4.3 μm where there is stronger absorption but the low prevalence of DFB lasers that operate in the mid-infrared region is a hindrance.

The use of line pairs for the purpose of isotope ratio measurement poses other problems. If two lines of similar absorption strengths are chosen then it may affect the measurement precision due to the disparity in their absorption depths. However, if this is overcome by considering lines of unequal strengths, temperature dependencies of the lower transition states come into play once again affecting the precision. A solution was proposed in the form of a balanced absorption setup[34] where the major and minor isotopes were measured with different pathlengths so as to compensate for the large difference in their concentration. The minor constituent ($^{13}CO_2$) was measured using a pathlength which was 72 times greater than that used for the major constituent ($^{12}CO_2$). This ratio is comparable to the ratio of their natural abundances and hence both have similar absorption depths. At the same time line pairs of equal lower state energy distribution can be chosen so that any temperature fluctuation will reflect equally on both the lines. In order to avoid problems caused by optical interference fringes in multi pass cells, a complex cell design such as the off-axis resonator (Herriott) was used. A precision of 0.2‰ was reported[34].

Many other TDLAS based systems have been developed[35, 36] for the non-invasive

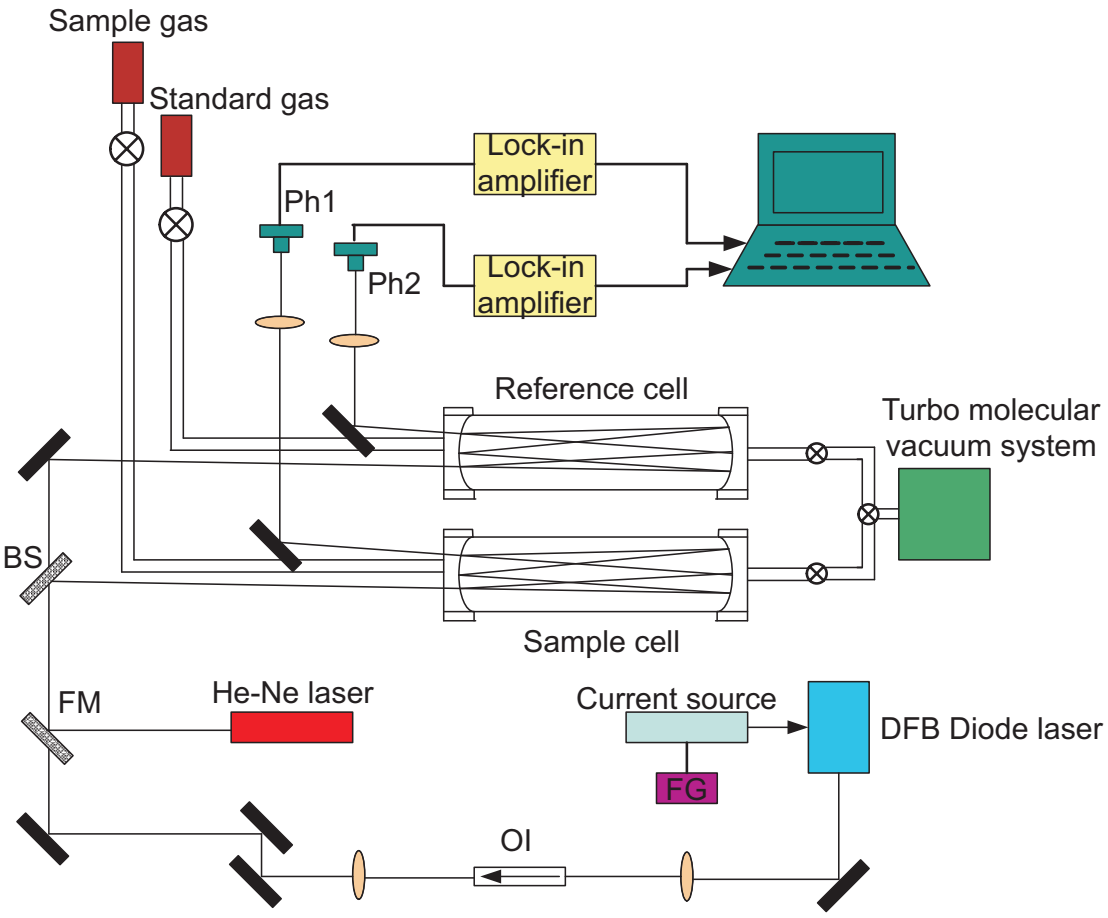

FIGURE 3.2: Schematic diagram of the TDLAS experimental setup, redrawn from [2]. FG, function generator; FM,flipping mirror; BS, beam splitter; OI, optical isolator; Ph, photodiode

diagnosis of *H.pylori*. These systems used lead salt lasers that were operated in the 4.3 μm region which offers the most suitable IR window for carbon isotope analysis due to sufficient absorption strength, prevalence of well isolated lines and absence of interference from other compounds having coincidental absorption bands. However, the use of lasers and MCT (mercury cadmium telluride) or InSb detectors which require adequate cooling adds to their cost and design complexity. CO_2 laser systems with intracavity absorption cells have also been used for isotope analysis in atmospheric samples[37, 38].

3.4 Other Related Work

With UBT gaining increased popularity and acceptance as an effective non-invasive diagnostic tool, focus was also turned to evaluate its performance in comparison with other existing methods for diagnosis. For instance, urea blood tests were compared with UBT and tests were performed on several patients[39]. Results showed 95% agreement between the two. These blood tests eliminated the need for any basal tests. However, the blood samples had to be analysed using IRMS which involved shipping costs and delays in getting the results. UBT was also found to be as accurate and sensitive as antral histology, rapid urease test and CLO test[40, 41, 42]. But the accuracy and sensitivity of UBTs are affected by the dosage of C-13 meal and also the postdose measurement time[43]. Lower carbon dioxide concentration in exhaled breath (<2%) has been shown to decrease the specificity and accuracy of these tests[44]. Holding the breath for 5s before exhaling seems to improve the situation. Several recommendations for the improvement of test accuracy, specificity and sensitivity have been made in the form of improved test protocols such as breath collection procedures, optimum C-13 enriched dose and postdose measurement time and also the need for fasting and abstinence from any drug intake prior to the test[45, 46, 47]. Studies have also been conducted to further simplify the procedure by eliminating the collection of basal breath samples provided the post-dose samples are collected 30 minutes after urea intake[48, 49]. A rather recent form of invasive technique for the diagnosis of *H.pylori* infection was developed with the use of ion-sensitive field effect transistor (ISFET)[50]. It consists of a solid phase tip coated with a monoclonal antibody towards *H.pylori*'s urease which adsorbs the enzyme after 15 minutes of immunological interaction with a gastric mucus sample. This urease is analysed in a measuring cell containing urea solution. The pH change of urea solution after 55 seconds was measured using a pair of reference and measuring ISFET thereby indicating the presence of urease enzyme. Results showed a 92% sensitivity and 98% specificity using UBT as a gold standard.

3.5 Proposed Instrument Design

As stated in section 1.4, the prime objective of this research project is to develop a low cost and effective spectroscopic instrument that could be a possible clinical alternative to the IRMS. It must not be prone to environmental fluctuations in

temperature or pressure and must provide a stable response with sufficient accuracy and precision so that it can be employed for breath tests. On the basis of the literature review and issues presented in the previous sections, it was concluded that such an instrument will have to be one that is based on non-dispersive IR spectroscopy.

In order to avoid problems posed by unequal line strengths, a balanced absorption system configuration was designed making whole band integrated absorption measurements rather than comparing individual line pairs. The IR window of 4.3 μm was chosen for performing the measurements due to the strong absorption of CO_2 ν_3 mode. Besides, IR technology in the mid-infrared region offers a variety of optical materials, transmission windows and suitable detectors. A comprehensive study of the various possible interfering compounds present in human exhaled breath was published by Mansfield[26] and it showed that this particular IR region was free from all such coincident absorption bands. It is necessary to avoid coincident absorption bands because a change in such bands can be misinterpreted as a change in C-12 or C-13 bands and hence reduces the responsivity of the system. Figure 3.3 presents an overall schematic of the proposed spectroscopic instrument.

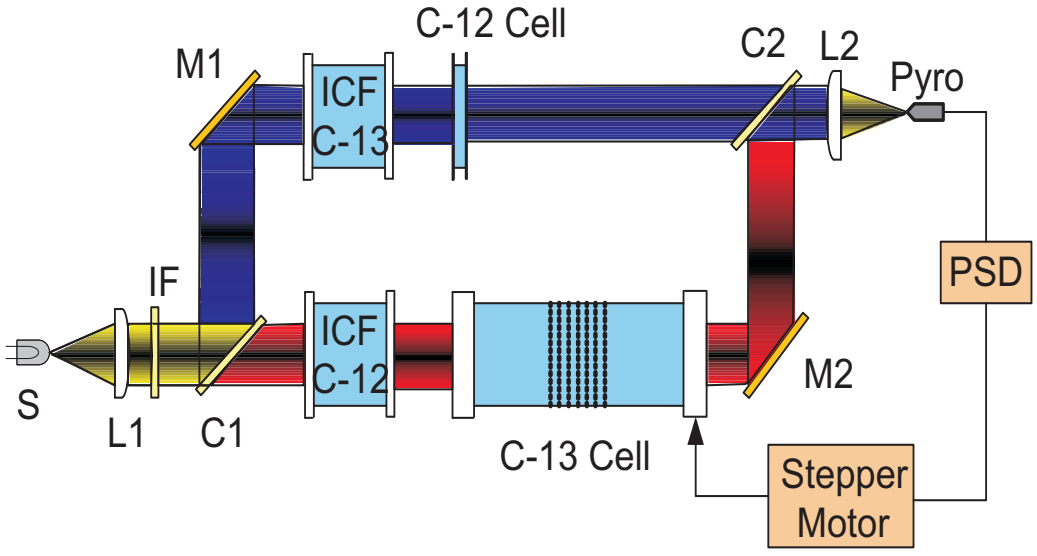

FIGURE 3.3: Schematic diagram of the proposed two channel non-dispersive infrared spectrometer

The proposed instrument[51, 52] involves the use of a single broad band IR source, S (any blackbody) that interacts with the two isotopomer channels individually. The beam is collimated by lens L1 and then passed through an IR interference

filter, IF, to restrict the bandwidth to the region of interest, 4.1 μm - 4.6 μm approximately. This window spans from the P(60) line of $^{13}CO_2$ to the R(60) line of $^{12}CO_2$ covering 99.9% of the total band strength. The beam is then redirected alternately along the two channels by the reflective chopper C1, as described later in this section. Henceforth, $^{12}CO_2$ will be represented as C626 which denotes the mass numbers of the constituent atoms, O(16)-C(12)-O(16). Similarly, $^{13}CO_2$ will be represented as C636. A major unique feature of this setup is the use of isotope correlation filters (ICF) to enhance selectivity. These filter cells are made of almost 100% pure C-13 or pure C-12 depending on which isotopomer is being measured. The C-13 channel thus contains an ICF filled with pure C-12 (C626) whereas the C-12 channel ICF is made of pure C-13 (C636). This eliminates cross-interference caused by the overlapping spectra of the two isotopomers. Figure 3.4 gives a pictorial representation of the use of ICF.

The beams are then passed through the gas cells containing first the baseline or reference sample prior to urea administration and then the breath sample after urea intake. The transmitted beams are then made to fall on the same detector. This is made possible by the second chopper C2 which is synchronised to be at anti-phase relative to C1. The novelty of this design lies in the use of a variable length gas cell for the C-13 channel. The two cell lengths are roughly in the ratio of the natural abundances of the two isotopomers (90:1), implying that the C-13 channel cell length is around 100 times that of the C-12 channel cell length. This ensures balanced absorption for both the channels. The measurement is based on a novel feedback mechanism whereby the C-13 cell length is initially adjusted so that the detector gives a null output for equal basal integrated transmittances. In the case of excess ^{13}C after urea administration, the unequal absorption will unbalance the system. The error signal from the phase sensitive detector (PSD) will then cause the servo loop to change the pathlength of the C-13 cell so as to drive the system back to balanced condition or null output. The subsequent change in length of the C-13 cell will then be a direct measure of the increase in $^{13}CO_2$ concentration from which the delta value can be evaluated. A point to be noted here is that this system essentially performs a ratioing of the two channel lengths and hence measures the relative change in concentrations and not the absolute concentrations of the two isotopomers. This ratioing feature significantly reduces its vulnerability to ambient fluctuations, variations in detector responsivity, source temperature variations or other possible interferences as long as they affect both the channels equally.

The detector plays a very important role as far as S/N ratio is concerned and it was

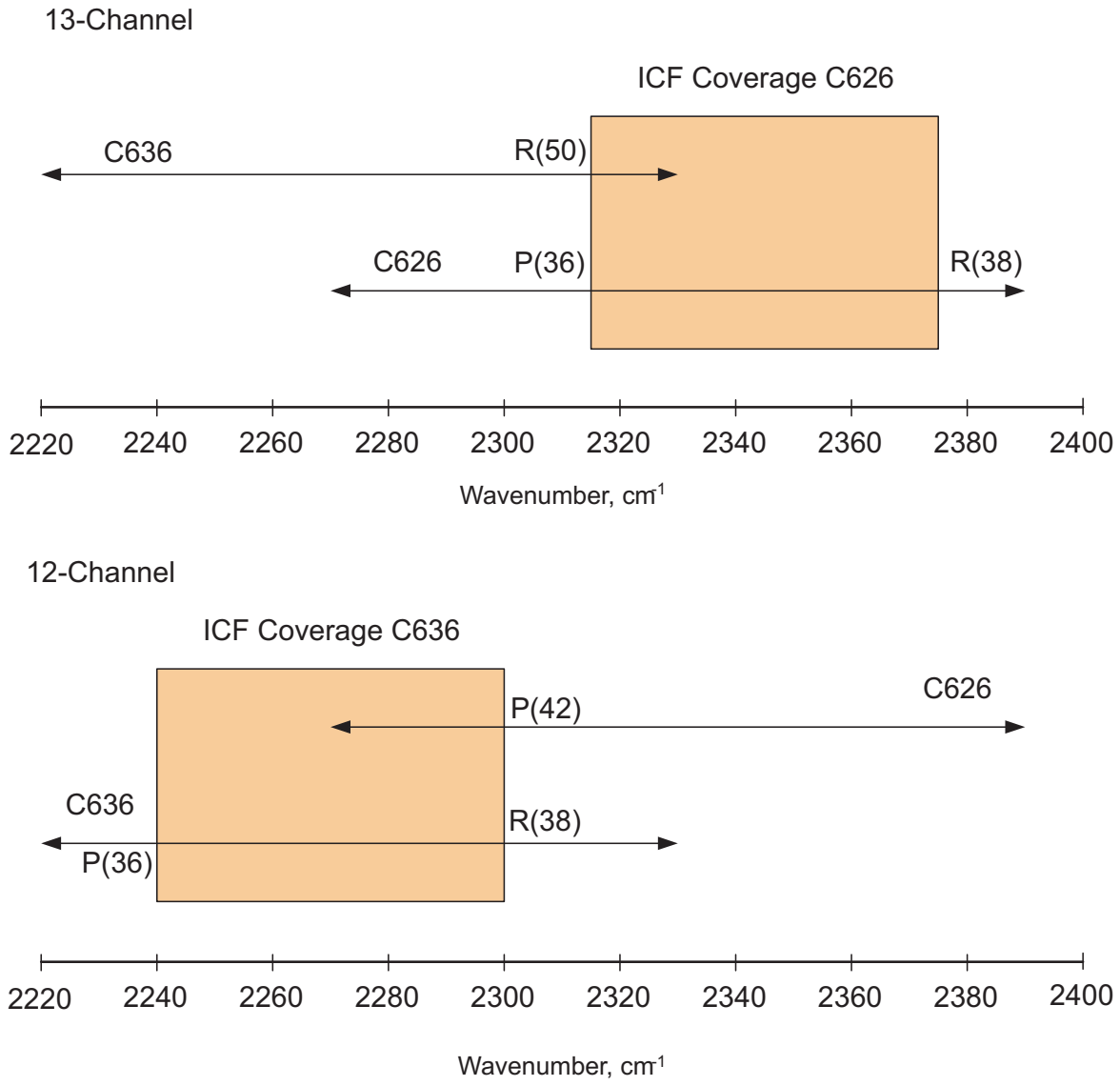

FIGURE 3.4: Schematic diagram of filter cell domains. The rectangular boxes represent the ICF domains whereas the bars represent the total spectrum spread of the individual isotopomers

decided to use a very sensitive pyroelectric detector due to its high sensitivity, low cost and operation at room temperature thereby eliminating the need for a liquid N_2 cooling arrangement. Since the scheme involves a slow measurement process, faster response times such as those offered by MCT or InSb were not required. The only requirement is for the IR radiation to be chopped since pyroelectric detectors respond only when a temperature change occurs in the element. The signal from the detector is applied to a phase sensitive detector which generates the required signal to drive the feedback servo loop. The polarity of this output from the phase sensitive detector provides the directional information for the servo loop and this

determines whether to increase or decrease the C-13 cell length. The magnitude of this output signal indicates how far off the system is from balance and hence represents the proportional term of the loop.

Another unique feature of this instrument design is the proposed use of a pair of synchronised chopper systems, C1 and C2, that also act as reflecting mirrors. This innovative design avoids the use of costly beam splitters and also avoids the undesirable consequence of 50% power loss that is normally associated with 50-50 beam splitters. The choppers will be synchronised and inclined at an angle of 45° with the beam axis. When the incoming radiation strikes the reflective blades of C1, it gets reflected and redirected along the C-12 channel after striking mirror M1. C2 will remain open for the same period of time and allow the transmitted beam to fall on the detector. Similarly, when C1 allows the beam to pass through the C-13 channel, it gets reflected by mirror M2 and falls on the the blades of C2 which will reflect the beam on to the detector. This ensures that only one beam is recorded at a time by the detector which also receives the reference signal from the choppers.

As seen from the above, the proposed instrument incorporates several unique features in terms of the measurement technique involved, the components used and the overall layout. The use of a feedback servo loop to achieve balanced integrated absorption along the two channels avoids the need to make any absolute concentration measurements, unlike most of the other conventional designs. Instead, a change in cell length is used as a measure of change in concentration and this variable path length design is a novelty in field of isotope ratio measurements. The ratioing method involved ensures automatic cancellation of common noise sources and hence provides the system better immunity from such interferents. The use of synchronised reflecting choppers is another novelty and to the best of our knowledge, this has not been attempted before in the field of isotope ratio studies. This has a significant effect in keeping the overall cost of the instrument low thus making it a very attractive solution for practical and commercial applications. The use of small and simple optical and electronic components lends greater portability to the overall instrument and this will help in meeting the stated objective of a portable and low cost diagnostic tool that requires minimum human intervention. The research work presented here thus explores the feasibility of a unique instrument that combines innovative design features and measurement methodologies.

Chapter 4

Computational Studies and Analysis

4.1 Development of CO_2 Spectroscopic Model

In order to fully understand the behaviour and analyse the performance of a CO_2 spectroscopic instrument as described in the previous chapter, it was imperative to develop a highly accurate spectroscopic model of the 4.3 μm ν_3 absorption mode. This computer model can then be used to perform several simulations to ascertain the effects of fluctuations in ambient conditions and other interferents that may result in spurious results. Development of such a spectroscopic model essentially involves the following three steps.

4.1.1 Modelling of Absorption Line Positions

The first step was to accurately determine the position of the various line transitions that needed to be included in the model. It must be noted that only those transitions that had the required impact on the calculation of a delta value were considered significant enough to be incorporated in the model[26]. The vibrational rotational energy in wavenumbers is given by equation 4.1 where the spectroscopic constants G_v, B, D and H were derived from HITRAN (High-resolution TRANsmission) database[53, 54, 55, 56, 57].

$$\Delta E_{v+r}(\nu, J) = (G'_v - G''_v) + B'J'(J'+1) - D'J'^2(J'+1)^2 + H'J'^3(J'+1)^3... \\ .... - B''J''(J''+1) + D''J''^2(J''+1)^2 - H''J''^3(J''+1)^3 \quad (4.1)$$

where G'_v-G''_v is the band centre also denoted by $\bar{\nu_o}$, B is the rotational constant, D is the centrifugal distortion constant and H is the anharmonicity constant. All the single primed and double primed values denote the upper and lower states respectively. The same equation can be applied for the P, Q and R branches by simply altering the values of J' and J'' as mentioned in section 2.3.

4.1.2 Modelling of Absorption Line Strengths

Once the position of the line transitions were determined, the individual rotational line strengths, $S(T)$[cm^{-1}/molecule cm^{-2}] were computed using equation 4.2

$$S_{v+r}(T) = [\frac{\Delta E_{v+r}}{\bar{\nu_o}}][\frac{S_v^0 L_{J''l} E_{J''} F_{J''}}{Q_R}][1 - exp(\frac{-hc\Delta E_{v+r}}{KT})] \tag{4.2}$$

where S_v^0 is the rotationless band strength from HITRAN, $L_{J''l}$ is the Honl-London factor, $E_{J''}$ is the Boltzmann distribution, $F_{J''}$ is the Herman-Wallis factor, T is the temperature, 296K, K is the Boltzmann's constant, h is the Planck's constant, c is the speed of light and Q_R is the rotational partition function.

The probability of a transition is not a constant but depends on the number of available degenerate levels in the upper transition state and this is represented by the Honl-London factor which gives the number of participating rotational levels at a given value of J''. This is given by

$$L^P_{J''l} = \frac{(J''+l)(J''-l)}{J''} \tag{4.3}$$

$$L^Q_{J''l} = \frac{(2J''+l)(l^2)}{J''(J''+1)} \tag{4.4}$$

$$L^R_{J''l} = \frac{(J''+l+1)(J''-l+1)}{J''+1} \tag{4.5}$$

where the superscripts P, Q and R denote the respective branches.

Herman-Wallis factor accounts for effects such as Fermi Resonance, Coriolis Interaction and Centrifugal Distortion that arise from the interaction between rotation and vibration which may alter the bond strength. For P and R branches, this is given by

$$F_{J''} = (1 + a_1 m + a_2 m^2 + a_3 m^3)^2 \tag{4.6}$$

where m equals -J'' for P branch and J''+1 for R branch. For a Q branch, the

Herman-Wallis factor is given by

$$F_{J''} = (1 + b_2 m^2)^2 \tag{4.7}$$

where m is equal to J''. Here a_1, a_2, a_3 and b_2 are the Herman-Wallis coefficients.

The intensity of a transition line depends on the population of the lower transition level. The population of a rotational level is related to the rotational partition function Q_R which is a normalising factor that is used to give a constant intensity as the intensity distribution varies with temperature. Thermal distribution $E_{J''}$ is given by

$$E_{J''} = exp\frac{B''hcJ''(J''+1)}{KT} \tag{4.8}$$

For rigid harmonic oscillators at normal temperatures, the partition function can be expressed as[58]

$$Q_R = \frac{KT}{Bhc} + \frac{1}{3} + \frac{1}{15}\frac{Bhc}{KT} + \frac{4}{315}(\frac{Bhc}{KT})^2 + \frac{1}{315}(\frac{Bhc}{KT})^3 + ... \tag{4.9}$$

For small B and large T, the rotational partition function can be evaluated using a simpler expression[58] given by

$$Q_R = \frac{KT}{Bhc} \tag{4.10}$$

Both equations 4.8 and 4.10 when combined alters the intensity profile of each rotational line depending upon the change in temperature. The vibrational contribution to the partition function Q_v can be easily evaluated if anharmonicities are neglected. These can be neglected safely only for lower vibrational levels for which the neglect of the interaction of vibration and rotation is also permissible. This has been included in the rotationless band strength S_v^0 obtained from HITRAN database.

4.1.3 Line Shapes

The final step is to develop the line shape. IR absorption does not take place at one single frequency but it has a measurable width. At normal pressures of 1 atm, this width is mainly due to collisional broadening and is described by the normalised Lorentzian function as given in equation 4.11

$$f_L(\bar{\nu_o}) = \frac{\gamma/\pi}{[(\bar{\nu_o} - \Delta E_{v+r})^2 + \gamma^2]} \tag{4.11}$$

where γ is the pressure broadening coefficient or the half line width at half intensity. However, at low pressures, Doppler effect becomes the dominant broadening factor and this results in a Gaussian line shape. In the present case, Lorentzian line shape is considered since the study is carried out at atmospheric pressures.

The above procedure is followed for each of the transitions being considered and finally the line strength is multiplied with the line shape taking into account contributions from other lines whose Lorentzian tail will significantly increase the intensity. This product then represents each rotational line's wavenumber dependent absorption coefficient. These are then summed together to obtain a continuous branch profile. This is repeated for the P, R and Q branches as required and finally added together to get the complete CO_2 spectrum. The same procedure is repeated for both the isotopomers but with different constants as provided by the HITRAN database[57]. The entire modelling work was accomplished by writing MATLAB codes (see Appendix B). The overall absorption spectrum for both the isotopomers in the 4.3 μm region present in their natural abundance is shown in figure 4.1. Henceforth $^{12}CO_2$ and $^{13}CO_2$ will be referred to as C626 and C636 respectively, as shown in the figure, for convenience. This spectrum was simulated at a standard temperature and pressure of 296K and 1 atm using a data resolution of 0.005 cm^{-1}. As seen in the figure, C636 has a much reduced absorption because its isotopic abundance is almost 100 times lower than C626. It can also be observed that the R branch of C636 has been distorted due to the saturated absorption from the P branch of C626.

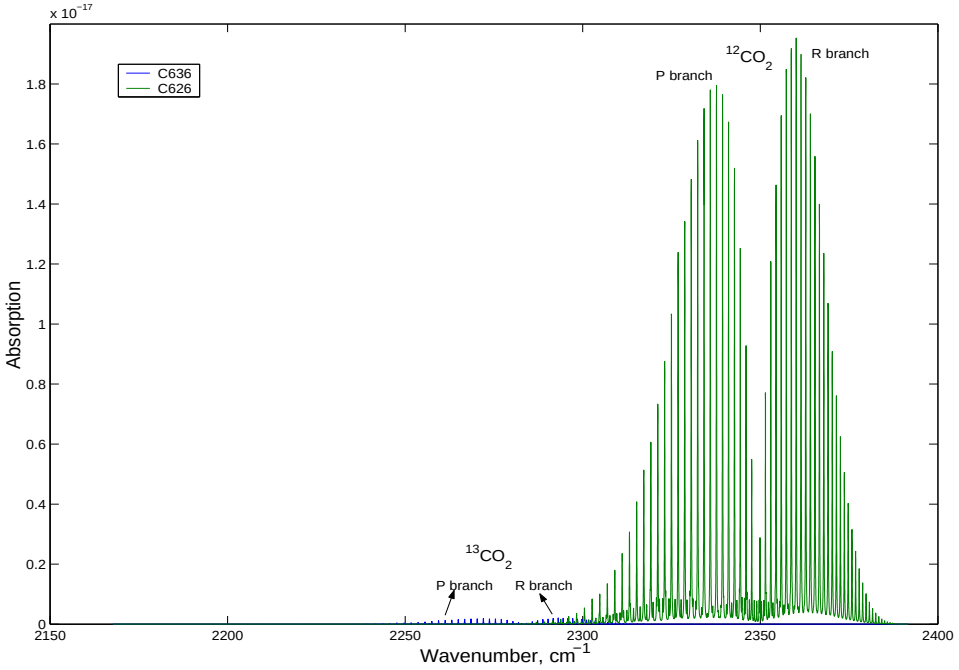

FIGURE 4.1: Simulated overall absorption spectrum of C626 and C636

4.1.4 Validation of the Model

Before the spectroscopic model developed can be used to perform simulation studies to predict the instrument responses, it needs to be tested for its accuracy. The accuracy of the model was determined by comparing the line positions and intensities obtained from the model with those obtained from the HITRAN database. Results of these comparisons showed excellent agreement between the two as represented by figures 4.2 and 4.3.

Figure 4.2 shows the error in line positions for P and R branches of C626 fundamental transition. As can be seen, the maximum error is around 0.00004 cm^{-1} which translates to roughly 1.2 MHz. Considering that the average rotational line width of a C626 fundamental transition at FWHM (full width half maximum) is about 4.8 GHz, this error is only about $1/4000^{th}$ of a typical line width indicating the high accuracy of the model.

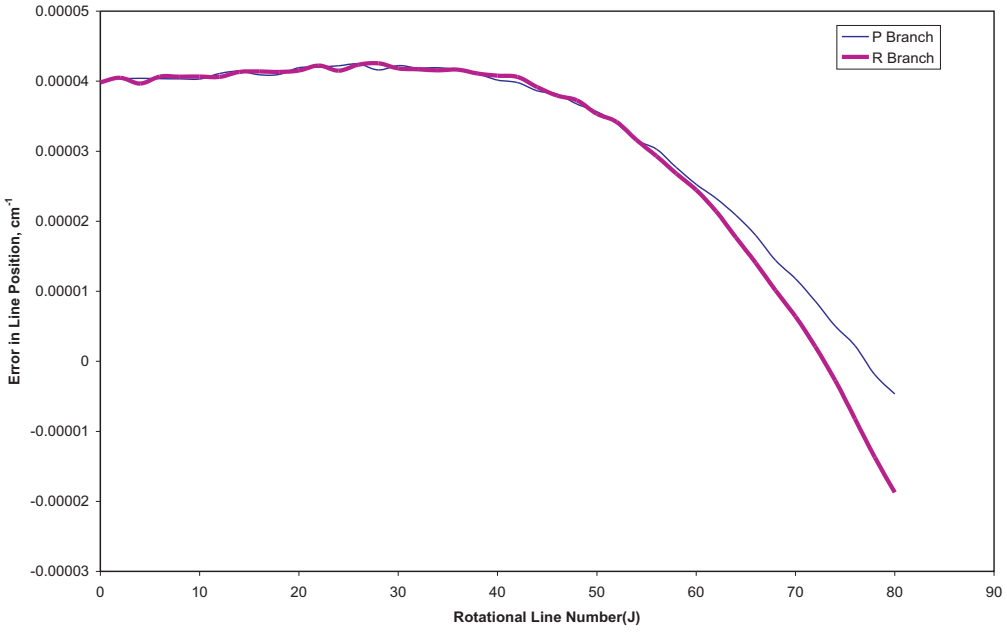

FIGURE 4.2: Error in line position for P and R branches of C626 fundamental transition

Figure 4.3 shows the percentage error in line strengths for C626 fundamental transition. Near the branch's maximum intensity (J=16), the error is around 0.02% which rises to about 0.8% for J=60. Since rotational lines from J(0) to J(60) cover about 99.9% of the branch intensity distribution, it can be safely concluded that majority of the branch has been modelled to a high degree of accuracy. Similar results were also obtained for C636 fundamental and other hot band transitions. Hence a highly reliable and accurate spectroscopic model has been developed which can be used for further simulation based studies.

The effect of varying temperature and pressure on the absorption profile of CO_2 can also be seen from the spectroscopic model as further proof of its validity and reliability. Let us first examine the effect of increased pressure on the absorption spectrum. If pure CO_2 is considered, then an increase in gas pressure will lead to an increase in the number of molecules. This causes increased collisions between the various molecules which eventually leads to pressure broadening of the rotational lines. For CO_2, the pressure broadening rate is about 7 MHz/Torr or 0.17 cm^{-1}/bar. Since the integrated area under the line is representative of the number of molecules, an increase in pressure will result in broadened line widths but having the same peak intensity so as to have an increase in overall area under the curve. This fact is shown in figure 4.4 and the increase in line width is about 0.08 cm^{-1} on one side which gives a total increase in line width of 0.16 cm^{-1}. This

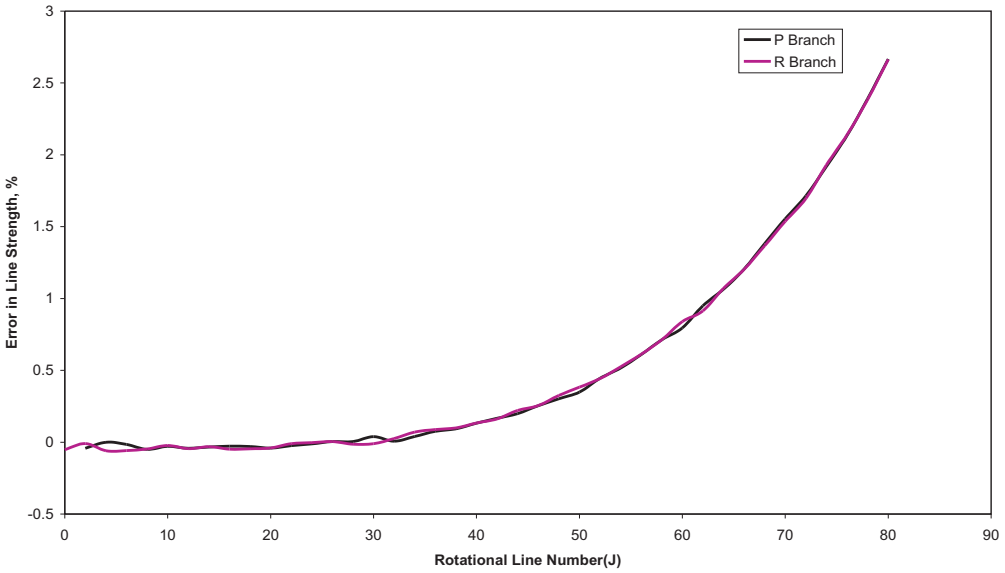

FIGURE 4.3: Error in line strength for P and R branches of C626 fundamental transition

is very much in agreement with the predicted value and is further testimony to the accuracy of the model.

A change in temperature also alters the absorption band profile of the gas under investigation. In the case of fundamental transitions, increase in temperature shifts the peak towards higher J rotational lines, which is towards lower wavenumbers for P branch and higher wavenumbers for R branch. This is clear from figure 4.5. It can also be seen that the lower rotational lines get weaker whereas the higher rotational lines get stronger.

4.2 Channel Spectral Profiles

The next step towards the realisation of a working instrument was to develop a model for the complete device by integrating the various individual components. Such a model when fully developed will exhibit all the properties and behavioral characteristics of the final instrument. This is necessary to perform instrument response simulations and characterisation. The basic instrument setup was shown earlier in figure 3.3. Values of key parameters such as concentration of gas cells and filter cells and their optimum lengths were determined for a balanced transmission in both the channels. Considering 4% of human exhaled breath is made of CO_2[59],

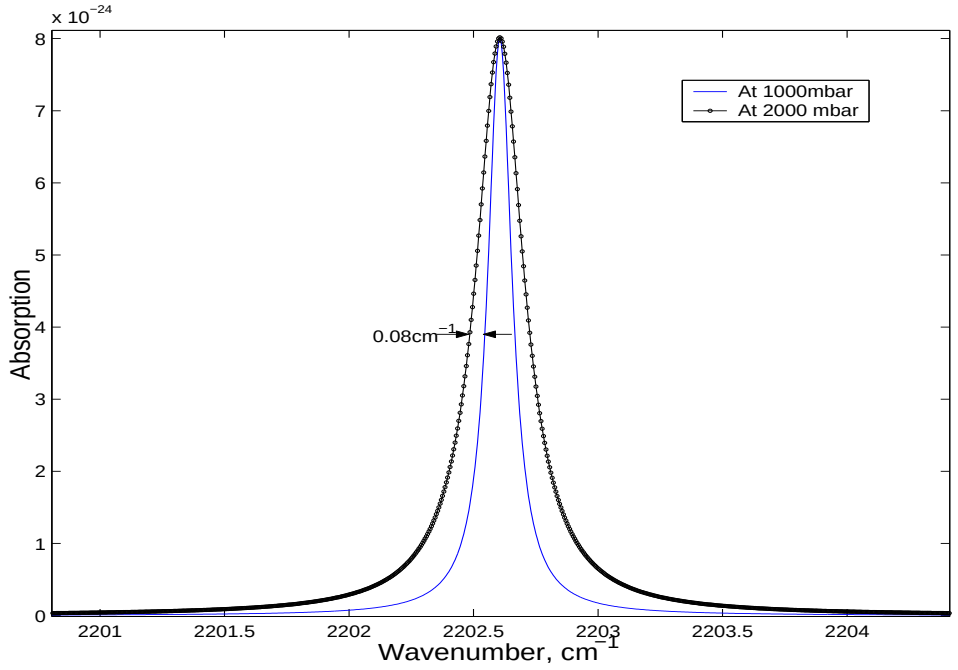

FIGURE 4.4: Figure showing pressure broadening effect in pure C636 J(40). Increased pressure leads to broadening of the line with the same peak intensity leading to an increase in the overall area under the curve

concentration of $^{13}CO_2$ is 1.1836×10^{16} mol/cm^3 and that of $^{12}CO_2$ is 1.064×10^{18} mol/cm^3 at STP. With a broadband infrared source at 674K (which corresponds to a peak emission wavelength of 4.3 μm), it was found that a 12-channel cell pathlength of 0.1 cm will require a 13-channel cell pathlength of 10.245 cm in order to achieve balanced absorption along both channels. Both the filter cells had an effective concentration (length$\times$concentration) of 3.766×10^{19} mol/cm^3 at 100% isotopic purity. The IR filter was assumed to be a square pass band filter having a pass band covering the entire IR region over which CO_2 absorption has been modelled i.e. from 2167.7 cm^{-1} to 2391.7 cm^{-1} or from 4.18 μm to 4.61 μm. Using these values, codes were written for instrument response simulations. The transmission spectrum for both the filter and sample cells were first developed to give a better understanding of the utility of filter cells and how it avoids channel cross-sensitivity.

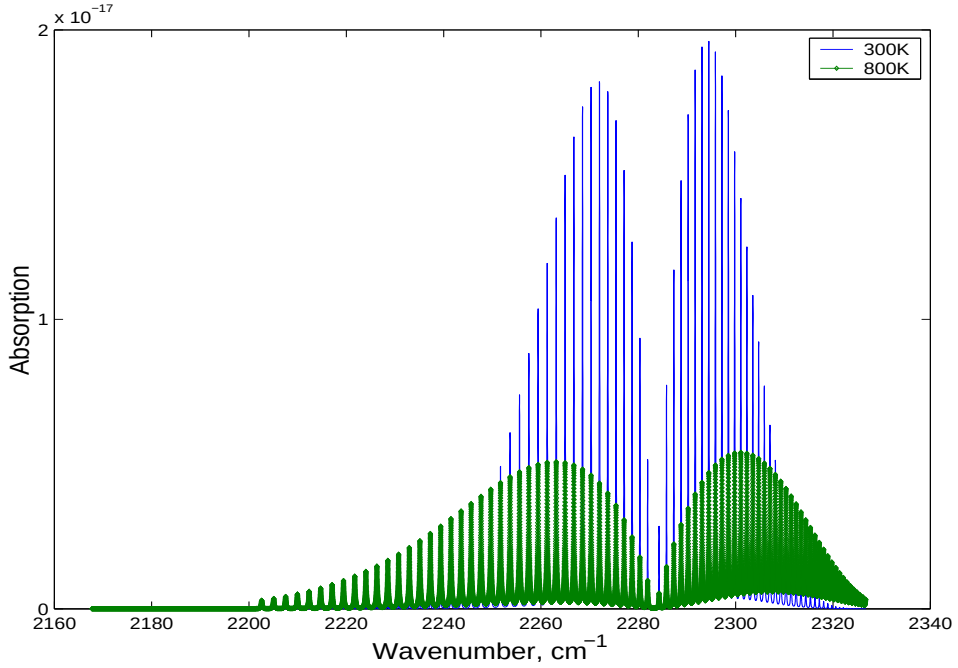

FIGURE 4.5: Effect of temperature increase on band profile for C636 fundamental

Figure 4.6 shows the 12-channel filter and sample cell spectral profile. Similarly figure 4.7 represents the 13-channel spectral profiles for the filter and sample cells. The distortion of C636 R branch by saturated C626 P branch can be clearly seen in figure 4.7(B).

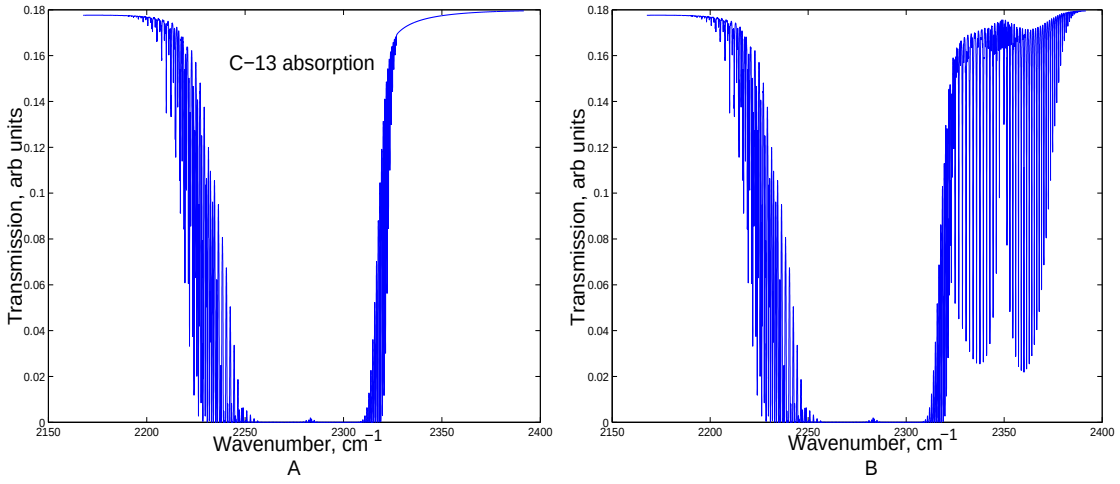

FIGURE 4.6: Simulation of 12-channel filter cell transmission profile containing 100% pure C636(A) and overall channel transmission profile(B)

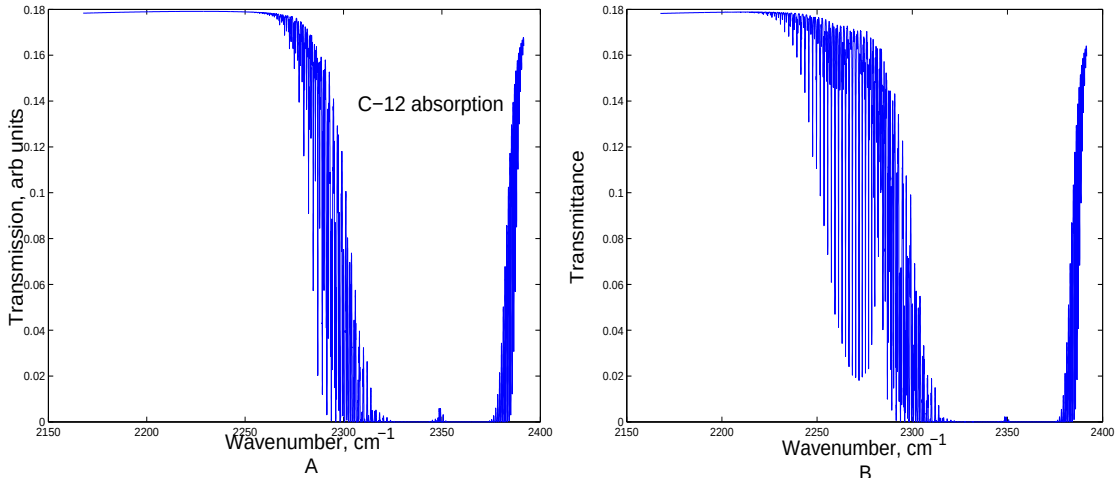

FIGURE 4.7: Simulation of 13-channel filter cell transmission profile containing 100% pure C626(A) and overall channel transmission profile(B)

4.3 Simulation of Spurious Results

Various sources of interferents were identified[26] that will produce spurious results by generating apparent delta. These spurious results reduce the accuracy and sensitivity of the instrument and will result in false positive or false negative results which will have greater repercussions for the patient, apart from reducing the specificity of the instrument. With the development of an instrument model, simulations were performed to evaluate the effect of these interferents individually on the final delta value. Based on these results, proper control measures can be put in place to ensure reliability of the diagnostic result. The results are detailed below.

4.3.1 Effect of Source Temperature Stability

For the blackbody radiation to have a peak value at 4.3 μm, the source should ideally be at 674K. A deviation from this temperature will only alter the equilibrium 13-channel pathlength required for balanced absorption but it will have no effect on the final delta value as long as the same source temperature is maintained throughout the course of the experiment. This can be attributed to the inherent ratio nature of the system and can be proved by measuring the equilibrium lengths required for different source temperatures as shown in figure 4.8.

From the figure it is evident that as source temperature increases the optimum 13-channel cell length required decreases. At first glance this seems strange since

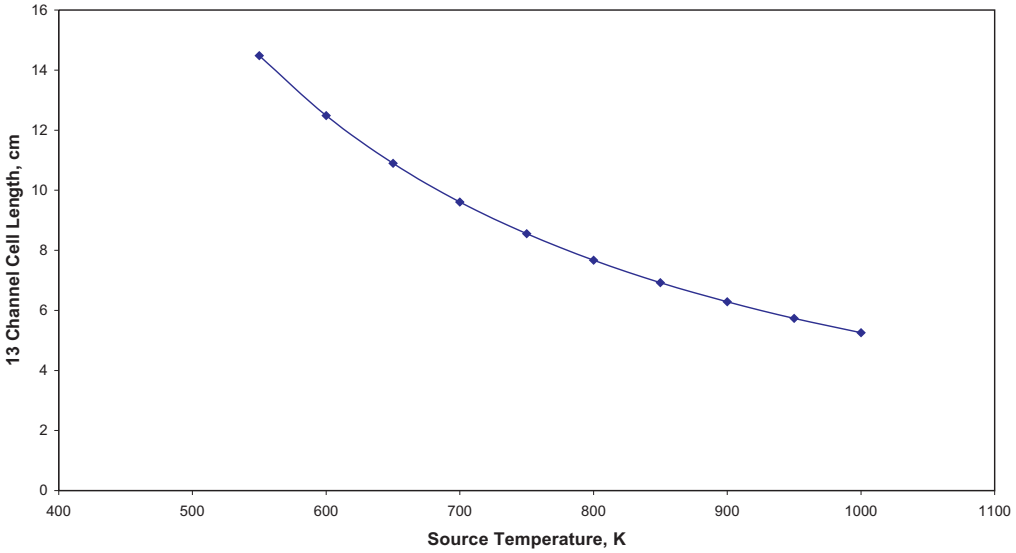

FIGURE 4.8: 13-channel cell length required for equilibrium absorption at various source temperatures

an increase in source temperature will cause the blackbody curve to shift towards the lower wavelength region implying greater C626 absorption. Hence in order to balance out the intensities from both channels the 13-channel cell length will also have to be increased which is contrary to what the figure shows. The reason for this can be understood if one takes into account the complete absorption process sequentially starting from the filter cells. For this purpose the following arrangement was considered. Let I1 and I2 be the infrared intensities emanating from the pure C-13 and pure C-12 filter cells respectively and let I3 and I4 be the intensities from the 12-channel and 13-channel sample cells respectively. Simulation studies were performed to determine the ratio of intensities I1/I2 and I3/I4 at various source temperatures and figure 4.9 shows the results. At temperatures below 674K, the blackbody curve shifts towards the higher wavelength C-13 region and hence there will be greater absorption in the 12-channel filter. As a result I1 will be less than I2 and the ratio I1/I2 will be less than one. Since the sample cell lengths have been chosen for equilibrium absorption, I3/I4 will also be less than one. In order to bring the system back to balance, the 13-channel cell length will have to be increased beyond 10.245 cm to bring down I4, as shown in figure 4.8. At temperatures above 674K, the reverse process takes place with increased 13-channel filter absorption and a subsequent decrease in 13-channel cell length for balanced absorption. It can be noted that at 674K, I1/I2 is still slightly less than one. This is due to the fact that the blackbody curve is not exactly symmetrical

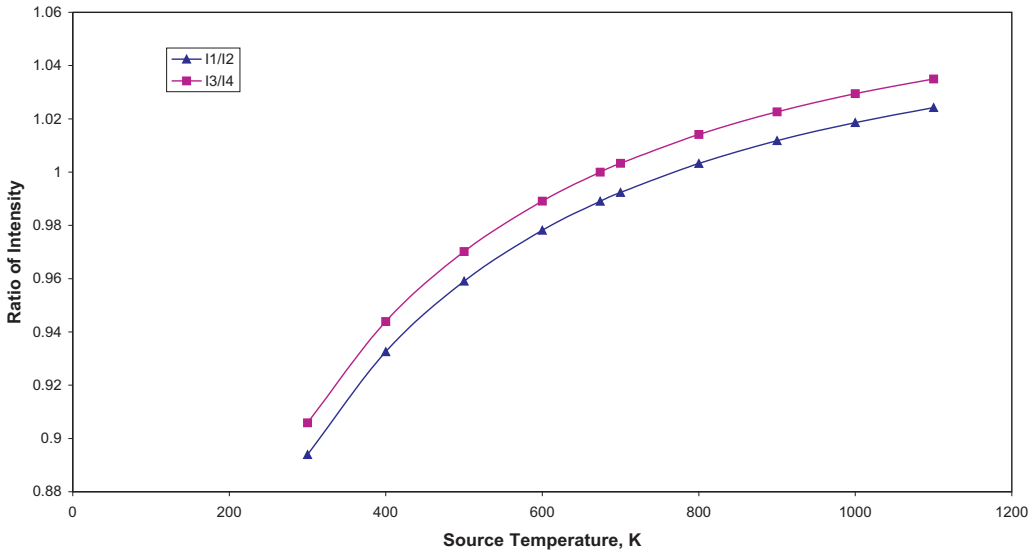

FIGURE 4.9: Ratio of IR intensities from both the channels at various temperatures

around 4.3 μm and hence resulting in more C636 absorption. However, this offset is compensated for by choosing appropriate cell lengths for both the channels so that I3/I4 is exactly equal to one.

However, if the source temperature varies between the basal and sample tests, it will result in serious apparent delta values as shown in figure 4.10. Here the basal temperature was maintained at 674K but the experimental temperature was varied from 550K to 1000K. Figure 4.11(A) shows us that at 674K, a temperature change of 1K produces an apparent delta of about 2.5‰ or in other words, source temperature has to be stabilised to around ±0.4K for a 1‰ precision. The source temperature is currently set by controlling the voltage supplied to it from the power supply. If the source temperature fluctuation is beyond permissible limits, active temperature control using a thermistor or RTD will be required in order to eliminate apparent delta values that will give rise to spurious results. However, if we were to operate the source at higher temperatures, it seems that the apparent delta produced by 1K change decreases in a more or less linear fashion. This is clear from figure 4.11(B) where 1‰ is produced by a temperature change of about 0.65K when source temperature is 1074K. This indicates that operating the source at higher temperatures is more beneficial as it slightly eases the constraints imposed by source temperature stability.

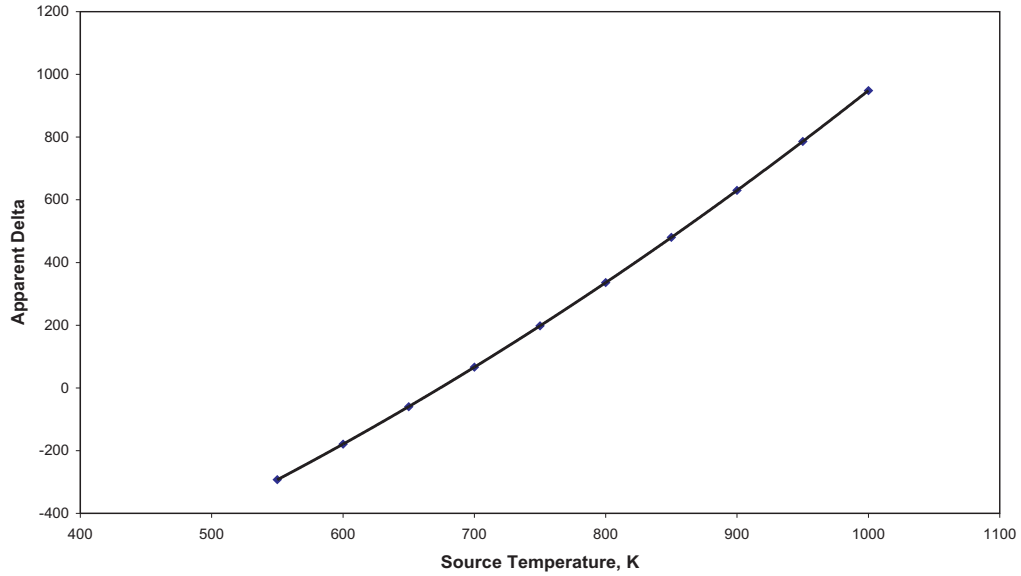

FIGURE 4.10: Apparent delta due to source temperature variation with a basal temperature of 674K

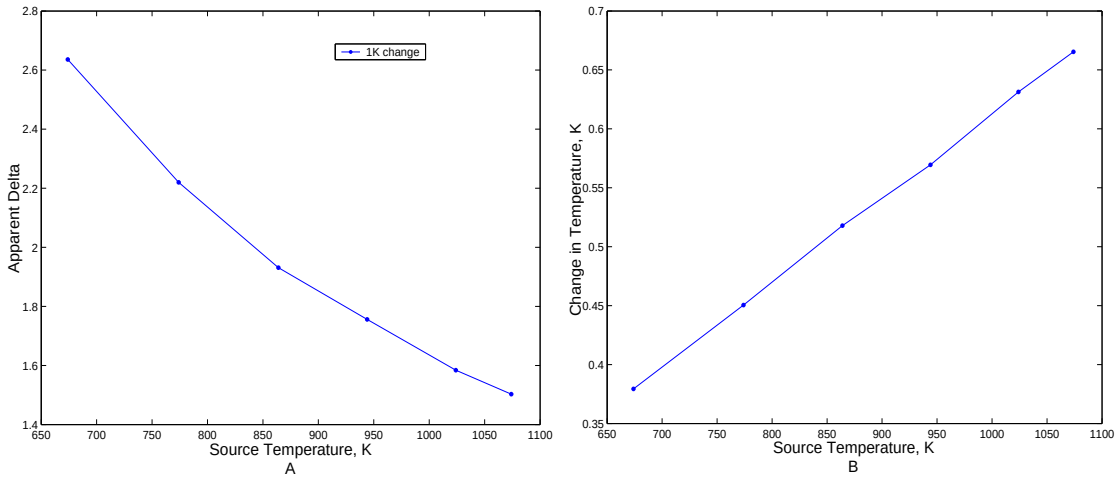

FIGURE 4.11: Apparent delta produced by 1K shift in source temperature(A) and maximum tolerable temperature shift for 1‰(B)

Operating the source at higher temperatures will cause the equilibrium 13-channel cell length to decrease as shown in figure 4.8. This is due to the shifts in the blackbody curve with temperature as shown in figure 4.12. For ease of comparison, exitance has been normalised in the figure. It can be seen that at temperatures below 674K, there is a significant change in the shape of the curve that falls within the IR filter window, with respect to the reference curve shape at 674K. At higher temperatures, the shift is not so severe. This explains the reason for the dramatic change in the equilibrium cell length required for temperatures below 674K as

evidenced from the steep slope of the curve in this region in figure 4.8.

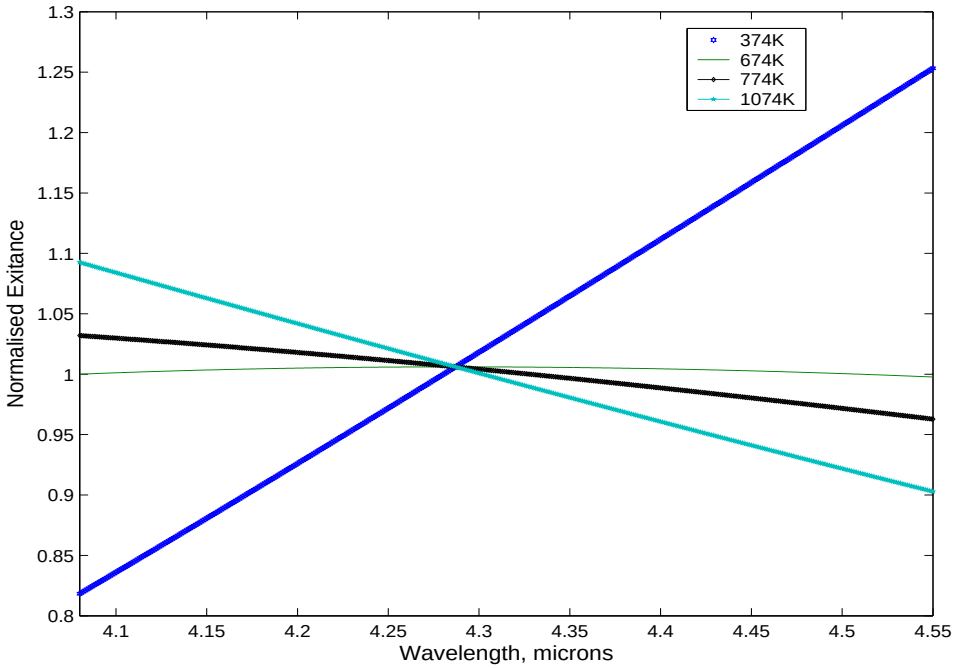

FIGURE 4.12: Blackbody curves with normalised exitances at various temperatures

4.3.2 Etalon Temperature Stability

Another source of spurious results investigated by Mansfield[26] was etalon temperature effect. The windows for the filter and sample cells act as low finesse etalons producing multiple beam interference. This leads to modulation of the transmitted intensity of infrared radiation as given by equation 4.12

$$I/I_0 = \frac{1}{1 + F \sin^2 \delta/2} \tag{4.12}$$

where F is the finesse and δ is the phase difference. Figure 4.13 shows the modulation of transmitted intensity by etalon fringe effects.

If the temperature of the windows remain the same throughout the course of the entire test, these fringe effects will be ratioed out as background. However, a change in the temperature during the course of a test will shift the fringes causing a change in the delta value.

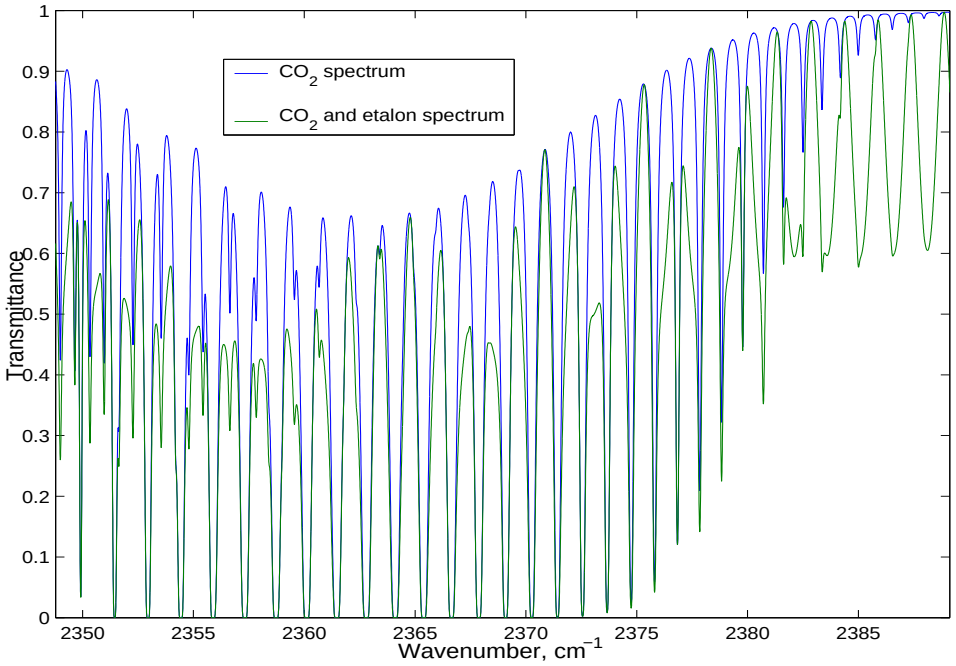

FIGURE 4.13: Modulation of transmission spectrum by etalon fringes at 296K for a 2mm thick calcium fluoride window

Fringe shift for CaF_2 windows is shown in figure 4.14. Maximum modulation of the transmission, T% takes place over one FSR (Free Spectral Range which is the distance between two peaks) and T_{FSR} is the temperature required to move over a distance of 1 FSR. Among the various window materials commonly used, fluorides are considered to be a better choice due to their higher T_{FSR} and lower cost. Modulation of delta in the case of CaF_2 is shown in figure 4.15 indicating a T_{FSR} of around 18K. A solution to this problem is to wedge the face of the window thereby introducing a deliberate difference in thickness. The phase difference induced produces Fizeau fringes that incoherently add up to give almost no interference. The wedge angle depends on the optimum number of fringes that will minimise this effect and this is represented by equation 4.13. The upper limit of wedge angle is set by the resultant optical deviation.

$$\theta = \frac{N\lambda/2}{na} \tag{4.13}$$

where N is the number of fringes, a is the window thickness and n is the refractive index of the medium. For CaF_2, it was shown that a wedge angle of 0.82 mrad producing 10 fringes was ideal[60].

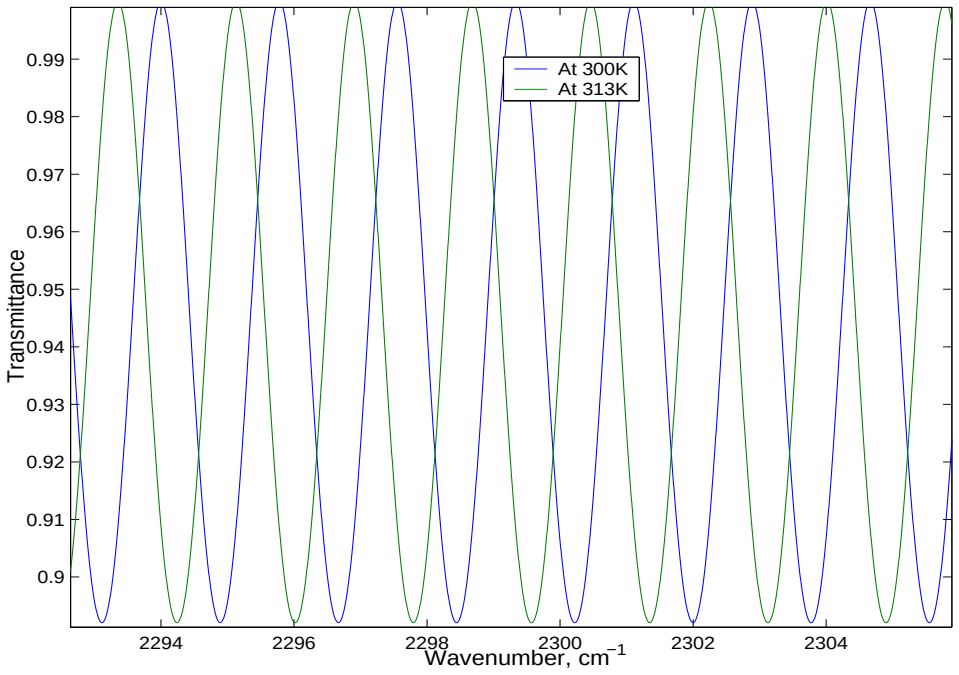

FIGURE 4.14: Etalon shift due to temperature variation in calcium fluoride

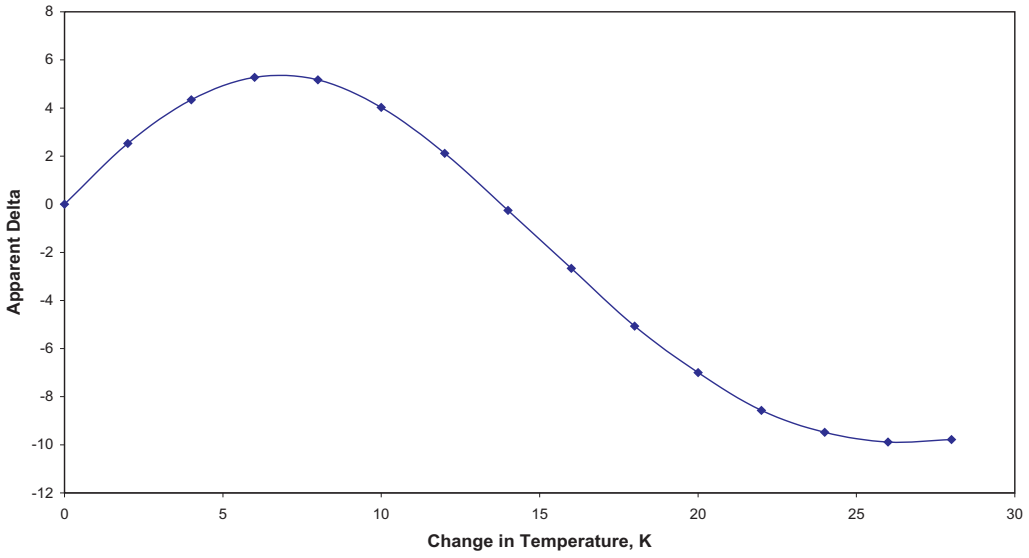

FIGURE 4.15: Modulation of delta due to etalon temperature instability for calcium fluoride window

4.3.3 Effect of Ambient Temperature and Pressure

Temperature and pressure inside the cells were also found to affect the observed delta as they will alter the absorption profile of CO_2. Simulations were performed by changing the temperature of the cells between the basal and sample tests assuming thermal equilibrium among the cells themselves. The basal temperature was maintained at 296K and the sample test temperature was then gradually varied. The results are shown in figure 4.16. It can be seen that a change of 1K in temperature produces a change of -2.1‰. This implies that in order to restrict the delta variation to 1‰, cell temperature stabilisation of ±0.5K is required. In order

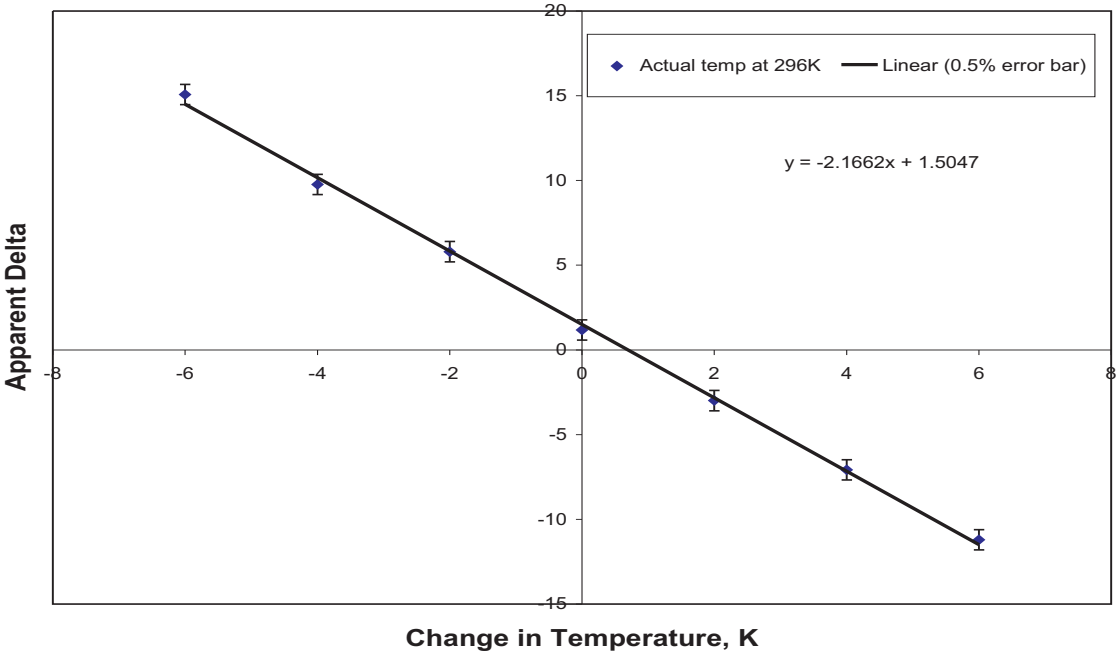

FIGURE 4.16: Effect of ambient temperature variation on apparent delta

to monitor real time cell temperature variations, a temperature sensor LM35CZ (c.f. Figure A.1) will be attached to the walls of the filter and sample cells. The signal from the sensor can be used to perform calibrations in real time in case the temperature fluctuation exceeded permissible limits. Further analysis and control measures will be devised after observing real time variations of temperature.

Pressure effects were also studied by running simulations at various pressures and the results are presented in figure 4.17. Average fluctuation in pressure is about 1-2 mbar/hr which will result in a change of only 0.4‰. Since the effect of ambient pressure was much less significant, it was decided that no pressure controls are necessary although a monitoring of the cell pressures will be done. The pressure in the filter cells remains constant as it remains sealed once filled with the

pure isotopomer. During the filling process, pressure gauges will be employed to regulate the flow. However, for the sample cells, a pressure sensor SDX15A2 (c.f. Figure A.2) from Sensym will be connected to the gas delivery tubes that enter the sample cells. This will help to constantly monitor any abrupt pressure fluctuations although they are unlikely.

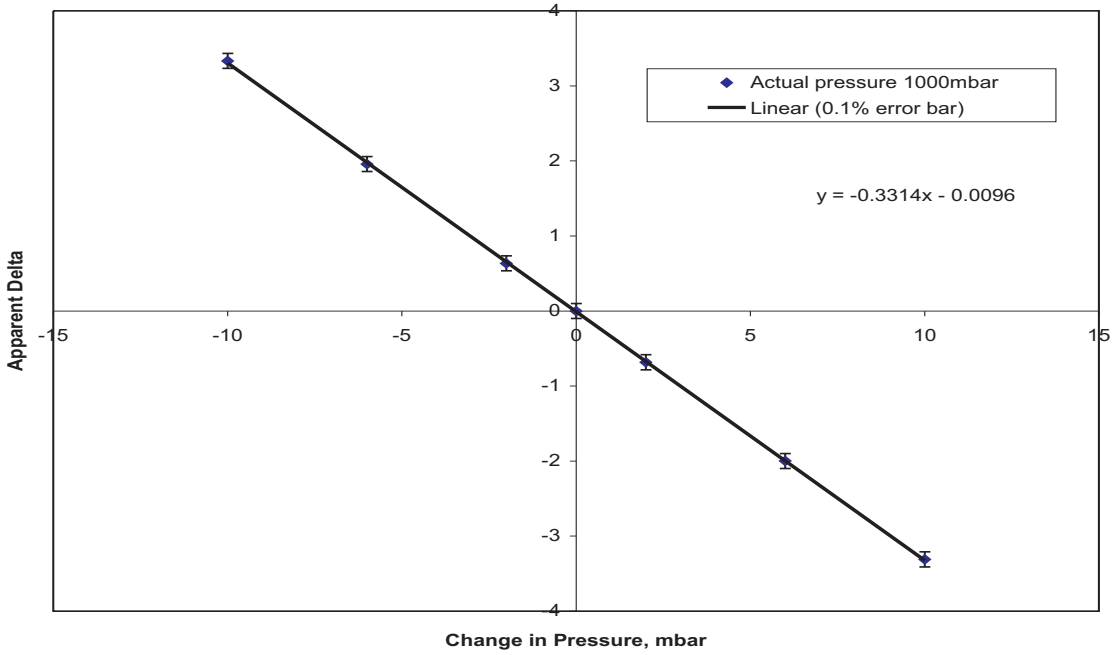

FIGURE 4.17: Effect of ambient pressure variation on ambient delta

4.3.4 Water Vapour Effects

Presence of moisture or water vapour in the cells can cause problems in the form of additional spectral features and it can also pose problems for the optical components such as windows. A study of the line strengths of H_2O and CO_2 was done in the region 2200 cm^{-1} to 2400 cm^{-1}. All C626 lines were much stronger than the water lines present in the defined IR region. For C636, lines up to P(50) were found to be at least five times stronger than the H_2O lines. Hence water vapour does not pose any problems that will result in apparent delta and generate spurious results. However, anti-condensation mechanisms in the form of molecular sieves such as Drierite ($CaSO_4$) will be used to ensure better protection for the optical windows. These Drierite beads will be inserted into the delivery tubes that carries the breath sample to the gas cells thereby absorbing any moisture content in the breath sample and making the gas cells moisture free.

4.3.5 Background CO_2

Fluctuation of CO_2 concentration in the non-sample pathlength (nsp) will also result in spurious results. This is more serious in the case of C-12 channel due to high natural abundance of C-12. It was found that a nsp of 20 cm with ambient CO_2 level of 1200 ppm (considering a poorly ventilated room) has an effective concentration that is 6 times greater than the sample cell[26]. Thus it is essential to purge the instrument beam path. This can be done using a purge of dry N_2 gas having a purge quality of less than 2 ppm. This will make the nsp effective concentration 100 times less than that of the sample cell. Another important issue involved is that of purge stability. A variation in purge quality will upset the balanced transmission of the two channels with greater effect on the C-12 channel. It was determined that a compromise between nsp and purge stability was required. Greater the nsp, better the purge stability required. A typical nsp of around 30 cm will require a purge stability of better than ± 0.1 ppm for an apparent delta tolerance of less than 1‰ [26]. Another way of circumventing this problem of background CO_2 is to use a CO_2 absorber material such as Ascarite. Since the whole instrument will be enclosed from all sides, a layer of Ascarite can be placed within the walls of the instrument cover. This will ensure that the nsp is always free from background CO_2. This avoids all the complexities involved in using a dry N_2 purge, although it will necessitate replacement of the Ascarite layer once it has been fully replaced by sodium carbonate. Besides, the use of materials that emit less amounts of CO_2 for the various components and fittings within the instrument such as the tubings will also help to keep the nsp free from background CO_2.

Chapter 5

Component Development and Characterisation

5.1 Source Characterisation

An IR broadband source IR-12 (c.f. Figure A.8) from Scitec was chosen as the blackbody source. It had a thermocouple probe attached to it for accurate monitoring of the source temperature. The source has a peak operating temperature of about 1074K when driven at 4.5 V/1.8 Amps. In order to characterise this blackbody source, its output power was measured as a function of source temperature. For this purpose, an IR detector LTIQ2 (c.f. Figure A.9) from Scitec was used. The detector was fitted with a CaF_2 window and had a responsivity of 250 V/Watt and a detectivity greater than 8.0×10^8 cmHz$^{1/2}$W^{-1}. The source was chopped at 30 Hz and was placed 7.5 cm, 9.0 cm, 10.0 cm and 12.5 cm away from the detector. The measurements are shown in figure 5.1. The temperature of the source was measured by using the attached thermocouple probe and a digital thermometer.

The figure shows that the output of the detector varies in a quadratic fashion with respect to the source temperature in contrast to a fourth power variation according to Stefan-Boltzmann law which is expected in an ideal case. The law states that the total radiant exitance emitted from a unit surface area of a blackbody, $M_e(T)$, is directly proportional to the fourth power of the blackbody's temperature, T.

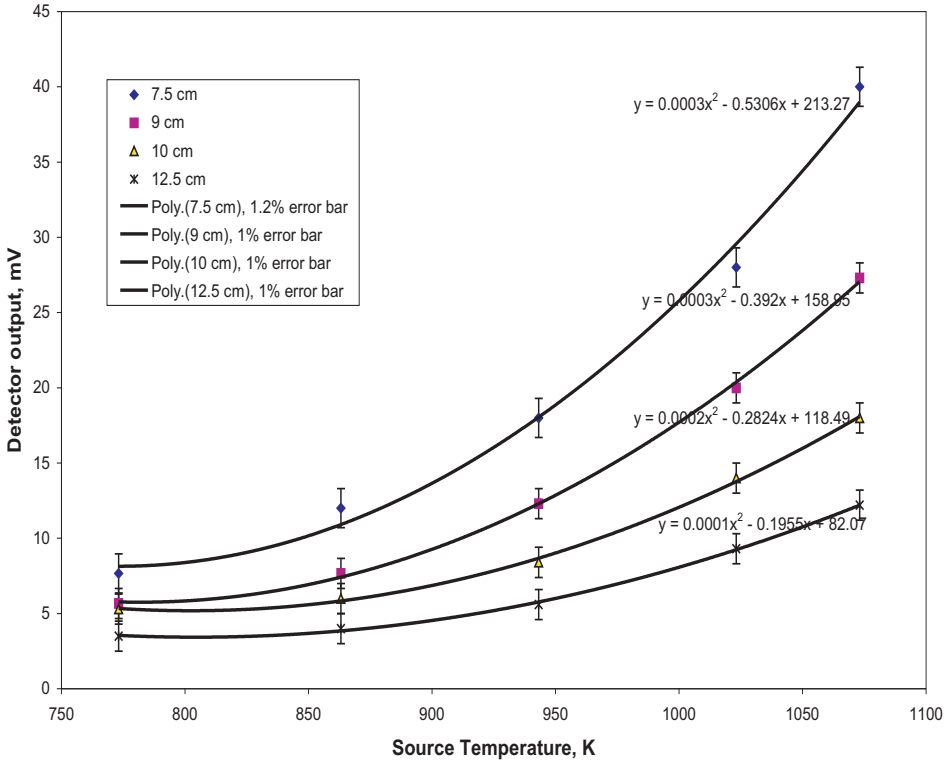

FIGURE 5.1: Characterisation of blackbody source by measuring source exitance as a function of source temperature

That is,

$$M_e(T) = \sigma T^4 \tag{5.1}$$

where σ is the Stefan-Boltzmann constant. This law, however, is based on the assumption that the blackbody under consideration is a true blackbody with emissivity equal to 1, which is not valid under the present circumstances. Besides, absorption in the mean pathlength between the source and the detector also needs to be considered during practical test conditions. As a result, deviation from the law is expected which explains the observed quadratic dependance rather than a fourth power dependance. The detector linearity was also checked by calculating $1/r^2$ fall off of the detector output. There was good agreement between the expected and experimental values for 7.5 cm and 9.0 cm.

However, the most critical evaluation for the source is its temperature stability since any fluctuation in the source temperature greater than ± 0.4K during the course of the experiment will affect the overall accuracy of the instrument. For this purpose, simulations were performed to calculate the approximate detector output for the configuration shown in figure 5.2.

L1 and L2 are CaF_2 plano-convex lenses having a focal length of 10 cm each that

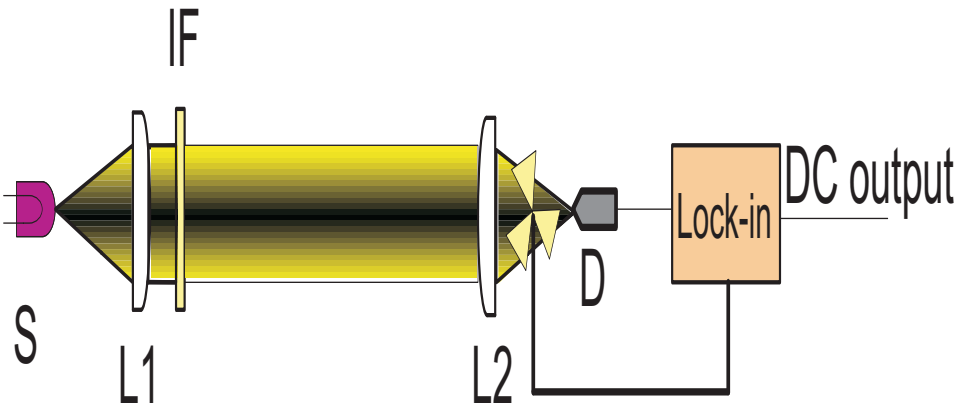

FIGURE 5.2: Setup used to study source temperature stability

will finally form part of the complete design. L1 collimates radiation from the source, S, whereas L2 focusses it on to the detector, D. The source and detector were placed at the focus of these lenses as shown. An IR band pass filter, IF, from FK Opticals was placed just after L1 since it is be better for a collimated beam to be passed through the filter. More on this filter will be discussed in the next section. The distance between the two lenses was about 30 cm which will roughly be the case in the final instrument setup, giving enough room for the filter and sample gas cells. A chopper running at the proposed chopping frequency of 10 Hz was placed in front of the detector. Optical alignment of the components was checked using a laser beam. The output of the detector was fed to a lock-in amplifier to extract the DC signal to get a measure of source temperature stability. Power loss due to optics and beam divergence was incorporated in the simulation codes to calculate the output voltage from the detector. Figures 5.3 and 5.4 show the recorded waveforms at 1074K and 774K. The waveform at 10 Hz is the detector output and the DC signal on top is the output of the lock-in amplifier. For 1074K, the experimental detector output of 27.50 mV was in excellent agreement with the calculated value of 27.9 mV. At 774K, deviation of the experimental value of 5.77 mV from an expected value of 7.0 mV was observed implying better agreement at higher temperatures. This may be because at 774K, the source is being operated at a temperature close to the shorter end of its operating range and hence the deviation in its performance. Besides, at temperatures close to 674K, the detector signal is more sensitive to variations in ambient CO_2 levels since the peak of the blackbody curve coincides with the ν_3 absorption mode of CO_2. But the point

of real interest was the source stability as represented by the DC output from the lock-in. At both the temperatures, the DC line was adequately stable and remained constant over the entire period of observation which was 20 minutes.

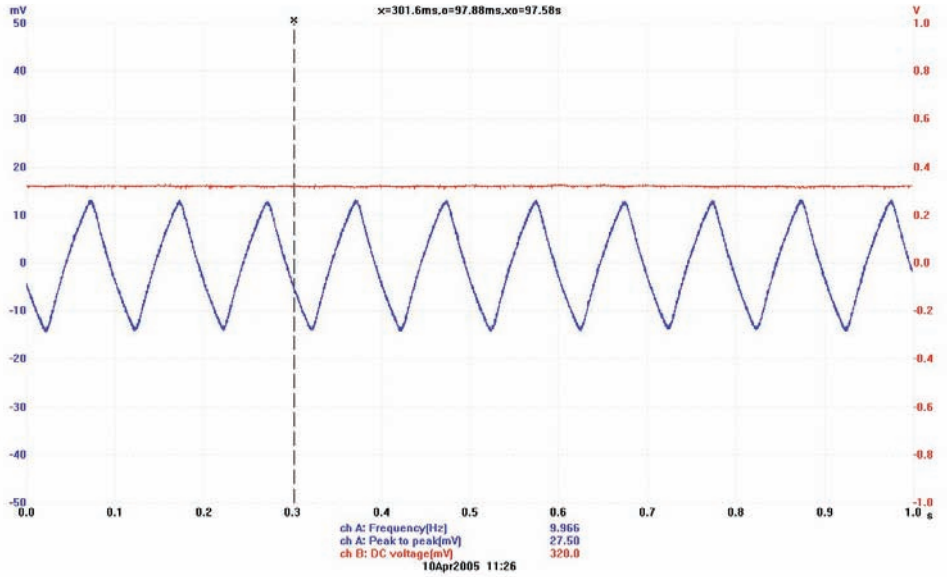

FIGURE 5.3: Source stability check at 1074K

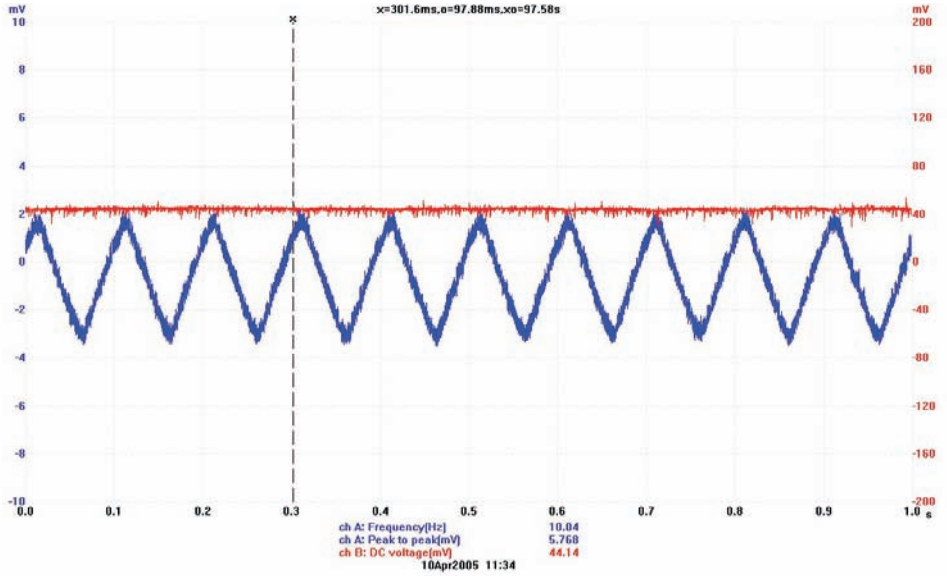

FIGURE 5.4: Source stability check at 774K

For a more quantitative analysis of source stability, the standard deviation of the DC values at 774K and 1074K were calculated. When converted to absolute temperature scale, these standard deviations provide a measure of source stability. It was found that at 1074K, this value was about 0.3K whereas at 774K, the stability was even better with a standard deviation of less than 0.05K. This clearly

demonstrated that the IR-12 source under test was adequately stable and met the stability criteria for our instrument by a good measure. Hence it was concluded that no special control measures for stabilising the source was needed at the moment and this concluded our source stability analysis.

5.2 Infrared Interference Filter

As discussed in chapter 4, the interference filter IF to be used in the instrument should ideally have a passband ranging from approximately 4.1 μm to 4.6 μm, thus covering almost 99% of the total band strength for CO_2. This particular infrared region is most suitable for our application as it is relatively free from other interfering compounds that have coincident absorption bands. One such filter was obtained from FK Opticals which had a passband from 4.1 μm to 4.5 μm with a central wavelength of 4.3 μm. The transmission profile of the filter was obtained from an FTIR spectrometer and is shown in figure 5.5. To get a clearer picture, the filter profile was superimposed over the C12 and C13 absorption profiles as shown in figure 5.6. The filter had a transmission greater than 60% in the passband region and fully blocked the out of band regions.

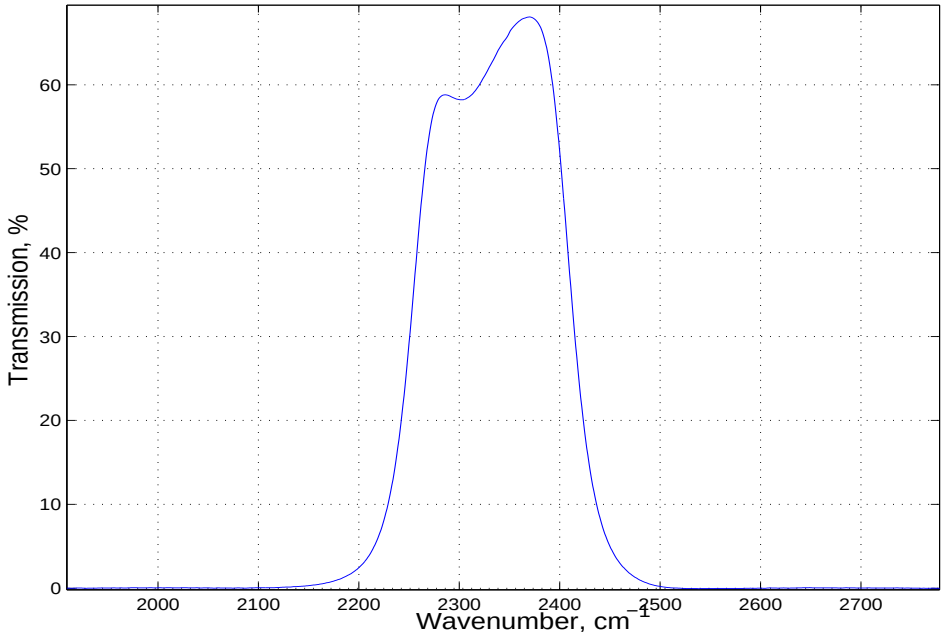

FIGURE 5.5: Interference filter transmission profile recorded using a FTIR

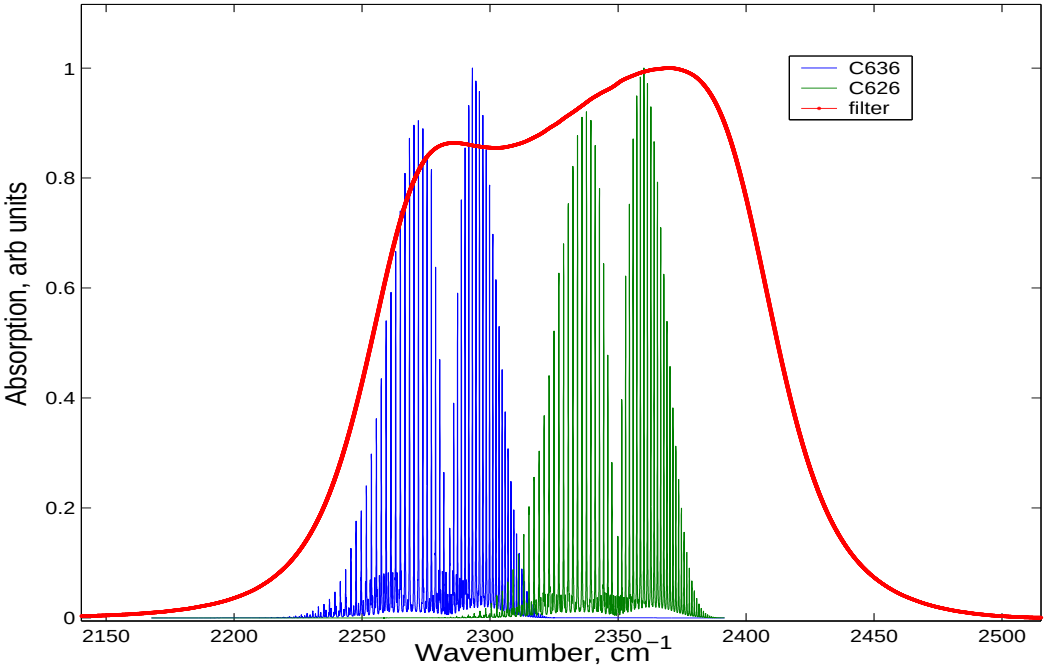

FIGURE 5.6: Filter profile superimposed over C12 (C626) and C13 (C636) absorption profiles

5.3 Gas Cell Design and Construction

5.3.1 Isotope Correlation Filter Cells

The proposed two channel IR spectrometer requires four gas cells in all. Each of the two channels has two gas cells, an isotope correlation filter (ICF) cell for enhancing selectivity and a sample gas cell containing the breath sample. The ICF cell in the 12-channel will contain pure $^{13}CO_2$ while the ICF cell in the 13-channel will contain pure $^{12}CO_2$. The optimum ICF effective concentration (which is concentration times pathlength) for these filter cells was found to be 3.766×10^{19} mol/cm^3[26] at 100% isotopic purity. This is equivalent to a pathlength of around 1.4 cm for these ICF cells. The length of these cells depends on the isotopic purity of the constituent isotopomer. A preliminary enquiry revealed that obtaining ultra pure ^{13}C labelled CO_2 will be very expensive. However, the prices come down to a reasonable level at 99% isotopic purity. Hence if we consider 99% purity for the 12-channel ICF cell, its pathlength will increase slightly to 1.41 cm so as to maintain the required effective concentration of 3.766×10^{19} mol/cm^3. Using 99% isotopic purity in the ICF cell will have no adverse effect on the working of the instrument. The only consequence of using reduced purity is a change in the optimum 13-channel sample cell length. This will deviate from the actual

10.245 cm required for balanced absorption. A simulation revealed that decreasing isotopic purity resulted in a decrease in the 13-channel equilibrium cell length as shown in table 5.1. In the case of 13-channel ICF cell, this will not be a problem

^{13}C Purity, %	*Equilibrium Cell Length, cm*
100	10.245
99	10.077
98	9.91
97	9.741
95	9.402

TABLE 5.1: Equilibrium cell length for different 12-channel ICF purity levels

since ^{12}C labelled CO_2 is available with very high purities of 99.95% at reasonable costs. Using these dimensions, the two ICF cells were made with provisions for valve connections at the top. These cells were then fitted with specially wedged CaF_2 windows which were purchased from EKSMA. These windows were 38.0 mm in diameter and had a deliberate wedge of around 4.0 min (1.16 mrad) to overcome the effect of etalon temperature instability as discussed previously in section 4.3.2. The windows were glued on to the cells using a special ECOBOND adhesive whose constituents were mixed in the appropriate ratio so as to make it slightly flexible. The circular frame into which the windows fit were made of brass since brass had a thermal expansion coefficient similar to that of CaF_2 thereby reducing the chances of the window snapping along its cleavage lines due to thermally induced stress. A mechanical drawing of the ICF gas cell body has been included in the appendix for reference(c.f. Figure C.1).

5.3.2 Sample Gas Cells

The sample gas cells will hold the breath samples in both the channels. As discussed previously, at 674K, the length of these cells will be 0.1 cm and 10.245 cm for the C626 and C636 channels respectively. These lengths are roughly in the ratio of the absorption strengths of C626 and C636 and will hence ensure a balanced absorption in both channels. A sketch of the 1 mm 12-channel cell is provided in figure 5.7.

The design is simple and straightforward apart from the fact that the gap between the two end windows was just 0.1 cm. Provisions for gas inlet and outlet were made on either side of the circular frame that holds the windows. 4 mm PFA

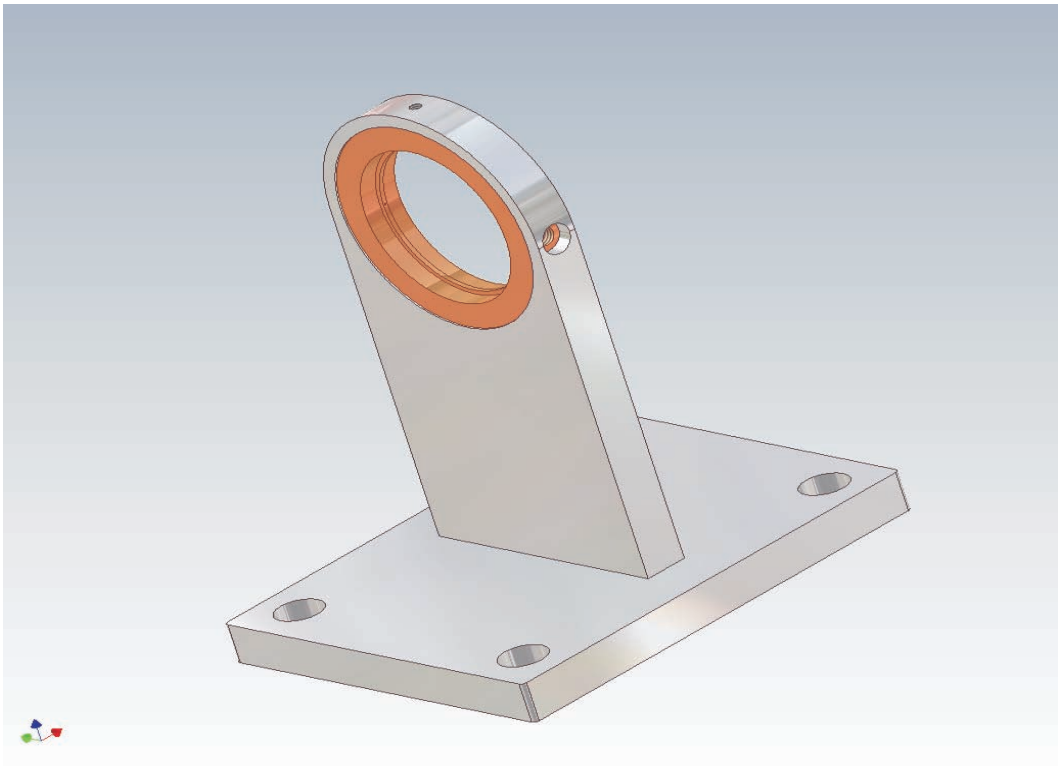

FIGURE 5.7: 1 mm gas cell for C-12 channel

tubes were connected to the cell using brass push-in fittings. The CaF_2 windows were then glued on to the cells as before.

The design for the longer cell in the 13-channel was more complicated. One of the major features of the proposed instrument is its ability to maintain balanced absorption in both channels by virtue of a unique feedback mechanism where the length of the 13-channel cell is constantly adjusted to obtain null output from the detector. Such a condition is indicative of an equilibrium in channel absorptions. A delta value of 1‰ requires a 70 μm change in length whereas 100‰ will require the cell length to be changed by about 7 mm. Hence the design of the longer gas cell had to provide for adjustable pathlength. This was accomplished by having a section of the cell body made of edge welded bellows. As mentioned earlier, for a source temperature of 674K, the equilibrium cell length was about 10.245 cm for 100% isotopic purity in the ICF cells. However, if the source was driven at higher temperatures, the length decreases to about 4.6 cm at 1074K. In order to ascertain any other secondary effects this decreased cell length might have, a calculation of the signal strength falling on the detector was made taking into account all possible sources of power loss such as reflection and divergence losses. The specifications of the source and detector as found in the data sheets were used for this purpose. The difference in the channel intensities due to 1‰ were

calculated and shown in table 5.2.

Temperature, K	*Difference in Channel Intensities, nW*
674	0.50
874	1.20
1074	1.97

TABLE 5.2: Difference in channel intensities for 1‰ at various source temperatures

It can be seen that as the temperature increases there is greater difference in the channel intensities making it easier for detection. This is due to the change in the shape of the blackbody curve with respect to the absorption profile of the two isotopomers which can also be deduced from the series of blackbody curves that were plotted in figure 4.12. Also the relative change in length at various delta is the same for both 674K and 1074K as seen from the slope of the curves in figure 5.8.

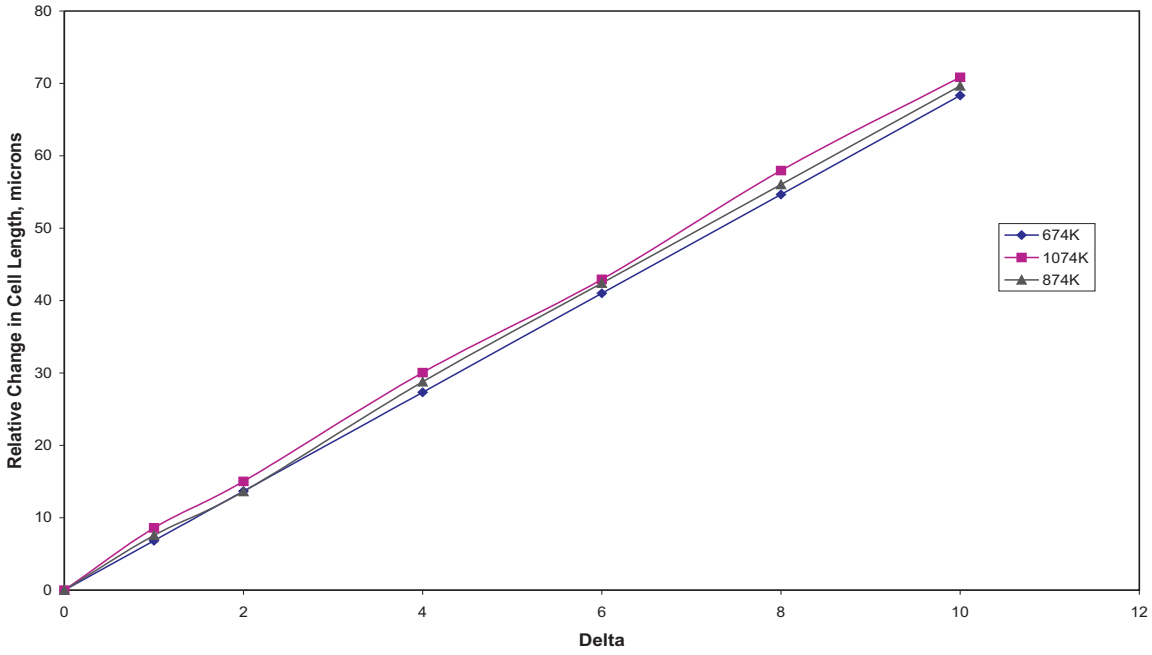

FIGURE 5.8: Relative change in cell length for various delta at different temperatures

Thus responsivity of the measurement system will not be affected by increased source temperature. Hence it is beneficial to drive the source at higher temperatures, say 1074K, implying that the 13-channel cell length will have to be reduced to about 4.6 cm. However, it was decided to initially carry out tests at 674K as

decreasing the free length of the cell is always possible at a later stage. Hence the free length of the whole tube was set at about 10 cm with a stroke of 25 mm to be provided by the bellows section. This implies that the length of the tube can be effectively varied from about 8.5 cm to 11.0 cm thereby covering the required range of lengths for reasonable delta values. The tube section was purchased from Nor-Cal UK. Some additional changes to the tube section were made in order to house the end windows. With the addition of windows, the total length of the gas cell can be varied from 9.5 cm to 12 cm. A sketch of the gas cell is shown in figure 5.9.

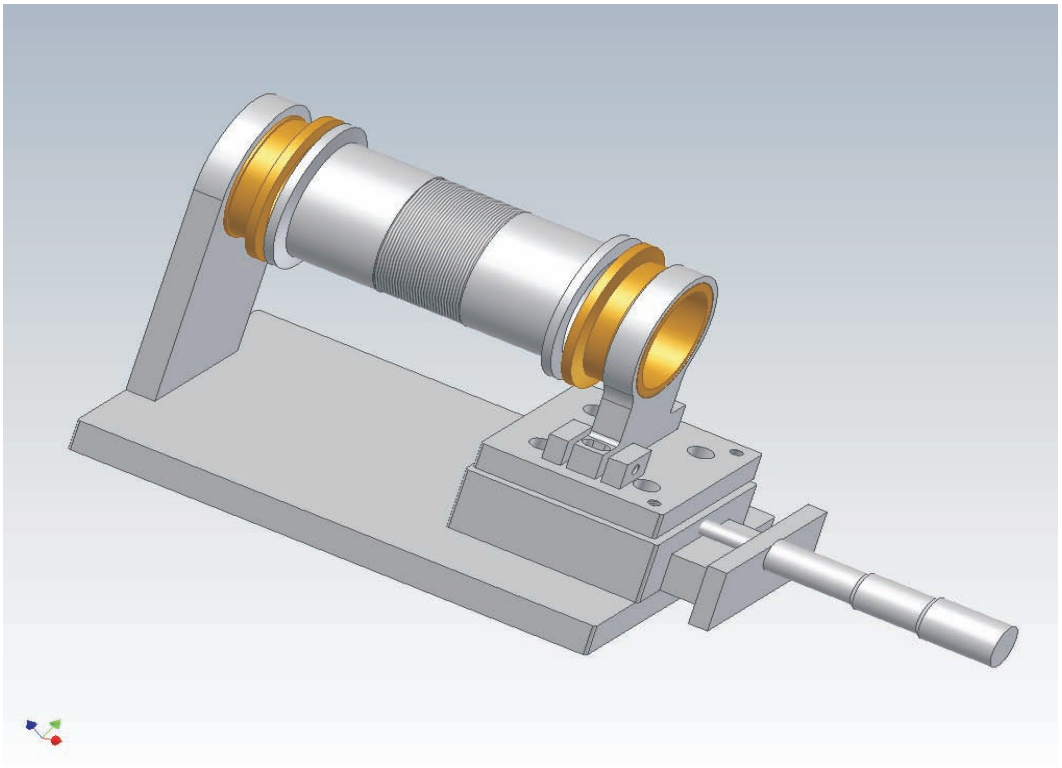

FIGURE 5.9: Variable length gas cell in the 13-channel with micrometer arrangement

As seen in the figure a special arrangement consisting of a single axis translation stage was incorporated into the cell structure to provide the necessary cell length manipulation. The micrometer connected to the linear translator will eventually be driven by a motor that will form part of a position control feedback mechanism that derives its error signal from the phase sensitive detector connected to the pyroelectric detector. A screw arrangement was also provided for adjusting the horizontal alignment so that the end windows remain parallel to each other.

5.4 Phase Locked Optical Choppers

5.4.1 Electronic Phase Locking

The use of two synchronised optical choppers as a substitute to beam splitters was briefly mentioned in chapter 3. Beam splitters are frequently employed in many optical instruments in order to split the incoming light or to combine light from two different channels. Such a scheme works well in most cases and their simplicity is an added advantage. However, in our application, beam splitters pose certain issues and problems that are further compounded by the highly sensitive and low power signal detection nature of the measurements involved. Beam splitters normally used are 50:50 beam splitters where only 50% of the input power is received at the output. The use of two such beam splitters, one for splitting and directing the beams along the two channels and the other to recombine and redirect them onto the detector, will reduce the amount of power falling on the detector by 75% or a factor of 4. This 75% loss in optical power will reduce the S/N ratio at the detector which is undesirable. Secondly, beam splitters in the mid infrared region are quite expensive and the use of two such beam splitters will not be a good choice for a low cost diagnostic instrument. Besides, polarisation related problems in the form of slightly different reflectances for the s and p polarised light will result in slightly different intensities of infrared radiation falling on the detector, thereby upsetting the balanced nature of the system and giving rise to spurious delta. Such small variations will have a profound effect on the final outcome since we are precisely looking for such small variations to detect changes in the isotopic ratio.

All this led to an alternative idea of using synchronised optical choppers that also act as mirrors. As discussed in section 3.5, two such optical choppers, one at the input and the other at the output, will perform the same task as the beam splitters. Two sets of three blade choppers were thus designed and made from aluminium. The blade surfaces were lapped and then polished using a diamond compound in order to make them reflective. One such chopper is shown in figure 5.10.

As seen in the figure, the edges of the blades were deliberately cut back by 45° so as to prevent light from being reflected off these edges. This was be necessary since the choppers were inclined at an angle of 45° with the optical axis. The choppers were mounted on two low inertia dc servo motors from McLennan (c.f. Figure A.10, Figure A.11) with built in encoders for feedback purposes. The next step was to phase lock them such that both the motors have the same chopping

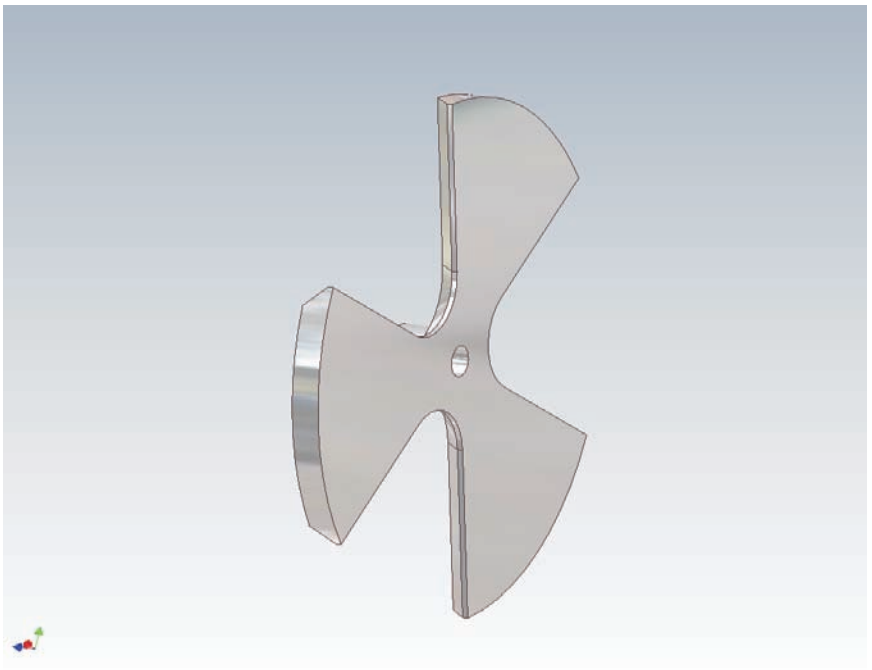

FIGURE 5.10: Three blade reflective chopper

frequency of 10 Hz but are 180° out of phase. Referring to figure 3.3 in chapter 3, when C1 alternatively reflects light along the C-12 channel and transmits light through the C-13 channel, C2 being in anti-phase with the first, will alternatively transmit light from the C-12 channel and reflect light from the C-13 channel. This ensures synchronous detection of the two channel intensities without any loss of power. At any given time, the detector receives light from only one of the two channels. Hence it is essential to maintain a phase locked relation between the two choppers. In order to obtain a more quantitative information about the extent of phase lock required and the effect of a phase perturbation, the intensity profile of the two channels had to be computed. To get this intensity profile, it was necessary to develop a mathematical expression to define the area of the beam that is exposed as the chopper blades sweep across it. This can be pictorially represented by figure 5.11.

Consider a beam diameter of radius r with the centre at point O fully blocked by a chopper blade whose edges are formed by CP and DP where P is the centre of the 3 blade chopper. Let length of OP be equal to R. This represents a case where the entire beam diameter fits perfectly within the reflecting surface of the chopper blades. As the chopper rotates, a a part of the beam is exposed and falls on the detector and this is represented by the shaded portion with AP forming the new position of the edge CP. Hence, the area of the shaded portion is required to compute the intensity of light falling from each channel and their combination

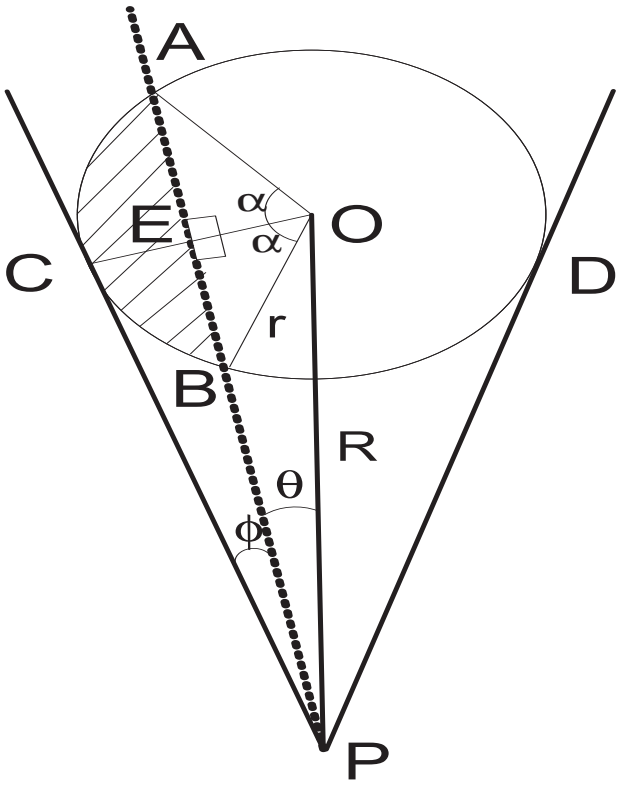

FIGURE 5.11: Diagram representing the IR beam being chopped by one of the chopper blades with the shaded area being the exposed portion

then gives the total intensity falling on the detector. Referring to figure 5.11, for a 3 chopper blade with 1:1 mark to space ratio,

$\angle$CPD = 60°
$\angle$OPD = $\angle$OPC = 30°
OP = R
OA = OB = OC = r which is radius of the beam.
Let $\angle$CPA = ϕ.
$\therefore$ $\angle$APO = 30° - ϕ = θ
From $\triangle$OEP, $\angle$OEP = 90°, since $\triangle$AOB is an isosceles triangle.
$\therefore$ OE = R$\sin\theta$

From $\triangle$OPC, sin30 = r/R
$\therefore$ R = 2r, which is true if the beam fits perfectly between the chopper blades.
From $\triangle$OEB, EB = $\sqrt{r^2 - OE^2} = \sqrt{r^2 - R^2 sin^2\theta}$

$\therefore$ AB = $2\sqrt{r^2 - R^2 sin^2\theta}$

Now area of the segment (shaded portion) = area of sector AOB - area of $\triangle$AOB.
Area of sector AOB = 1/2 $\times$ r^2 $\times$ 2α = $r^2\alpha$ = $r^2\cos^{-1}(R\sin\theta/r)$ — A

Area of $\triangle$AOB = 1/2 $\times$ AB $\times$ OE = 1/2 $\times$ $2\sqrt{r^2 - R^2 sin^2\theta}$ $\times$ Rsinθ
= $\sqrt{r^2 - R^2 sin^2\theta}$ $\times$ Rsinθ — B

$\therefore$ Area of segment = A - B
Area of segment = $r^2\cos^{-1}(R\sin\theta/r)$ - $\sqrt{r^2 - R^2 sin^2\theta}$ $\times$ Rsinθ = fn(R,r,θ)

By using the above expression for the area of beam exposed, it was possible to plot the intensity profile of the two channels as a function of chopper position as shown in figure 5.12.

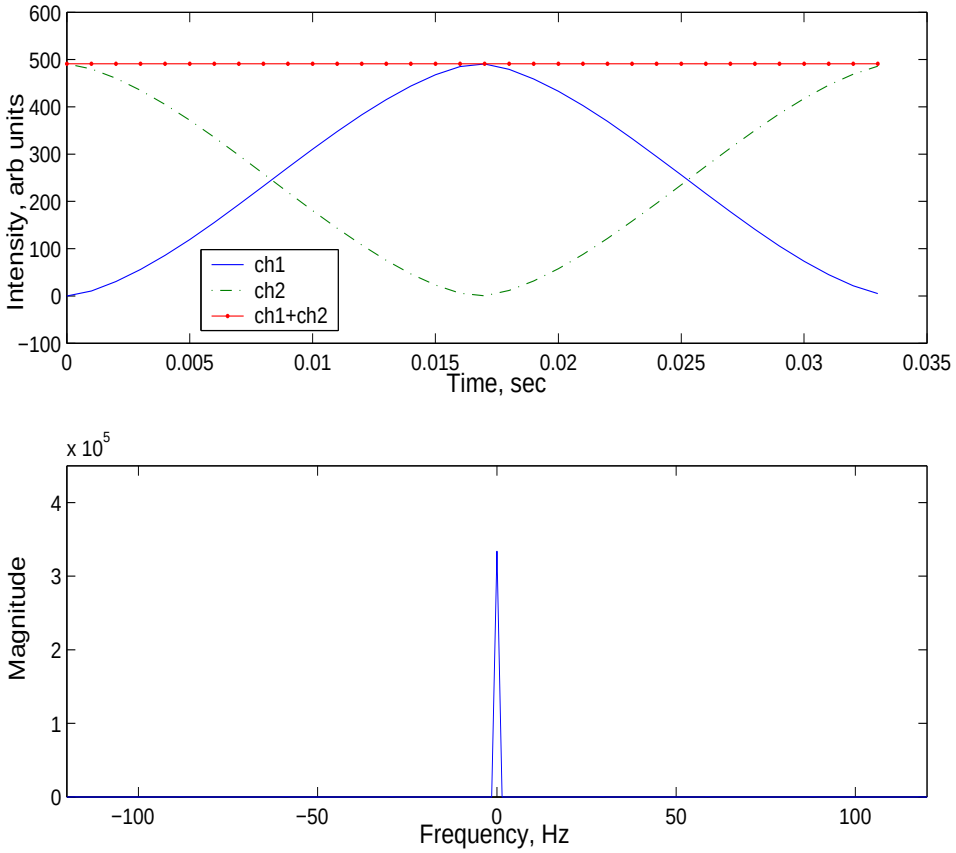

FIGURE 5.12: Channel intensities at 180° phase shift. The top graph shows the intensity profile of the individual channels and their sum whereas the bottom graph is the FFT of the sum

Here the top graph shows the intensities of both the channels individually and their combination falling on the detector as one chopper blade completely sweeps the infrared beam i.e. the beam goes through a full cycle of being fully transmitted to fully reflected. The bottom graph is the FFT of the overall sum intensity showing the frequency components. As seen, when the two choppers are exactly 180° out of phase, the total intensity falling on the detector remains a constant value and the FFT shows a peak at DC or 0 Hz. As a result, the detector gives a null output since it responds only to changes in input intensity. This is the ideal condition. However, if a slight perturbation in the phase lock is present, thereby shifting the phase relation from 180° to 180°+θ, the combined intensity falling on the detector will assume a more sinusoidal shape indicating the presence of harmonics in the FFT. This is shown in figure 5.13 where the phase shift is 185°. The chopping frequency was assumed to be 30 Hz. The small bumps at 60 Hz, 90 Hz and 120 Hz are the even and odd harmonics that will be picked up by the detector. In a similar fashion, the intensity amplitude at different values of θ were computed for the various harmonics as shown in figure 5.14. Here w represents the fundamental frequency of 30 Hz. As observed from figure 5.14, initially the second harmonic $2w$ dominates but very soon the fundamental increases sharply almost in a quadratic fashion. The even and odd harmonics will be filtered out by the phase sensitive detector and what remains is the fundamental w. The next step is to find the maximum value of θ that can be tolerated which gives rise to an unbalance in channel intensities equivalent to the one produced by a 1‰ ^{13}C enrichment. On the basis of the above obtained results, this was found to be around 0.3°. Hence this clearly implies that a very tight and stable phase lock is required to eliminate any spurious results and achieve a high precision.

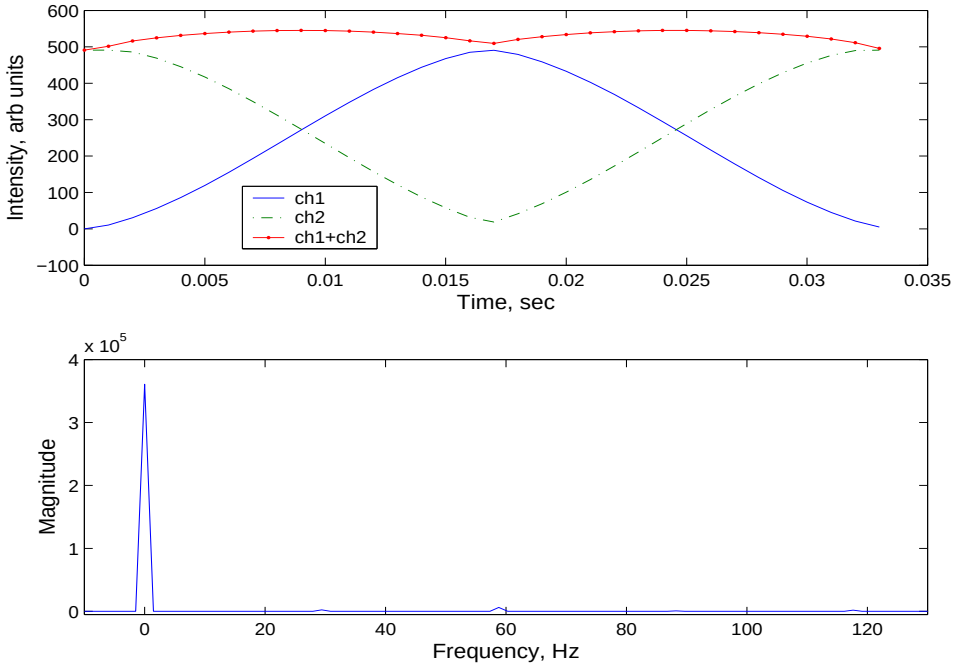

FIGURE 5.13: Channel intensities at 185° phase shift. The top graph shows the intensity profile of the individual channels and their sum whereas the bottom graph is the FFT of the sum

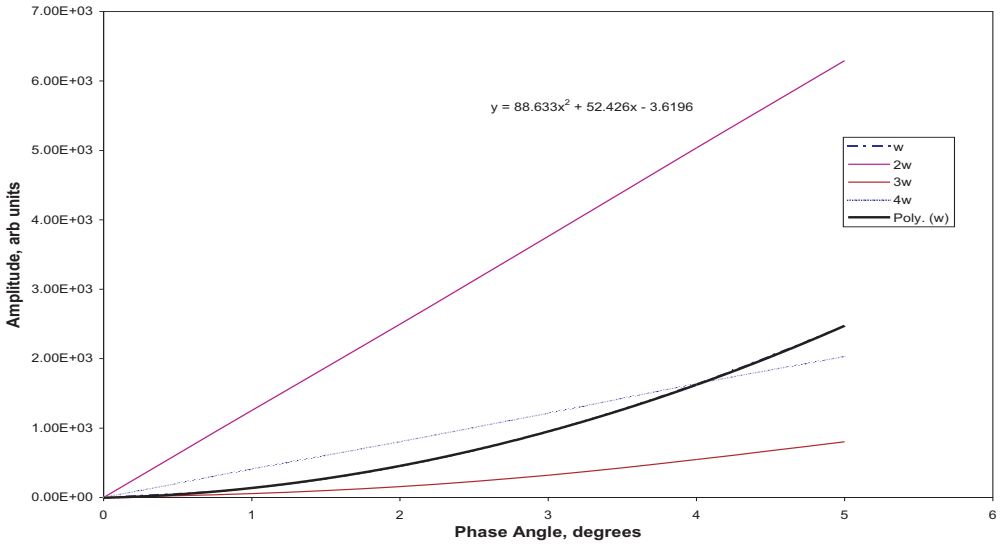

FIGURE 5.14: Amplitude of different harmonics at various phase shift angles, θ

Thus a stable phase locked loop (PLL) is required in order to maintain the speed and phase relationship between C1 and C2 within the acceptable tolerance limits. This can be done electronically by considering a master-slave configuration for the two choppers where C1 will be the master motor and C2 the slave. A speed control loop for C1 will ensure that it runs at a stable 10 Hz chopping frequency (200 rpm

motor speed for a 3 blade chopper) and C2 will then follow C1 and maintain the same frequency by virtue of the PLL. A Pulse Width Modulation (PWM) scheme as shown in figure 5.15 was used to control the speed of C1.

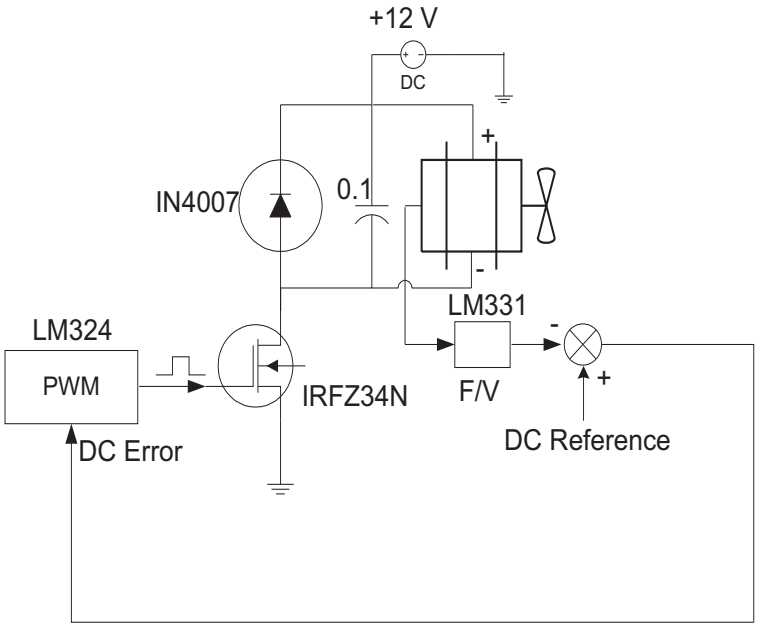

FIGURE 5.15: PWM speed control of master chopper C1

A LM324 quad opamp was used to generate the PWM signals required to run the motor. Feedback signal from the motor encoder was fed to a frequency to voltage converter (F/V) LM331 (c.f. Figure A.3, Figure A.4) whose output was then compared with the reference DC voltage. The resultant error signal was used as the DC level to generate the PWM pulses by comparing it with a triangular wave. Hence by setting the DC reference voltage at the appropriate value by means of a potentiometer, the required speed was attained. The motor was driven by a power MOSFET IRFZ34N and set to run at 3.33 Hz so that the chopper blades chopped the light at 10 Hz. The chopping frequency was obtained from the reflective sensor attached in front of the motor as shown in figure 5.16. The encoder signal for the motor running at 200 rpm (3.33 Hz) was recorded as shown in figure 5.17. The signal has a frequency of 1.66 KHz which is equivalent to 3.33 Hz since the encoder gives 500 lines per revolution.

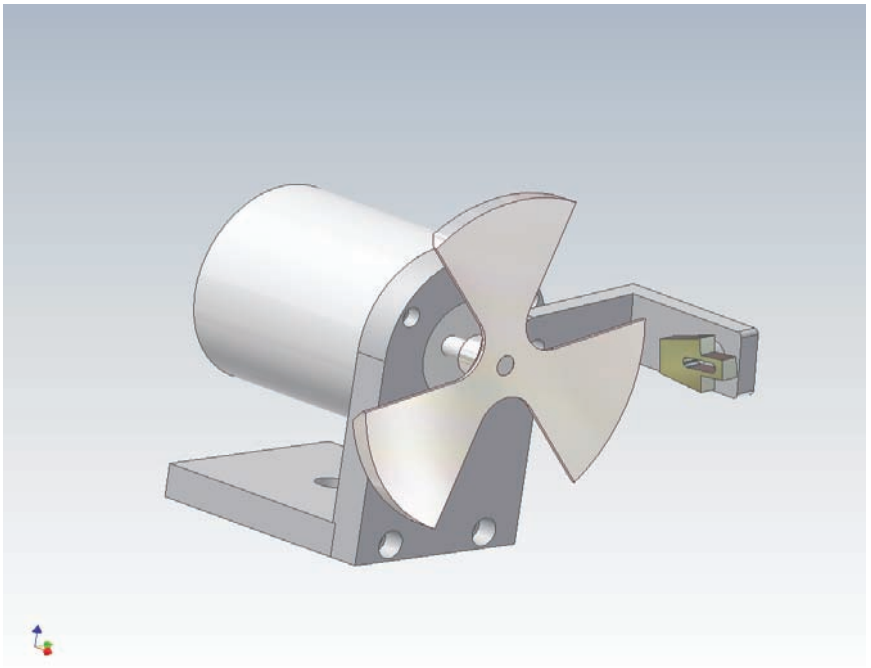

FIGURE 5.16: Motor with the chopper blades and reflective sensor attached

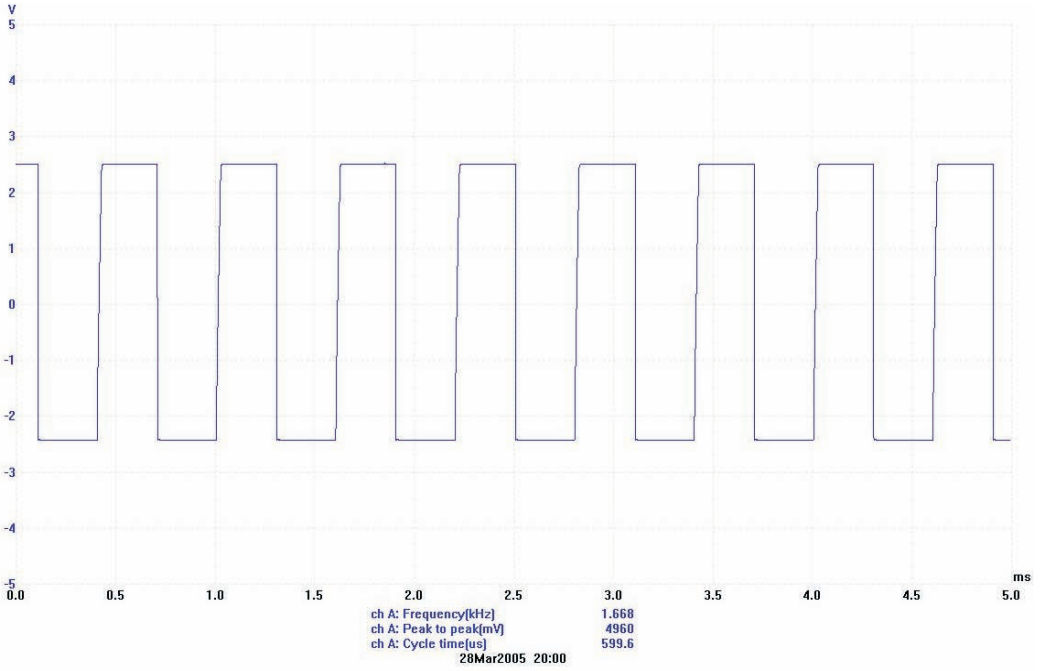

FIGURE 5.17: Motor encoder signal at 200 rpm

In order to check the stability of the speed control system, a transient analysis was performed by applying step and ramp inputs using the DC reference voltage. The corresponding changes in the F/V output were recorded as shown in figure 5.18. The graph shows very good stability with very little oscillations and overshoots and the F/V output faithfully follows the changes in the input.

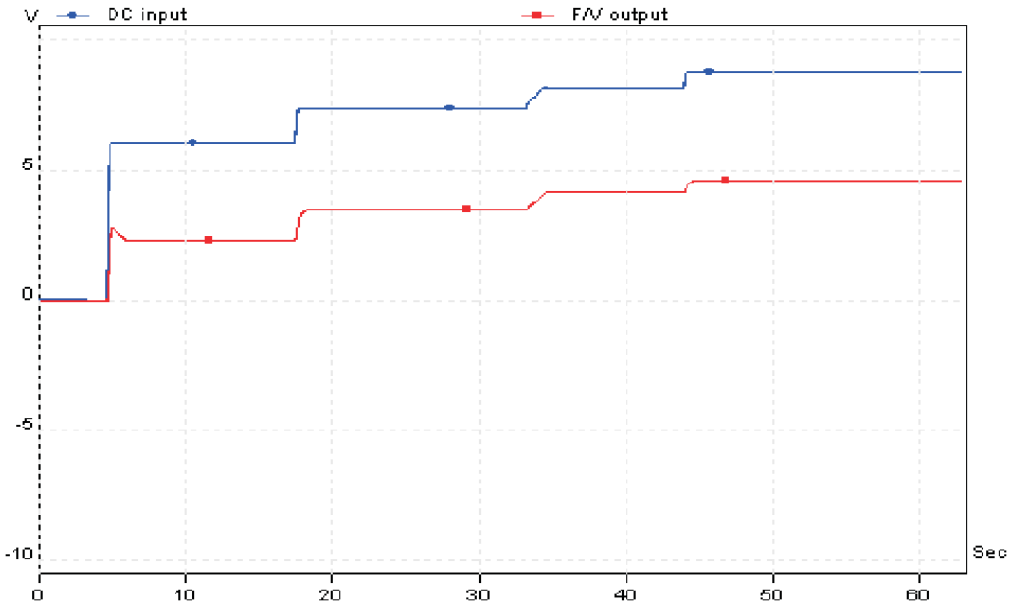

FIGURE 5.18: Transient analysis of the motor speed control

The next step was to phase lock chopper C2 with the master chopper C1. This required C2 to run at the same speed as C1 but in anti-phase. Hence a frequency and phase control was required. In order to implement this, a PLL IC HEF4046 (c.f. Figure A.5, Figure A.6, Figure A.7) from Philips Semiconductor was employed. The schematic is shown in figure 5.19. Phase comparator type 2 (PC2) present in HEF4046 was used for establishing a phase lock. PC2 received two inputs, the signal input from C1 and the comparator input from C2 as shown. If the two signals varied in frequency, the output will then swing to one of the supply levels depending on which input was faster. If however the signals had the same frequency but differed in phase, the output will then be a train of square pulses whose amplitude range will depend upon which input was ahead. The comparator gave a mid-rail dc value only if the two inputs were at the same frequency and phase. Since PC2 locked only at 0°, it was necessary to initially invert the signal from C1 using an inverter so that C2 locked on to this inverted C1 which effectively made C1 and C2 to be 180° out of phase. The output from PC2 was fed to an integrator with a corner frequency of 0.159 Hz to get the mean dc value. This

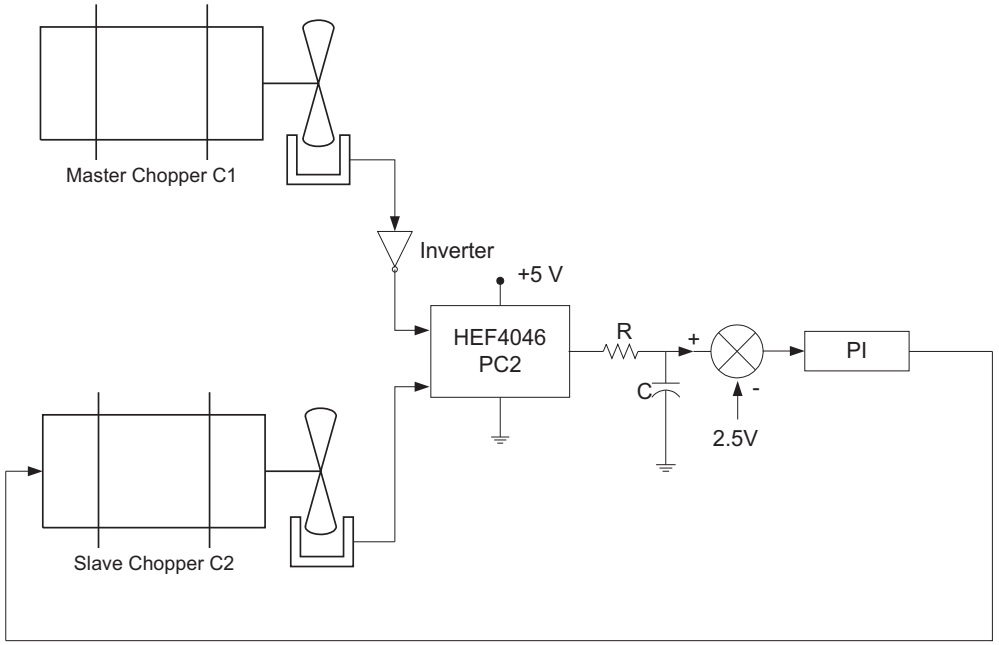

FIGURE 5.19: Phase locking of the two optical choppers

was then compared with the mid-rail value using LM833 to generate the required error signal. This error signal was then fed as input to the PI controller whose output was used to drive C2. When a lock was achieved the error signal will be zero and the integrator will hold on to the previous output value and maintain the locked condition. In case of any changes in the speed of C1, this control loop will ensure that C2 followed the changes continuously maintaining the phase relation.

The phase lock scheme described here was implemented and put to test. It was observed that although C1 was constantly chopping at a fixed frequency of 10 Hz, C2 was not able to lock on to the master signal with the desired accuracy. The photoreflective signal for C2 was seen to be constantly fluctuating about the mean position although it was successfully tracking frequency variations in C1. This suggested a loop instability problem with the oscillation in the C2 signal exceeding acceptable levels. In order to study this systematically, the entire control loop was modelled and the loop transfer function was computed. Loop stability was analysed using the control system toolbox in MATLAB. Bode plots were generated and gains for the PI controllers were varied for maximum loop stability. Although marginal improvements in the phase lock were observed, the absolute phase accuracy achieved did not meet the design criteria of $\pm 0.3^{\circ}$. Since further work on this electronic phase lock circuit was required, it was decided to move on to an alternative design and then revisit the problem once the other objectives were met. Implementation of an electronic phase lock scheme will not

only add to the novelty of the system but will also act as a precursor for a more advanced digital control scheme that can be incorporated in a future version of the diagnostic system.

5.4.2 Mechanical Phase Locking - An Alternative Approach

Due to the above mentioned difficulties that were encountered in implementing an electronic phase lock, an alternative mechanical design was conceived to circumvent the issue. The design basically consisted of a single motor driving both the chopper blades C1 and C2. The motor was centrally attached to a horizontal aluminium bar which was mounted on two vertical steel supports at the two ends. The two chopper blades were then attached to these vertical supports making sure the mirrored surfaces faced opposite sides. The entire assembly is shown in figure 5.20. Since a frequency or phase lock was not required, the speed of the motor was set using a PWM scheme in an open loop configuration. The use of a single motor to drive both the choppers ensures perfect speed match between C1 and C2 as long as the gear linkages and interconnecting belts do not contribute any additional disturbances. Hence a symmetrical assembly design was chosen so that in the event of any unwanted jitter or drifts, both the arms are equally affected thereby ensuring continuous speed synchronisation. For this purpose, good quality rollers and steel reinforced belts were used to link the motor shaft with the individual choppers. The choppers were initially positioned such that they were more or less 180° out of phase with each other and this provided the coarse phase adjustment. For finer phase adjustments, provision was made for two micrometers to be attached to one of the chopper arms of the assembly. These micrometers acted in opposition on the belt connected to the chopper, increasing or decreasing the tension on the belt as they were rotated either clockwise or anticlockwise and thus providing the required fine adjustment in phase. This was monitored by observing the output from both the photoreflective sensors as shown in figure 5.21.

In order to eliminate unwanted triggering due to the presence of spikes on these signals, a waveform shaping circuit shown in figure 5.22 had to be designed at the output of the photoreflective sensors. The signals from C1 and C2 were fed to a low power dual comparator LM393N (c.f. Figure A.12) where they were compared against a set reference voltage. The outputs were then wired to the inputs of two schmitt triggers using LM833N (c.f. Figure A.13, Figure A.14) which were designed to trigger at 1.03 V and hold until 0.9 V. This removed all the unwanted

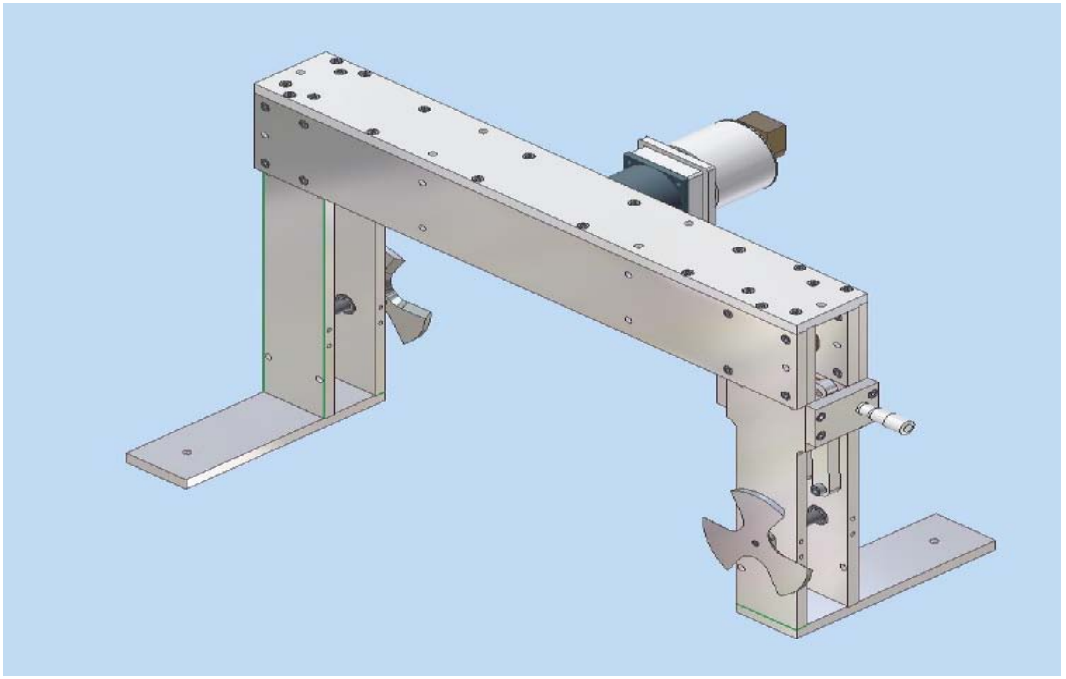

FIGURE 5.20: Mechanical assembly for phase locking of optical choppers

triggering in the raw signals from C1 and C2 and a neat and stable 0-5 V square signal was obtained for both C1 and C2 as in figure 5.21.

Although speed and phase lock was thus established, more significant was the absolute phase accuracy that the mechanical system could provide. This was monitored on a scope by triggering on one of the chopper signals and measuring the shift experienced in the other signal about its mean position. This was observed to be around 200 μsec which translates to 0.7° for a 10 Hz signal. Hence the two choppers were locked in anti-phase with an absolute phase accuracy of 180°±0.7°. In terms of delta, this is equivalent to more than 2‰. Although this was not nearly as good as the required figure of 0.3°, under the circumstances it was decided to go ahead with this level of accuracy for performing all initial tests and experiments. It is worth noting that phase jitter is averaged out by the output time constants of the phase sensitive detector and hence much of the 200 μsec does not matter. Long term drifts are much less of an issue due to the symmetrical mechanical design thereby affecting both channels equally.

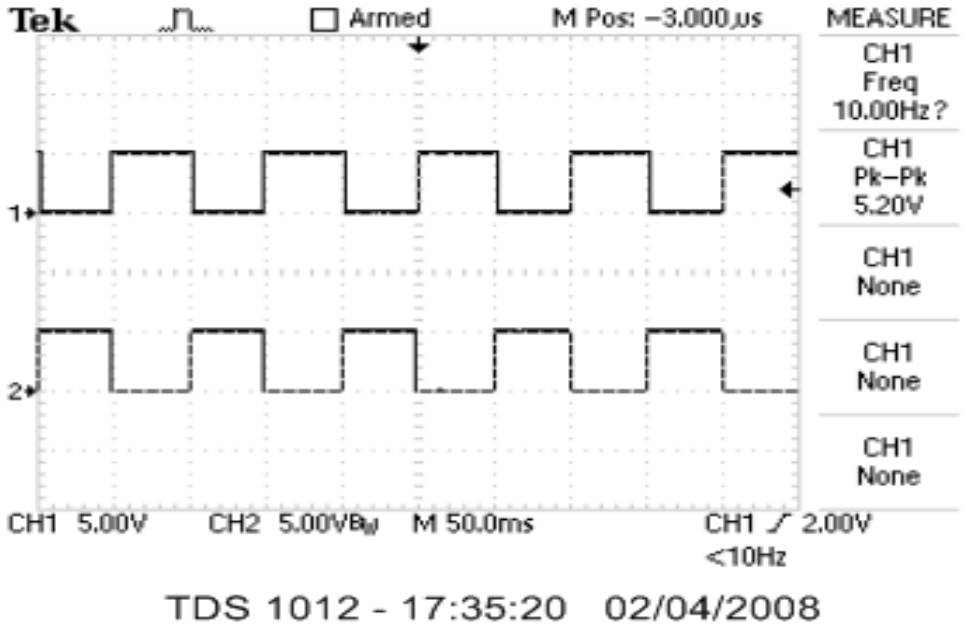

FIGURE 5.21: Photoreflective sensor signals from choppers C1 and C2 showing both the choppers are in anti-phase to each other

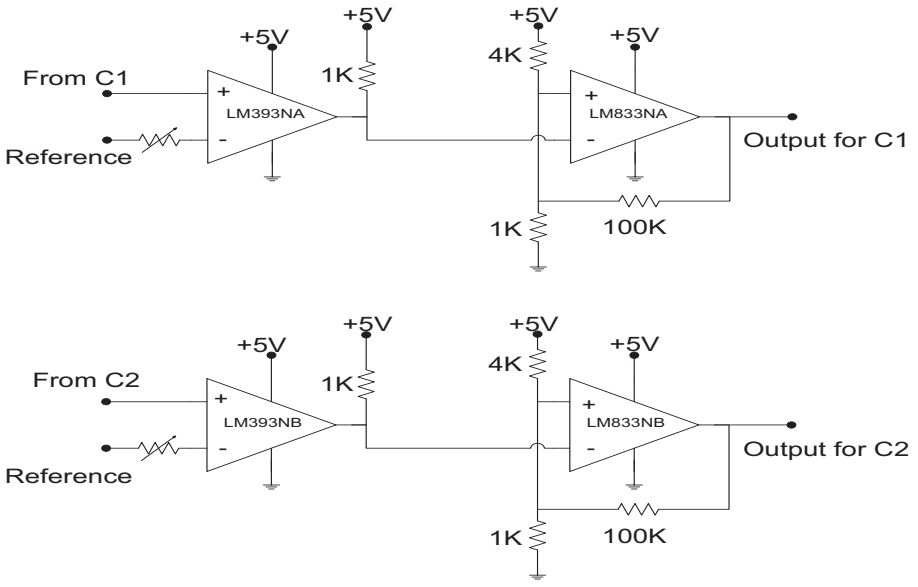

FIGURE 5.22: Wave shaping circuit for the photoreflective sensors

5.5 Gas Delivery Rig

An easy and efficient gas delivery mechanism was required to fill the filter cells with the isotopomers at appropriate pressure, minimising any wastage of the gas and eliminating any leaks. The same system will be used to fill the sample gas cells with calibration gas mixtures for initial experimental tests. For this purpose a dedicated gas delivery rig as depicted in figure 5.23 was put up. Both isotopomer gases were

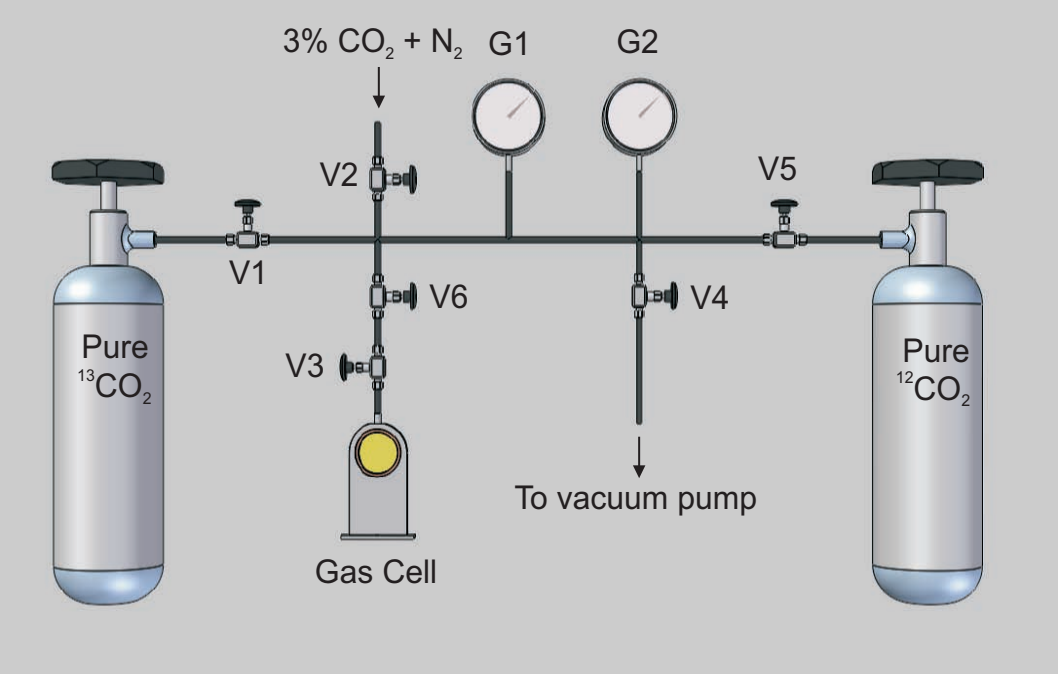

FIGURE 5.23: Dedicated gas delivery rig for filling the ICF and sample cells

supplied in lecture bottles at slightly above atmospheric pressure. Hence regulators were not required to control their flow into the gas cells. $^{13}CO_2$ at 99% enrichment procured from Spectra Gases and a 1 litre $^{12}CO_2$ lecture bottle generally used for welding purposes were used as pure isotopomer gases. The flow of standard calibration mixture of 3% $^{12}CO_2$ and balance N_2 from a pressurised cylinder was regulated and connected to one branch of the gas rig. This mixture was used to simulate normal breath samples during the initial studies that were carried out. Two pressure gauges, one for monitoring gas pressure (G1) and a Pirani gauge for monitoring the quality of vacuum (G2), were used. Initially V3/V6 and V4 were opened to pump the cell down to vacuum. Typically pressures as low as 0.04 mbar were achieved on the Pirani guage. Then V4 was closed and the appropriate gas valve opened in order to fill the cell. Fill pressures were maintained slightly above atmospheric pressure so as to detect any gas leakage after sealing. Once filled and sealed, the cells were detached from rest of the system and used for the

tests. High quality vacuum seals and epoxies were used to minimise leakage from the cells and various joints on the rig. Considerable time and effort was put into making the rig as leak proof as possible so that undesirable gas exchanges, which will affect the measurement precision, were eliminated.

This dedicated gas filling rig was designed such that both the filter cells and the sample gas cells can be connected to it for appropriate gas delivery. However, if gas mixtures containing varying concentrations of both $^{12}CO_2$ and $^{13}CO_2$ were required then this will necessitate proper mixing of the two to ensure a homogenous composition throughout the gas cell. Such gas mixtures are ideal to check the sensitivity and responsivity of the system and also to carry out performance evaluation tests of the whole system. For this purpose special gas sampling bags from Adtech Polymer Engineering were used. These bags were fitted with a universal thread connection that was mated with the gas rig. In this way the appropriate gas mixtures were first prepared in these sampling bags before they were transferred to the sample cells. Since the bags were made of Tedlar PVF, mixing of the constituent gases was done by simply pressing and squeezing the bags once they have been filled. The gas mixture was then forced out into the sample cells after about 10 minutes giving enough time for both $^{12}CO_2$ and $^{13}CO_2$ to mix thoroughly to form a uniform mixture. The sampling bags had a maximum capacity of about 3 litres. If the 13-channel sample cell was to be filled, it was initially purged with dry N_2 so as to expel any other interfering gases present inside it, including atmospheric CO_2. Considering a cell length of about 11 cm and CaF_2 windows of 38 mm dia, the cell volume is 0.125 litres. Hence a 3 L gas bag ensured enough supply of the gas mixture to fully replace the already existing dry N_2 inside the cell.

5.6 Temperature and Pressure Sensors

The use of sensors for continuous monitoring of cell temperature and pressure was discussed previously under section 4.3.3. It must, however, be noted that it is not the absolute ambient or cell temperature and pressure that is of concern here but the variation in ambient conditions during the course of a test. A change in the absolute ambient temperature or pressure can be accounted for by running the spectroscopic model previously developed at these new ambient conditions. The resultant absorption coefficients will then determine the new equilibrium cell length for the 13-channel cell. However, if a temperature or pressure variation

occurs between the basal and sample test of an experiment, this will result in spurious delta values. Since delta evaluation is essentially a ratiometric method, it is important to maintain the same set of ambient conditions during the basal and sample tests. Simulation studies showed that a temperature variation of ±0.5K will result in a delta variation of 1‰. Hence it was decided to monitor the cell temperatures in real time by using temperature sensors such as LM35CZ. Since the sample and filter cells within each channel were placed in close proximity, it was fair to assume thermal equilibrium between them. However, the same cannot be said when considering temperatures across the two channels. Therefore two such sensors were used for monitoring cell temperatures in the two channels separately. One sensor was attached to the walls of the C636 channel gas cell and the other was attached to the 1 mm gas cell placed in the C626 channel. The signal from these sensors were recorded and displayed using a virtual instrument interface software such as LABVIEW. If the variations were found to exceed the tolerance limits, then appropriate temperature stabilisation techniques will be employed. A basic low noise amplifier circuit was connected at the output of the sensors.

Although pressure variations were not expected to be dramatic enough to affect delta measurement, cell pressure was monitored using SDX15A2 which is a temperature compensated pressure sensor. Since the entire gas flow system was sealed once the cells were filled, gas pressure remained the same in both channels. Hence a single sensor attached to the gas delivery tube was sufficient for pressure monitoring. Figure 5.24 shows a picture of the SDX15A2 used for pressure monitoring. Since the sensor gives a differential output, additional circuitry had to be designed

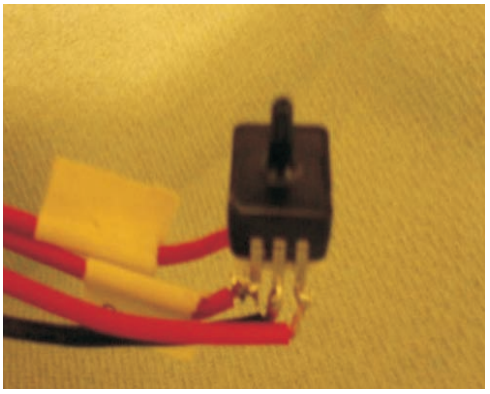

FIGURE 5.24: Picture of the SDX15A2 pressure sensor

to convert it to a single ended voltage signal. Also, the SDX sensor had low common mode output voltage and hence it required special circuitry that can work with input common mode voltages close to ground. High precision single supply instrumentation amplifiers such as AMP04FP (c.f. Figure A.15) were ideally

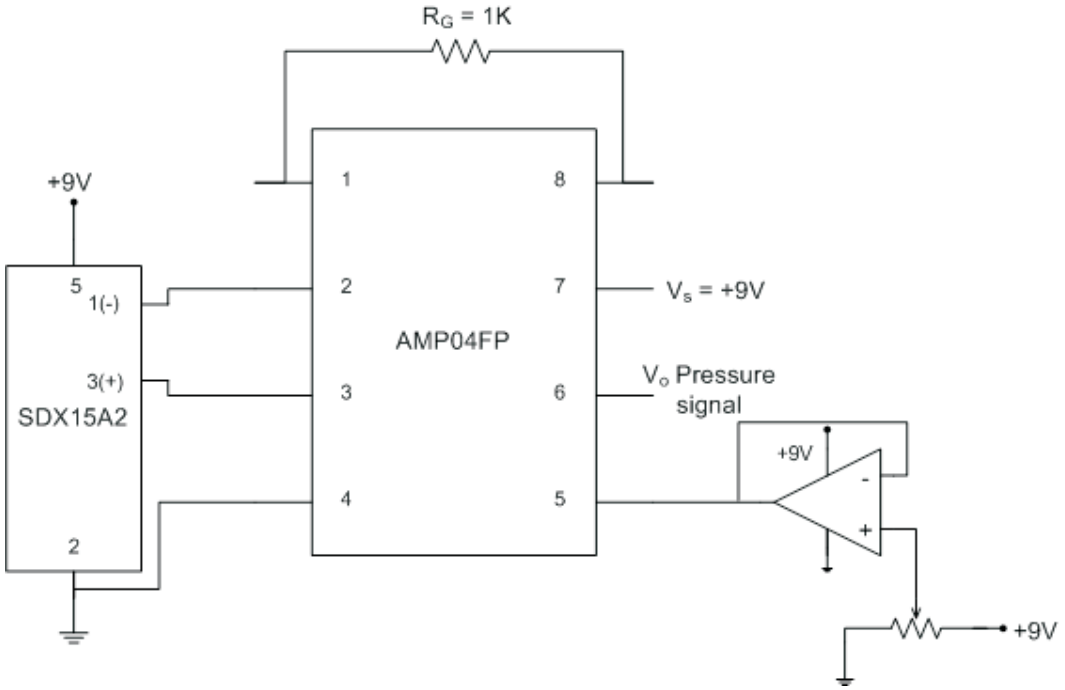

FIGURE 5.25: Signal conditioning circuit for pressure sensor SDX15A2

suited for this application. The signal conditioning circuit for the SDX pressure sensor using AMP04 is shown in figure 5.25.

Referring to the SDX data sheet (c.f. Figure A.2), the sensor gives an output of 0.09 V at 15 psi for a supply voltage, Vs, of 12 V. The design goals for the circuit were set as follows:

- Power supply, Vs = 9 V
- Span = 6.5 V ± 0.1 V at 14.5 psi
- Amplifier gain, Av = 100 KΩ / R_G (from AMP04 data sheet)

Sensor output = 0.09 × (9/12) × (14.5/15) = 0.65 V
Gain Av = 6.5 V/0.65 V = 100
Hence, R_G = 1 KΩ

Thus, for a given pressure P, final output voltage, V_0 = 100 × 0.09 × (9/12) × (P/15). Any offset nulling was achieved by adjusting the common mode voltage of the instrumentation amplifier. In the present circuit this was done by changing the reference voltage at pin 5 of AMP04 using the variable resistor as shown in figure 5.25. All the electronic circuits for both the temperature and pressure sensors were enclosed within an aluminium box and placed in between the channels

as shown in figure 5.26. For calibration purposes, the prevailing ambient temperature and pressure values were obtained from a reliable source[61] and used as the reference value.

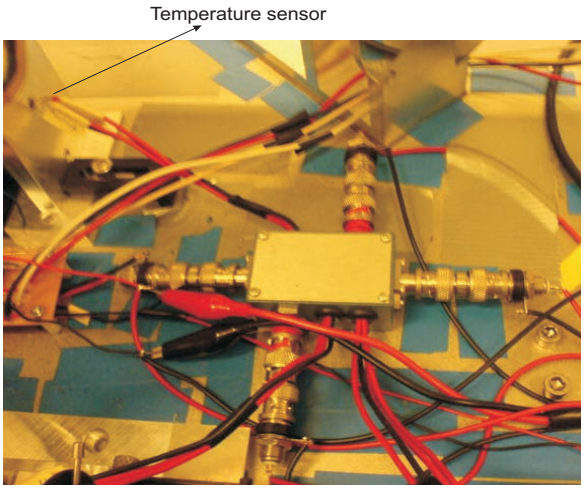

FIGURE 5.26: Picture of the aluminium box housing all the amplifier and signal processing circuits for both the temperature and pressure sensors

5.7 Detector Electronics

As previously stated, the LTIQ2 pyroelectric detector from Scitec Instruments was used in this work. It has a stated responsivity of 210 V/W at 10 Hz and a specific detectivity, D* of 8.10^8 cm$\sqrt{Hz}$/W. For an element size of 2 mm × 2 mm, the noise equivalent power (NEP) is 0.25 nW. Previous simulations and calculations had shown that 1‰ corresponds to a power change of about 0.3 nW at the detector. Hence the current detector specifications are capable of detecting such minute power variations. Since the detector was configured in a voltage mode, the integrated preamplifier was a voltage follower JFET with a high input impedance (gate resistor) of the order of giga ohms. A low noise drain current supply circuitry was built using an additional JFET as recommended by the supplier. The overall circuit diagram is shown in figure 5.27. A low noise FET input opamp such as the OPA2604 (c.f. Figure A.16) was used for final signal conditioning providing a gain of 100 over a pass band of 2-160 Hz.

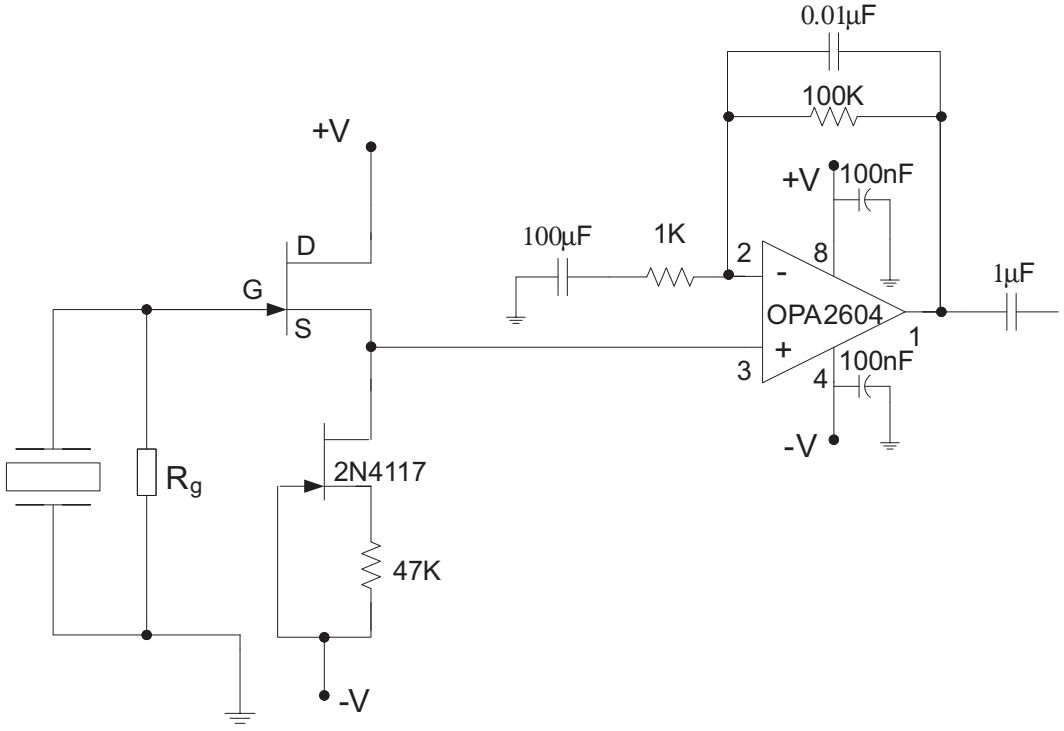

FIGURE 5.27: Detector circuit for high precision and low noise application

The entire detector circuit was assembled and enclosed in an aluminium casing provided with BNC connectors. In order to evaluate the response of the detector, an experiment was conducted to measure the detector output voltage as a function of source temperature. The schematic shown in figure 5.28 was used for this

purpose.

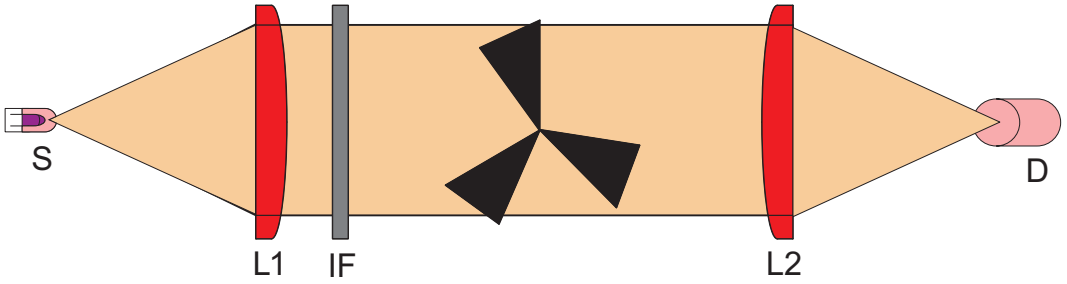

FIGURE 5.28: Experimental setup for detector output measurement

IR radiation from the source S was made to pass through the lens L1 and filter IF before being refocussed onto the detector D using L2. The radiation was chopped at 10 Hz. Source temperature was varied from 674K to 1074K and the corresponding detector signals were recorded and compared with expected values obtained from simulations. Figure 5.29 shows that both simulation and experimental values are in good agreement with each other taking into account uncertainties involved in estimating the source temperature accurately. The detector response to varying

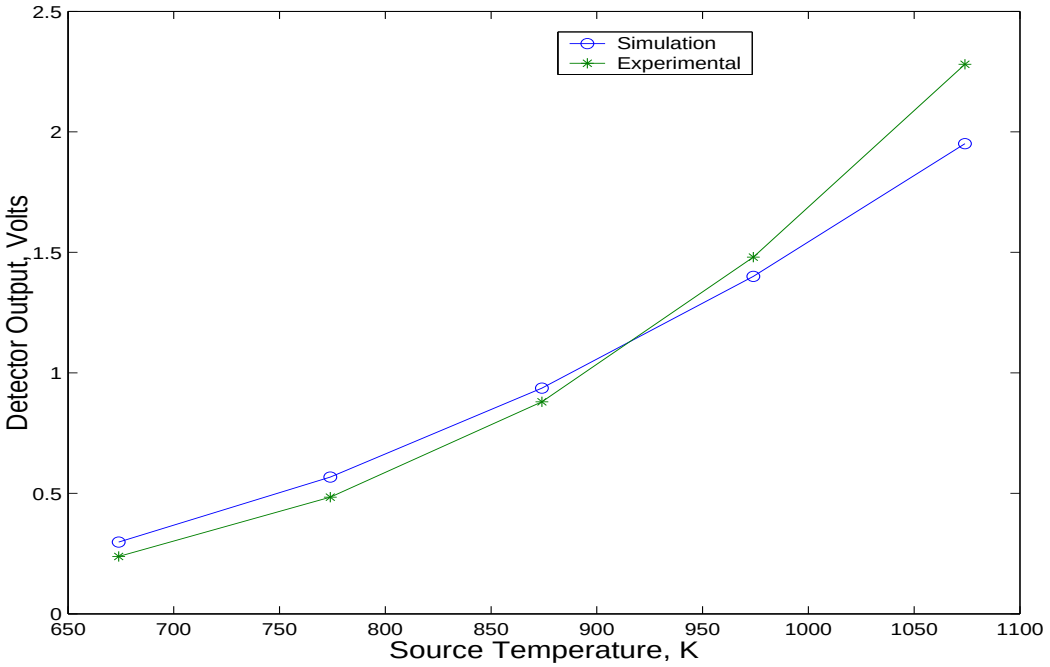

FIGURE 5.29: Variation of detector output with source temperature

isotopomer concentration was also studied by placing a filter cell filled with $^{13}CO_2$ in the beam path. The isotopomer concentration in the cell was varied (with balance N_2) and detector output was measured for different source temperatures. All optical losses from the lenses, IF filter, windows and beam divergence were taken

into account and the results were compared with simulation. Figure 5.30 shows the experimental results to be in good agreement with the simulation values.

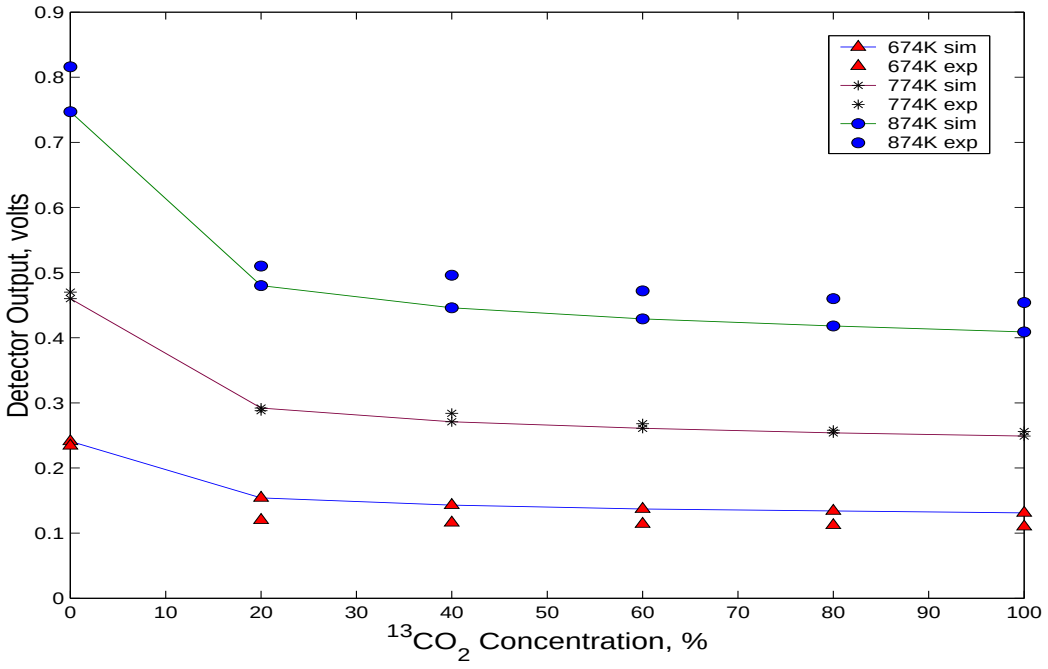

FIGURE 5.30: Detector output at different source temperatures as a function of $^{13}CO_2$ concentration. Balance is filled with N_2

The solid lines indicate the simulation values at 674K, 774K and 874K. Any deviation from the expected values can be attributed to the uncertainty in estimating the source temperature and in determining the exact isotopomer concentration in the gas cell. It was also observed that as the concentration increased beyond 60%, the absorption lines became saturated and very little change in detector output was observed.

Further simulations were carried out to study the relative absorption of C626 and C636 at different isotopomer concentrations for various source temperatures and the detector output was plotted. Figure 5.31 shows that C636 is definitely the stronger absorber of the two since it yielded lower detector output values. The corresponding surface plot for C626 absorption is shown in figure 5.32. All these simulations were carried out by considering the IF filter transmission characteristics over the wavenumber range used for absorption calculations.

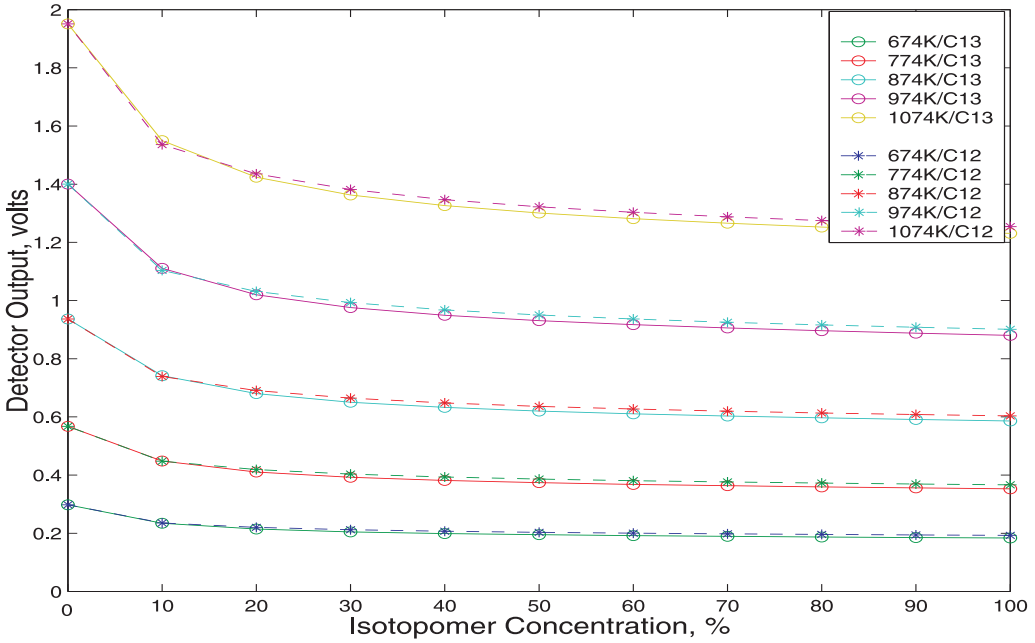

FIGURE 5.31: Comparison of isotopomer absorption strength as a function of source temperature at different concentrations

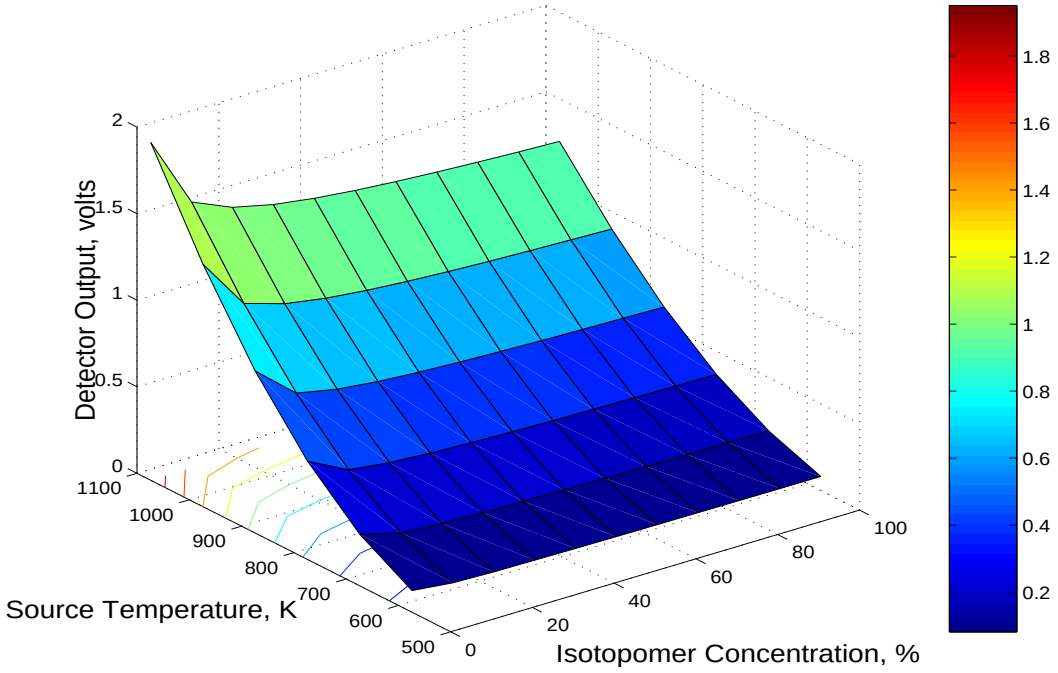

FIGURE 5.32: 3D plot of C626 absorption as a function of source temperature at different isotopomer concentrations

Next individual channel signals and the combined signal falling on the detector were recorded. This was implemented by setting up the system as it will be in its final configuration with both the isotopomer channels in place. Empty sample cells were introduced into their respective beam paths. However, filter cells with pure isotopomers were not used because their introduction will make the remaining unpurged beam path sensitive to absorption by atmospheric CO_2 thereby upsetting the balance of the system. The various optical components and mechanical chopper assembly were positioned and aligned using a He-Ne laser beam. Each channel was individually measured by blocking off the other with a suitable material. Laser spots from the individual channels were made to focus at the same spot on the detector window so that the detector did not see any effective change in temperature or power as the two channels were chopped in a synchronous manner. This will imply a balanced absorption system with equal transmittances along the two channels since the absorption losses along the path length and reflection losses from the optics and cell windows were exactly the same in the two channels. Under such balanced conditions, a null detector output was expected since the detector responded only to changes in temperature. The laser was then replaced by the broadband infrared source maintained at 674K and the detector output was monitored. However, due to slight alignment and focussing errors, perfect balance was not attained initially. An iris diaphragm was therefore introduced in the C626 channel to attenuate the signal in order to achieve equal channel intensities. The optical setup is shown in figure 5.33. The signals were viewed on the oscilloscope and their peak to peak voltages were compared.

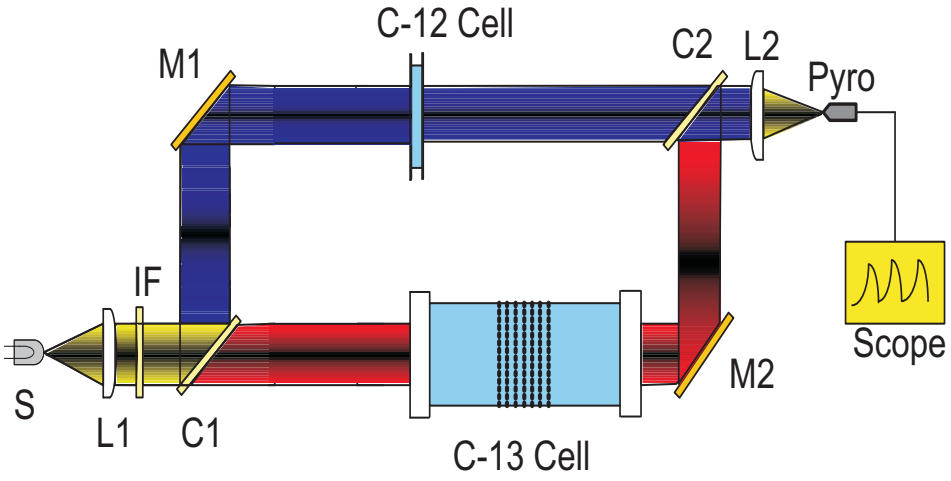

FIGURE 5.33: Experimental setup used to observe both individual channel signals and the combined signal falling on the detector under balanced conditions

Figure 5.34 and figure 5.35 below shows the individual channel signals.

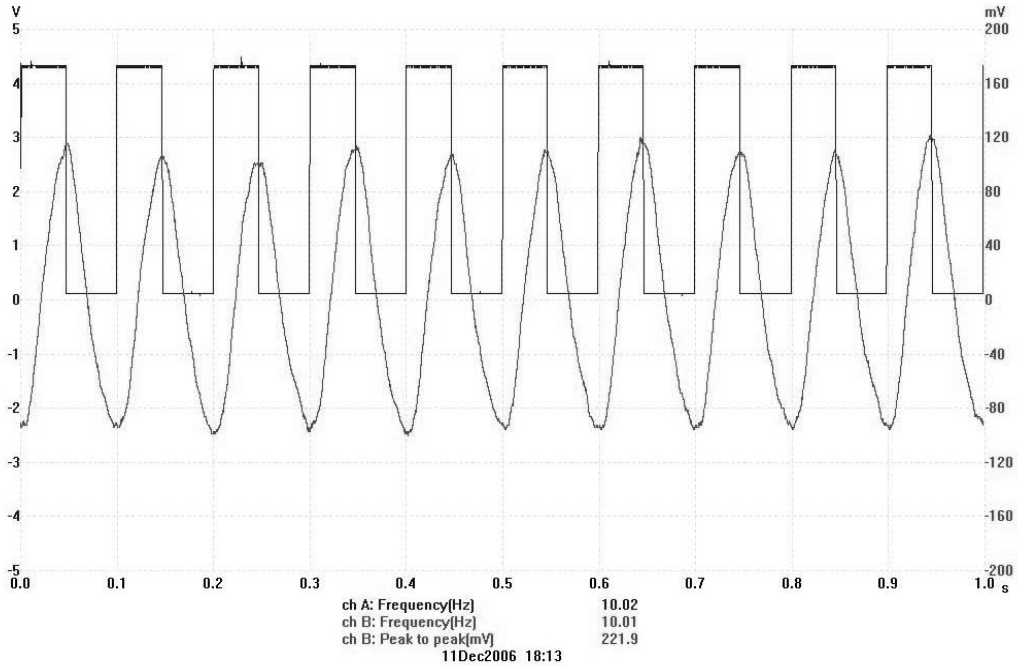

FIGURE 5.34: Detector output signal for C626 channel

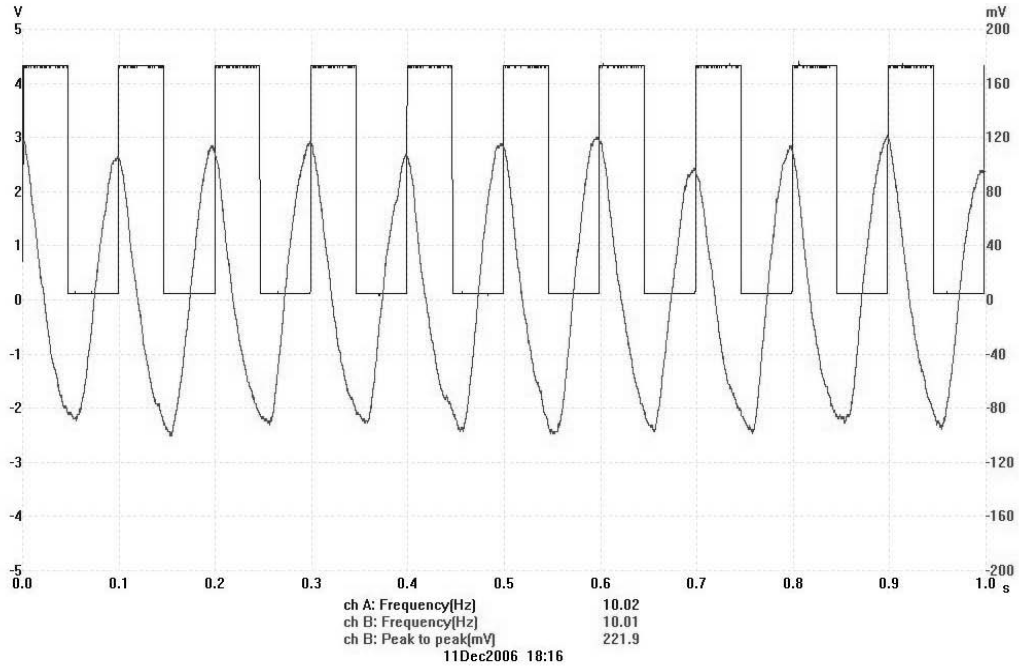

FIGURE 5.35: Detector output signal for C636 channel

As expected the C626 and C636 channel signals exhibited a phase shift of 180° with respect to each other due to the anti-phase arrangement of the choppers C1 and C2. Signal from the C626 channel (figure 5.34) is aligned along the falling edge of the 10 Hz reference signal whereas the C636 channel signal (figure 5.35) is aligned along its rising edge. It should be noted here that the 10 Hz reference signal can be obtained from the photoreflective sensor attached either to C1 or C2. This will not have any impact other than swapping the position of the two individual channel signals with respect to the reference when viewed on a scope. It will of course change the polarity of the final phase sensitive detector output when the system is unbalanced and eventually determine the direction of rotation of the feedback stepper motor.

However, the combined signal from both the channels had a strong second harmonic component (20 Hz) as shown below in figure 5.36 which was contrary to the expected dc signal or null output at balance. At first sight this seems intriguing but a careful analysis of the individual channel signals offers a satisfactory explanation. The appearance of this 20 Hz signal can be attributed to the fact

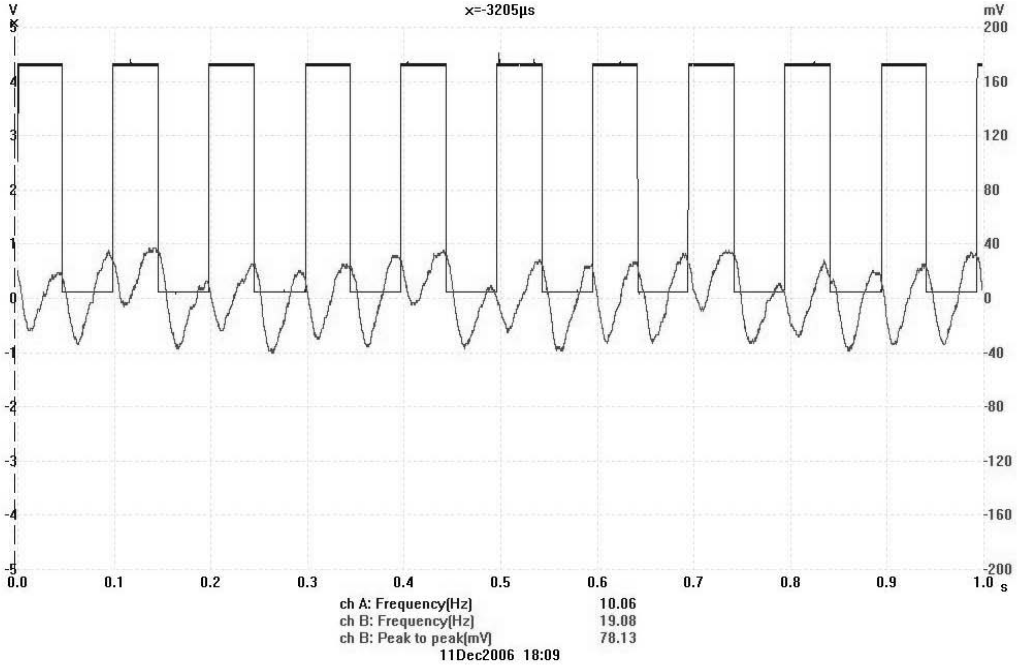

FIGURE 5.36: Combined detector output when both the channels are transmitting showing a distinct 20 Hz component

that the shape of the detector output waveform for the individual channels is not symmetric and hence when the two signals add up, they do not exactly cancel out each other resulting in a waveform with twice the frequency of the original signals. This can be proven by simulating the individual pyroelectric detector signals from

each channel and then computing the fourier transform of the combined signal to reveal the various frequency components present in the output. A pyroelectric output signal can be effectively modelled as a RC low pass filter output signal by the proper choice of R and C values. Consider two such signals of 10 Hz each as shown in figure 5.37 which are in anti-phase, thus emulating the two individual channel signals. If the two signals are made to have exactly the same peak to peak values at all points, they then cancel out each other completely on addition resulting in a null output as shown in the bottom half of figure 5.37.

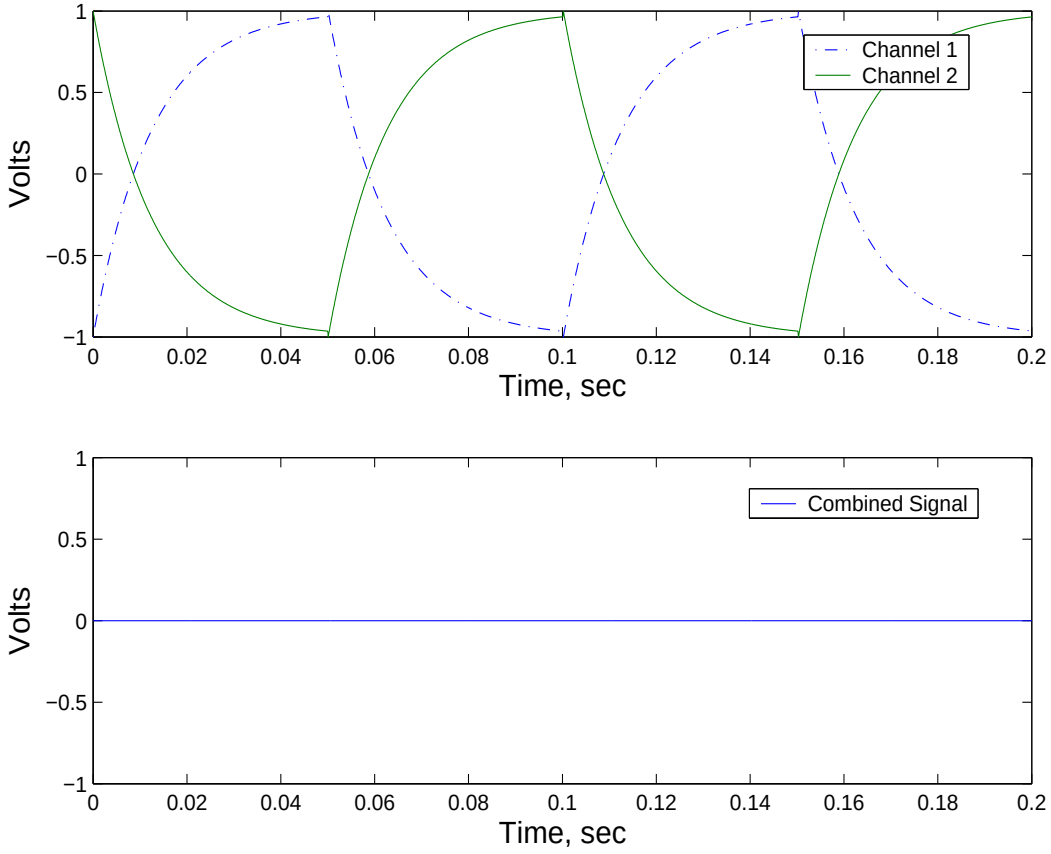

FIGURE 5.37: Individual channel signals of exactly the same amplitude and the resultant combined signal

However, this condition is extremely difficult to obtain in an experiment because small variations in the reflectivity of the chopper blades or a slight misalignment of the channel beams will result in a signal having slightly different amplitudes for each peak. Now consider a similar case where the two signals have slightly different amplitudes at each peak. This approximates a real experimental signal more closely. The top half of figure 5.38 shows the two channel signals and the bottom half represents the combined signal. This combined signal now shows a second harmonic feature which was absent in the earlier case. FFT spectra of the

individual channel signal and the combined signal are shown in figure 5.39. The spectrum for the combination signal now clearly shows a dominant 20 Hz component which was absent when the channel signals had the exact same amplitudes. This analysis thus offers a reasonable and logical explanation for the presence of a strong second harmonic component at the detector output even when the system was at balance.

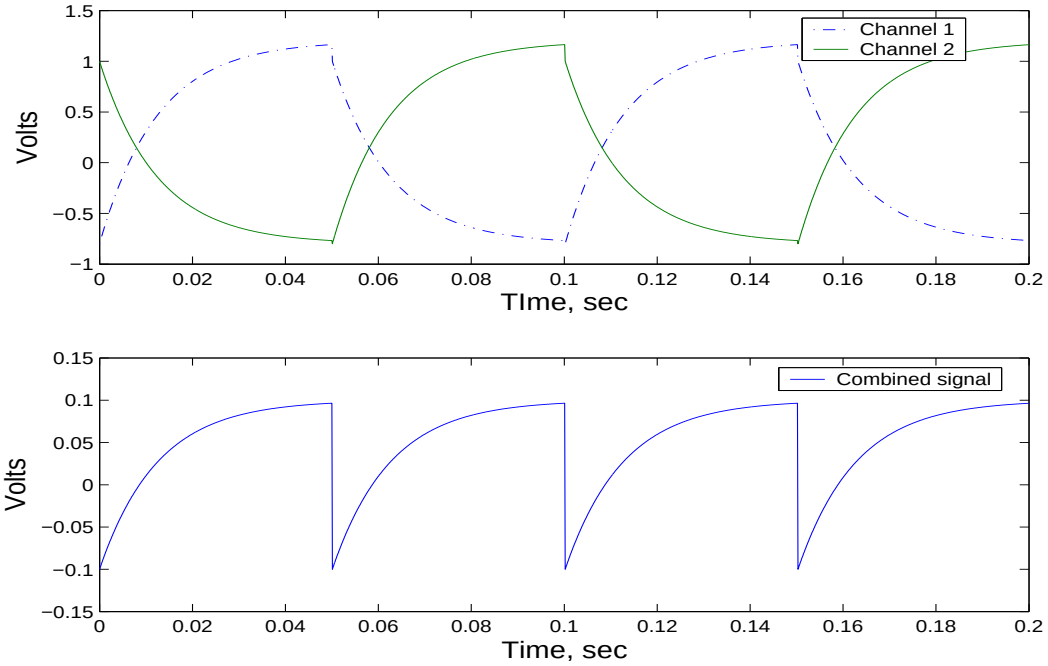

FIGURE 5.38: Individual channel signals of slightly different amplitudes and the resultant combined signal

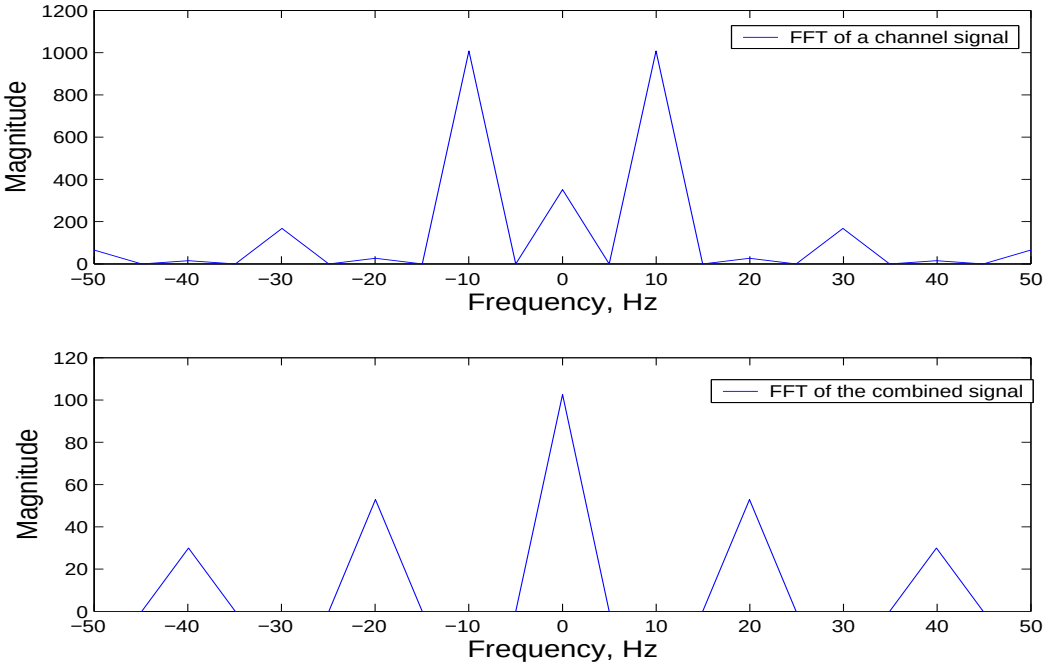

FIGURE 5.39: FFT spectra of the individual channel signal at 10 Hz and the combined signal when both channels have slightly different amplitudes. Note the presence of a strong second harmonic component at 20 Hz

5.8 Cell Length Adjustment and Feedback Servo Loop

A unique feature of the diagnostic system presented here is its ability to maintain equal integrated transmittances along the two channels. This is done by restoring the system to the balanced point as represented by a null detector output. This process of self-balancing is implemented by the use of a feedback servo loop that uses the unbalanced detector output to drive the C636 channel sample cell length in the required direction so as to maintain balanced absorption. Hence the response and behaviour of the feedback mechanism plays a vital role in the proper functioning of the system. For precise length adjustment and accurate determination of the length varied, it was decided to use a stepper motor which will be attached to the micrometer head of the sample cell assembly. The use of a stepper motor also makes digital control feasible by the use of an appropriate driver card. This renders greater flexibility to the design in terms of step size and direction control. A unipolar stepper motor 16HS-110 (8 leads) from Mclennan (c.f. Figure A.17) which provided 200 steps/revolution under full step mode was used for this purpose. To achieve finer step resolution, a gear head with 12.5:1 gear ratio was also attached to the motor. A driver card RSSM2 (c.f. Figure A.18)

was used for controlling the stepper motor. The driver card was configured to run the motor in full step mode with the clock input signal (CKI) derived from an externally generated square wave signal. This clock input was simulated in LABVIEW and delivered to the driver card via the analog output channel A0.0 of a USB multi-function DAQ 6008 from National Instruments. More details on the DAQ are provided in the following section. Similarly, direction control was also implemented via analog output channel A0.1 of the DAQ. The ENB terminal was held high (+5V) to enable CKI. The four phase leads of the stepper motor (leads 1, 2, 3 and 4 in c.f. Figure A.17) were wired to the appropriate phase terminals PHA, PHB, PHC and PHD on the driver card. Leads 1' and 2' and leads 3' and 4' were tied together since in a full step mode only one of the phase windings was energised at a time. Forcing resistors (R_f) were used to limit the current in the motor windings when driven at higher voltages for higher speeds. The value for R_f was calculated as follows:

$$R_f = \left[\frac{Supplyvoltage, Vs}{Current/phase, Im}\right] - Resistance/phase, Rm \tag{5.2}$$

Here, Vs = 24 V, Im = 0.5 A (from data sheet), Rm = 7.2 Ω
Hence, R_f = 40.8 Ω
Two resistors of 22 Ω each were connected in series to give a total R_f value of 44 Ω.
The total current through each phase now became 0.468 A with a power dissipation for R_f equalling $0.468^2 \times$ 22 = 4.83 W
Hence R_f with 22 Ω/9 W ratings were used.
The interface and connections between the stepper motor driver card and the motor itself is shown in figure 5.40.

5.9 Virtual Interface - LABVIEW Implementation

For the entire instrument to work effectively as a single unit, it is essential to ensure proper and timely collection of data from the various sensors and also acquisition of detector signals. The information then needs to be processed and converted to command signals to actuate the stepper motor assembly to perform the feedback control process. In order to make the entire measurement and control process

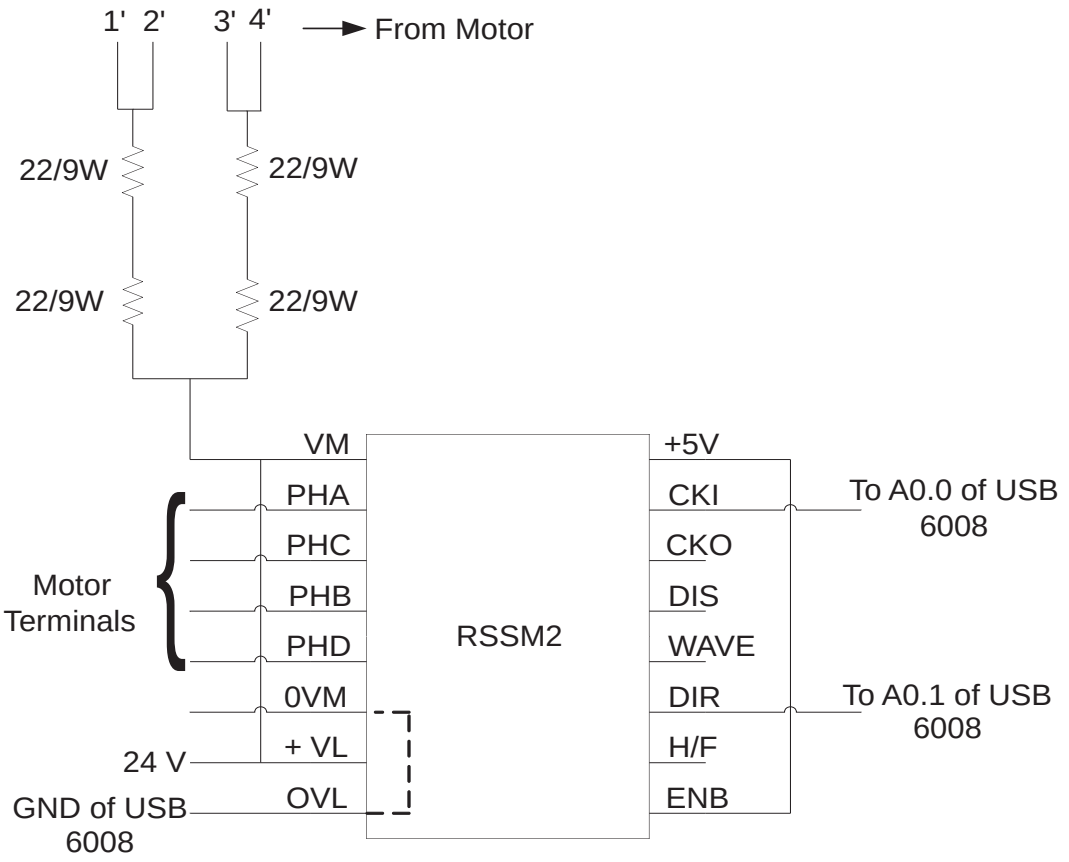

FIGURE 5.40: Stepper motor interface with the driver card RSSM2

totally automated, the controlling software needs to be seamlessly integrated with the hardware. LABVIEW provides a very professional and industry relevant means of implementing this by building a Virtual Interface (VI).

As mentioned previously, NI USB 6008 DAQ was used for acquiring signals and data from various sensors and detectors. Figure 5.41 shows the front panel of the VI used for acquiring and displaying temperature and pressure data from the sensors. Also indicated are the detector output (Det o/p) and the 10 Hz reference signal (Ref) from the chopper. As can be seen from the figure, the C13 and C12 temperature data was very stable and the fluctuation observed was much less than ± 0.5K to require any active temperature control measures. The pressure data also showed good stability with a standard deviation less than ± 1 mbar which was equivalent to a spurious delta of 0.3‰. Depending on the nature of the detector output, the signal processing scheme in LABVIEW was used to generate the DIR signal (figure 5.40) which was used to turn the stepper motor either in the clockwise or anticlockwise direction, so as to restore the system to balance. The direction of rotation was determined by checking the polarity of the PSD signal. By implementing a set of relays in LABVIEW, it was possible to

turn the stepper motors ON and OFF and also to control the direction of rotation with a 0 V signal indicating a clockwise direction and a 5 V dc signal indicating anti-clockwise direction.

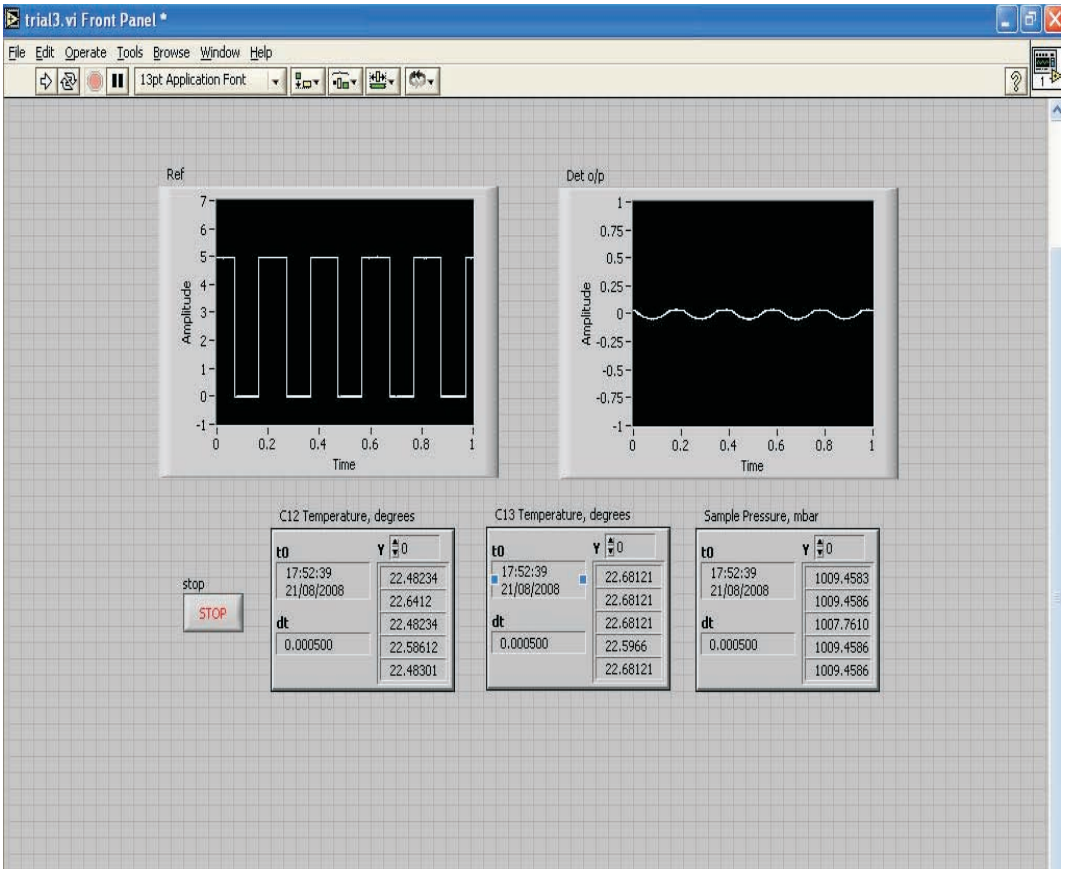

FIGURE 5.41: LABVIEW VI showing acquisition and display of data from the pressure and temperature sensors and also form the pyroelectric detector

5.10 Overall Instrument Enclosure

Once all the subsystems and various components were ready, the next step was to integrate them all within a closed environment which will eventually become the instrument enclosure. Such an enclosure needs to have an environment free from ambient CO_2. The presence of ambient CO_2 in the non-sample pathlength will seriously hamper accurate measurement of isotopomer ratios due to the relatively greater abundance of $^{12}CO_2$ in comparison to the rarer isotopomer $^{13}CO_2$. This will result in an increased absorption along the C626 channel leading to imbalances in the integrated transmittances between the two channels. The introduction of filter cells containing pure isotopomers further compounds the problem

by rendering the system more sensitive to absorption effects along the non-sample path length of the beams. All this necessitates the removal of background CO_2 from within the enclosure. It was suggested earlier in section 4.3.5 that the use of CO_2 absorbing materials was a possible solution to this problem. Ascarite is one such popular CO_2 absorber and is actually made of sodium hydroxide coated with amorphous silica. The initial plan was to place a tray of Ascarite within the enclosure. Another way was to apply a layer of Ascarite along the walls of the enclosure. This will ensure sufficient surface area for absorption of background CO_2. However, further examination of the chemical properties[62] of this absorber revealed that the handling of Ascarite had to be treated with utmost care and caution. Ascarite is highly corrosive in nature and can cause severe burns through all exposure routes. The health hazards associated with it requires that all engineering controls and personal safety measures are in place before it is put to use. The use of such a chemical will cause a lot of inconvenience since frequent access and handling of optical and electronic components within the enclosure will be a necessity. Hence it was decided to drop the idea of using Ascarite. Instead, a continuously purged environment within the enclosure is also equally effective in eliminating background CO_2. A well monitored and regulated feed of dry nitrogen into the enclosure can keep the background CO_2 levels sufficiently low. Besides, the sample cells will have to be purged with N_2 prior to the introduction of the sample gas. A purge of the gas cells will also be required each time a new sample of same or different concentration is fed into them. Hence, the use of N_2 purge cannot be avoided. An effective and simple design for gas pathways will accomplish the twin tasks of purging the enclosure as a whole and the individual gas cells. The use and placement of valves to isolate the gas cells also needs to be considered carefully.

Figure 5.42 is a schematic sketch of the enclosure showing the purge pathways. For convenience, only the two sample gas cells have been shown. As can be seen, valve V1 controls the flow of dry N_2 into the enclosure. A part of the purge is fed straight into the top of the enclosure through a special arrangement that allows the gas to pass through a number of small orifices. This flow is maintained long enough until the background level of CO_2 has dropped to permissible limits. A similar arrangement at the opposite end of enclosure provides outlet for the purge gas. A part of the inlet purge is also directed into the C636 sample cell using V2 and V3. The gas enters near one end of the gas cell and exits near the other end, thereby ensuring a proper purge of the entire volume of the gas cell. If the inlet and outlet points where placed at the same end, some residual gas can possibly

remain unpurged at the other end thereby interfering with a fresh sample that is fed into it. The outlet valve V4 then feeds N_2 into the 1 mm gas cell in the C626 channel and the gas then leaves via V6 as shown.

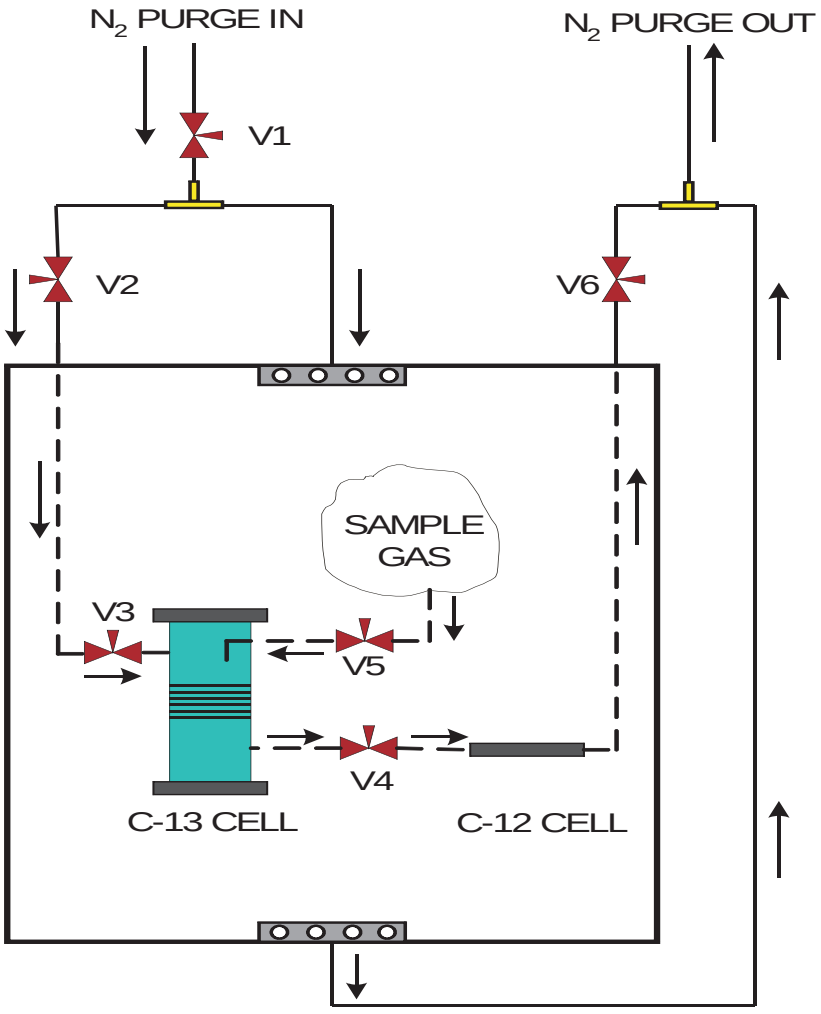

FIGURE 5.42: Overall instrument enclosure depicting purge gas and sample gas flow pathways

The advantage of using this scheme is that once the sample cells have been sufficiently purged, the flow of N_2 into them can be regulated using valves V2, V3 and V6. A rectangular box having dimensions of 110 cm x 60 cm x 50 cm was made using light weight aluminium frames and transparent windows on all four sides and the top. The front face window was made detachable so as to gain easy access into the enclosure. Holes were drilled at appropriate places for the feedthrough tubes to be inserted. The enclosure was made as leak tight as possible to minimise exchange of gases with the ambient. A flow regulator was also attached to the frame of the enclosure. All the exposed tapped holes on the optical table were also sealed to prevent escape or entry of gases through them. Since the entire enclosure

and not just the beam paths is being purged, the amount of purge time required depends on the volume of the enclosure. A background air level of less than 0.1% is sufficient to ensure no significant absorption along the non-sample path length. The actual amount of CO_2 will be much lower since CO_2 only constitutes about 0.04% of ambient air. If we assume 50% mixing each time a volume of purge gas equivalent to the enclosure volume is fed through, then it will take 10 such mixings to get the background air levels down to less than 0.1%. For an enclosure of the above dimensions, it will take about 300 litres of dry N_2 to completely occupy the box. Ten times this volume will mean the total amount of dry N_2 required to establish 0.1% of background air is 3000 litres. With an acceptable flow rate of about 25 lt/min, the total purge time is roughly two hours. After this time, the purge flow rate can be reduced to about 1-2 l/min to maintain the purge quality throughout the course of the experiments. The overall instrument setup sealed within the enclosure is shown below in figure 5.43. The PVF gas sampling bag can be seen attached at the top of the enclosure.

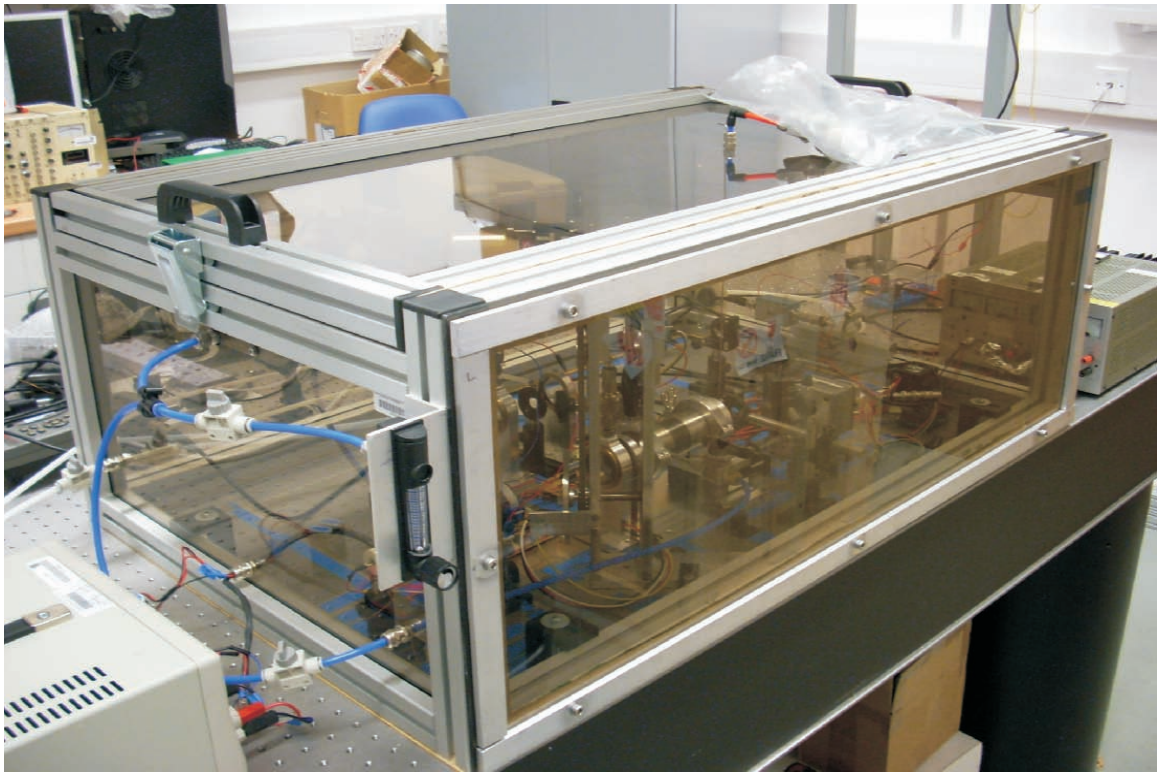

FIGURE 5.43: Overall setup within the instrument enclosure with the gas sampling bag attached at the top

Chapter 6

Experimental Results and Analysis

6.1 Initial Experiments and Tests

In the previous chapters, a detailed discussion of the overall instrument configuration and its various sub systems was provided. A thorough understanding of the performance requirements was acquired and the possible sources of interference that can result in spurious measurements and ways to overcome their effects were also discussed. Once all the necessary electronics and data acquisition system were put in place, the next logical step was to carry out preliminary gas based tests and compare the results with data obtained from simulated tests. For this purpose, a custom made gas filling rig was also designed. Before conducting gas based trials, it was important to check and ensure that the gas cells were leak proof and that there was no possibility of exchange of gases with the surroundings. Presence of leaks will change the concentration of the sample gas within the cells, thereby altering the absorption profile along the two channels. The gas cells themselves are unlikely to be a source of leak since both the filter and sample gas cells were well sealed with CaF_2 windows using a special adhesive. However, the same cannot be said about the valve connections and other gas tube attachments that were made.

To check the presence of leaks, a Magnahelic differential pressure gauge was used to monitor the cell pressure relative to the ambient pressure. The longer C-13 gas cell was subjected to a leak test and the ability to change its length provided an added advantage in performing the test. The gas cell length was initially maintained at 11 cm and the cell was continuously purged with N_2. A 60-0-60 Pascals Magnahelic

differential pressure gauge was connected to it to monitor differential pressure relative to the ambient. As expected the gauge indicated a reading close to 0. The cell length was then increased to 11.3 cm and the pressure reading suddenly dropped to -30 Pascals but then gradually rose back to the 0 mark indicating a leak. The length was then decreased to 10.7 cm and a similar behaviour was observed with the pressure reading rising sharply to 40 Pascals and then returning back to 0 in under 15 minutes. All this showed that the gas cell suffered from considerable leakage. In order to further establish the presence of leaks, a test using the FTIR (Fourier Transform Infrared Spectrometer) was carried out. The gas cell was filled with the 3% CO_2 sample gas mixture and the length maintained at 10.7 cm. Figure 6.1 shows the transmission spectra of the gas cell obtained using the FTIR with a scan resolution of 1 cm^{-1}. Subsequent spectra were also recorded after intervals of 2 hours and 4 hours and a final spectra was recorded the following day. The FTIR spectra clearly indicate a progressive reduction in absorption in the gas cell with the passage of time, finally resulting in very little or almost no absorption the following day.

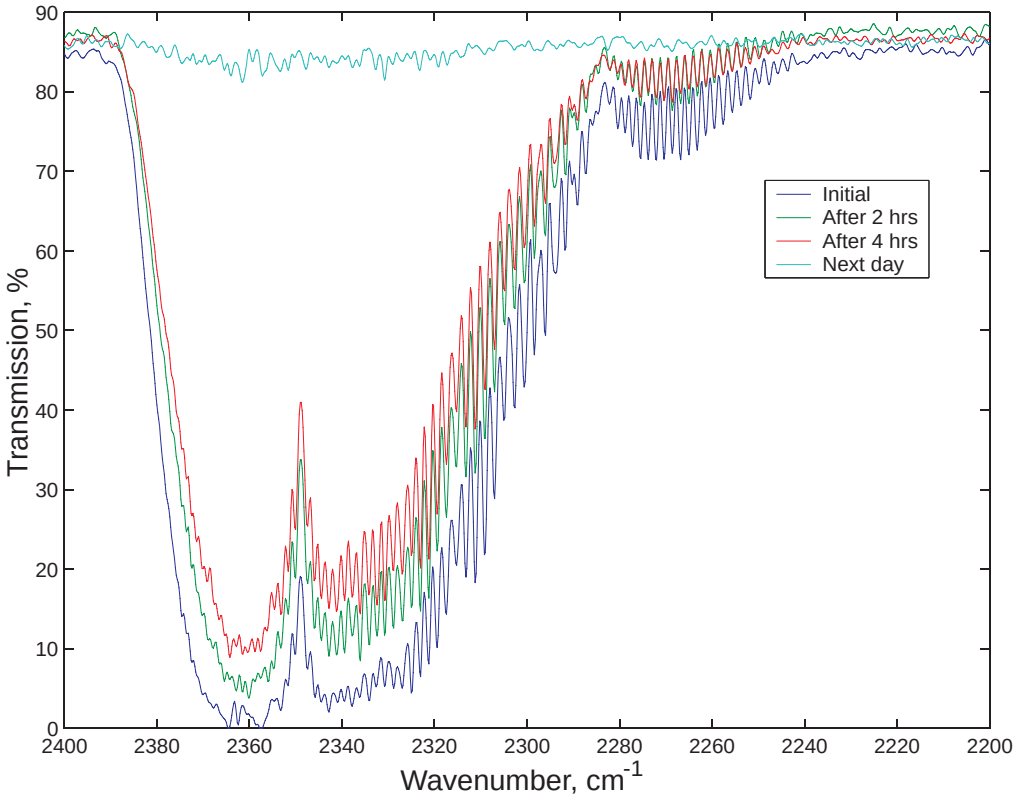

FIGURE 6.1: FTIR spectra showing reduction in absorption in the gas cell due to the presence of leaks. Scan resolution was 1 cm^{-1}

The above tests confirmed the presence of leaks from the gas cell. Valves V3, V4 and V5 attached to the gas cell along with the tube connections were the most likely sources of these leaks. These were ordinary plastic finger valves with push-in connections at either ends. They where chosen due to their low cost and ease of connecting to the gas delivery tubes. The gas cell was then subjected to a leak test using a helium leak detector to identify the exact points of leak. As suspected, considerable leakage signal was picked up in and around the valves and the tube connections. The cell window ends on the other hand did not show any signs of leakage. All the valves were immediately replaced with superior quality Swagelok ball valves and fittings and the cell was subjected to another round of leak tests which came out satisfactory. Similar valve replacements were also carried out for the 1 mm gas cell and the filter cells. Another round of pressure tests using the Magnahelic was conducted and this time the drop in pressure recorded was less than 10 Pascals /hour. This indicated a significant improvement from the previous pressure change of 40 Pascals in 15 minutes. A picture of the C-13 sample cell with improved connections and valve fittings is shown below in figure 6.2.

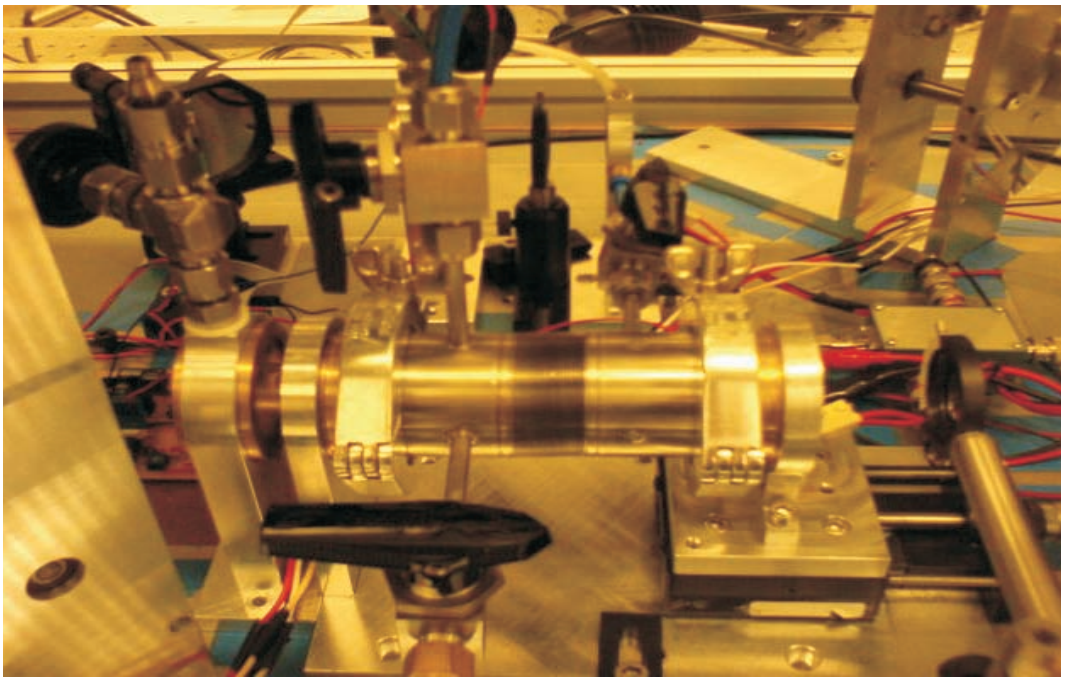

FIGURE 6.2: Photo of the C-13 sample cell with Swagelok connections and valve fittings for a better leak proof system

During the course of these pressure tests, it was also realised that the gas sampling bag had to be left attached to the C-13 cell with valve V5 open while making actual length change measurements. If V5 was closed, any change in the length of the C-13 cell will simply have the effect of changing the pressure inside gas

cell leading to pressure broadening of the absorption lines with a drop in its peak intensity. This, however, will not change the integrated absorption measured as the area under the curve since the amount of gas present in the cell remains the same. Hence, variation in length under such conditions will not alter the channel integrated transmittance preventing the feedback loop from driving the system to equilibrium or balanced absorption. But by maintaining V5 in the open position, a change in length will either draw in extra gas into the cell or drive out excess gas from the cell into the sample bag thereby maintaining constant pressure. This has the effect of changing the integrated absorption along the channel. An increase in length will draw in extra gas from the gas bag thereby increasing absorption and a decrease in length will therefore result in decreased absorption. This is evident in the low resolution FTIR scans taken from the gas cells with the bag attached as shown in figure 6.3. The scans were recorded at different lengths of 9.9 cm, 10.7 cm and 11.7 cm and the corresponding increase in absorption or drop in transmission can be clearly seen for increasing lengths.

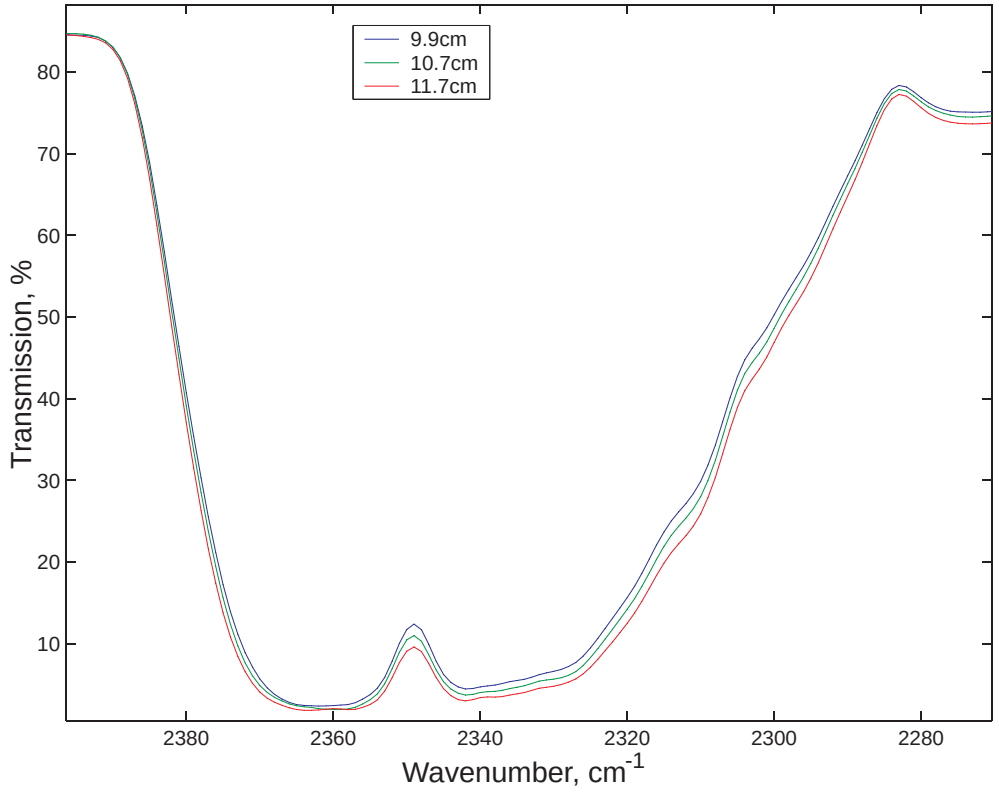

FIGURE 6.3: FTIR spectra showing change in overall absorption when gas bag is attached to the sample cell. Scan resolution was 4 cm^{-1}

Using the gas filling rig, the filter cells were filled with the corresponding pure

isotopomers. They were then placed in their respective channels. The source temperature was varied from 674K to 874K in steps of 50K and the corresponding detector output voltage was recorded and compared against expected value obtained from simulation studies. These measurements were later repeated with the empty sample cells also placed in the beam path.

Figures 6.4 and 6.5 show that the experimental data confirms well the simulation results which validates the accuracy of the simulation model and the systematic approach adopted so far.

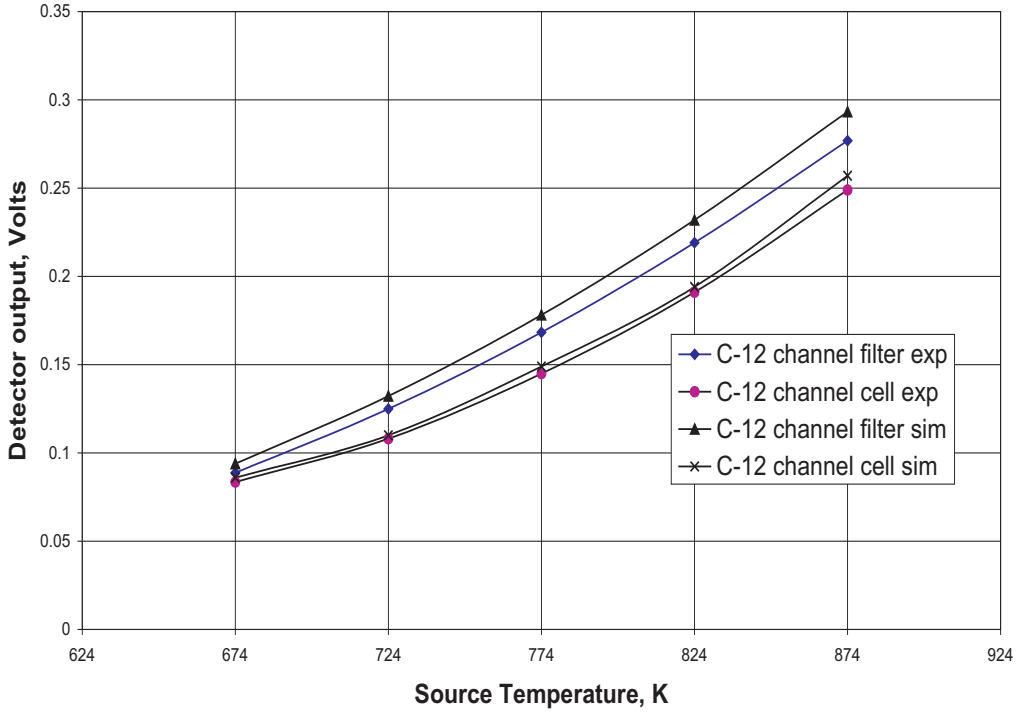

FIGURE 6.4: Plot showing comparison between C-12 channel simulated results and actual experimental values for detector output at various source temperatures

Since all the tests conducted so far yielded satisfactory results, it was decided to check how the entire instrument setup responds when the sample cells were filled with the 3% gas mixture. More specifically, the objective was to determine if the system can detect a variation in the integrated channel absorptions. The output from the detector was fed to a SRS 530 dual channel lock-in amplifier from Stanford Research Systems. The PSD received its 10 Hz reference signal from the photoreflective sensors discussed previously. The dc output from the PSD was then used to study the response of the system when there is a change in channel transmittances. This can be done either by using the X/Y mode or the R/ϕ mode

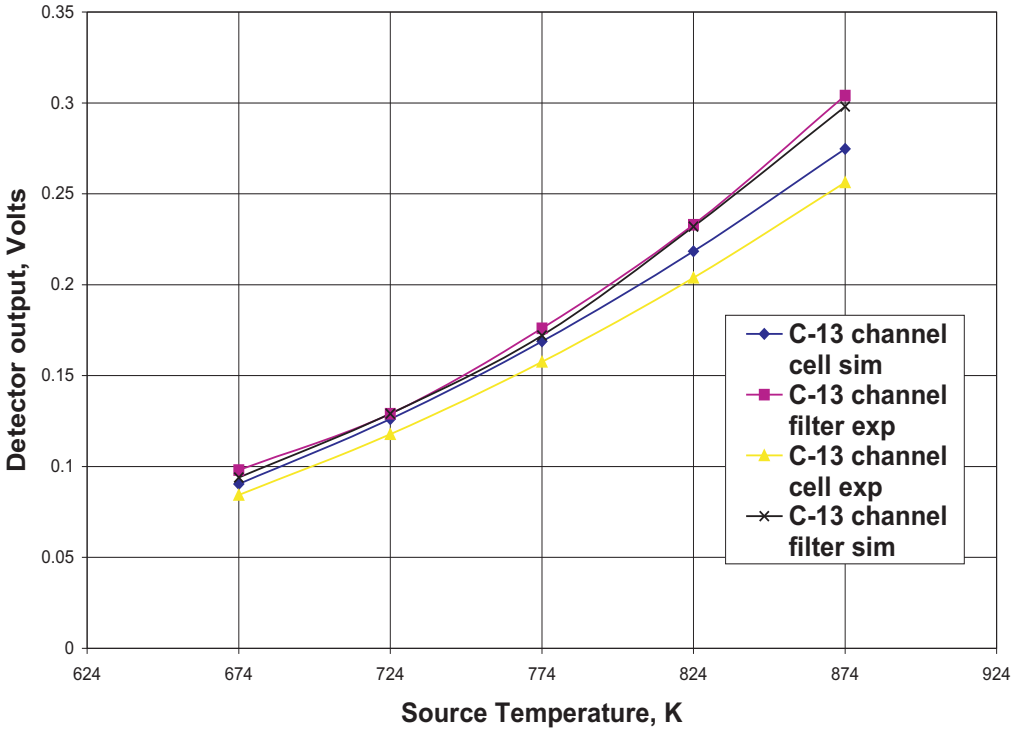

FIGURE 6.5: Plot showing comparison between C-13 channel simulated results and actual experimental values for detector output at various source temperatures

on the SRS 530. Both convey the same information although in different forms. A suitable integration time constant of 10 seconds was chosen. The procedure adopted was as follows. Before making use of the filter and sample cells, it was necessary to have proper phase setting on the PSD. The channels were made to balance initially without using any of the gas cells. The source temperature was maintained at 674K and the choppers were turned on. The inherent imbalance in the system due to the slightly different channel intensities was corrected by making use of an iris that was placed in the C-12 channel. Once satisfactory balance was achieved, the system was unbalanced by blocking one of the channels and the PSD was switched to X/Y mode. The detector output signal at this point coincided either with the leading or falling edge of the 10 Hz square wave, depending on which channel had been blocked indicating that it was 90° out of phase with respect to the reference. In order to maximise the output, the phase was adjusted to obtain a maximum positive value (cos 0° is positive) or maximum negative value (cos 180° is negative) for the unbalanced signal. If now the other channel was blocked and the first one exposed, X value on the PSD output will swing to a maximum value with reverse polarity. Hence by observing the polarity of the X value, it was possible to determine which channel was stronger and by

how much it was stronger. The same information can also be obtained using the R/ϕ mode which gives a direct measurement of the phase value.

Once the PSD has been properly set for measurements, the filter cells were placed in their respective beam paths along the with the empty sample cells. The entire enclosure was closed and purged continuously at 25 lt/min for approximately two hours. During this period, the sample cells were also continuously purged to expel any CO_2 containing ambient air within them. It was observed that at the beginning of the purge session, the C636 channel signal appeared stronger than the C626 channel signal. This was seen by observing the detector output on an oscilloscope as shown in figure 6.6. Also the PSD output was positive indicating a stronger C636 channel signal. This was expected because once the filter cells were placed in the beam paths, the unpurged beam path beyond the filter cells will result in increased C626 absorption due to its greater abundance in the ambient unpurged air. Hence the C636 channel peaks falling on the leading edge will become stronger. But as the enclosure continues to get purged driving out excess

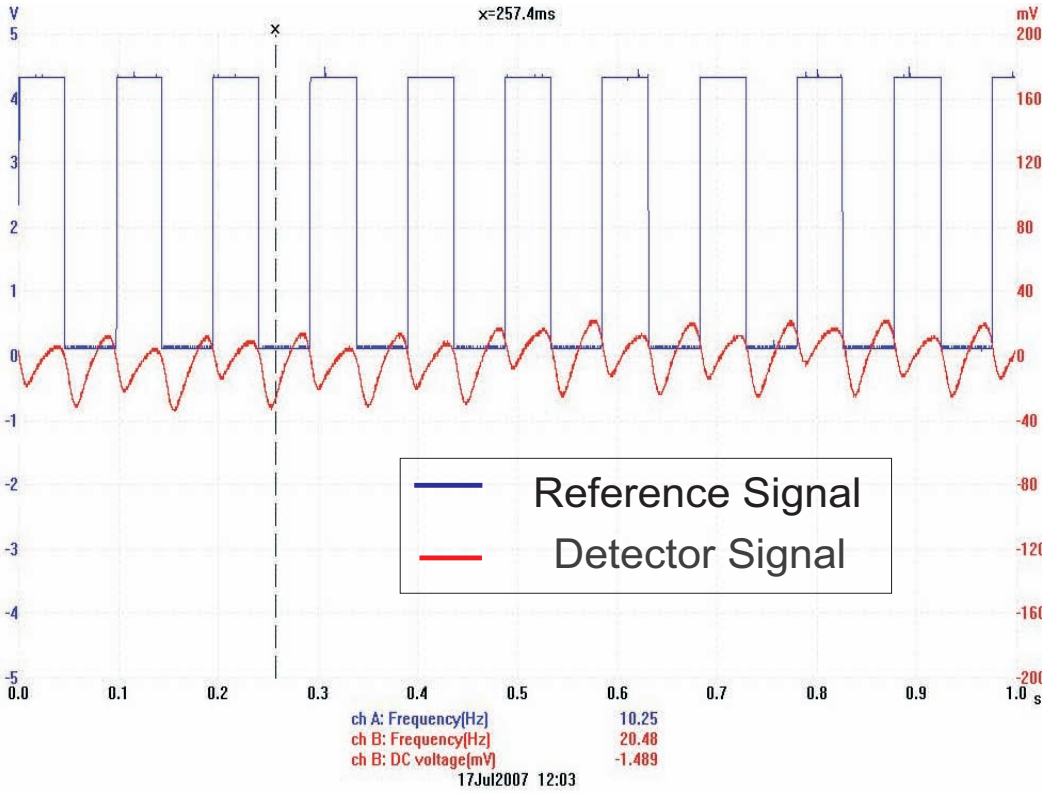

FIGURE 6.6: Oscilloscope display showing combined signal at the beginning of the purge session with the C636 channel signal(leading edge peaks) more stronger than the C626 channel signal(falling edge peaks)

CO_2 from the non-sample pathlength, a reduction in the imbalance can be observed as illustrated in figure 6.7. Both the channel peaks now have nearly the same peak to peak intensity.

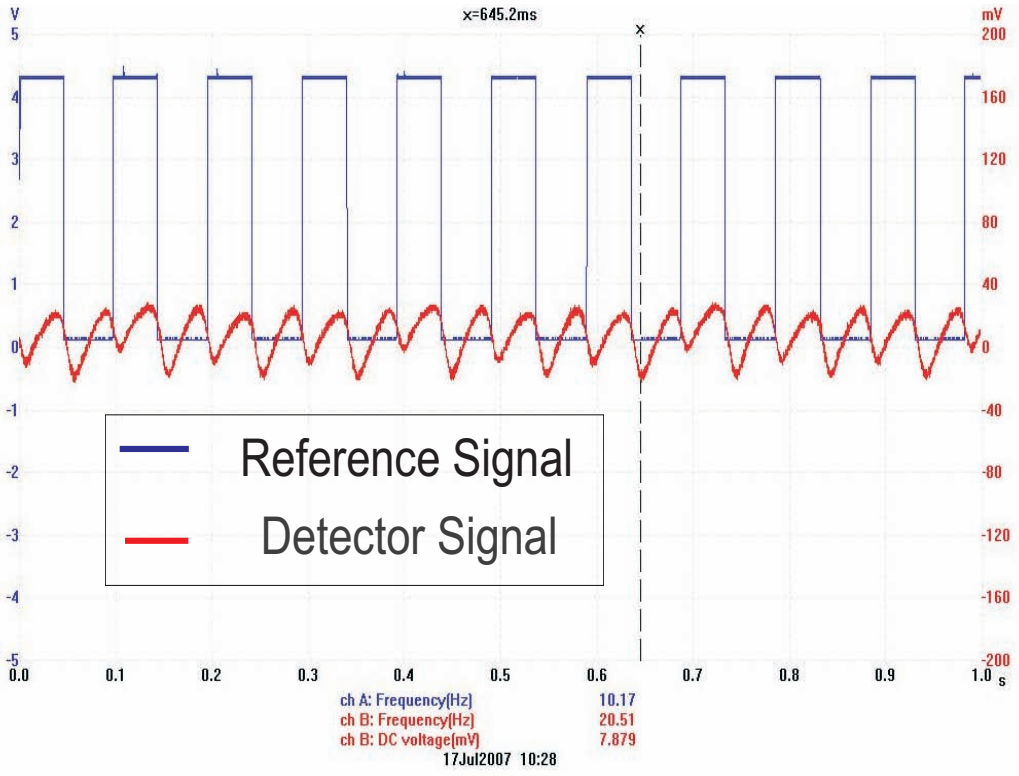

FIGURE 6.7: Oscilloscope display showing combined signal at the end of the purge session with both channel peaks of nearly the same intensity

At the end of the purge session, one channel was individually blocked and the PSD output was recorded in real time using a PICO oscilloscope. The sample gas mixture containing 3% CO_2 and balance N_2 was fed into the sample cells using the gas filling rig and the sample air bag. The results are shown in figure 6.8. The data was recorded for over 300 seconds. When the C626 channel was blocked, the PSD output started at a strongly positive value indicating a strong C636 signal. But when the sample gas was fed into the cells after 100 seconds, the output recorded a dip in its value due to increased C-13 absorption along the unblocked path. Similarly, when the C636 channel was initially blocked, the PSD output started at a negative X value indicating a stronger C626 channel signal but once the gas mixture was fed into the cells after 150 seconds, the PSD output became less negative indicating a drop in signal strength. The direction of change in the output recorded for both the channels was precisely what was expected since the addition

of the sample gas drove the PSD output towards the equilibrium point. Hence a signal that initially had a large positive value became less positive and a signal that initially had a large negative value became less negative after introduction of the sample gas. The change in these PSD values is less pronounced in figure 6.8 because the system starts from an unbalanced point with a strong unbalanced background signal. To better demonstrate this effect, the same procedure was repeated with the system initially in a balanced state. It should be noted that both these tests were conducted under open loop conditions in the absence of any feedback servo control for cell length manipulation. In this test, after the sample cells were purged with N_2, one of the gas cells was completely sealed using the inlet and outlet valves. Sample gas was thus fed to only one of the sample cells at a time and the corresponding change in PSD output was recorded as before. This is shown in figure 6.9. When the C-12 channel was sealed, the output started from a value very close to 0 volts indicating the balanced state and remained so until about 150 seconds when the sample gas was introduced into the C-13 sample cell. This immediately had the desired effect on the output making it more negative indicating an increased absorption along the C-13 channel and hence a stronger C-12 channel signal (negative value). On the contrary, when the C-13 cell was sealed and sample gas filled into the C-12 cell, the opposite effect was observed. The output initially started close to 0 volts and remained so until 200 seconds when the introduction of the sample gas caused the signal to become more positive. This was indicative of a stronger C-13 channel signal due to increased absorption along the C-12 channel. Furthermore, it can also be observed that the shift in values is more dramatic when the C-13 cell was sealed. This is because the introduction of the sample gas into the C-12 cell causes a bigger change from the equilibrium point than that caused by absorption in the C-13 cell on account of the greater isotopic abundance of C626 than C636. Hence, it can be safely said that the above tests completely validates the understanding of the absorption mechanism and also the instrument response to gas based experiments.

6.2 System Noise Analysis

A systematic analysis of noise is essential in order to completely characterise a system. This will provide us with key information such as noise floor which eventually determines the sensitivity of the measurement setup. In our current system, there are four major possible sources of noise, namely:

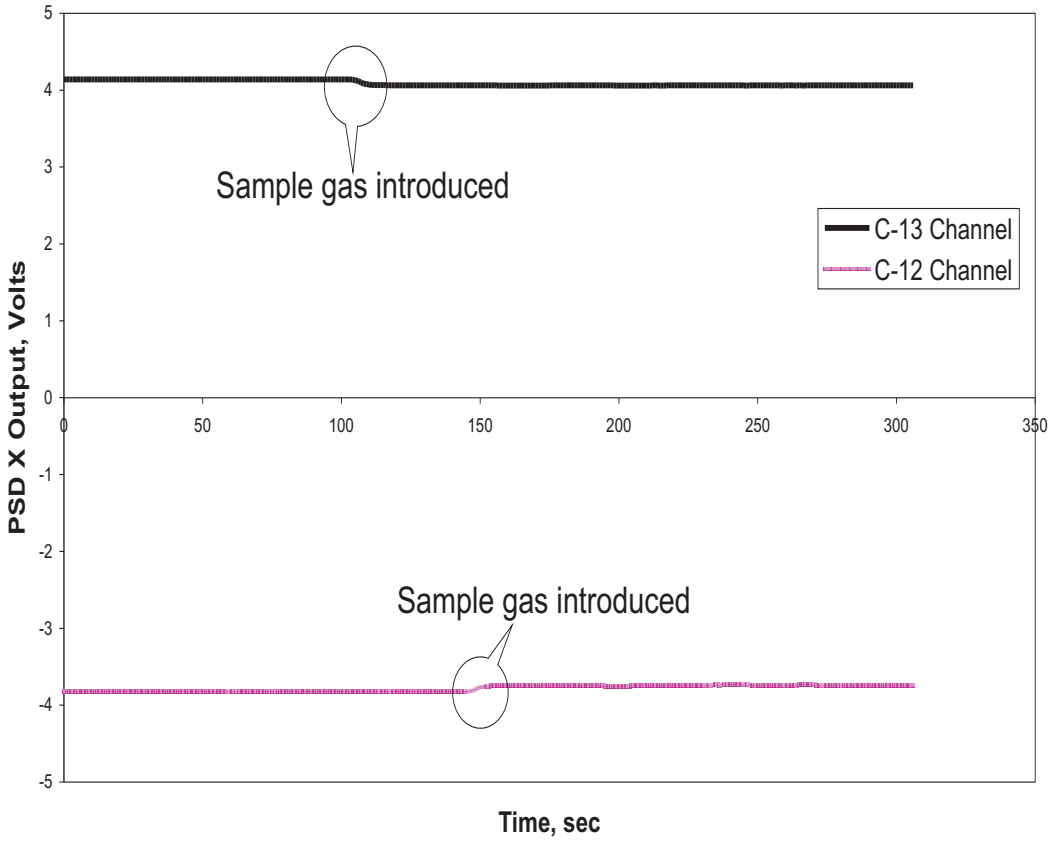

FIGURE 6.8: Variation of PSD output when sample gas is introduced into the system already in an unbalanced state

1. Pyroelectric detector noise
2. Noise from low noise FET op-amp
3. Input noise of the PSD
4. Johnson noise from resistors in external low noise circuit

6.2.1 Pyroelectric Detector Noise

The LTIQ2 pyroelectric detector acts as a major source of noise in our measurement setup. It has an integrated JFET pre-amplifier configured as a voltage follower. The main sources of noise within a pyroelectric detector are:

- Temperature noise, V_{RT}, due to the statistical behaviour of heat exchange between the responsive element and its surroundings
- tanδ noise, V_{RD}, which describes the thermal noise of the element resistance

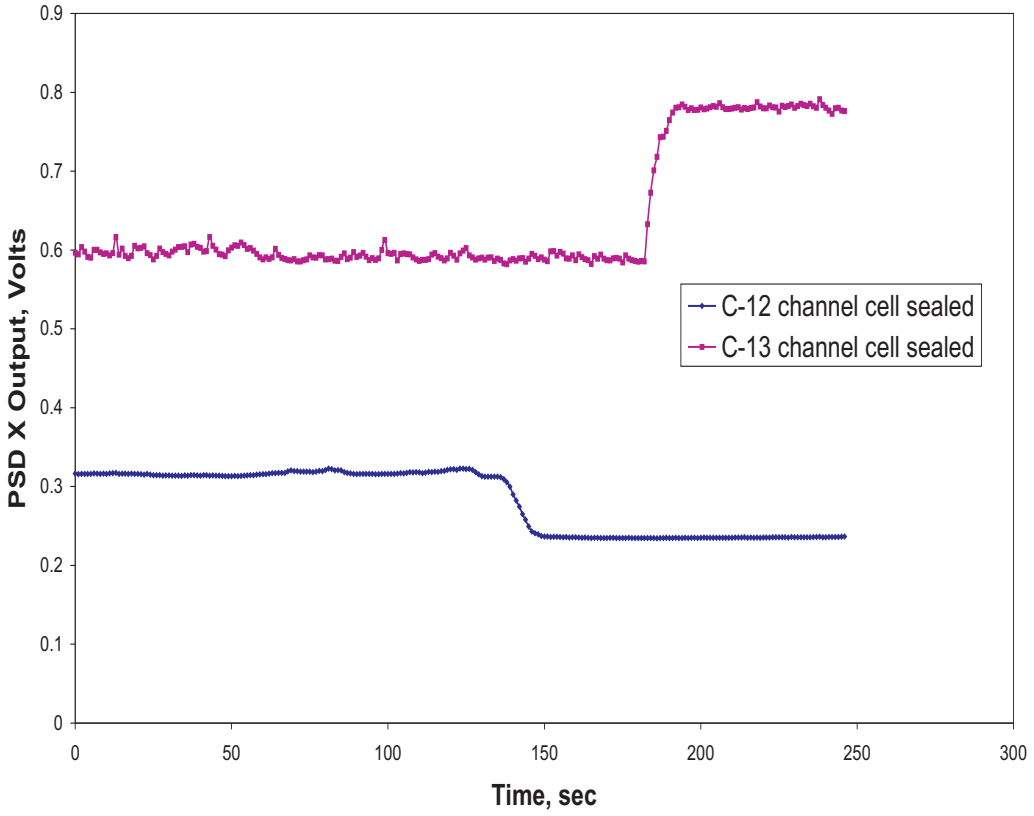

FIGURE 6.9: Variation of PSD output when sample gas is introduced into the system starting from a balanced position. The change in output is therefore more noticeable in this case

- Thermal noise, V_{RR}, of the FET input resistance which is usually in gigaohms
- Current noise of the FET expressed as a voltage by considering the FET resistance, V_{RI}
- Voltage noise of the FET, V_{RV}

Taking into account contributions from all these sources, the total normalised noise voltage from the detector can be expressed as

$$V_D^2 = V_{RT}^2 + V_{RD}^2 + V_{RR}^2 + V_{RI}^2 + V_{RV}^2 \tag{6.1}$$

The quoted overall noise density in the data sheet for this detector is 80 $nV/\sqrt{Hz}$.

6.2.2 Noise from FET op-amp

The low noise FET op-amp at the output of the detector provides the necessary signal filtering and amplification for making sensible measurements. It has a quoted voltage noise density, V_{FET} of 25 nV/$\sqrt{Hz}$ for an operating frequency of 10 Hz.

6.2.3 PSD Input Noise

The lock-in amplifier (PSD) SRS 530 has a quoted noise density, V_{PSD}, of 7nV /$\sqrt{Hz}$ as given in the manufacturer's data sheet. The actual amount of noise at the output of the system is, however, determined by the Equivalent Noise Bandwidth (ENBW) set by the output low pass filter of the PSD. ENBW is the range of frequencies contained within an ideal square pass band that has the same power density as that of a real filter. It depends on the time constant and filter roll-off set on the PSD. The low pass filter at the output of the PSD acts as a bandpass filter centered around the externally provided reference frequency and the filter cut off determines the detection bandwidth. In other words, it becomes the limiting bandwidth in the measurement process.

6.2.4 Johnson Noise

Johnson noise or thermal noise is produced due to the thermal motion of charge carriers in resistive elements. This motion sets up a local charge gradient. The rms noise voltage is given by

$$V_J = \sqrt{4KTRj\Delta f} = 0.13\sqrt{R}\Delta f \tag{6.2}$$

where R is the value of resistance and Δf the noise bandwidth. From figure 5.27, we see that a 100K, a 47K and a 1K resistor is used. Neglecting the 1K resistor due to its insignificant contribution, the total Johnson noise from the resistors is approximately 50 nV/$\sqrt{Hz}$. To summarise, table 6.1 lists the noise sources and their corresponding noise contributions.

Hence we see from the above table that detector noise is the dominant source of noise as desired. Improving the noise performance of the FET op-amp thus offers little benefit. The overall noise value is the square root of the sum of the squares

Noise Source	***Noise Density, nV/$\sqrt{Hz}$***
Pyroelectric Detector, V_D	80
FET op-amp, V_{FET}	25
PSD, V_{PSD}	7
Johnson Noise, V_J	50

TABLE 6.1: Various sources of noise present in the system and their respective theoretical noise contributions

of these individual noise contributions. This is given by

$$V_T = \sqrt{V_D^2 + V_{FET}^2 + V_{PSD}^2 + V_J^2} \tag{6.3}$$

Substituting the above values, V_T = 98 nV/$\sqrt{Hz}$. The output rms voltage noise is given by

$$V_{rms} = V_T \times Gain \times \sqrt{ENBW} \tag{6.4}$$

The low noise amplifier circuit gain is 100. As discussed before, ENBW depends on the output filter characteristics set on the lock-in amplifier. Here we have used a single stage RC filter with a 6dB/octave roll off. Hence the value of ENBW becomes $\sqrt{1/4RC}$. Using this, the rms noise values were computed for different time constants and listed below in table 6.2.

RC Time Constant, seconds	***RMS Noise, μV_{rms}***
3	2.82
10	1.55
30	0.9

TABLE 6.2: Computed noise values for various integration time constants selected on the PSD

These theoretical noise values are the noise floors of the system and hence determines the minimum detectable delta values. In order to convert these noise values into corresponding delta values, a calibration curve was simulated in MATLAB as shown in figure 6.10. Here the detector output voltage for various delta values was computed for an optimum C-13 cell length of 10.245 cm. Based on the curve, a 3 second time constant implies a minimum measurement of 1‰ whereas a 10 second time constant implies 0.5‰.

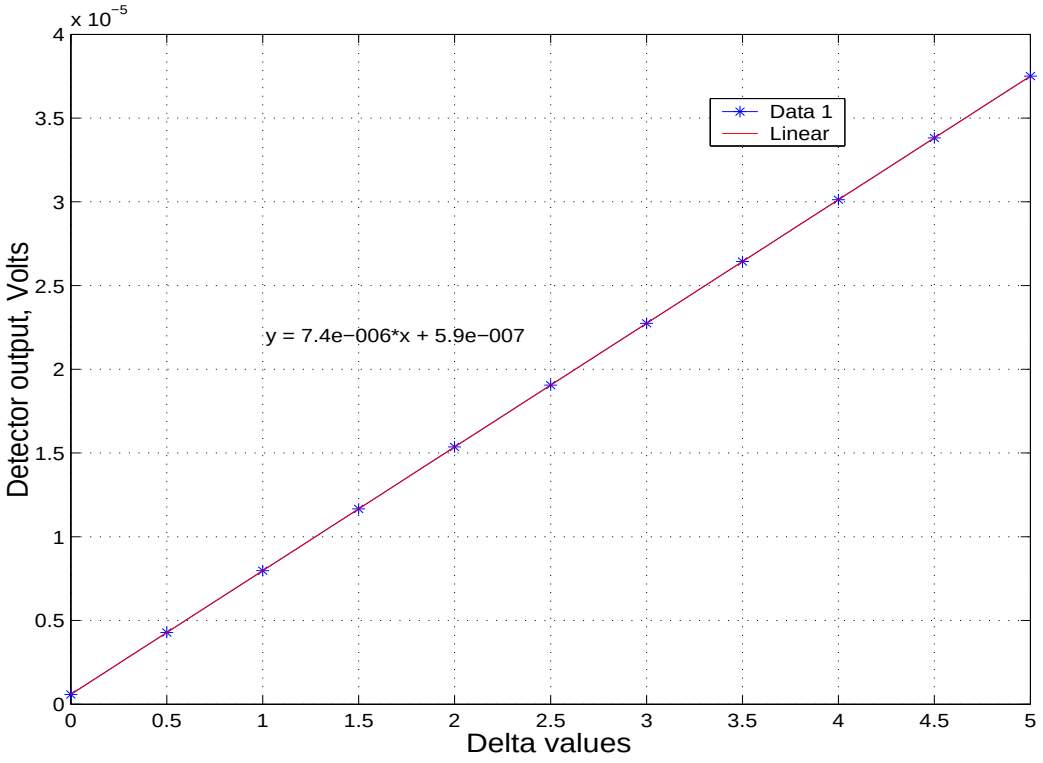

FIGURE 6.10: Theoretical calibration curve showing the detector output for various delta values. The curve is then used for the estimation of measurement sensitivity and minimum detectable delta

6.2.5 Experimental Estimation of Noise

The previous section indicates that the current design should enable us to detect changes of the order of 1‰ using a convenient time constant of 3 seconds. To experimentally verify this, the system was initially maintained in a balanced absorption state and the PSD output was recorded using the PICO scope as before. Then the system was unbalanced by changing the iris aperture thereby disturbing the equilibrium state and the PSD output either increased or decreased depending upon the direction of iris change. The PSD output was recorded until it attained a steady state value. The rise or fall time depended on the time constant chosen on the PSD. From the recorded values, noise was calculated by measuring the standard deviation of the steady state values. Figures 6.11 and 6.12 show the measured standard deviations for a time constant of 10 and 3 seconds respectively as the system goes from a balanced to an unbalanced state. It can be seen that in both cases the noise level increases as we move from a balanced state to an unbalanced state which is indicative of a noise generating mechanism being present within each channel. Under balanced conditions, the effect of these noises is ratioed out and reduced due to the symmetrical design of the system. Further evidence of this behaviour is presented later in this section. Referring back to the calibration curve, we can deduce that the experimental analysis suggests a minimum delta measurement of 1.1‰ to 2.14‰ for a 10 second time constant. For a 3 second time constant, the values range from 3.37‰ to 5.77‰.

The observed discrepancy in the theoretical and experimental noise estimates is in the range of a factor of 2 to 6 for various measurements. This points to the possibility of other noise sources that have been ignored in the simulation studies for ease of evaluation. For instance, the theoretical studies were carried out under the assumption that the source temperature remains constant throughout the course of measurement. However, in reality noise contribution from source temperature fluctuation can reduce detection sensitivity. The discrepancy may also be due to the difference in test conditions prevalent during the experimental work from the assumed test conditions. Lack of a purged environment during the experimental tests will result in fluctuations in the ambient CO_2 concentration.

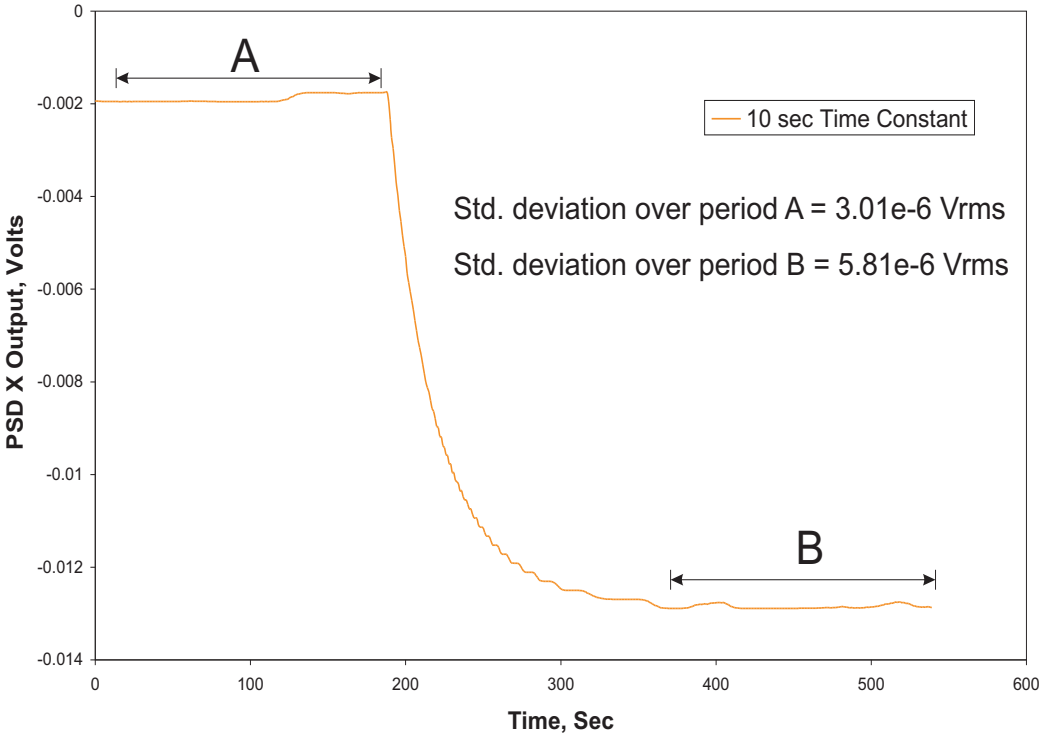

FIGURE 6.11: Noise estimation with a time constant of 10 seconds

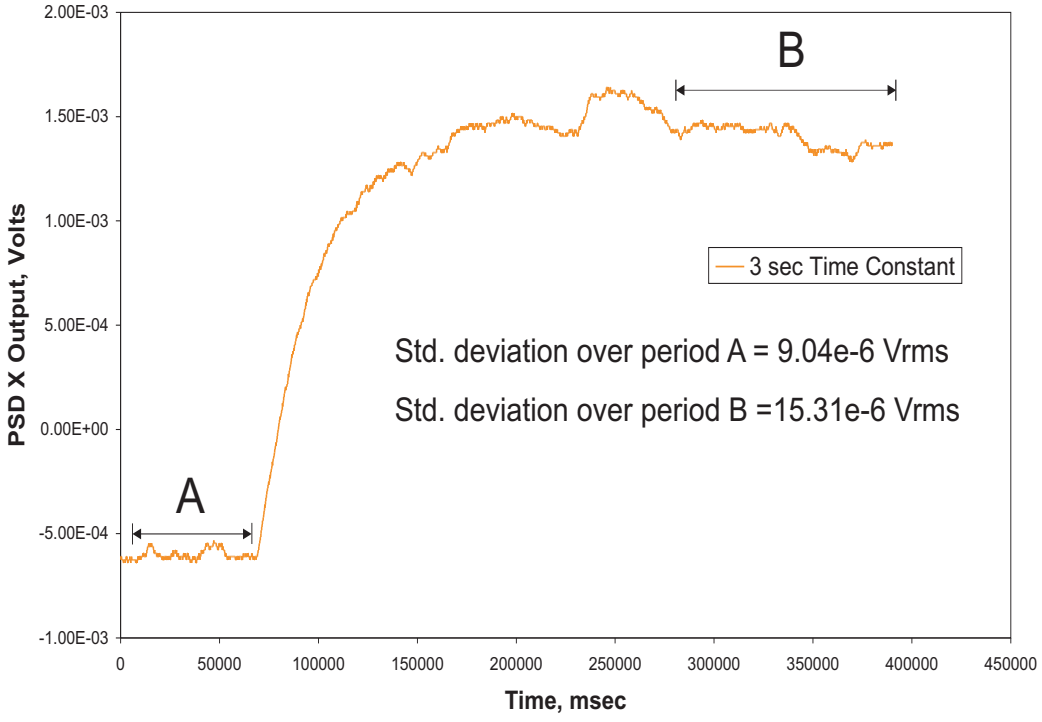

FIGURE 6.12: Noise estimation with a time constant of 3 seconds

A comprehensive study was carried out in order to further understand noise generation in the system. Individual tests were carried out to ascertain noise contribution from the detector and the effect of possible interference or pick up from the chopper motor. Noise from each channel when present alone along with the combined noise was also evaluated. To determine the detector noise, the source and the choppers were turned off and the detector alone was switched on. A PSD with a time constant of 10 seconds was used to make the measurement. A reference signal of 10 Hz was provided by a separate function generator. In this case, since no optical signal is being measured, noise can be calculated from the average of the observed values. Figure 6.13 shows the data recorded at the PSD output when used in the R/ϕ mode. The random jumps in the phase value indicates that true noise is being measured and the PSD is not detecting any meaningful signal. The observed noise value for the detector (including noise from the FET amplifier and the PSD) was 1.64 μV which compared very well with the theoretical value of 1.55 μV as listed in table 6.2. Next the source was turned on and the

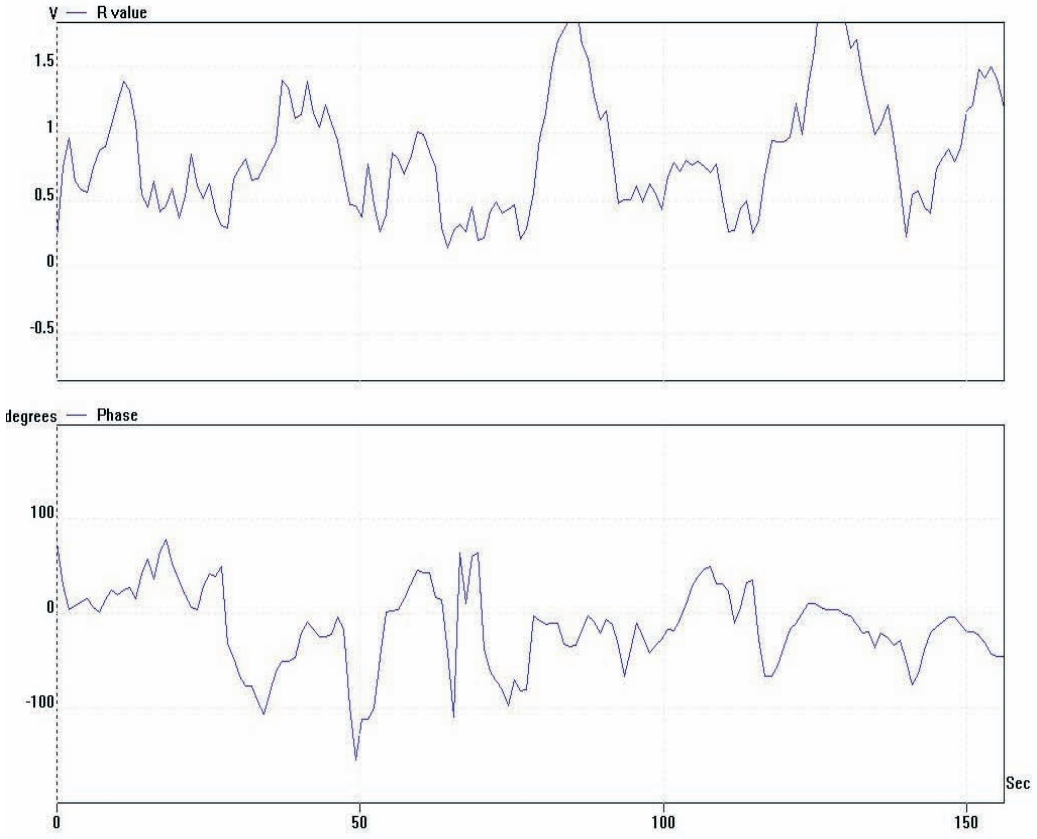

FIGURE 6.13: Plot showing the record of PSD output in magnitude and phase when the detector alone was switched on

broadband IR radiation was allowed to fall on the detector. The measurement process was repeated as above and the observed noise was measured to be 1.72

μV. The recorded PSD output is shown in figure 6.14. Hence there was no significant deviation from the previous noise value when the source was turned off. This agrees with the expected result since no additional source of noise was introduced and the pyroelectric detector does not suffer from any shot noise contribution. Then the chopper motor was turned on but the optical beam was blocked and the signal falling on the detector was monitored. The recorded values from the PSD are shown in figure 6.15. Once again, no significant difference was noted and the measured noise of 1.8 μV agreed well with previously obtained values. Since no optical signal was being detected, we can safely eliminate any pick up from the chopper motor as a source of interference that may have a significant bearing on measurement sensitivity.

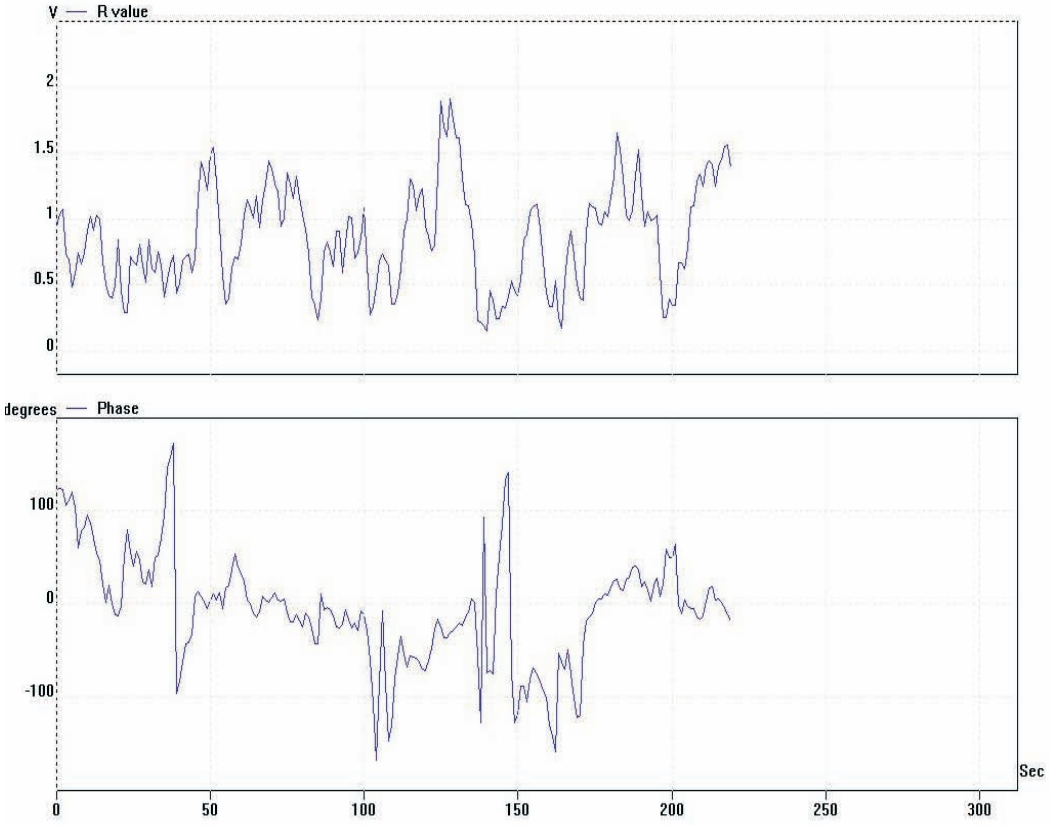

FIGURE 6.14: Plot showing the record of PSD output in magnitude and phase when the detector was exposed to the optical beam from the source

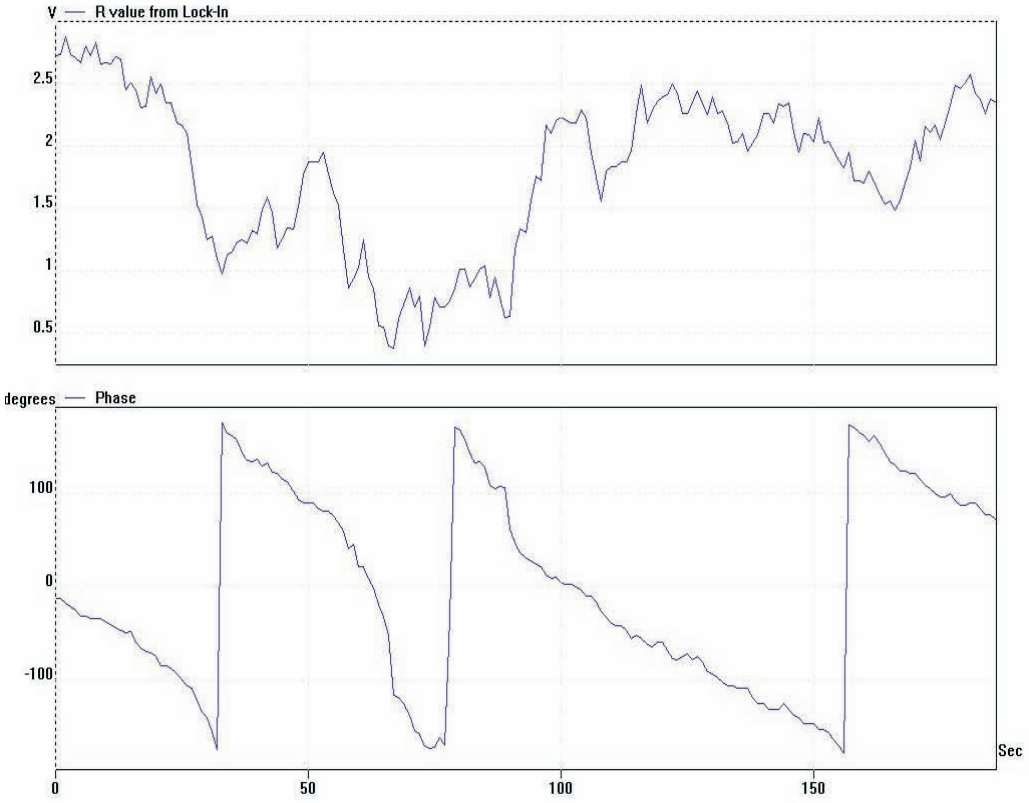

FIGURE 6.15: Plot showing the record of PSD output in magnitude and phase with the choppers turned on

Individual channel noise was also measured in a similar way. One channel was blocked at a time and the standard deviation of the PSD output was calculated. Several measurements were recorded and it was found that each channel contributed on an average 85 μV of noise. This figure is much higher than the previous measurements suggesting significant noise generation when detecting IR radiation chopped by the mechanical chopper assembly. This can be due to an irregular chopping pattern arising from any chopping frequency fluctuations that exhibits itself in the form of noise. More discussion on this will be provided in a later section. Also the phase signal now showed a steady value indicating that a 10 Hz signal was being constantly measured by the system. However, when noise measurements were made under balanced absorption conditions using both the channels, noise was significantly reduced to 5.64 μV. This observation strongly suggests that the noise generation mechanism present in each of the channels tend to counteract or oppose each other thereby reducing the overall noise when the two beams are combined at the detector. This is not surprising because of the fact that both the choppers are in anti-phase resulting in an automatic elimination of common noise sources present along the two channels. In fact, this is one of

the salient features of the measurement system attributed to its unique symmetric design thereby ensuring cancellation of common interferences and noises. A record of the data for the balanced condition is shown in figure 6.16. The phase signal now indicates a constant value which implies that even under balanced or near balanced conditions, an optical signal is being detected by the PSD. This directly relates to the 20 Hz signal that we observed previously when the two channels were balanced and an explanation for its appearance was also provided earlier in section 5.7. The need for suppression of this 2ω signal will be taken up in a later section.

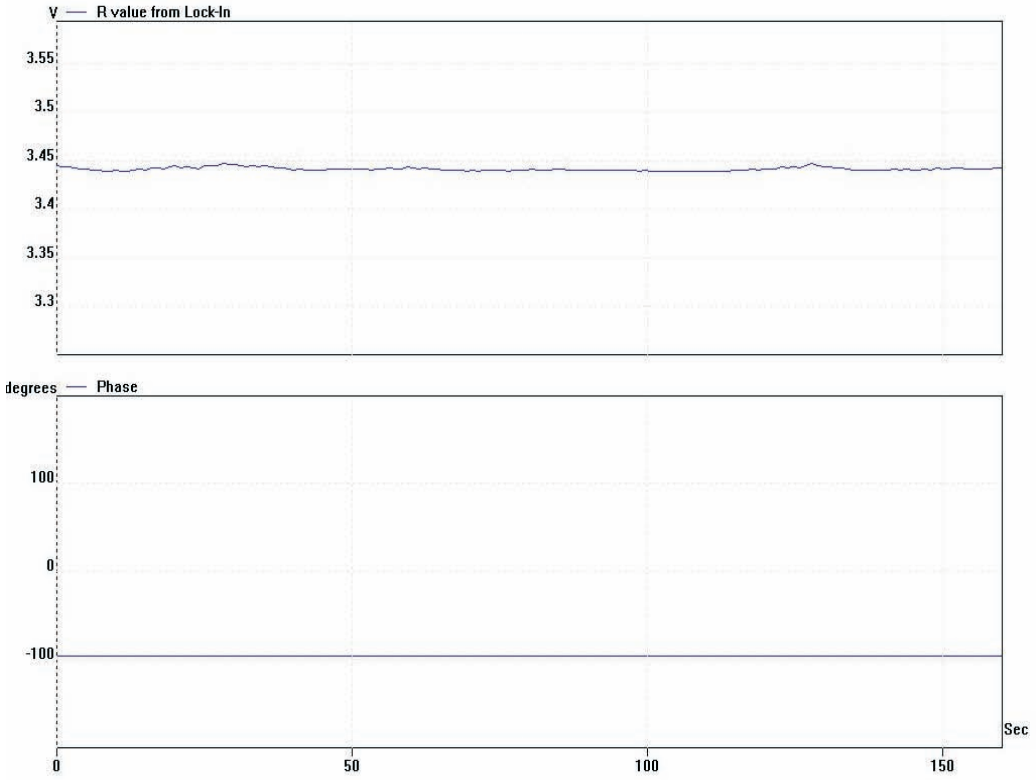

FIGURE 6.16: Plot showing the record of PSD output in magnitude and phase when the both the channels were exposed and the system was maintained in equilibrium

To summarise, noise contribution from the detector alone was found out to be 1.64 μV for a 10 second time constant. This corresponds very well with the theoretical calculation of 1.55 μV presented earlier in table 6.2. The overall noise for the balanced condition was experimentally determined to be 5.64 μV. This value is also in good agreement with the rms noise value shown in figure 6.11. A summary of the noise values determined experimentally has been listed below in table 6.3

Noise Source	***Evaluated Noise, μVrms***
Detector alone	1.64
Detector + source	1.72
Detector + chopper	1.8
Individual channels	85
Balanced	5.64

TABLE 6.3: Various sources of noise present in the system and their respective noise figures

6.3 Source Temperature Stability

In the previous section, it was stated that the source temperature was assumed to be constant for the purpose of simulation studies. For the blackbody curve to peak at 4.3 μm, the source temperature must be maintained at 674K. It was earlier show in chapter 5 that a source temperature stability of $\pm$0.5K will ensure a measurement sensitivity of around 1‰. Section 5.1 dealt with the issue of source stability by performing experimental tests and it was concluded that the IR-12 broadband source was adequately stable. However, this does not rule out the possibility of turbulent convection related temperature fluctuation (as opposed to slow drifts over time) and hence this aspect was also investigated. Heat transfer from the source by radiation does not exceed 1-2% of the total heat transfer through the gas at temperatures around 600K[63]. The source heats up the air around it and as result the hot air rises up and this establishes a convective current in the vicinity of the hot source. In certain cases, this leads to turbulence which will exhibit itself as a random source temperature fluctuation at the detector and produce noise. To determine if the primary mode of heat transfer is conduction or convection, Rayleigh number (R_a) for the particular case needs to be computed. Rayleigh number is a dimensionless number that is associated with the heat transfer within a fluid. If the value of R_a is below a critical value, R_{ac}, then heat transfer by conduction dominates. When it exceeds the critical value, heat transfer is primarily in the form of convection. The value of R_{ac} is typically taken as 1700 for a closed top boundary configuration or the Benard Configuration (as in the present case) and if R_a>5500, the convection becomes turbulent[64].

The Rayleigh number is actually a product of two other dimensionless numbers, the Grashof number (G_r) and the Prandtl number (P_r).

$$R_a = G_r \times P_r \tag{6.5}$$

The Grashof number approximates the ratio of buoyancy to viscous forces acting on a fluid[65] and is given by

$$G_r = \frac{g\beta(Ts - T\infty)L^3}{\nu^2} \tag{6.6}$$

where g is acceleration due to gravity, β is volumetric thermal expansion coefficient which is approximately equal to 1/T (T is absolute temperature), Ts is source temperature, T∞ is quiescent temperature, L is characteristic length and ν is kinematic viscosity.

The Prandtl number gives the ratio of viscous diffusion rate to thermal diffusion rate and is given by

$$P_r = \frac{\nu}{\alpha} \tag{6.7}$$

where α is thermal diffusivity. Typical value for P_r is 0.7 for air and most gases[66].

By substituting appropriate values in equation 6.6, we obtain a value for G_r = 1033 for a characteristic source length L of 3.5 mm (from data sheet). Using P_r = 0.7, equation 6.5 gives a value for R_a = 723.1 which is less than 1700 that is required for convective heat transfer to dominate. Since this calculated R_a value falls well short of 5500 that is required to set up turbulence, we can conclude that no turbulent heat transfer mechanism exists which can make a contribution to the measurement noise. However, it should be noted that the safety margin is not large and an increase in source temperature Ts or more significantly an increase in the characteristic length L (since it changes as a cube) can easily cause the value of R_a to exceed 1700.

6.4 Frequency Stabilisation and Control

While performing various tests discussed previously, it was observed that the reference frequency signal derived from the choppers showed sudden small shifts in value during the course of a measurement. Since this reference signal was fed to the PSD for the purpose of locking on to the output signal from the detector, the resultant DC output from the PSD also showed some variations. These frequency fluctuations can result in erroneous measurements since the basal and enriched sample test measurements may be carried out at different chopping frequencies.

Figure 6.17 below shows this unstable frequency characteristic that was observed.

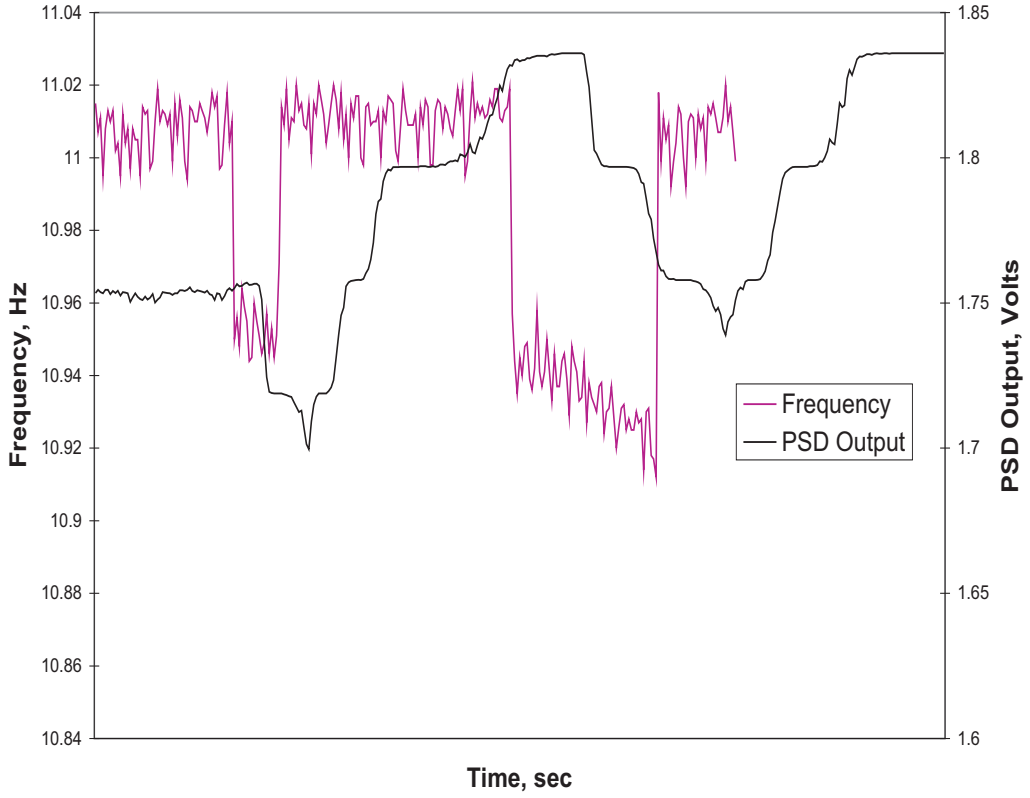

FIGURE 6.17: Figure showing the unstable nature of the reference chopping frequency and its effect on the measured PSD output

The chopping frequency was set to 11 Hz. It can be seen that a drop in frequency (two such drops are clearly recorded in the figure) triggers a similar effect immediately afterwards on the measured PSD values. The output values decrease at first and then slowly rise back to the previous value after the frequency has returned to its set value. This is the reason why the PSD output values had to be recorded for a longer period of time than the frequency values and hence the time axis values were deliberately not displayed due to the difference in record duration. The step like behaviour of the PSD output values is a result of the resolution limit imposed by the PICO scope used for recording the data. With an 8 bit resolution on the PICO scope and ± 5 V setting, the minimum step size is $\frac{10}{2^8}$ which is about 40 mV. This agrees with the step size seen on the plot. Any changes in the PSD output below 40 mV will not be recorded by the PICO. The shape of the frequency and PSD output plots strongly suggests a strong correlation between chopping frequency fluctuation and fluctuation in the PSD output. This output fluctuation

gives rise to a spurious signal that will result in an erroneous measurement of delta values. Thus a control mechanism for frequency stabilisation needs to be incorporated into the design. The reference chopping frequency is obtained by using photoreflective sensors as mentioned previously. The speed of the chopper motor was set using a PWM scheme whereby the motor frequency was varied by changing the DC signal fed to the PWM chip. This open loop control scheme was modified to provide a closed loop control of the chopping frequency. The modified circuit diagram is shown below in figure 6.18.

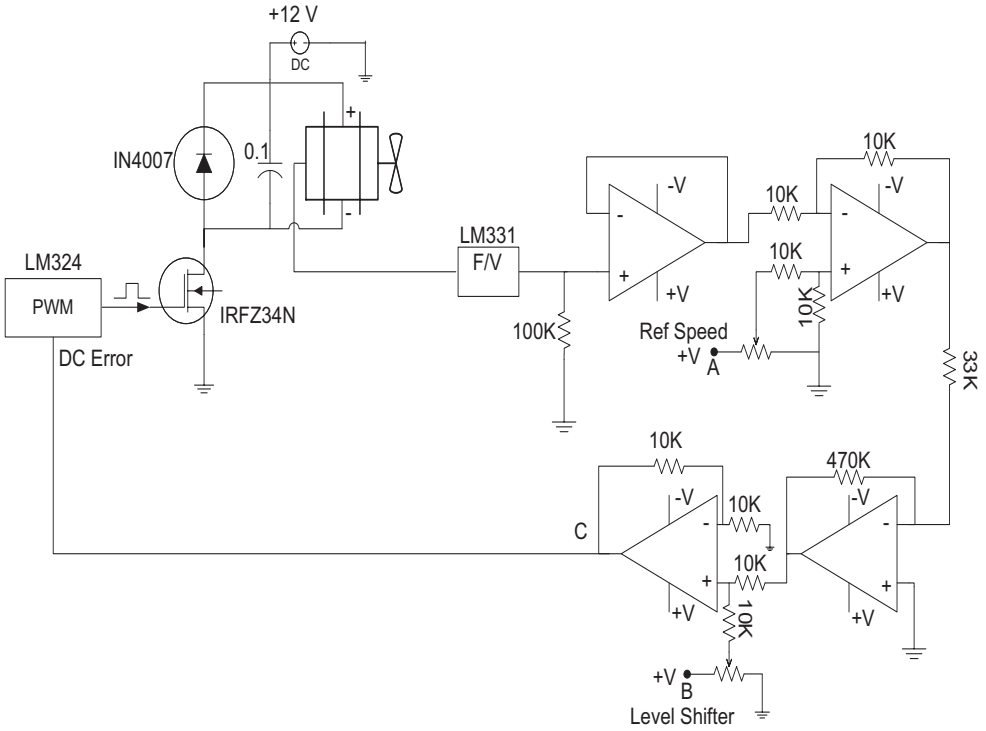

FIGURE 6.18: Circuit schematic of the closed loop frequency control implemented for chopper frequency stabilisation

The motor encoder signals were fed to a LM331 frequency to voltage converter. The output was then compared with a reference signal that set the reference speed through a potentiometer. The error signal was then amplified and level shifted by using a summing circuit and the output was then fed back to the PWM chip as the DC signal that sets the pulse width. The level shifter was used so that the DC signal at point C lies in the mid range of the triangular wave generated by the PWM chip. By adjusting the voltage at point A, the speed of the chopper motor was set and any deviation from the set speed will cause the signal at C to vary

the pulse width accordingly. The implementation of this closed loop frequency control resulted in significant improvement in the frequency stability as seen in figure 6.19. No significant jumps or shifts in the frequency was observed and the standard deviation in the recorded frequency was down to 0.002 Hz from a previous value of 0.33 Hz. This improved frequency control was essential in making more reliable and accurate measurements possible.

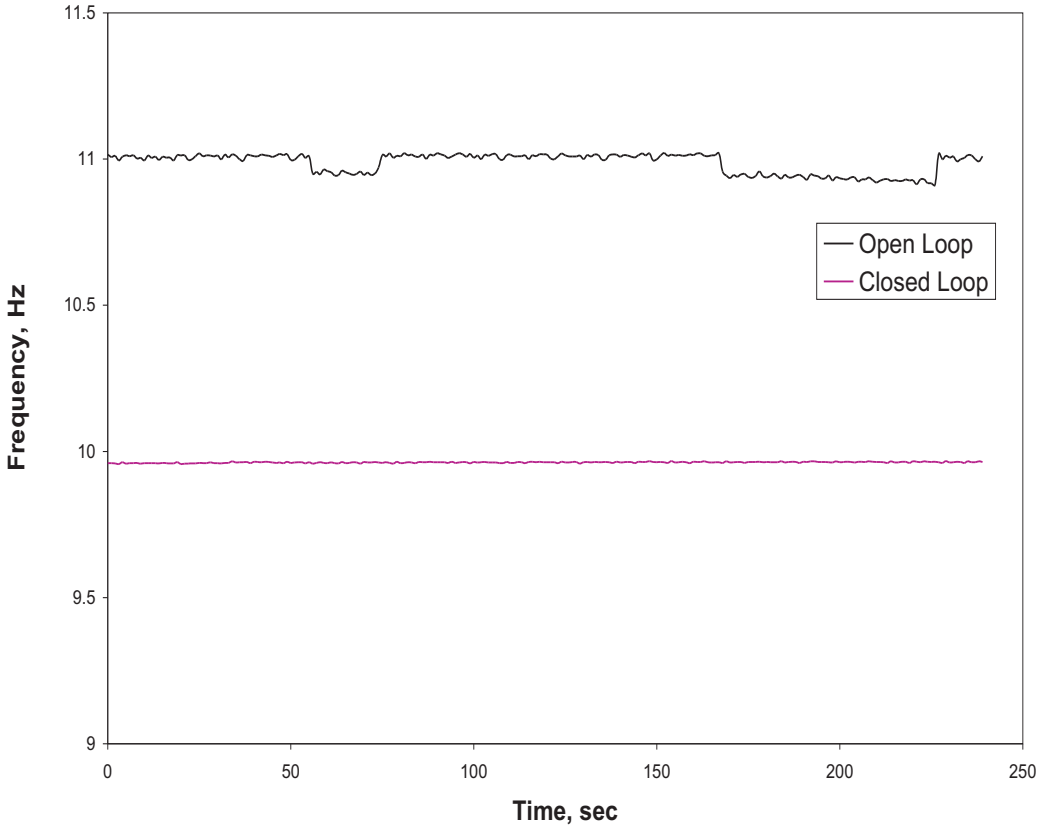

FIGURE 6.19: Figure showing significant improvement in chopping frequency stability by implementing a closed loop control circuit

6.5 Resolution Measurements Using Fine Wires

The experiment using an iris to balance or unbalance the system can also be employed for determining measurement resolution. That is, by causing a change in the iris aperture when the system is in balance, the power transmitted along one of the channels can be changed and hence the system response can be monitored. This way, the smallest detectable change in power can be found which in turn gives us a measure of minimum delta. From the calibration curve in figure 6.10,

we see that 1‰ implies a voltage change ΔV of 8 μV_{pk-pk} which is equivalent to a power change ΔP of 0.38 nW with a detector responsivity of 209 V/W and a gain of 100. However, using the iris imposes a limitation in the form of the smallest change that can be produced by manually adjusting the iris lever. With a slow and cautious approach, the smallest change in the iris aperture that was manually possible resulted in a change in output voltage of 2 mV_{pk-pk}. This was too large a change to reveal any information about the measurement resolution. To produce much smaller changes in the channel transmitted power, very fine wires of various thicknesses were chosen and introduced into the beam path of one of the channels. The wires were held stretched using clamps and placed across the middle of the cell windows so that it lies across the middle of the optical beam. The resultant change in optical power was calculated from the beam diameter and the wire thickness. Any change in the PSD output was recorded using a time constant of 3 seconds. The results are summarised in table 6.4. The table shows that the

Wire dia, mm	***Change in Power ΔP, μW***	***Delta***
0.25	0.104	293‰
0.127	0.053	150‰
0.05	0.021	59‰
0.025	0.010	28‰

TABLE 6.4: Table showing various fine wires used and the corresponding change detected both in terms of optical power and delta values

minimum simulated delta that can be detected with adequate accuracy using a 3 second time constant and a 0.025 mm thick wire is 28‰. Previous experimental noise studies indicated the possibility of measuring down to 6‰ with the present system. This however could not be reproduced here because of the non availability of wires that were thinner than 0.025 mm.

6.6 Suppression of 2ω Component

The cause of the 2ω component of the chopping frequency appearing at the output of the detector with the system in balance was discussed previously in section 5.7. It was expected that the use of a lock-in amplifier would prevent this 2ω (20 Hz) component from interfering with the measurement. This is because the output low pass filter in the lock-in will only allow signals that are in a narrow bandwidth around the reference frequency of 10 Hz while rejecting all others. However, in the present case, this does not hold true. This can be understood if we carefully

analyse how a lock-in amplifier functions. A lock-in or a PSD can be visualised as a combination of a multiplier followed by a low pass filter. The two inputs to the multiplier are the reference frequency from the chopper which is a 10 Hz signal in this case and the detector output which happens to be a 20 Hz signal under balanced absorption. The multiplier produces as its output both the sum and difference frequency components, that is, a 10 Hz and a 30 Hz signal. These are then applied directly to output low pass time constant set on the PSD. A 3 second time constant gives a low pass cut off at 0.053 Hz. Considering a single pole output stage with a 6 dB/octave roll off, the 30 Hz signal will be adequately attenuated but the 10 Hz signal will be attenuated by 48 dB or 250 times. In other words, if we consider a 250 mV signal, the dc output of the PSD will be modulated by a 1 mV signal at 10 Hz. Hence we see that the 2ω component at the input manifests itself as a break through 10 Hz modulation on the dc output. Another possible reason for 2ω component affecting the output is the harmonic rejection offered by the lock-in amplifier. Analog lock-in amplifiers such as the the SRS 530 detect and produce a dc response even to the harmonics of the internally generated reference signal. Their stated harmonic rejection of -55 dB (less than 1000 times) is not sufficient enough to fully suppress this effect. Hence, even under balanced absorption, the PSD detects a signal which contributes to the output and gets recorded. This residual balance signal will impact the resolution of the measurement process. Ideally at perfect balance, the output of the PSD should represent a noise signal in which case the magnitude or the R value will be noisy and very close to zero with the phase oscillating randomly from +180° to -180°. As the system moves away from balance, the value of R increases and the phase becomes steady and constant indicating detection of a true unbalanced signal. Figure 6.20 shows a plot of the magnitude in terms of R, X and Y values and the phase as function of iris aperture diameter. The system was taken through its balance point which can be identified by the lowest point on the R curve. At the same time, phase of the signal also undergoes a 180° reversal as seen in the figure.

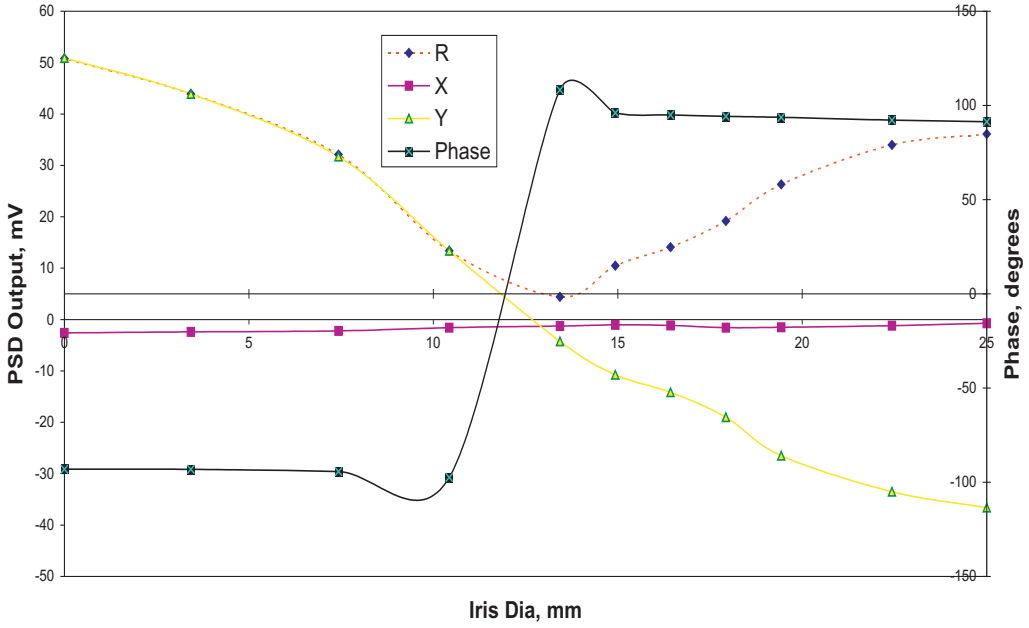

FIGURE 6.20: Variation of PSD output as a function of iris aperture diameter. The values were recorded as the system passed from an unbalanced state to a balanced point and then back to an unbalanced state with the associated phase reversal

Figure 6.21 provides a magnified view of the magnitude and phase values near the balance point. The minimum residual value of R was 1.5 mV. By manually adjusting the iris, it was not possible to bring the system to the actual balance point. However, the broad shape of the R value in the vicinity of the balance point indicates the presence of a strong residual signal near balance. If pure noise alone was present at balance, the R curve would have been much narrower with a sharp drop in its value at balance.

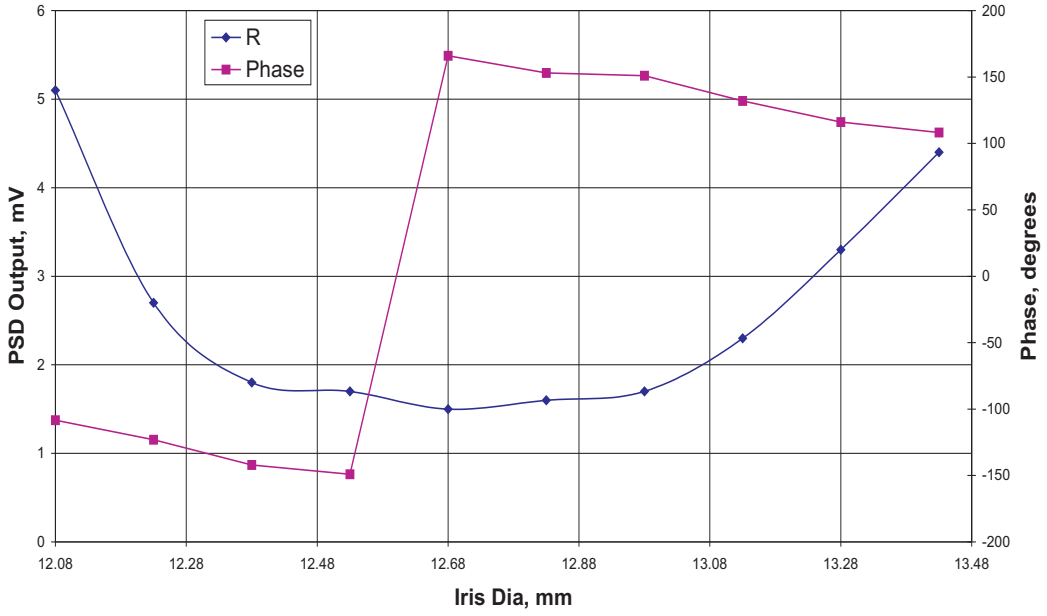

FIGURE 6.21: Magnified view of variation in magnitude and phase near the balance point

In order to suppress the 2ω component, a low noise voltage pre-amplifier SRS 560 that includes a low pass filter was connected at the output of the detector before the signal was fed to the PSD. The pre-amplifier was operated using a 10 Hz cut off and similar set of measurements were recorded. These were compared with the previous data obtained in the absence of the pre-amp and shown below in figure 6.22. The phase reversal was observed as before and the magnitude curve was much narrower this time with a residual magnitude of 0.7 mV at balance (10 Hz curve in the plot). This represented a definite improvement over the previous case (curve indicated as none in the plot). To check the 2ω suppression, the 2F detection capability in the PSD was employed. The test was repeated and both the F and 2F outputs from the PSD were recorded and this is depicted in figure 6.23. As observed, when the system is grossly out of balance, the 10 Hz component dominates the PSD output with the phase dependant on which channel is stronger. However, as we move towards the balance point by manually adjusting the iris, the 10 Hz component begins to fall rapidly and finally at the balance point, it drops below the 20 Hz component. This correlates perfectly well with the appearance of a 2ω component at balance.

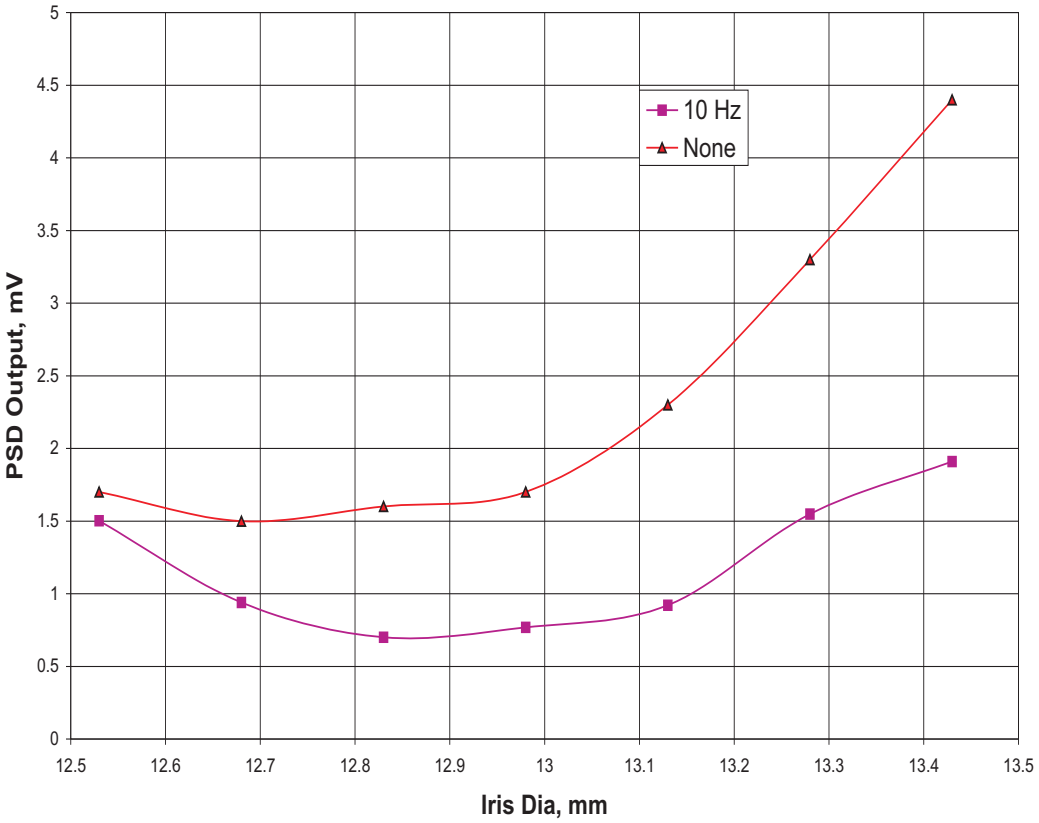

FIGURE 6.22: Plot showing variation of magnitude with iris aperture after using a low noise pre-amplifier. The magnitude curve is much narrower when compared to the initial case

Although the use of a low noise pre-amplifier has helped in reducing the residual magnitude, it is evident from figure 6.23 that the 2ω component has not been fully suppressed. This necessitated the use of a dedicated filter design to effectively eliminate the 20 Hz component at balance thereby improving the overall detectability of the system. For our work, ideally we require a filter that offers the following characteristics:

- Maximum steepness in roll off.
- The phase response of the filter should be smooth around the cut off frequency without any sudden changes that prevents us from making an accurate phase measurement, since phase of the detector signal indicates which channel is stronger.
- Easy to design and implement.

Various types of active filter designs were considered such as Butterworth, Cheby-

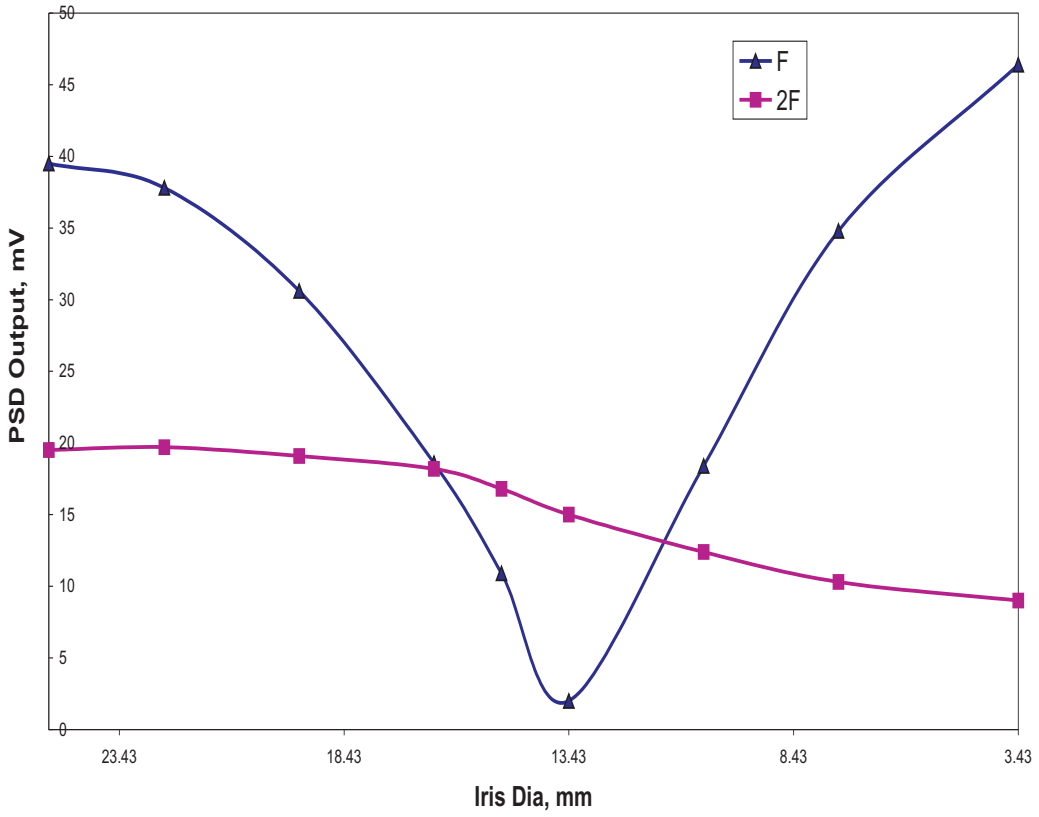

FIGURE 6.23: Figure showing both the F and 2F outputs from the lock-in as a function of iris diameter. When the system is away from balance, the 10 Hz component dominates but at the balance point it falls below the 20 Hz component

shev and Bessel filter configurations. They vary from one another in their performance characteristics such as pass band and stop band characteristics and also in their roll off steepness. A trade off between filter performance and design complexity is inevitable. Butterworth filters have a very flat response in their pass band with very little ripples. However their roll off rate is not the steepest. Chebyshev filters on the other hand provide the steepest roll off but also generate ripples in the pass band. These are also called equiripple filters and the number of ripples increases with the number of poles. However, to achieve the same degree of performance, a Chebyshev requires less number of poles than a Butterworth filter. The amount of ripples can also be controlled and maintained within a certain level (0.5 dB) by the judicious use of components with proper tolerance limits. In spite of the presence of pass band ripples, it is more advantageous to use a Chebyshev design for higher order filters because some amount of ripple will almost always appear in the pass band even in a Butterworth filter. This is due to the deviation of the components from their predicted responses as a result of their finite toler-

ances. Elliptical filters which are an extreme case of Chebyshev filter allow ripples in the stop band as well in order to obtain even steeper roll off. A comparison of roll off steepness for Butterworth and Chebyshev filters is shown in figure 6.24. Bessel filters on the other hand have maximally flat time delay in the pass band

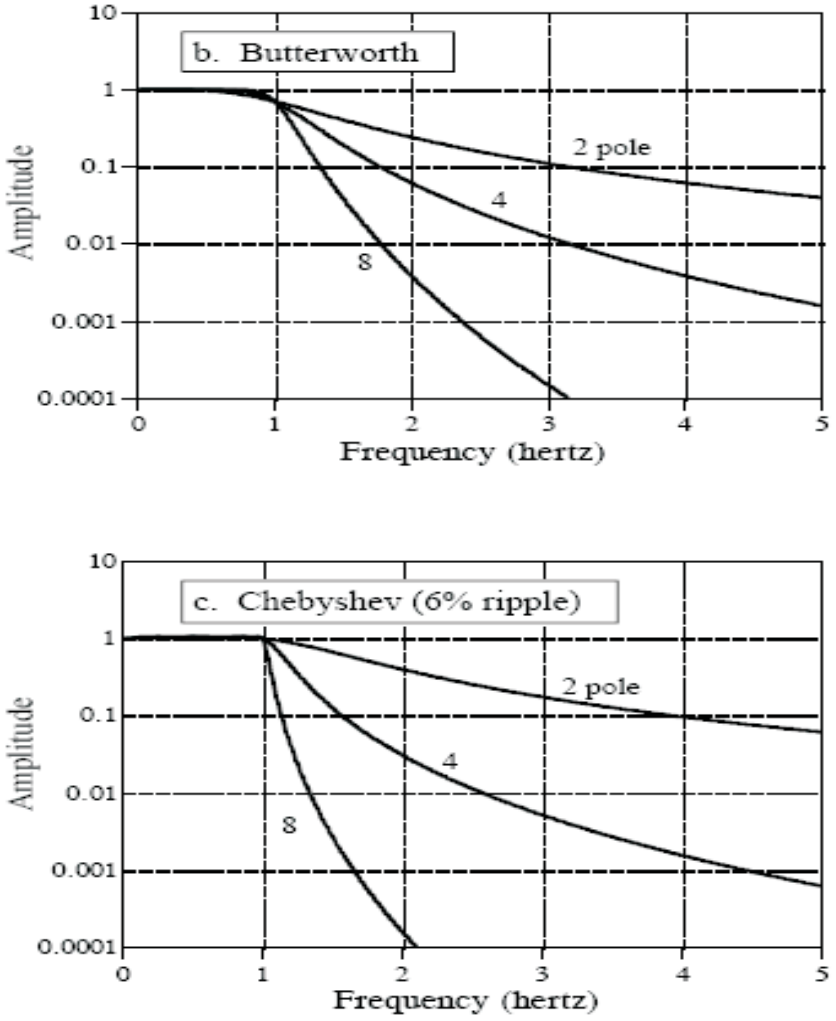

FIGURE 6.24: Figure comparing roll off for a Butterworth and Cheybyshev filter with 1 Hz cut off frequency. Y-axis in log scale(taken from [3])

thereby minimising waveform distortion. However, flat time delay is not a consideration in the present case. Besides, their roll off has poor steepness even in comparison to a Butterworth filter. The various filters and their characteristics have been summarised in table 6.5 below.

In the present case, the most important criteria for filter selection is steepness of the roll off since the aim is to eliminate all unwanted frequencies above 10 Hz and provide maximum suppression for the 20 Hz component. The best performance in this regard is offered by the Chebyshev filter. Although they allow pass band

Filter Type	***Characteristics***
Butterworth	Very flat response in pass band Poor roll off Requires more stages than a Chebyshev for similar performance
Chebyshev	Steepest roll off Ripples in pass band can be kept within tolerable limits Less complex design and requires fewer stages
Bessel	Maximally flat time delay in pass band, no wave distortion Roll off steepness poorer than Butterworth

TABLE 6.5: Table showing various types of filter designs that were considered and their associated characteristics

ripples and have poorer performance in this regard in comparison to Butterworth filters, this is not a critical factor in our application. Simplicity and ease of design is always an advantage and the Chebyshev filter requires reduced number of poles for equivalent performance when compared to a Butterworth filter. The only area where Bessel filters are useful is in providing flat time delay response but this again is not important in the current application. From the above discussion, it was decided that a Chebyshev filter was the ideal choice for our filter requirements.

Figure 6.25 shows a typical single stage 2 pole Chebyshev filter, also known as a Sallen Key filter with a 12 dB/octave roll off. The cut off frequency, f_c is given by

$$f_c = \frac{1}{2\pi\sqrt{R_1 R_2 C_1 C_2}} \tag{6.8}$$

For increased attenuation, a two stage 4 pole filter was designed by using FilterPro which is an active filter design application software provided by Texas Instruments[67]. Each stage provided 12 dB/octave or 40 dB/decade attenuation with a total attenuation of 24 dB/ocatve or 80 dB/decade. The circuit was implemented using standard op-amps and the filter response was evaluated experimentally for different cut off frequencies of 10 Hz, 11 Hz and 12 Hz and plotted as in figure 6.26.

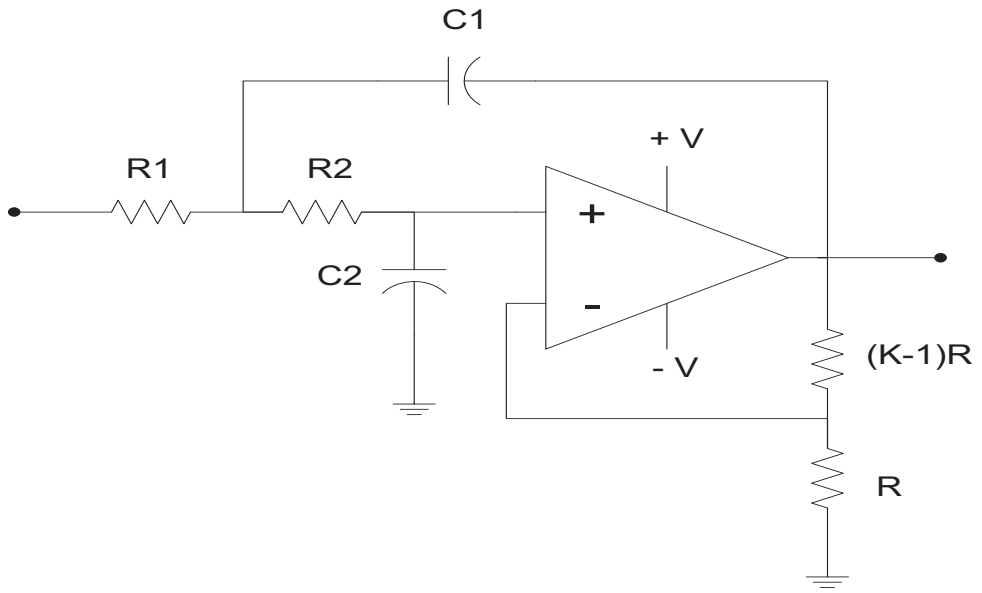

FIGURE 6.25: A single stage 2 pole Chebyshev filter

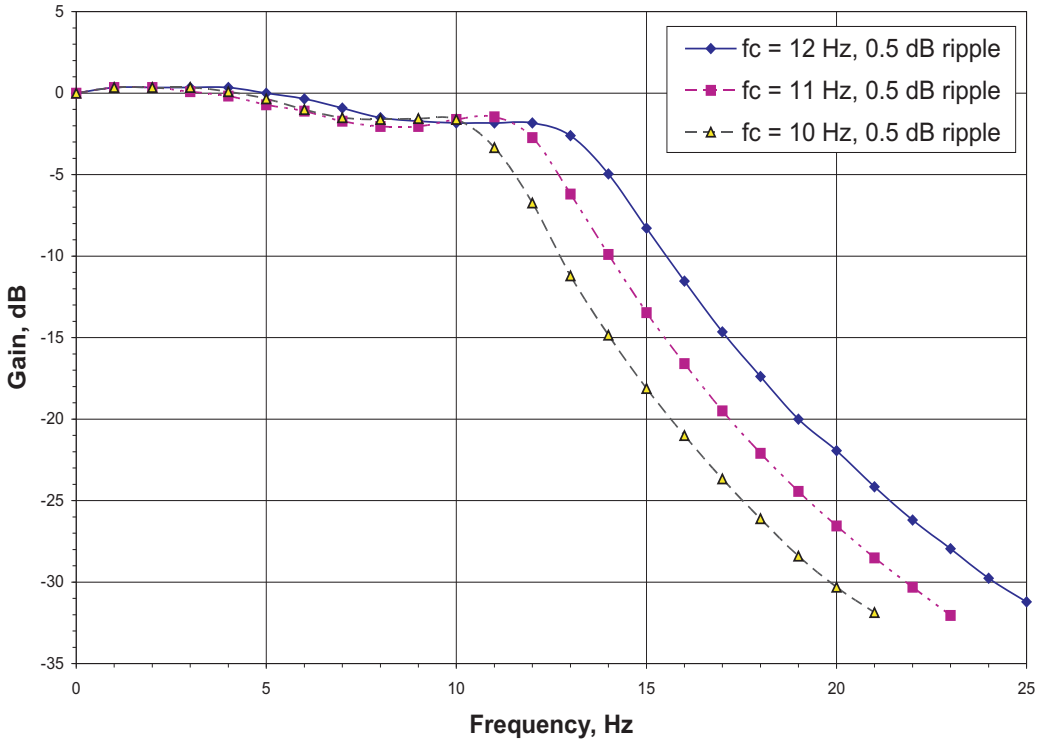

FIGURE 6.26: Figure showing experimentally evaluated frequency response of a 2 stage 4 pole Chebyshev filter with different cut off frequencies

The component values were chosen so that the pass band ripple was below 0.5 dB. The experimentally obtained attenuation was close to 28 dB/octave for the case where f_o was 10 Hz. The overall circuit for the two stage 4 pole filter with f_c of 10 Hz is shown below in figure 6.27. This filter was then used in conjunction with the low noise SRS 560 and the PSD output was again recorded as a function of iris aperture. The results are displayed in figure 6.28. The magnitude plot is much narrower and the phase reversal much steeper than before.

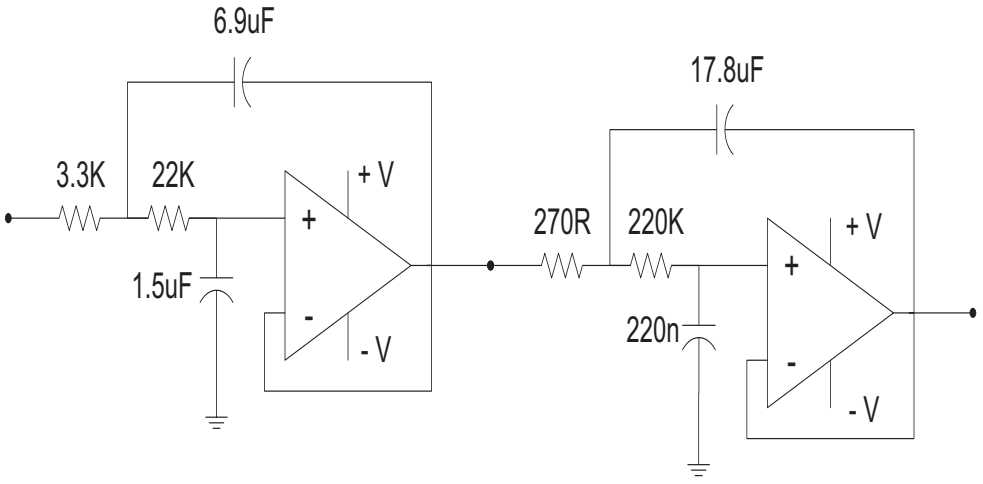

FIGURE 6.27: Circuit diagram of a 2 stage 4 pole Chebyshev filter with a cut off frequency of 10 Hz and 0.5 dB ripple

The improvement in the suppression of the 2ω component can be further understood from figure 6.29 which shows dramatic improvement in comparison to figure 6.23.

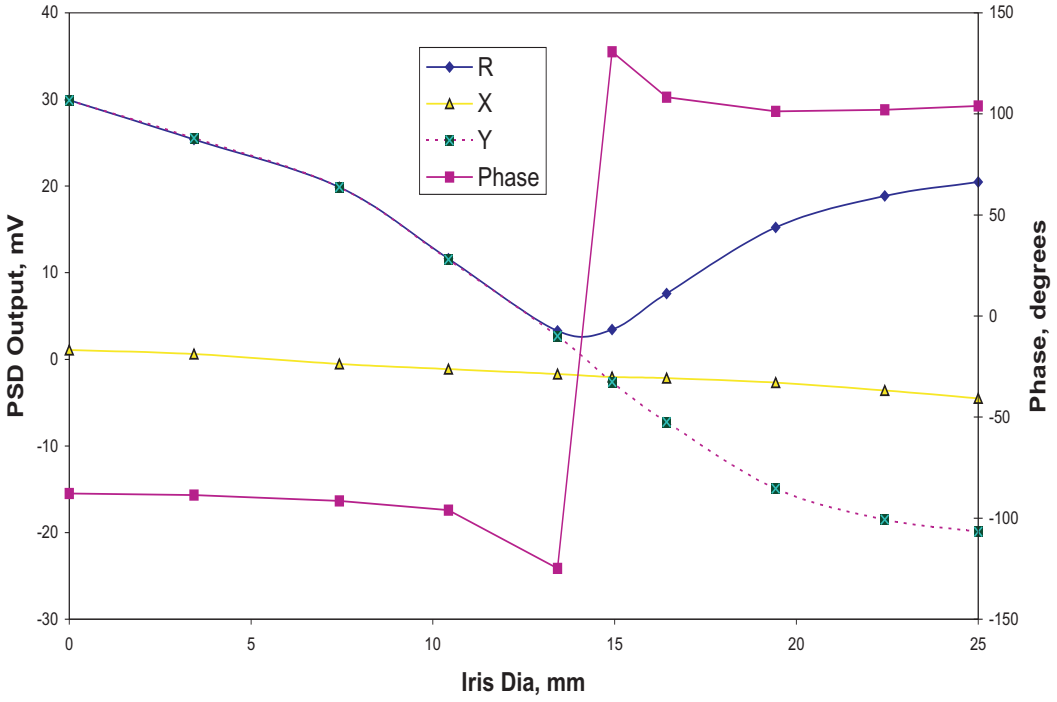

FIGURE 6.28: Plot of PSD output variation when a Chebyshev filter is used in conjunction with the low noise pre amplifier SRS 560

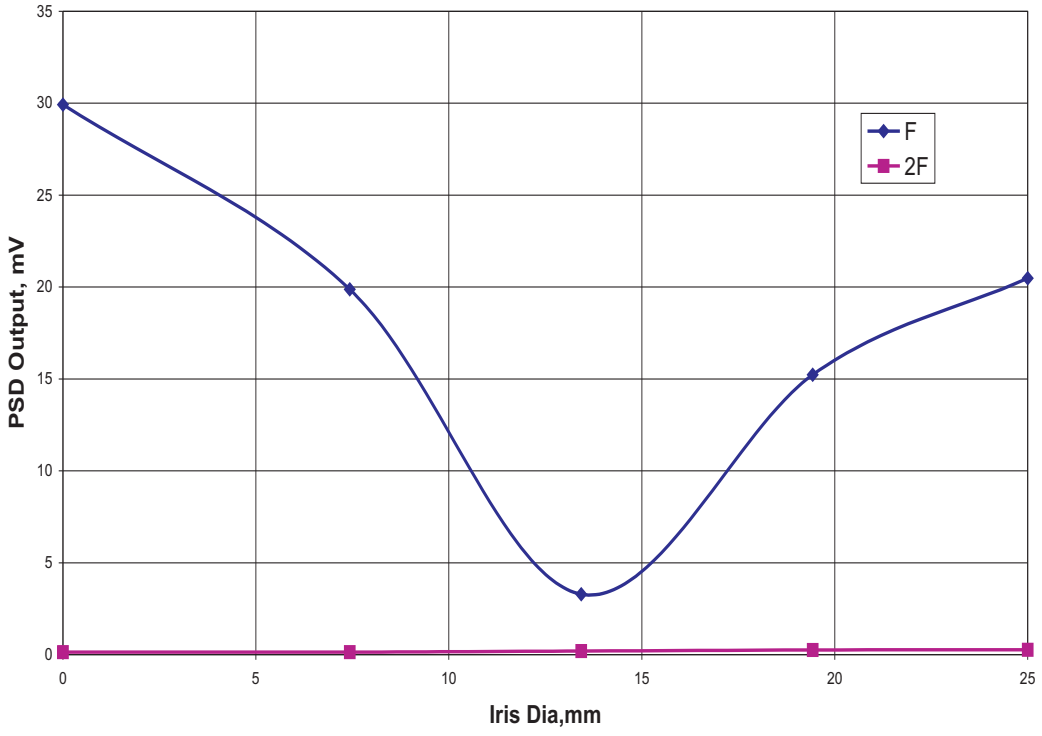

FIGURE 6.29: Figure showing suppression of the 2F component in the PSD output when a Chebyshev filter was used. At balance, the 10 Hz signal clearly dominates the 20 Hz component

Further improvement in reducing the residual balance signal was possible by replacing the SRS 560 with a dual channel low noise filter SRS 650. The overall schematic from the detector to the PSD is shown below in figure 6.30. The two filters present in SRS 650 can be operated independently of each other and hence offers greater design flexibility. By configuring one channel as a high pass filter with a cut on frequency of 8.5 Hz and the other as a low pass filter with a cut off at 11.5 Hz, the two can be cascaded to form a bandpass filter covering the frequency range of interest. A gain of 10 dB was set on each channel and once again the PSD output was recorded and this is represented by figure 6.31. The residual balance signal recorded for this scheme was only 0.22 mV which is the best result that was obtained so far. The R value still does not hit the origin because of the difficulty in obtaining, by manual iris adjustments, the precise iris diameter that corresponds to the equilibrium point.

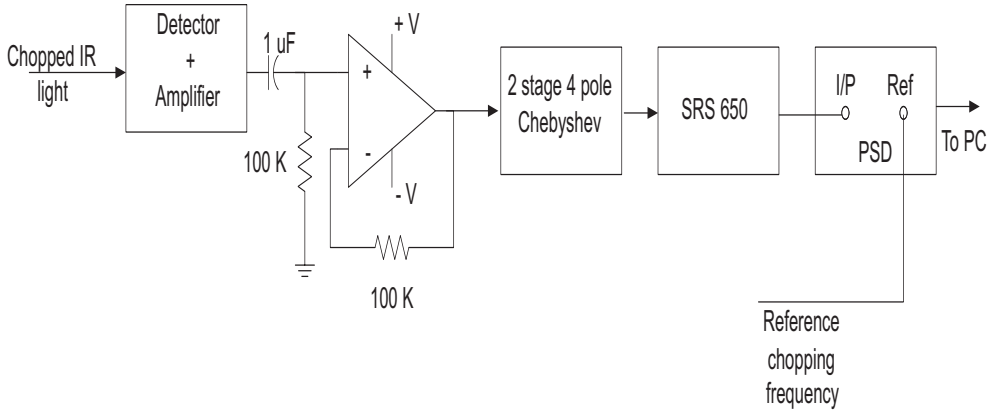

FIGURE 6.30: Figure showing the schematic setup of signal flow from the pyroelectric detector to the PSD through the Chebyshev filter

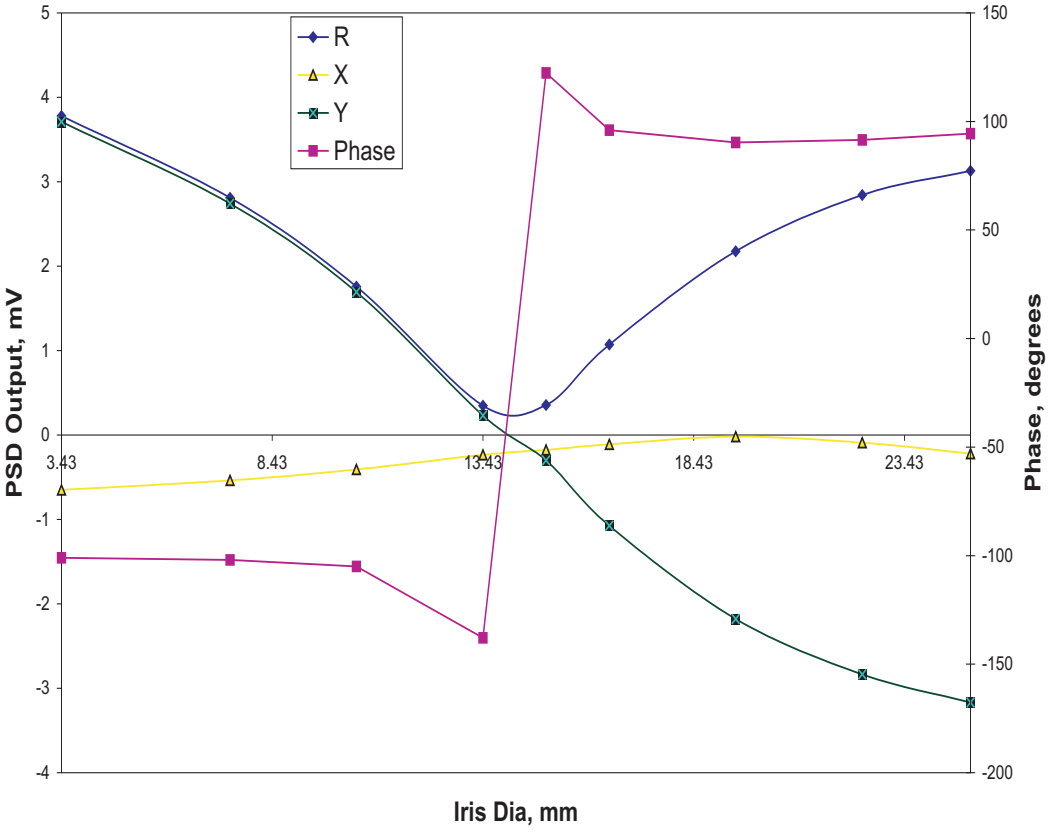

FIGURE 6.31: Plot of PSD output variation when a combination of Chebyshev filter and low noise filter SRS 650 was used to provide improved performance

By using this combination of Chebyshev filter and SRS 650, it can be said with reasonable confidence that the problem arising due to the second harmonic component or 20 Hz signal has been eliminated. Figures 6.32 and 6.33 were recorded from the oscilloscope. The combined trace now shows an expected signal at balance and clearly, no signs of a 20 Hz signal are visible. This is in stark contrast to the earlier situation as shown in figure 5.36 in section 5.7.

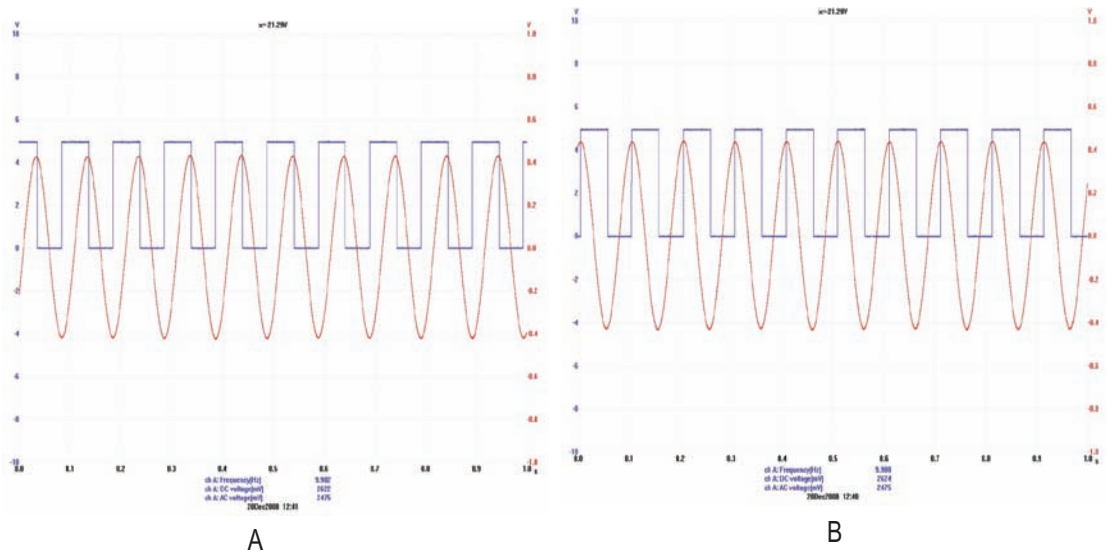

FIGURE 6.32: Figure showing detector output signals from each channel individually, C626 channel (A) and C636 channel (B)

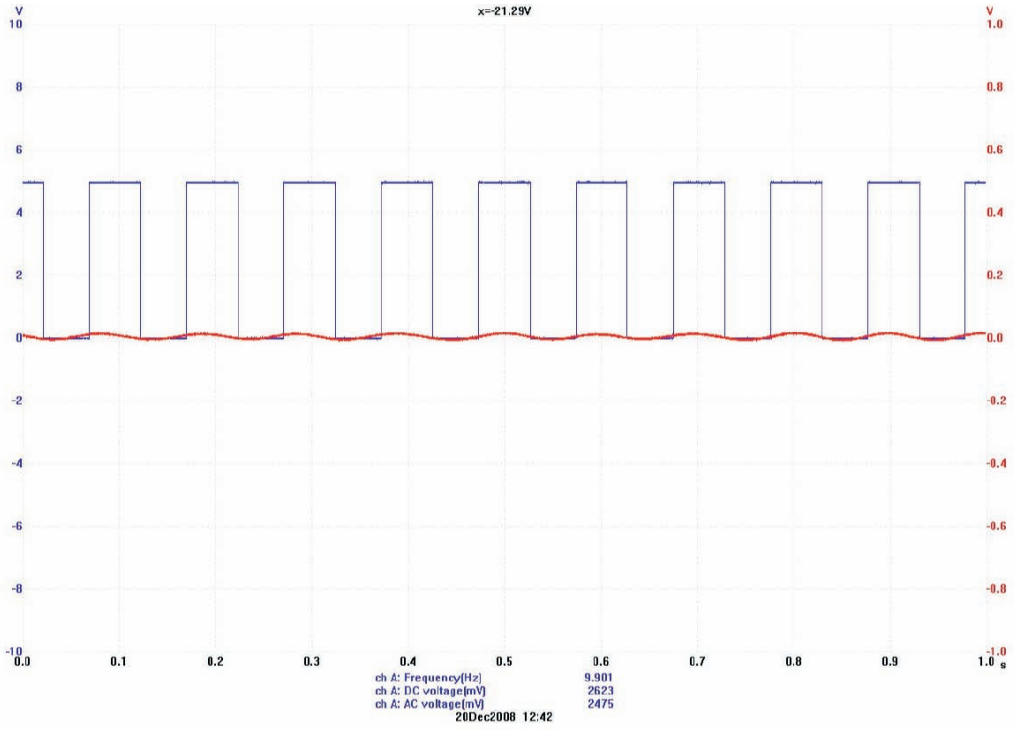

FIGURE 6.33: Figure showing the combined detector output when both channels are transmitting without the presence of any 20 Hz signal

6.7 Gas Based Experiments

So far it has been established that the two channel balanced absorption setup can detect changes in the channel integrated transmittances and respond as expected. This is characterised by a reversal of phase as the system goes through the balance point. The final phase of instrument development involves the use of actual gas mixtures to test and determine the instrument behaviour and response and thereby validate the underlying theory and operating principle. To conduct these gas based tests, the usual operating procedure was followed for setting up the correct phase on the PSD. The filter cells were filled with pure isotopomers and placed in their respective channels. The PSD, as expected, indicated a stronger C636 channel signal, as before, at this stage. The length of the C636 sample cell was maintained around the theoretical equilibrium length of 10.245 cm. The 3% sample gas mixture was then fed into both the sample cells by using the sample gas bag. The interconnecting valve between the two channels was closed so as to isolate them from one another. The instrument enclosure was closed and purged with nitrogen for about 2 hours. At the end of the purge session, 5 ml of pure $^{13}CO_2$ was injected into the C636 cell by using a microsyringe and the PSD output was observed. There was a sudden flip in the phase to a positive value indicating a stronger C626 channel signal. This was due to the increased absorption along the C636 channel as a result of the extra $^{13}CO_2$ that was added. Subsequent filling of N_2 into the sample cell resulted in another phase reversal with the phase value becoming negative, thus indicating a stronger C636 channel signal. This again agrees with theory because virtually no absorption is taking place in the C636 channel whereas the C626 channel sample cell still contains the 3% gas mixture that was initially fed into it. This test thus indicated that the instrument responds to gross changes in channel transmittances which was induced by the introduction of extra absorbing gas into one of the channels. However, 5 ml of pure $^{13}CO_2$ translates to a very high delta value. Hence to test the response of the instrument to lower delta values, the experiment was repeated by following the same procedure but using a different concentration of enriched sample gas. 3 ml of pure $^{13}CO_2$ was added to a bag containing 3 litres of N_2 and mixed thoroughly. About 20 ml of this mixture was extracted using the microsyringe and slowly fed into the sample cells at the end of the purge session. This is akin to the situation where an enriched breath sample obtained after the ingestion of C-13 labelled test dose is fed into the measurement system after initially balancing the setup by varying the C636 cell length. When an amount of extra $^{13}CO_2$ corresponding to an equivalent delta of 11‰ was added, a phase reversal was observed indicating a stronger C626 channel

signal. This was accompanied by a drop in the magnitude (R value) as the phase shifted by 180°. This is clearly visible in figure 6.34 shown below and the pattern is similar to the results obtained from earlier experiments using the iris. Repeated trials produced similar phase reversals for equivalent delta in the range of 10.5‰ to 11.5‰. These tests confirm the fact that the balanced absorption measurement

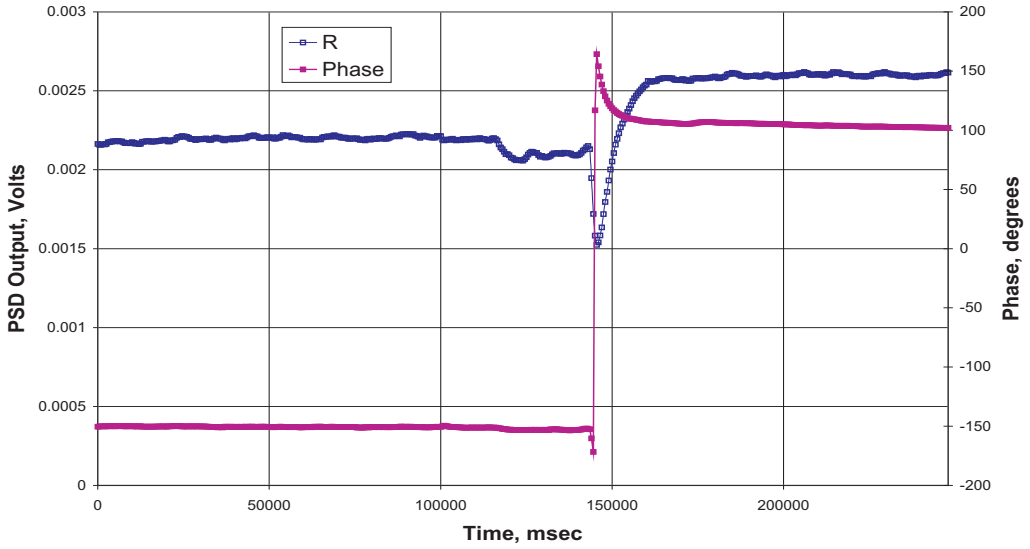

FIGURE 6.34: Figure showing the phase and magnitude response of the system when an enriched sample equivalent to 11‰ was fed into it

system responds to imbalances caused by changes in channel transmittances. The instrument in the present configuration is certainly capable of detecting changes of the order of 11‰. Previous noise analysis, however, suggests that the detection limit is in the vicinity of 5‰ to 6‰. To confirm this, the tests were repeated with lower concentrations of enriched sample gas. However, these tests failed to produce any conclusive results that indicated a delta detection capability lower than 11‰.

A change in length of the C636 cell without the addition of any enriched gas sample at the end of the purge session should also produce a change in the channel transmittances thereby contributing to a delta value. This is because, when the length of the gas cell is varied, it either draws in or pushes out more gas from or into the attached gas bag and hence this affects the absorption within the cell. A change in cell length is required to balance the two individual channel intensities and thereby restore the system balance. The instrument is initially balanced after the basal tests and then once the enriched sample is fed into it, the feedback loop drives the variable length gas cell in the required direction to restore system balance. It is this change in length that gives us a measure of the delta value. To

test this, the gas cells were filled with the 3% sample mixture and the C636 cell length was maintained near the theoretical equilibrium length of 10.245 cm. The enclosure was purged for 2 hours as before. Then the length of the gas cell was varied by using the servo loop and micrometer arrangement without adding any enriched gas sample. This was done by sending out a series of command pulses to the motor driver via the USB data acquisition card using the LABVIEW interface that was created. The length was varied initially from 10.245 cm to 9.9 cm which is equivalent to a delta change of about 35‰. This is well within the detection limit of the instrument. However, the PSD output did not show any sign of phase reversal or a significant change in the magnitude to suggest a change in absorption. The length of the cell was then increased to 11.5 cm past the equilibrium point but again no evidence of a phase reversal was observed. Repeated tests did not provide any satisfactory results that indicated a change in length resulting in a delta value and this was contrary to what was expected.

So the current problem was that no phase reversal was observed in the PSD output as a result of cell length variation. A closer examination of the PSD output revealed a likely source of the problem. After the channels were initially balanced using an iris in the absence of any gas cells, the filter and sample cells were placed in the beam path. At this point, as mentioned earlier, the C636 channel always appeared stronger due to the higher concentration of C626 in the unpurged non-sample path length. The entire enclosure was then purged for 2 hours. However, at the end of the purge session with the C636 cell length at or near its equilibrium value, it was observed that instead of having balanced absorption along the two channels, the C636 channel was still stronger than the C626 channel. This was also observed when the sample cells were purged with N_2 gas instead of the sample gas. According to previous calculations, a purge session lasting 2 hours at 25 l/min is sufficient enough to expel all the background CO_2 present inside the enclosure. A stronger C636 channel represents unequal absorption in the two channels implying that the system is in a state of imbalance at the end of the purge session which is contrary to what was expected. This can also be ascertained by referring to figure 6.34 where the phase at the beginning of the measurement (at the end of purge session) started from a negative value, again indicating a stronger C636 channel. However in this case, direct introduction of significant amount of pure $^{13}CO_2$ (20 ml) produced an immediate phase reversal. This indicates the presence of an equilibrium point and proves that the system responds to unequal absorptions along the two channels by producing a phase reversal as the system goes past the balance point. But when a similar imbalance was created using cell length variation

rather than isotopomer concentration variation, the same effect was not observed. This leads to the conclusion that at the beginning of the measurement process (end of purge session), the system was so far away from a balance point that the change in channel transmittances produced as a result of the length change that was possible with the current bellows and micrometer arrangement was not sufficient to push the system past the balance point and cause a phase reversal. The possibility of the equilibrium cell length of 10.245 cm being grossly inaccurate was considered as a likely cause for this. If this was true, then the maximum stroke offered by the current arrangement will be incapable of driving the system to balance. However, the possibility of a theoretical value of cell length that is in proportion to the relative abundances of the two isotopomers being incorrect is unlikely. In any case, this was put to test and the cell length was increased to 17 cm by attaching extensions to the cell tube. Tests were repeated but this did not help in solving the problem and no phase reversals were observed.

From the above it can be concluded that the key issue here was that the system became unbalanced at the end of the purge session and there were no means available to re-balance under purged conditions. This prevented the system from reaching an equilibrium point which prevented any phase reversal with cell length manipulation. Possible reasons for this imbalance even after purging are mentioned below:

1. The two channel beams falling on different areas on the pyroelectric detector.
2. Difference in reflectivities of the chopper mirrors.
3. Presence of dust particles in the beam path.

Further description of these are provided in the following chapter. It is imperative that any further improvement in the system performance can be made possible only if this problem is adequately resolved. This implies ensuring the system is in a state of balance with a null detector output at the end of the purge session. Additional mechanical adjustments will have to be made in order to accomplish this without having to open up the enclosure and loose the purge within. However, any further structural alterations will require further testing and this will entail additional time which unfortunately was not available at our disposal. Hence it was decided to conclude the experimental programme at this juncture and use the vast amount of data and knowledge generated to provide recommendations and suggestions for carrying this work forward. More details and discussions on this is

provided in the following chapter along with possible design modifications for an improved system performance.

Chapter 7

Summary and Conclusion

The previous chapters have described in detail the various experiments that were carried out in order to fully characterise the measurement system and this had generated abundant information and useful results. Through various simulations and experimental results it was shown that the present system was capable of detecting less than 11‰. However, some issues remain that prevents us from achieving any phase reversal with cell length manipulation. This chapter summarises and recapitulates the progress made so far, considers the remaining difficulties and makes recommendations for future work.

7.1 Recapitulation of Results

In order to gain a thorough understanding of the instrument behaviour and to predict its real-time response, it was imperative to develop a highly accurate spectroscopic model of CO_2. The various steps that were followed to obtain such a reliable model were detailed earlier in section 4.1. The high accuracy of the model was then validated by comparing it against line parameters obtained from the HITRAN database. The error in line position was $1/4000^{th}$ of a typical line width whereas the error in line strength was 0.02% for the maximum intensity lines. This model was then used as a basis for conducting an extensive range of computer simulations that were used to predict system response to various possible interferents that will result in spurious results. In each case, the effect of the interferent was assessed and suitable control measures were recommended if the effect was considered to be significant. On the basis of these simulations, it was concluded that source temperature fluctuations of ± 0.5K between the basal

and enriched sample tests can result in a delta variation of 1‰. The long term stability test of the actual blackbody source IR-12 is described in chapter 5 where it was observed to meet the necessary stability requirements. Etalon temperature instability of the cell windows was another possible source of interferent that was looked into[26] and the use of wedged windows for the gas cells was recommended. CO_2 temperature fluctuations were also found to generate spurious results and it was necessary to maintain a thermal equilibrium between the gas cells in the two channels. However, variation in gas pressure was not found to be a major problem and hence no control measures were put in place.

Chapter 5 deals with the fabrication and characterisation of the various sub-systems that form part of the measurement setup. Details regarding the blackbody source and the optical infrared filter were provided. Design and construction of the mechanical chopper assembly and the various sample gas and filter gas cells were described in detail. A dedicated gas filling rig was developed for use with the isotope filter cells and the sample cells. Integration of temperature and pressure sensors with the instrument and their associated electronics was also dealt with. This was followed by a discussion on the characteristics of the pyroelectric detector and the design details of the amplifier. Experiments were conducted to determine detector response at various source temperatures and also with varying isotopomer concentrations and the results showed extremely good co-relation with simulation results. The working of the feedback servo loop and the stepper motor interface was also discussed followed by a description of the virtual interface developed using LABVIEW. Finally, the overall instrument enclosure was described including the purge gas and sample gas flow pathways. The optimum purge flow rate was calculated and the purge procedure was also outlined. Thus chapter 5 systematically investigated the features and responses of the various sub-systems involved and set the stage for the gas testing phase.

Chapter 6 contains all the various experimental tests that were conducted in order to evaluate and quantify the overall system performance. Leak tests were conducted on the gas cells using a helium leak detector and a Magnahelic differential pressure gauge and suitable modifications were carried out. Lock-in amplifiers were coupled with the system and gas based measurements were recorded to demonstrate the change in output signal when an imbalance was deliberately introduced into the system. These are shown in figures 6.8 and 6.9. A very comprehensive and detailed analysis of the various noise sources was carried out. The overall system noise was thus calculated and this defined the minimum detection limit of the spectroscopic instrument. The major sources of noise identified were:

1. Pyroelectric detector
2. FET op-amp at the detector output
3. PSD input noise
4. Johnson noise from the resistors

Theoretical calculations showed the instrument responsivity to be limited by the pyroelectric detector which was the largest contributor to the overall noise with a noise density of 80 nV/$\sqrt{Hz}$. Referring to the calibration curve shown in figure 6.10, the overall noise voltage of 2.82 μV represented a minimum detection of 1‰ for a 3 sec time constant. In order to experimentally verify this, a deliberate imbalance was created in the system by changing the iris aperture and the fluctuation in the output response was measured. A 3 sec time constant corresponded to a minimum delta measurement of 3.4‰ to 5.7‰. Although this was higher than a desired value of 1‰, it was a reasonable performance to expect from an initial experimental design. The observed discrepancy between the theoretical and experimental values may be due to the lack of a purged environment that can result in fluctuations in the ambient CO_2 concentration. Further experiments were conducted to study noise emanating from individual components such as the detector and the chopper motor and the results were found to be along expected lines. Although these contributions were small, they help in explaining the observed discrepancy in the minimum delta measurement. Noise from the two channels were recorded individually by blocking the other channel and then the combined overall noise was also experimentally measured using a PSD. It was found that a much higher level of noise, around 85 μV, was present when the channels were operated individually. However, this large noise present in both the channels disappeared to a very large extent when both the channels were used in a balanced state bringing the overall noise down to 5.6 μV. This clearly implied that the noise generating mechanism present in the individual channels was the same but in anti-phase, resulting in elimination of common noise sources when the two channels were present together. This was one of the key features of the spectroscopic instrument presented here and can be attributed to the overall symmetrical design of the measurement system. Possibility of noise arising from source temperature fluctuation due to convection was also investigated in great detail. However, the results obtained from a mathematical analysis were not indicative of any such process occurring in the background and hence the hypothesis was ruled out, although the safety margin was small.

Finally gas based experiments were conducted to check how the system responded when an imbalance was created by feeding in extra sample gas containing pure $^{13}CO_2$. Figure 6.31 shows a phase reversal as the system goes past the balance point due to the increased absorption along one of the channels. The PSD output magnitude (R value) hits a minimum at the balance point and then increases again as one of the channels becomes stronger. Similar experiments were carried out by further reducing the concentration of $^{13}CO_2$ and similar results were obtained. Figure 6.34 shows the magnitude and phase response when an enriched sample equivalent to 11‰ was fed into the sample cells. As expected an immediate phase reversal was observed that confirmed the instrument's ability to detect changes as low as 11‰. However, repeated attempts to reproduce this phase change by varying the C-13 cell length did not succeed. Gross errors in calculating the equilibrium cell length was considered to be a potential cause for this but this was ruled out after tests with much longer cell lengths failed to provide any satisfactory results. Further diagnosis revealed the true nature of the problem and it was realized that at the end of the purge session, the instrument started from a position of imbalance due to a stronger C636 channel, instead of a balanced state. Hence, the balance point that corresponded to a null detector output was much farther away than what can be compensated merely by a cell length change. Figure 7.1 below is a pictorial representation of the current problem. The figure on the left represents the current scenario where the system starts from an unbalanced position and hence the R vector resides well within the top left quadrant that represents a stronger C636 channel. A subsequent change in length is unable to take the R vector past the balance point. Instead it simply reduces the value of R as indicated by the arrow without actually hitting the equilibrium (the 0 origin). In an ideal case, however, if the system was present in a balanced state, the cell length manipulation will reduce the R vector significantly and push it towards the origin. In the vicinity of the origin, noise starts to dominate and the signal will have a random phase. Further change in length will take it past the equilibrium point and cause the R vector to flip its phase and come out through the bottom right quadrant as depicted in the figure.

Although there were severe time constraints as far as the project was concerned, as a final effort, it was decided to incorporate another iris in the C636 channel with an arrangement to externally adjust the aperture diameter. This enabled us to manually restore the system to a balance point at the end of the purge session without having to open the enclosure and break the purge in the process. Once the balance was restored, the cell length was varied once again to observe any

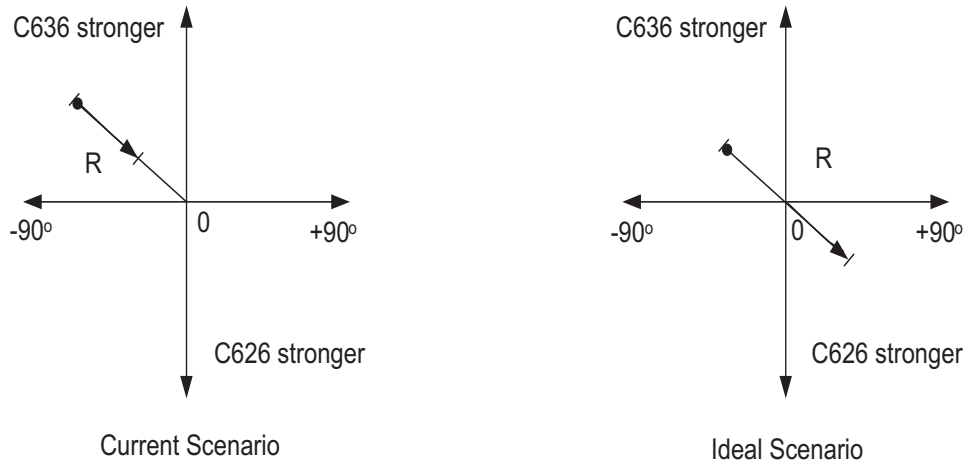

FIGURE 7.1: Pictorial representation showing why a phase reversal is not observed under the present circumstances merely by a change in cell length

phase changes in the PSD output. The R vector constantly fluctuated around the zero mark but again no phase reversals were observed. Some long term drift on the R value was seen however. Besides, the external mechanical adjustment for the iris aperture had significant backlash making it extremely difficult to get the exact balance point.

7.2 Major Challenges Encountered

During the course of this research endeavor some challenging situations were encountered which had a serious impact on the time line of the project. One of the most intriguing and unexpected observations was the appearance of the 2ω component at the output of the detector under balanced absorption conditions. This was contrary to the DC signal that was expected at balance. With the help of computer based simulations, it was possible to offer a logical explanation and justify the source of this 20 Hz signal in the detector output. This has been covered in chapter 5. It was initially assumed that this 20 Hz signal will be removed by the low pass filter at the output of the PSD and hence will not interfere with the measurement process. However, experiments conducted by varying the iris aperture showed that a dominant 2ω component existed at the balance point when practically no signal should have been detected. In fact, even this high quality PSD was incapable of adequately suppressing the 2ω component. To the best of

the author's knowledge, this situation is rare. A 2 stage 4 pole chebyshev filter was designed and developed to suppress this 2ω component and satisfactory results were obtained as a result. The fluctuation in the reference frequency derived from the mechanical choppers was a problem that could not be easily traced initially. The problem manifested itself in the form of steps or jumps that were observed in the PSD output as shown in figure 6.17. PSDs would normally be considered insensitive to such small variations in reference frequency and so this effect must be some detail of the internal design. This problem was circumvented by building a closed loop frequency control circuit based on PWM technique to stabilise the chopping frequency.

7.3 Recommendations for Future Work

The aim of this research undertaking was to develop a low cost spectroscopic instrument capable of making carbon isotope ratio measurements for possible use in Urea Breath Tests (UBTs). In light of the achievements and results achieved so far, it can be safely said that the work described in this document demonstrates the feasibility of such a diagnostic system that incorporates several innovative features. The low cost feature of this instrument lies in the use of non-expensive optical components and a simple broadband source instead of using costly tunable diode lasers and its associated controllers. Pyroelectric detectors offered the required responsivity and this also eliminated the need for cooling arrangements. This makes the system an attractive option for a commercial product. Whole band integrated absorption measurements were made rather than using absorption line pairs to ascertain concentration of the absorbing species. Another unique feature of the instrument is its highly symmetrical design and the ratioing nature of the setup ensured that it is not vulnerable to external interferences such as variations in source temperature, ambient fluctuations or detector responsivity since they affect both the channels to the same extent. The novel concept of variable length gas cell with a feedback servo loop was also tested and implemented for the first time. This avoided the need to make any absolute concentration measurements. Although the detection limits predicted from noise analysis was less than 6‰, experimental trials were only able to demonstrate levels of 10.5‰ to 11.5‰. From all of the above it can be concluded that further improvement in detection limits can be achieved only by incorporating certain modifications in the implementation of the design. An attempt has been made below to describe some of the possible areas of modification with a view of creating an improved system that is much

closer to a fully commercially viable product.

One alteration that will decrease the size of the overall system will be the use of beam tubes to cover the beam path from the source all the way upto the detector, and passing along the two channels. These beam tubes should have adequate provisions for gas inlet and outlet. This will greatly reduce the volume that needs to be N_2 purged thereby cutting down the duration of the purge session from the current 2 hours to possibly under 30 minutes. This will have an obvious effect during the system development phase by reducing the overall time required for the measurement process. Another advantage arising from this modification is that even during the purge session, it offers the user adequate access to the various optical and non-optical components to manoeuvre them. This is especially useful when the need arises to rebalance the system or perform a diagnostic check on the various electronic circuit boards. This is not possible in the present case without breaking open the purge. However, some careful consideration needs to be given to the actual construction of the beam tubes around the mechanical chopper and mirror assembly. The 45° inclination of these components may require the tubes to have adequate windows to contain the purge along the other sections.

Another useful feature that can be incorporated is the use of motorised irises along the two channels for achieving balanced absorption. This makes it possible to achieve precision control of the aperture by using suitable driver software such as LABVIEW. Fine adjustments can thus be done at the end of the purge session to bring the system closer to the balance point before introduction of the sample gases.

Driving the IR source at a higher temperature will also prove beneficial as more power falls on the detector. Table 5.2 shows that the relative difference in channel intensities gets bigger as source temperature increases and this makes it possible to carry out more sensitive measurements. Increase in source temperature causes the peak of the blackbody curve to shift towards the $^{12}CO_2$ absorption region but as long as the temperature is adequately stable over the entire measurement process, it will not have any adverse effect on the responsivity of the system.

Another possibility that needs to be explored in more detail is the use of electronically locked synchronised choppers that can replace the current mechanically linked choppers. Some initial work in this regard has already been done as described previously in section 5.4. If successfully implemented, electronic phase locking of the choppers C1 and C2 will reduce phase jitter and backlash that is normally associated with mechanical systems. This will result in improved phase

accuracy from the present ±0.7°and reduced overall noise present in the system. This will greatly help in achieving the desired 1‰ measurement precision. It avoids the use of gear linkages and belts which undergo gradual wear and tear, thereby inducing additional uncertainties with respect to position of the chopper blades and their frequency stability. Besides, it eliminates the use of bulky steel frames to connect the two choppers as in the present case. This greatly improves the design of the instrument by reducing its overall size and making it more compact and portable.

The inability of the instrument to achieve a balance point by cell length manipulation demands a deeper investigation into the problem. One of the contributing factors to this is the absence of balanced absorption along the two channels at the end of the purge session. The likely reasons for this have been listed below:

- If one of the channel beams falling on the detector window only partially covers the detector active area, the other channel will then appear stronger and result in a virtual imbalance. By using an iris, balance can be achieved initially at the beginning of the purge session. However, once the background CO_2 levels have been sufficiently reduced by purging the enclosure, inequalities in channel beam intensities become more visible. He-Ne lasers were used to check the alignment of the two channel beams with respect to the detector, but it was not possible to get the two spots to overlap each other completely and occupy the exact same spot on the detector active area. Introduction of the filter cells after balancing the channels can produce a further shift in the beam alignment, thereby reducing the channel strength and causing an imbalance.

- Difference in the reflectivities of the two chopper mirrors C1 and C2 can also result in a slight imbalance in channel intensities. As mentioned earlier, the two chopper mirrors were manually diamond polished to make their surfaces reflective. However, it is not possible to guarantee that both C1 and C2 have the same reflectivity and hence one channel may be better reflected than the other leading to unequal intensities.

- Another possible reason may be the presence of dust particles on the windows that will reduce the intensity of the channel beam and thus create an imbalance.

Under normal circumstances, all the above listed problems can be resolved by balancing the two channels with the irises. However, in the present case this

cannot be done without breaking the purge within the enclosure and hence the recommendation for motorised irises that can be externally controlled.

7.4 Key Remaining Issue

Even after re-balancing the system using a second iris along the C-13 channel, variation in cell length did not push the system towards the balance point. Phase reversals were observed when enriched gas samples were fed to the sample cells but the same could not be replicated by cell length manipulation. This strongly suggests a problem with gas flow from the air bag attached to the sample cell when the length of the C636 cell is varied. Extensive studies were carried out using a Magnahelic pressure gauge and leak detectors to identify any possible sources of leak from the gas cell and required modifications were made. This, however, did not improve the results obtained with cell length manipulation.

In the absence of any other logical explanation for the above, gas flow from the air bag still appears to be the most likely cause of this problem and this requires further testing and studying. It seems that some underlying phenomenon that governs the flow of gas from the air bag into the gas cell has not been considered and this needs to be examined in detail on a priority basis. Once this final stumbling block is overcome and the aforementioned modifications are incorporated, the measurement system presented here will prove to be a very useful diagnostic tool for the detection of *H.pylori*.

Appendix A

Data Sheets

This section contains data sheets for the following components:

- Temperature sensor LM35CZ
- Pressure sensor SDX15A2
- F/V converter LM331
- PLL IC HEF4046
- Infrared source IR-12
- Pyroelectric detector LTI Q2
- Low inertia DC servo motor M66CI-24
- Low power dual comparator LM393
- Low noise dual op-amp LM833
- Instrumentation Amplifier AMP04
- Dual FET input op-amp OPA2604
- Unipolar Stepper Motor 16HS-110
- Stepper Motor Driver Card
- CAD drawing for ICF cell

Data Pack E *Issued March 1997* **232-2958**

Data Sheet

Temperature sensor ic LM35CZ and LM35DZ

RS stock numbers 317-954 and 317-960

The LM35 is a precision semiconductor temperature sensor giving an output of 10mV per degree Centigrade. Unlike devices with outputs proportional to the absolute temperature (in degrees Kelvin) there is no large offset voltage which, in most applications, will have to be removed.

Accuracies of $^1/_4$°C at room temperature or $^3/_4$°C over the full temperature range are typical.

Absolute maximum ratings (Note 10)

Supply voltage _____ +35V to -0.2V
Output voltage _____ +6V to -1.0V
Output current _____ 10mA
Storage temperature, TO-92 package _ -60°C to +150°C
Lead temperature (soldering, 10 seconds) ____ 260°C
Specified operating temperature range
T_{MIN} to T_{MAX} (Note 2)
LM35CZ _____ -40°C to +110°C
LM35DZ _____ 0°C to +100°C

Features

- Output proportional to °C
- Wide temperature range -40°C to +110°C (CZ version)
- Accurate $^1/_4$°C at room temperature typical
- Linear output 0.2°C typical
- Low current drain (60µA typical)
- Low self heating (0.08°C typical)
- Output impedance 0.1Ω at 1mA
- Standard T092 package.

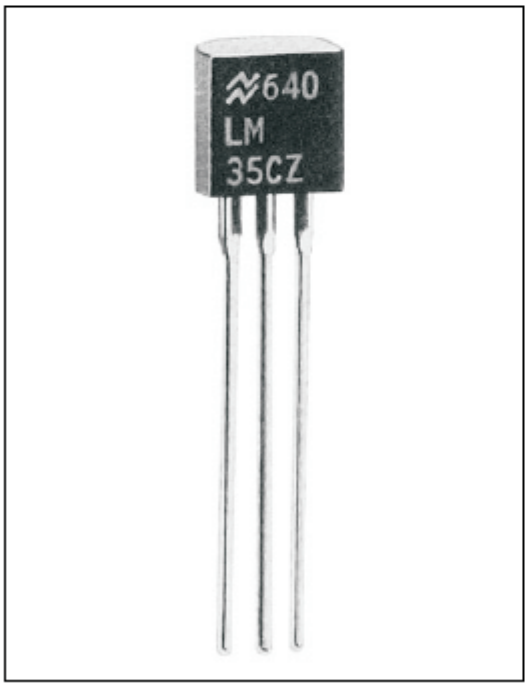

Pin connections

TO-92
Plastic package

BOTTOM VIEW

Package details

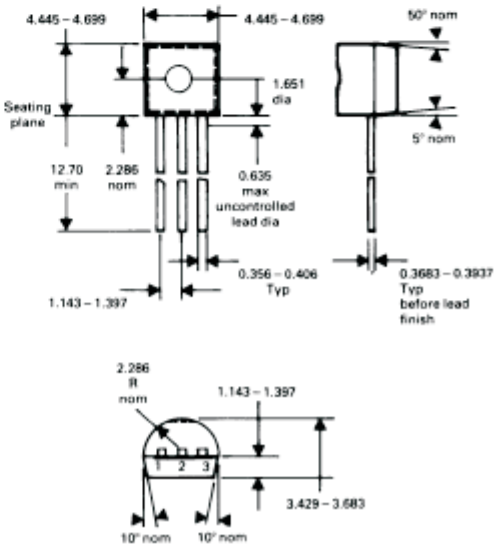

FIGURE A.1: LM35CZ

SenSym

SDX...A Series

Precision Compensated Pressure Sensors in DIP Package

FEATURES

- 0 - 1 to 0 - 100 psi
- Low cost dip
- Temperature compensated
- Calibrated zero and span
- Small size
- Low noise
- High impedance for low power applications

APPLICATIONS

- Medical equipment
- Computer peripherals
- Pneumatic controls
- HVAC

GENERAL DESCRIPTION

The SDX series sensors will provide a very cost effective solution for pressure applications that require small size plus performance. These calibrated and temperature compensated sensors give an accurate and stable output over a 0°C to 70°C temperature range. SDX devices are available in standard commercial and prime grades to allow optimization of accuracy and cost in any given application. This series is intended for use with non-corrosive, non-ionic working fluids such as air, dry gases and the like.

Devices are available to measure absolute and gage pressures from 1 psi up to 150 psi. The absolute devices have an internal vacuum reference and an output voltage proportional to absolute pressure.

The output of the bridge is ratiometric to the supply voltage and operation from any D.C. supply voltage up to +20 V is acceptable.

The SDX devices feature an integrated circuit sensor element and laser trimmed thick film ceramic housed in a compact solvent resistant case.

The package is a double wide (i.e., 0.600" lead spacing) dual-in-line-package. This is the same familiar package used by IC manufacturers except it is only 0.470" long and has a pressure port(s). The PC board area used by each DIP is approximately 0.26 square inches. This extremely small size enables the use of multiple sensors in limited available space. The DIP provides excellent corrosion resistance and isolation to external package stress.

The DIP mounts on a PC board like a standard IC with through-hole pins. The pins anchor the pressure sensor to the PC board and provide a more secure and stable unit than other types of packages.

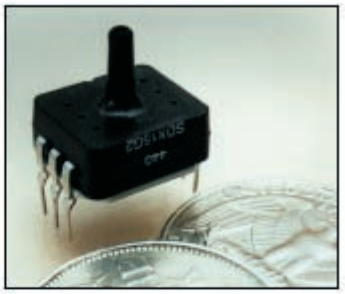

EQUIVALENT CIRCUIT

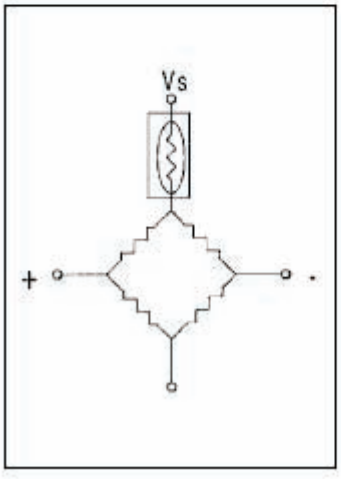

ELECTRICAL CONNECTIONS

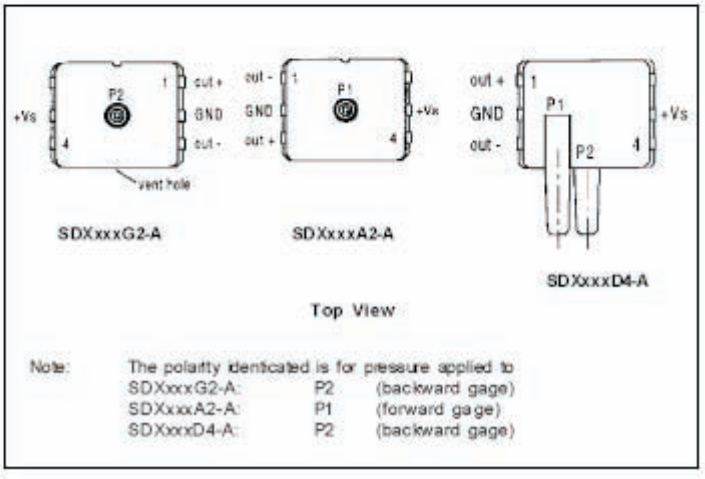

Note: The polarity identicated is for pressure applied to

SDXxxxG2-A:	P2	(backward gage)
SDXxxxA2-A:	P1	(forward gage)
SDXxxxD4-A:	P2	(backward gage)

SENSORTECHNICS
Aubinger Weg 27, 82178 Puchheim, Germany
Phone: +49 (0)89 80083-0, Fax: +49 (0)89 80083-33
http://www.sensortechnics.com

FIGURE A.2: SDX15A2

National Semiconductor

December 1994

LM131A/LM131, LM231A/LM231, LM331A/LM331 Precision Voltage-to-Frequency Converters

General Description

The LM131/LM231/LM331 family of voltage-to-frequency converters are ideally suited for use in simple low-cost circuits for analog-to-digital conversion, precision frequency-to-voltage conversion, long-term integration, linear frequency modulation or demodulation, and many other functions. The output when used as a voltage-to-frequency converter is a pulse train at a frequency precisely proportional to the applied input voltage. Thus, it provides all the inherent advantages of the voltage-to-frequency conversion techniques, and is easy to apply in all standard voltage-to-frequency converter applications. Further, the LM131A/LM231A/LM331A attains a new high level of accuracy versus temperature which could only be attained with expensive voltage-to-frequency modules. Additionally the LM131 is ideally suited for use in digital systems at low power supply voltages and can provide low-cost analog-to-digital conversion in microprocessor-controlled systems. And, the frequency from a battery powered voltage-to-frequency converter can be easily channeled through a simple photoisolator to provide isolation against high common mode levels.

The LM131/LM231/LM331 utilizes a new temperature-compensated band-gap reference circuit, to provide excellent accuracy over the full operating temperature range, at power supplies as low as 4.0V. The precision timer circuit has low bias currents without degrading the quick response necessary for 100 kHz voltage-to-frequency conversion. And the output is capable of driving 3 TTL loads, or a high voltage output up to 40V, yet is short-circuit-proof against V_{CC}.

Features

- Guaranteed linearity 0.01% max
- Improved performance in existing voltage-to-frequency conversion applications
- Split or single supply operation
- Operates on single 5V supply
- Pulse output compatible with all logic forms
- Excellent temperature stability, ± 50 ppm/°C max
- Low power dissipation, 15 mW typical at 5V
- Wide dynamic range, 100 dB min at 10 kHz full scale frequency
- Wide range of full scale frequency, 1 Hz to 100 kHz
- Low cost

Typical Applications

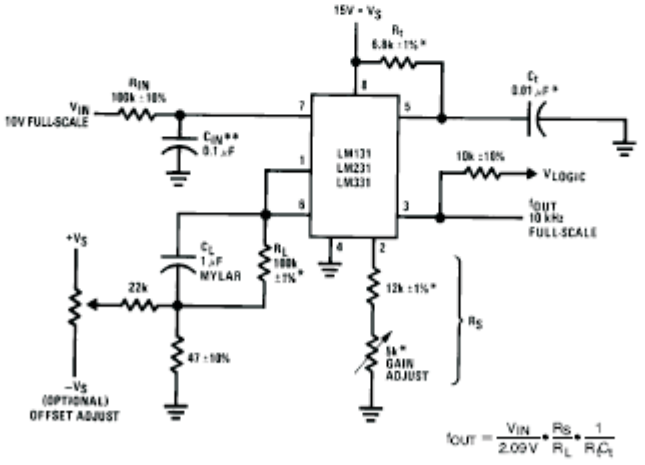

*Use stable components with low temperature coefficients. See Typical Applications section.

**0.1µF or 1µF, See "Principles of Operation."

FIGURE 1. Simple Stand-Alone Voltage-to-Frequency Converter with ± 0.03% Typical Linearity (f = 10 Hz to 11 kHz)

FIGURE A.3: LM331

Typical Applications (Continued)

DETAILS OF OPERATION, FREQUENCY-TO-VOLTAGE CONVERTERS *(FIGURES 5 AND 6)*

In these applications, a pulse input at f_{IN} is differentiated by a C-R network and the negative-going edge at pin 6 causes the input comparator to trigger the timer circuit. Just as with a V-to-F converter, the average current flowing out of pin 1 is $I_{AVERAGE} = I \times (1.1\ R_t C_t) \times f$.

In the simple circuit of *FIGURE 5*, this current is filtered in the network $R_L = 100\ k\Omega$ and $1\ \mu F$. The ripple will be less than 10 mV peak, but the response will be slow, with a 0.1 second time constant, and settling of 0.7 second to 0.1% accuracy.

In the precision circuit, an operational amplifier provides a buffered output and also acts as a 2-pole filter. The ripple will be less than 5 mV peak for all frequencies above 1 kHz, and the response time will be much quicker than in *Figure 5*. However, for input frequencies below 200 Hz, this circuit will have worse ripple than *Figure 5*. The engineering of the filter time-constants to get adequate response and small enough ripple simply requires a study of the compromises to be made. Inherently, V-to-F converter response can be fast, but F-to-V response can not.

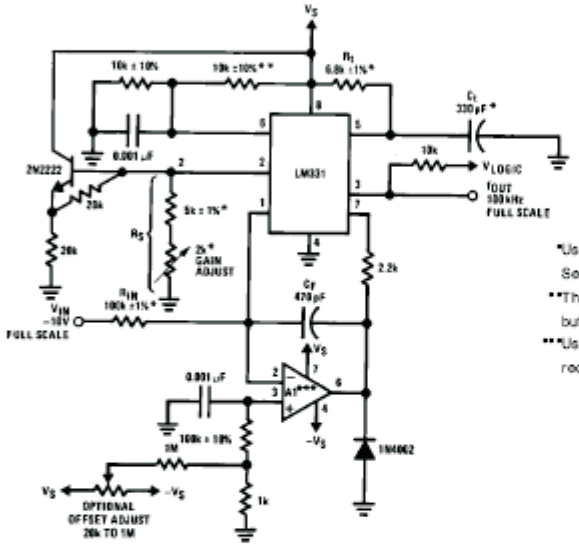

*Use stable components with low temperature coefficients. See Typical Applications section.
**This resistor can be 5 kΩ or 10 kΩ for V_S=8V to 22V, but must be 10 kΩ for V_S=4.5V to 8V.
***Use low offset voltage and low offset current op amps for A1: recommended types LF411A or LF356.

TL/H/5680–6

FIGURE 4. Precision Voltage-to-Frequency Converter, 100 kHz Full-Scale, ±0.03% Non-Linearity

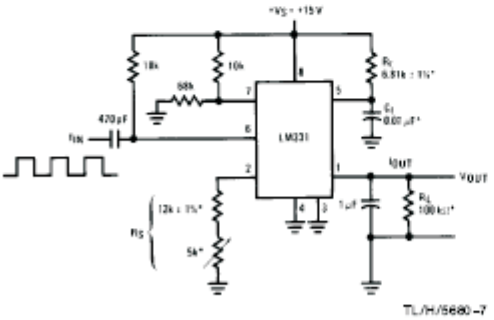

TL/H/5680–7

$$V_{OUT} = f_{IN} \times 2.09V \times \frac{R_L}{R_S} \times (R_t C_t)$$

*Use stable components with low temperature coefficients.

FIGURE 5. Simple Frequency-to-Voltage Converter, 10 kHz Full-Scale, ±0.06% Non-Linearity

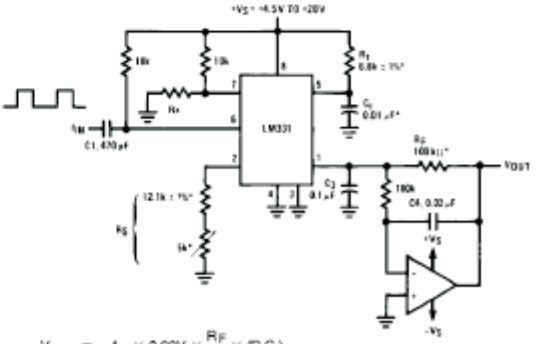

$$V_{OUT} = -f_{IN} \times 2.09V \times \frac{R_F}{R_S} \times (R_t C_t)$$

TL/H/5680–8

$$\text{SELECT } Rx = \frac{(V_S - 2V)}{0.2\ mA}$$

*Use stable components with low temperature coefficients.

FIGURE 6. Precision Frequency-to-Voltage Converter, 10 kHz Full-Scale with 2-Pole Filter, ±0.01% Non-Linearity Maximum

FIGURE A.4: LM331

Phase-locked loop

HEF4046B
MSI

DESCRIPTION

The HEF4046B is a phase-locked loop circuit that consists of a linear voltage controlled oscillator (VCO) and two different phase comparators with a common signal input amplifier and a common comparator input. A 7 V regulator (zener) diode is provided for supply voltage regulation if necessary. For functional description see further on in this data.

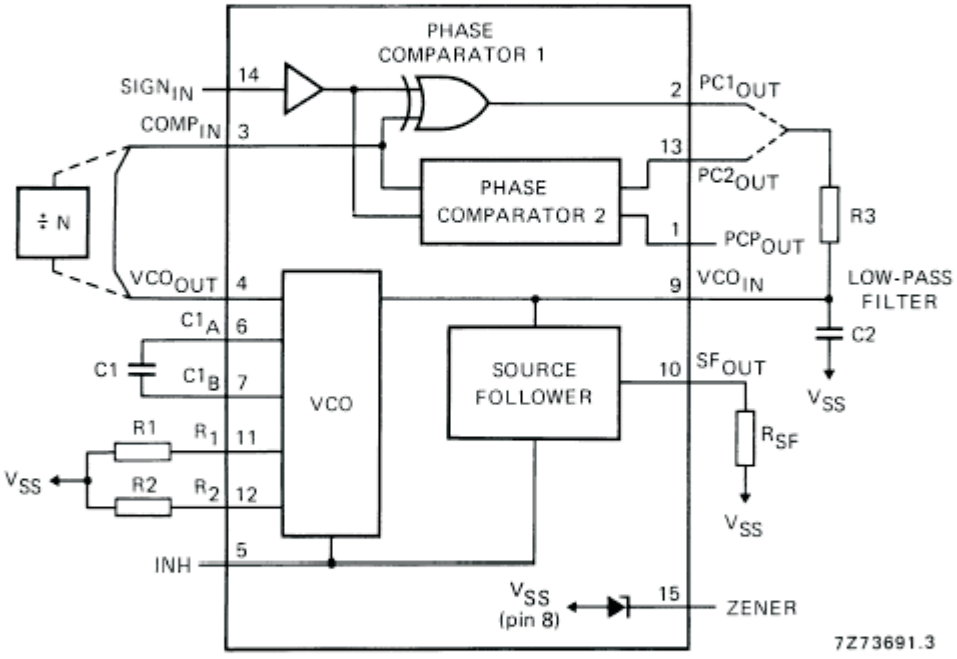

Fig.1 Functional diagram.

HEF4046BP(N):	16-lead DIL; plastic (SOT38-1)
HEF4046BD(F):	16-lead DIL; ceramic (cerdip) (SOT74)
HEF4046BT(D):	16-lead SO; plastic (SOT109-1)

( ): Package Designator North America

FAMILY DATA

See Family Specifications

I_{DD} LIMITS category MSI

See further on in this data.

FIGURE A.5: HEF4046 PLL IC

Phase-locked loop

HEF4046B
MSI

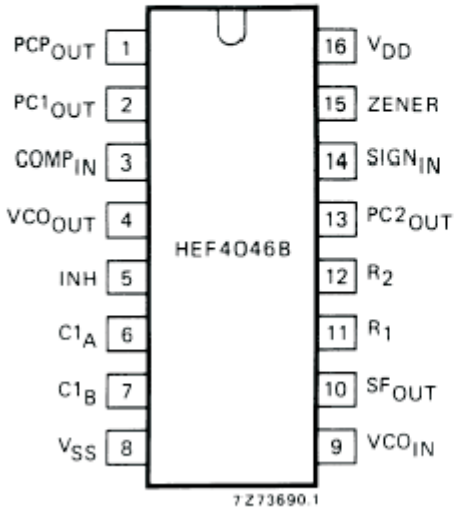

Fig.2 Pinning diagram.

PINNING

1. Phase comparator pulse output
2. Phase comparator 1 output
3. Comparator input
4. VCO output
5. Inhibit input
6. Capacitor C1 connection A
7. Capacitor C1 connection B
8. V_{SS}
9. VCO input
10. Source-follower output
11. Resistor R1 connection
12. Resistor R2 connection
13. Phase comparator 2 output
14. Signal input
15. Zener diode input for regulated supply.

FUNCTIONAL DESCRIPTION

VCO part

The VCO requires one external capacitor (C1) and one or two external resistors (R1 or R1 and R2). Resistor R1 and capacitor C1 determine the frequency range of the VCO. Resistor R2 enables the VCO to have a frequency off-set if required. The high input impedance of the VCO simplifies the design of low-pass filters; it permits the designer a wide choice of resistor/capacitor ranges. In order not to load the low-pass filter, a source-follower output of the VCO input voltage is provided at pin 10. If this pin (SF_{OUT}) is used, a load resistor (R_{SF}) should be connected from this pin to V_{SS}; if unused, this pin should be left open. The VCO output (pin 4) can either be connected directly to the comparator input (pin 3) or via a frequency divider. A LOW level at the inhibit input (pin 5) enables the VCO and the source follower, while a HIGH level turns off both to minimize stand-by power consumption.

Phase comparators

The phase-comparator signal input (pin 14) can be direct-coupled, provided the signal swing is between the standard HE4000B family input logic levels. The signal must be capacitively coupled to the self-biasing amplifier at the signal input in case of smaller swings. Phase comparator 1 is an EXCLUSIVE-OR network. The signal and comparator input frequencies must have a 50% duty factor to obtain the maximum lock range. The average output voltage of the phase comparator is equal to $\frac{1}{2} V_{DD}$ when there is no signal or noise at the signal input. The average voltage to the VCO input is supplied by the low-pass filter connected to the output of phase comparator 1. This also causes the VCO to oscillate at the centre frequency (f_o). The frequency capture range ($2 f_c$) is defined as the frequency range of input signals on which the PLL will lock if it was initially out of lock. The frequency lock range ($2 f_L$) is defined as the frequency range of input signals on which the loop will stay locked if it was initially in lock. The capture range is smaller or equal to the lock range.

With phase comparator 1, the range of frequencies over which the PLL can acquire lock (capture range) depends on the low-pass filter characteristics and this range can be made as large as the lock range. Phase comparator 1 enables the PLL system to remain in lock in spite of high amounts of noise in the input signal. A typical behaviour of this type of phase comparator is that it may lock onto input frequencies that are close to harmonics of the VCO centre frequency. Another typical behaviour is, that the phase angle between the signal and comparator input varies between 0° and 180° and is 90° at the centre frequency. Figure 3 shows the typical phase-to-output response characteristic.

FIGURE A.6: HEF4046 PLL IC

Phase comparator 2 is an edge-controlled digital memory network. It consists of four flip-flops, control gating and a 3-state output circuit comprising p and n-type drivers having a common output node. When the p-type or n-type drivers are ON, they pull the output up to V_{DD} or down to V_{SS} respectively. This type of phase comparator only acts on the positive-going edges of the signals at $SIGN_{IN}$ and $COMP_{IN}$. Therefore, the duty factors of these signals are not of importance.

If the signal input frequency is higher than the comparator input frequency, the p-type output driver is maintained ON most of the time, and both the n and p-type drivers are OFF (3-state) the remainder of the time. If the signal input frequency is lower than the comparator input frequency, the n-type output driver is maintained ON most of the time, and both the n and p-type drivers are OFF the remainder of the time. If the signal input and comparator input frequencies are equal, but the signal input lags the comparator input in phase, the n-type output driver is maintained ON for a time corresponding to the phase difference. If the comparator input lags the signal input in phase, the p-type output driver is maintained ON for a time corresponding to the phase difference. Subsequently, the voltage at the capacitor of the low-pass filter connected to this phase comparator is adjusted until the signal and comparator inputs are equal in both phase and frequency. At this stable point, both p and n-type drivers remain OFF and thus the phase comparator output becomes an open circuit and keeps the voltage at the capacitor of the low-pass filter constant.

Moreover, the signal at the phase comparator pulse output (PCP_{OUT}) is a HIGH level which can be used for indicating a locked condition. Thus, for phase comparator 2 no phase difference exists between the signal and comparator inputs over the full VCO frequency range. Moreover, the power dissipation due to the low-pass filter is reduced when this type of phase comparator is used because both p and n-type output drivers are OFF for most of the signal input cycle. It should be noted that the PLL lock range for this type of phase comparator is equal to the capture range, independent of the low-pass filter. With no signal present at the signal input, the VCO is adjusted to its lowest frequency for phase comparator 2 . Figure 5 shows typical waveforms for a PLL employing this type of phase comparator in locked condition.

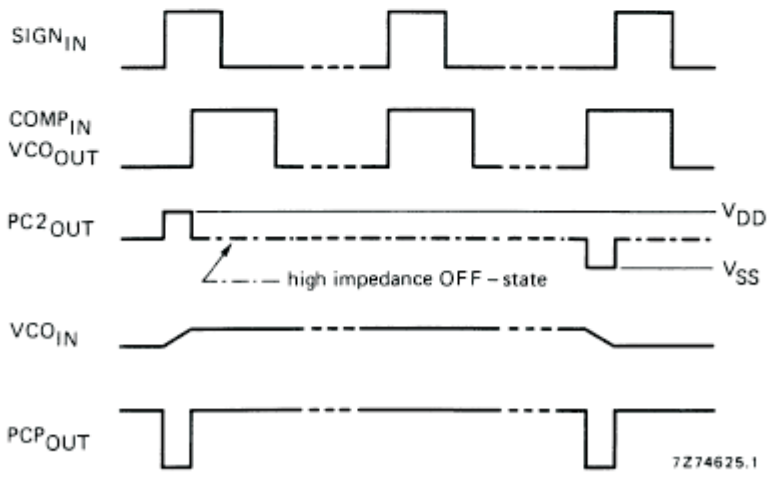

Fig.5 Typical waveforms for phase-locked loop employing phase comparator 2 in locked condition.

Figure A.7: HEF4046 PLL IC

SERIES 12
8 & 11 WATT INFRA-RED EMITTERS

This IR source is a thermal emitter with emissivity of approximately 80%. It is appropriate for use in lab or field instrumentation due to its long life and stable properties. Modulated versions are under development.

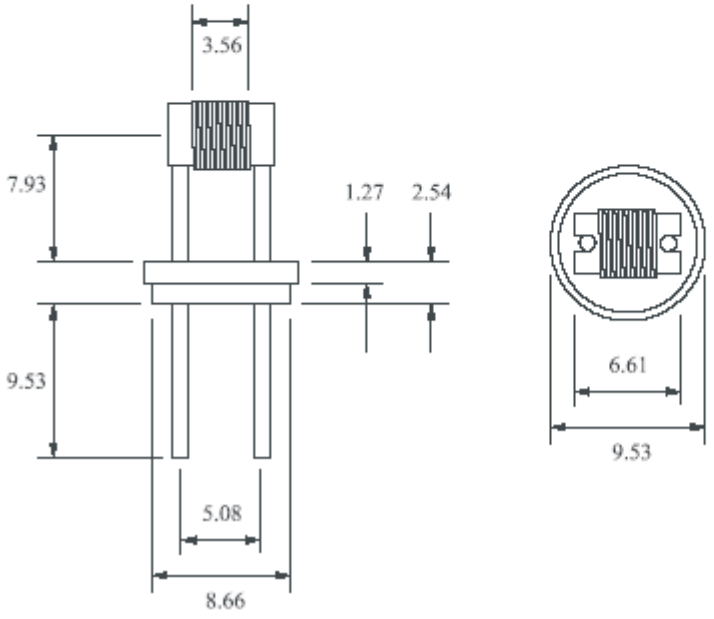

The standard IR-12 coiled resistance wire filament operates at 800°C (1073K) when powered with 4.5 volts @ 1.8 amps (8 watts). The radiating element is a coil of resistance wire which has a high emissivity in the infra-red spectral region. The coil is wound on a grooved cylindrical alumina substrate, resulting in the windings being electrically insulated from each other. This contributes to a more uniform radiating source.

Operation in a controlled or sealed atmosphere is not required.

The emitter support pins also are the power leads and are sealed in an 8.7 mm dia. glass base.

The IR-12K uses a different wire to make the element. This means it can operate at 975°C but has a lower stability than the standard part.

The Series 12 is offered as follows:

Part #	Description
IR-12	Standard. High Stability
IR-12K	High Temperature – Lower Stability

Operating Specifications:

Part	IR-12	IR-12K
Temperature	800°C (1073K)	975°C (1248K)
Voltage	4.5 volts RMS (AC or DC)	6.0 volts RMS (AC or DC)
Current	1.8 Amps	1.8 Amps
Active Area	3.5 x 3.5 mm	
Emissivity	~ 80%	
Lifetime	3+ years typical	

CE

Scitec Instruments Ltd
Barties Industrial Estate
North Street
Redruth
Cornwall TR15 1HR
United Kingdom

t. +44 [0]1209 314608
f. +44 [0]1209 314609
f2. +44 [0]870 1600860
i. www.scitec.uk.com
e. scitec@scitec.uk.com

FIGURE A.8: IR-12 Source

LTI Q2

Pyroelectric Single Element Detector for Measurement Applications

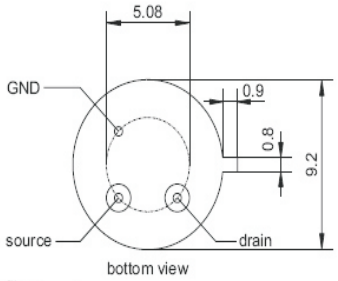

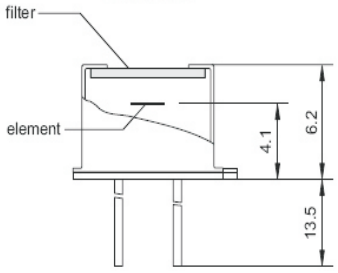

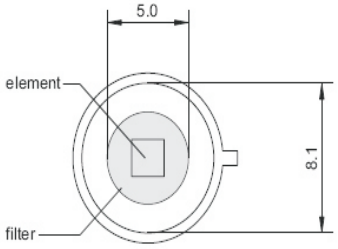

element size	2 mm × 2 mm
aperture	5.0 mm
filter[3]	custom-designed
responsivity[1,2]	>250 V/W
noise[1]	<80 nV/√Hz
specific detectivity[1,2]	>8·10[8] cm √Hz / W
offset voltage	0.4 to 1.5 V
operating voltage	2 to 18 V
housing	TO 39
operating temperature	–20 to 70 °C
storage temperature	–20 to 70 °C

1) frequency: 10 Hz, detector temperature: 25 °C
2) black body source temperature: 500 K, filter transmission: 100 %
3) other filters on request

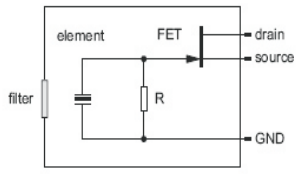

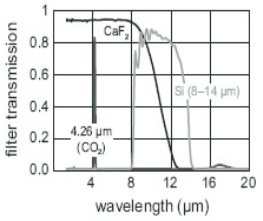

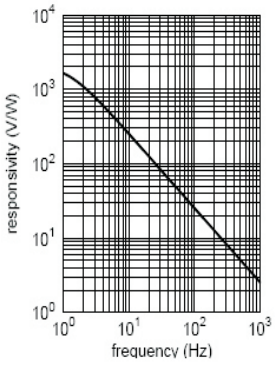

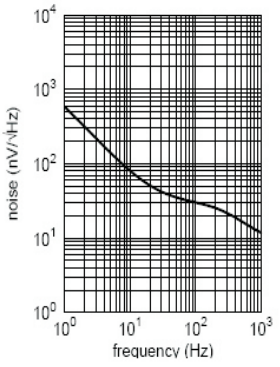

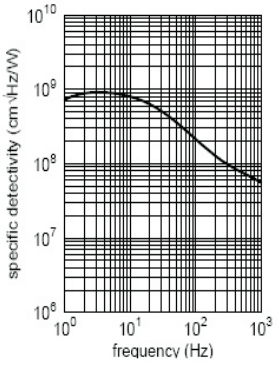

Scitec Instruments Ltd – Bartles Industrial Estate
North Street, Redruth, TR15 1HR UK
phone: +44 (0)1209 314 608 · fax: +44 (0)1209 314 609
e-mail: sales@scitec.uk.com · www.scitec.uk.com

FIGURE A.9: LTI Q2

Low inertia dc servo motor

M66 series

The M66CE is a high performance low inertia dc servo motor, providing up to 30W output power and offers smooth operation over a wide speed range. The M66CE motor incorporates a skewed ironless rotor thereby ensuring linear speed and torque characteristic combined with rapid acceleration and reversal capabilities.
The type M66CT includes an integral dc tachogenerator for optimum velocity control using analogue control techniques while M66CI series is provided with an integral dual track incremental encoder for use with digital control circuits.

Dimensions: mm

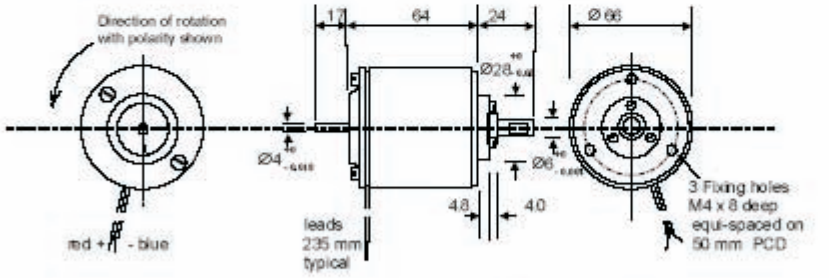

Servo motor
M66CE

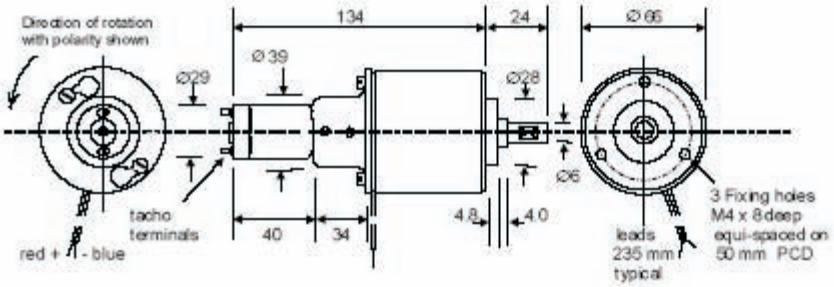

motor-tacho
M66CT

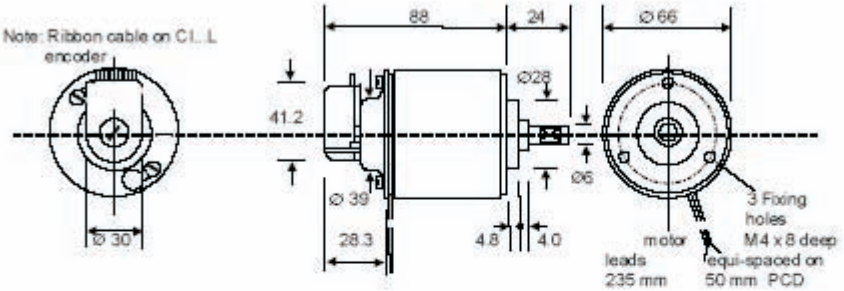

motor-encoder
M66CI

Typical performance

Motor	No-load Speed (rpm)	Rated Speed (rpm)	Rated Torque (Ncm)	Rated Current (Amps)	Peak Torque (Ncm)	using Servo Amplifier	DC Supply (Vdc)	Power Supply for AC operation (110-240 Vac)
M66-12 series	2,700	1,700	8	2.0	16	**MSE421**	12	suitable for use with 12 Vdc battery
M66 -24 series	2,300	1,600	9	1.0	27	**PM121-10***	N/A	integral in amplifier
	2,300	1,600	9	1.0	27	**MSE421-30**	24	MSE 171E
	2,300	1,600	12	1.3	27	**MSE421-60**	24	MSE 171E

Note* Specify PM121-10T when using matched M66 C24T3/T6-tacho unit

Mclennan Servo Supplies Ltd. Tel: +44 (0)8707 700 700 www.mclennan.co.uk Mclennan Issue 001

FIGURE A.10: DC servo motor

30 Watt Ironless rotor dc servo motor M66 series

Specification dc servo motor type M66CE

M66 Motor- options: M66CE-		-12	-24	Performance @ 24 Vdc
Nominal Voltage	(Vdc)	12	30	24
Maximum Output Power	(Watts)	15	30	20
No-load speed	(rpm)	2,700	2,900	2,300
Speed @ rated torque	(rpm)	1,800	2,300	1,600
Rated Torque	(Ncm)	8	12	12
Peak Torque	(Ncm)	25	36	27
Max. No load current	(milli Amps)	120	65	60
Rotor Inertia	($Kgcm^2$)	0.214	0.214	
Mechanical time constant	(millisecs)	24.5	17	
Torque Constant	(Ncm / A)	4.1	9.8	
Voltage Constant	(V / 1000 rpm)	4.27	10.3	
Rotor Resistance	(Ohms)	1.9	7.8	
Rotor inductance	(mH)	1.0	5.0	
Commutation		copper -graphite		
Bearings		pre-loaded ball		
Maximum radial load		100 N, 12 mm from bearing face		
Maximum axial load		15 N		
Ambient operating temperature range		-10 to +60 °C		

motor-tacho versions M66CT series

types:		M66C12 T3	M66C 24 T3	M66C24 T6
Nominal Voltage		12Vdc	24-30 Vdc	24-30 Vdc
Motor specification:		As above		
Tacho Specification		T.3 series		T.6 series
Voltage constant	V/1000 rpm	3.25		6.50
Average ripple	peak / peak	3% (ripple frequency 18 cycles per rev)		
Rotor resistance	Ohms	12		47
Max. continuous speed	rpm	3,000		

motor-encoder version M66-CI...series

types:		M66CI ...T-12		M66CI ...T-24
		M66CI ...L-12		M66CI ...L-24
Nominal Voltage		12Vdc		24Vdc
Motor specification:		As above		
Encoder type		CI...T		CI...L
Supply	Vdc	5 ± 0.5		5 ± 0.5
Max. Output signal	Vdc	5		5
Signal wave form		Square		Square
Output Circuit		TTL		RS 422
Output Configuration		Dual Track Quadrature		Dual Track + Index (complementary)
Number of Lines		100 or 500		100 or 500

Typical Motor-encoder part number: M66 CI 500 L-24

500 line dual track encoder with Index — 24-30 Vdc motor winding

Note:
M66 servo motors are also available with an integral parking brake (M66DB)
If a parking brake is required please contact us for full specification of M66DB options

FIGURE A.11: DC servo motor

LM193
LM293 - LM393

LOW POWER DUAL VOLTAGE COMPARATORS

- WIDE SINGLE SUPPLY VOLTAGE RANGE OR DUAL SUPPLIES : +2V TO +36V OR ±1V TO ±18V
- VERY LOW SUPPLY CURRENT (0.4mA) INDEPENDENT OF SUPPLY VOLTAGE (1mW/comparator at +5V)
- LOW INPUT BIAS CURRENT : 25nA TYP
- LOW INPUT OFFSET CURRENT : ±5nA TYP
- LOW INPUT OFFSET VOLTAGE : ±1mV TYP
- INPUT COMMON-MODE VOLTAGE RANGE INCLUDES GROUND
- LOW OUTPUT SATURATION VOLTAGE : 250mV TYP. (Io = 4mA)
- DIFFERENTIAL INPUT VOLTAGE RANGE EQUAL TO THE SUPPLY VOLTAGE
- TTL, DTL, ECL, MOS, CMOS COMPATIBLE OUTPUTS

N
DIP8 (Plastic Package)

D
SO8 (Plastic Micropackage)

P
TSSOP8 (Thin Shrink Small Outline Package)

S
Mini SO8 (Plastic Micropackage)

DESCRIPTION

These devices consist of two independent low voltage comparators designed specifically to operate from a single supply over a wide range of voltages. Operation from split power supplies is also possible.

These comparators also have a unique characteristic in that the input common-mode voltage range includes ground even though operated from a single power supply voltage.

ORDER CODE

Part Number	Temperature Range	Package			
		N	D	P	S
LM193	-55°C, +125°C	•	•	•	•
LM293	-40°C, +105°C	•	•	•	•
LM393	0°C, +70°C	•	•	•	•
Example : LM393D					

N = Dual in Line Package (DIP)
D = Small Outline Package (SO) - also available in Tape & Reel (DT)
P = Thin Shrink Small Outline Package (TSSOP) - only available in Tape &Reel (PT)
S = MiniSO Package (MiniSO) only available in Tape & Reel (ST)

PIN CONNECTIONS (top view)

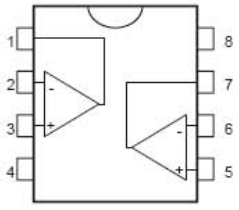

1 - Output 1
2 - Inverting input 1
3 - Non-inverting input 1
4 - V_{CC}^-
5 - Non-inverting input 2
6 - Inverting input 2
7 - Output 2
8 - V_{CC}^+

FIGURE A.12: LM393 Dual comparator

SGS-THOMSON MICROELECTRONICS

LM833

LOW NOISE DUAL OPERATIONAL AMPLIFIERS

- LOW VOLTAGE NOISE : **4.5nV/√Hz**
- HIGH GAIN BANDWIDTH PRODUCT : **15MHz**
- HIGH SLEWRATE : **7V/µs**
- LOW DISTORTION : 0.002%
- EXCELLENT FREQUENCY STABILITY
- ESD PROTECTION 2kV

N
DIP8
(Plastic Package)

D
SO8
(Plastic Micropackage)

DESCRIPTION

The LM833 is a monolithic dual operational amplifier dedicated to audio applications. The LM833 offers low voltage noise (4.5nV/√Hz) and high frequency performances (15MHz gain bandwidth product, 7V/µs slew rate).
In additionthe LM833 has also a very low distortion (0.002%) and excellent phase/gain margins.

ORDER CODES

Part Number	Temperature Range	Package	
		N	D
LM833	-40, +105°C	•	•

PIN CONNECTIONS (top view)

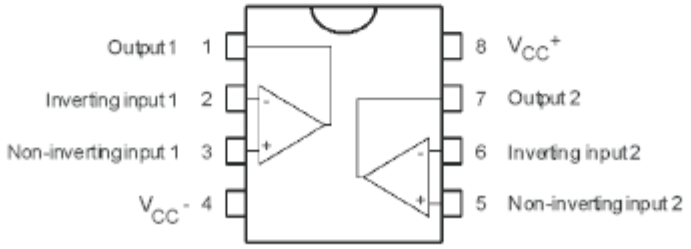

FIGURE A.13: LM833 Dual op-amp

LM833

SCHEMATIC DIAGRAM (1/2 LM833)

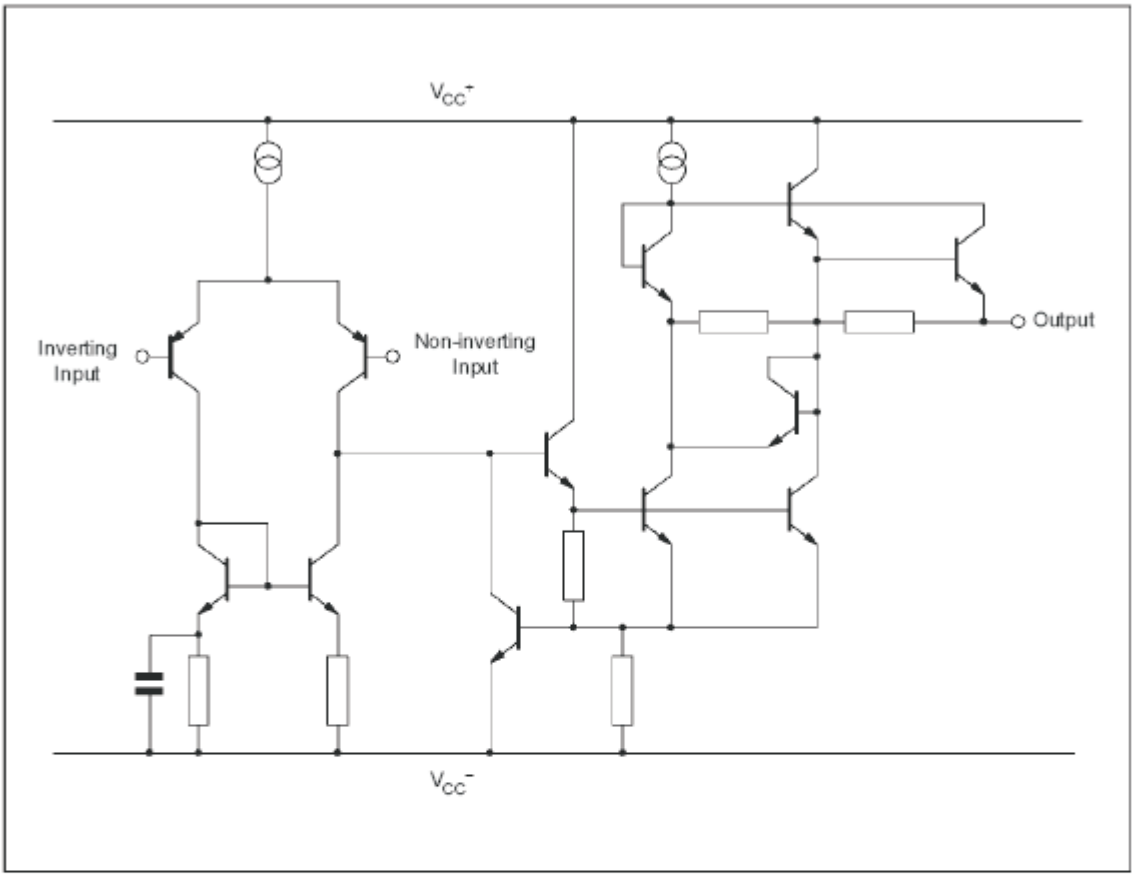

ABSOLUTE MAXIMUM RATINGS

Symbol	Parameter	Value	Unit
V_{CC}	Supply Voltage	±18 or +36	V
V_{id}	Differential Input Voltage - (note 1)	±30	V
V_i	Input Voltage - (note 1)	±15	V
	Output Short-Circuit Duration - (note 2)	Infinite	
T_{oper}	Operating Free-air Temperature Range	-40 to +105	°C
T_j	Maximum Junction Temperature	+150	°C
T_{stg}	Storage Temperature	-65 to +150	°C
P_{tot}	Maximum Power Dissipation - (note 2)	500	mW

Notes : 1. Either or both input voltages must not exceed the magnitude of V_{CC}^+ or V_{CC}^-
2. Power dissipation must be considered to ensure maximum junction temperature (T_j) is not exceeded

OPERATING CONDITIONS

Symbol	Parameter	Value	Unit
V_{CC}	Supply Voltage	±2.5 to ±15	V

FIGURE A.14: LM833 Dual op-amp

ANALOG DEVICES

Precision Single Supply Instrumentation Amplifier

AMP04*

FEATURES
Single Supply Operation
Low Supply Current: 700 μA Max
Wide Gain Range: 1 to 1000
Low Offset Voltage: 150 μV Max
Zero-In/Zero-Out
Single-Resistor Gain Set
8-Lead Mini-DIP and SO Packages

APPLICATIONS
Strain Gages
Thermocouples
RTDs
Battery-Powered Equipment
Medical Instrumentation
Data Acquisition Systems
PC-Based Instruments
Portable Instrumentation

FUNCTIONAL BLOCK DIAGRAM

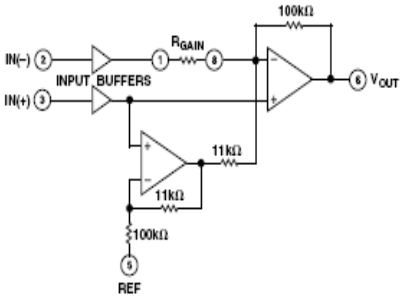

GENERAL DESCRIPTION

The AMP04 is a single-supply instrumentation amplifier designed to work over a +5 volt to ±15 volt supply range. It offers an excellent combination of accuracy, low power consumption, wide input voltage range, and excellent gain performance.

Gain is set by a single external resistor and can be from 1 to 1000. Input common-mode voltage range allows the AMP04 to handle signals with full accuracy from ground to within 1 volt of the positive supply. And the output can swing to within 1 volt of the positive supply. Gain bandwidth is over 700 kHz. In addition to being easy to use, the AMP04 draws only 700 μA of supply current.

For high resolution data acquisition systems, laser trimming of low drift thin-film resistors limits the input offset voltage to under 150 μV, and allows the AMP04 to offer gain nonlinearity of 0.005% and a gain tempco of 30 ppm/°C.

A proprietary input structure limits input offset currents to less than 5 nA with drift of only 8 pA/°C, allowing direct connection of the AMP04 to high impedance transducers and other signal sources.

The AMP04 is specified over the extended industrial (–40°C to +85°C) temperature range. AMP04s are available in plastic and ceramic DIP plus SO-8 surface mount packages.

Contact your local sales office for MIL-STD-883 data sheet and availability.

PIN CONNECTIONS

8-Lead Epoxy DIP (P Suffix)

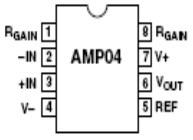

8-Lead Narrow-Body SO (S Suffix)

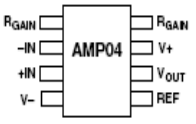

*Protected by U.S. Patent No. 5,075,633.

REV. B

One Technology Way, P.O. Box 9106, Norwood, MA 02062-9106, U.S.A.
Tel: 781/329-4700 World Wide Web Site: http://www.analog.com
Fax: 781/326-8703

FIGURE A.15: AMP04 Precision Instrumentation Amplifier

BURR-BROWN®

OPA2604

www.burr-brown.com/databook/OPA2604.html

Dual FET-Input, Low Distortion OPERATIONAL AMPLIFIER

FEATURES

- LOW DISTORTION: 0.0003% at 1kHz
- LOW NOISE: 10nV/√Hz
- HIGH SLEW RATE: 25V/µs
- WIDE GAIN-BANDWIDTH: 20MHz
- UNITY-GAIN STABLE
- WIDE SUPPLY RANGE: V_S = ±4.5 to ±24V
- DRIVES 600Ω LOADS

APPLICATIONS

- PROFESSIONAL AUDIO EQUIPMENT
- PCM DAC I/V CONVERTER
- SPECTRAL ANALYSIS EQUIPMENT
- ACTIVE FILTERS
- TRANSDUCER AMPLIFIER
- DATA ACQUISITION

DESCRIPTION

The OPA2604 is a dual, FET-input operational amplifier designed for enhanced AC performance. Very low distortion, low noise and wide bandwidth provide superior performance in high quality audio and other applications requiring excellent dynamic performance.

New circuit techniques and special laser trimming of dynamic circuit performance yield very low harmonic distortion. The result is an op amp with exceptional sound quality. The low-noise FET input of the OPA2604 provides wide dynamic range, even with high source impedance. Offset voltage is laser-trimmed to minimize the need for interstage coupling capacitors.

The OPA2604 is available in 8-pin plastic mini-DIP and SO-8 surface-mount packages, specified for the –25°C to +85°C temperature range.

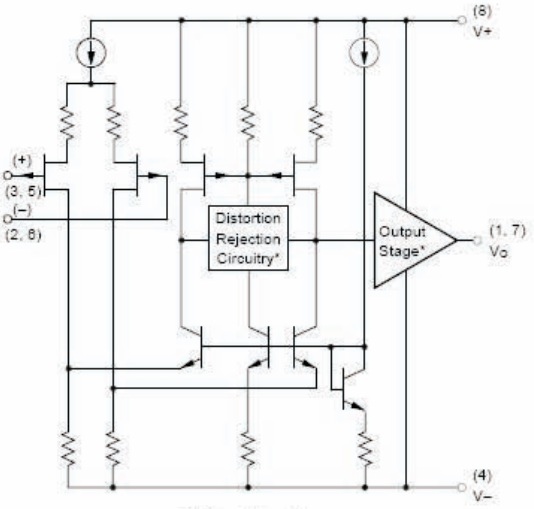

* Patents Granted:
#5063718, 5019789

International Airport Industrial Park • Mailing Address: PO Box 11400, Tucson, AZ 85734 • Street Address: 6730 S. Tucson Blvd., Tucson, AZ 85706 • Tel: (520) 746-1111 • Twx: 910-952-1111
Internet: http://www.burr-brown.com/ • FAXLine: (800) 548-6133 (US/Canada Only) • Cable: BBRCORP • Telex: 066-6491 • FAX: (520) 889-1510 • Immediate Product Info: (800) 548-6132

 PDS-1069E Printed in U.S.A. October, 1997

FIGURE A.16: OPA2604 Dual FET input op-amp

Size 16 hybrid stepper motor — 16 HS series

The 16 HS hybrid stepper motor provides 200 steps / revolution (400 steps /rev when operated in ½step mode) and is ideal for instrumentation drives requiring a combination of compact dimensions, high dynamic performance and accuracy. The motor is physically interchangeable with the larger 17HS model but it's reduced overall frame size and the reduced length of the 16HS-0 series makes it ideal for use in applications where space is at a premium.

The motor is available with a choice of windings to permit operation using either Uni-polar or Bi-polar drive circuits and offers an excellent combination of performance, reliability, and quality at economic prices ideally suited to OEM manufacturers of quality instrumentation products..

Dimensions: mm

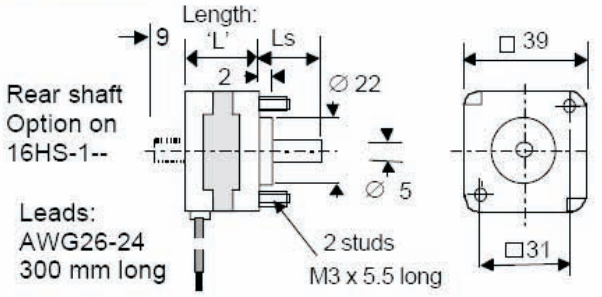

Shaft Length: mm

Motor	Shaft length
16HS-006	24 mm
16HS-012	12 mm
16HS-110 16HS-115 16HS-132	13 mm

Alternative shaft lengths are available to special order

Specification

motor type	length 'L' mm	holding torque Ncm	rotor inertia $Kgcm^2$	resistance per phase ohms	current per phase amps	inductance per phase mH	number of leads	mass Kg
Uni-polar types								
16HS-006	20.5	5	0.011	24	0.26	12.5	6	0.15
16HS-110	34	9	0.016	7.2	0.5	5.8	8	0.20
Bi-polar types								
16HS-012	20.5	8.7	0.011	6.6	0.6	8.5	4	0.15
16HS-115	34	11.5	0.016	4.4	0.75	5.6	4	0.20
16HS-132	34	12.0	0.016	1.2	1.6	1.4	4	0.20

Lead colours

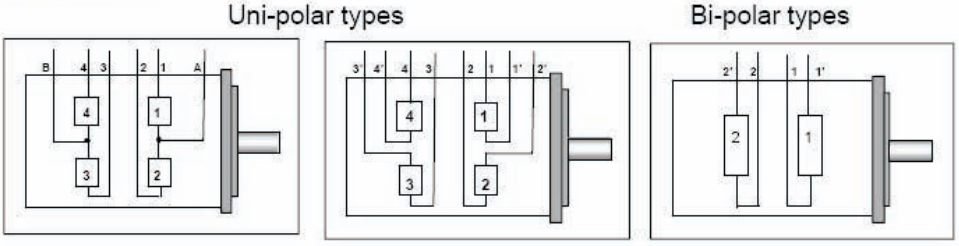

Lead colour identity:

Uni-polar types

6 lead versions

A	Black
1	Red
2	Red / White
B	White
3	Green
4	Green/White

8 lead versions

1'	Red/White
1	Red
2'	Yellow/white
2	Yellow
3'	Black/white
3	Black
4'	Orange/white
4	Orange

Bi-polar types

4 lead versions

1	Red
1'	Yellow
2	Black
2'	Orange

Mclennan Servo Supplies Ltd. Tel: +44 (0)8707 700 700 www.mclennan.co.uk Mclennan

FIGURE A.17: Unipolar Stepper Motor

V10900

GB **RS Stock No.**
240-7920

Description

The RSSM2 driver card is designed to drive a stepper motor in unipolar mode, (either with or without forcing resistors connected between motor commons and +volts). Full, half or wave mode, are selected, as is direction and speed external clock via the logic connections. (Speed can also be derived from an adjustable on board clock). An enable and disable input allow for a variety of start/stop control options to be implemented. the stepper motor must have four phases and either five, six or eight wires.
The RSSM2 card has two terminal blocks, and a trimmer pot. The first block is for connection of the motor and power supplies, the second block being for logic connection. The trimmer pot adjusts the speed of the on board clock. The logic inputs, outputs are generally TTL LS and CMOS (12 Volt max) compatible and are fitted with various series and pull up, or down resistors (See tables). The phase outputs are open drain power MOSFET (source to 0VM) with a fast diode between drain and +VM.

Connector block one

0VM Motor 0V (Connected internally to '0VL)
+VM Motor +Volts, 9-40VDC smoothed * ** #
PHA Motor winding Phase A (up to 2 Amp) #
PHB Motor winding Phase B #
PHC Motor winding Phase C #
PHD Motor winding Phase D #
+VL Logic/Control +Volts, 9-24VDC*
0VL Logic 0V (Connected internally to '0VM')

Connector block two

CKI Step Rate Input, 0-2000Hz (or half steps if selected).
CKO Output, 20-600Hz approx. (adjusted by on board trim pot).
DIS Input, 'CKI' enabled when low.
WAV Input, Motor stepped in wave mode when high.
DIR Input, Motor direction (clockwise when low).
H/F Input, half or full step select. Full step when low (Also 'WAV' = Low).
ENB Input, 'CKI' Enabled when high
+5V Output, +5V at up to 20mA with on board 180R resistor in series (can be used for tying inputs high).

Notes

* Can be the same power supply. (Motor volts then 9-24Vdc max.)
** 470µF capacitor on board is OK smoothing for low current motors.
\# Max motor discharge voltage +55 Volts peak.
Inputs Signal voltages are referenced to 'OVL' <1.5V = LOW > 3.5V = HIGH Max., input = 12VDC and Min., input = -0.6V 'ENB' is pulled high. All others input are pulled low if left unconnected. (Input impedance approx. 10K) 'CKI' Operates on rising edge.
Outputs 'CKO' 0-5 Volt square wave via 1K series resistor. '+5V' 5 Volts via 180R resistor.
PHA-PHD Phase orientation. Direction etc., may vary for different motors.

Power

20mA logic +VL (plus +5V Out)
Up to 4 Amp motor +VM (two windings driven) (2 amp per winding).

Half step sequence*

	PHA	PHC	PHB	PHD
1	ON	ON	OFF	OFF
2	OFF	ON	OFF	OFF
3	OFF	ON	ON	OFF
4	OFF	OFF	ON	OFF
5	OFF	OFF	ON	ON
6	OFF	OFF	OFF	ON
7	ON	OFF	OFF	ON
8	ON	OFF	OFF	OFF

Full step sequence*

	PHA	PHC	PHB	PHD
1	ON	ON	OFF	OFF
2	OFF	ON	ON	OFF
3	OFF	OFF	ON	ON
4	ON	OFF	OFF	ON

* Step sequence is reversed when 'DIR' is changed.

Wave step sequence*

	PHA	PHC	PHB	PHD
1	ON	OFF	OFF	OFF
2	OFF	OFF	ON	OFF
3	OFF	ON	OFF	OFF
4	ON	OFF	OFF	ON

* Step sequence is reversed when 'DIR' is changed.

CKI, Enable & display

CKI	ENB	DIS	
X	L	X	NO EFFECT
X	X	H	NO EFFECT
⊓	H*	L*	NO EFFECT
⊔	H*	L*	NEXT STEP

Step sequence select

DIR	WAVE	H/F	
X	L*	H*	HALF
X	L*	L*	FULL
X	H	X	WAVE
H	X	X	ANTI CLK
L*	X	X	CLK WISE

* = Or unconnected
H = High logic
L = Low logic
X = Don't care

Motor use connection

For low speed applications the motor can be simply connected between the phase and +VM terminals of the RSSM2, and then the correct motor voltage (check on the motor plate or motor manufacturers data) can be connected to the +VM and 0VM terminals. Motors with a rated winding current of up to 2Amps can be used in this way. It should be noted that a stepper motor running at maximum rated current may become very hot and need to be cooled. Please note that different motor manufacturers specify motors in various different ways. For the best performance the motor power supply should be as smooth (low ripple) as possible. A large electrolytic capacitor, with a low ESR is recommended.
For higher speed applications forcing resistors and winding discharge components can be added. The forcing resistor allows a higher motor voltage to be used. This voltage appears (mostly) across the motor at the start of each step, 'over coming' the motors inductance and 'forcing' current into the winding. The discharge component restricts the winding current at the end of the step. A number of points need to be considered. Firstly the increased size of motor power supply required.

FIGURE A.18: Stepper Motor Driver Card

Appendix B

Spectroscopic Modelling

This section contains extracts of the MATLAB codes used to generate the spectroscopic model for the ν_3 mode of CO_2. Only the fundamental band and a hot band transition for $^{12}CO_2$ have been show here.

```
%*********************************************************************
% C12 Spectroscopic modelling              Lower   Upper
% Following transitions were considered: 00001 - 00011 A  Fundamental
% All are parallel bands(no change in l)    01101 - 01111 B  Hotband
%                              02201-02211 C
%                              10002-10012 D  This is one of the levels in a fermi diad
%                              10001-10011 E  This is the other level of the fermi diad
%                              11102-11112 F
%                              03301-03311 G
%                              11110-11111 N
% Note: The notation from left to right is v1 v2 l v3 x where   v1: Raman fundamental at
around 1340cm^-1
%                                          v2: Bending mode at 667.3cm^-1
%                                          l:  Angular momentum quant no:
%                                          v3: Asymm stretching mode at 2349cm^-1
%                                          x:  Denotes fermi diad if its 2

C12=Carbon12;

%Transition C12 00001-00011
%--------------------------------------
w1=C12(1,3);
B1=C12(1,4);
D1=C12(1,5);
H1=C12(1,6);
b1=C12(1,7);
d1=C12(1,8);
h1=C12(1,9);
l1=C12(1,11); % this is the angular momentum quantum number
a11=C12(1,12);
a21=C12(1,13);
a31=C12(1,14);
b11=C12(1,15);
s1=C12(1,16);
P1=pposition(w1,B1,D1,H1,b1,d1,h1,JA);
R1=rposition(w1,B1,D1,H1,b1,d1,h1,JB);

%Transition C12 01101-01111 e  Note: e refers to the lower sub-level due to l-type doubling
%--------------------------------------
w2=C12(2,3);
B2=C12(2,4);
D2=C12(2,5);
H2=C12(2,6);
b2=C12(2,7);
d2=C12(2,8);
h2=C12(2,9);
l2=C12(2,11);
a12=C12(2,12);
a22=C12(2,13);
a32=C12(2,14);
b12=C12(2,15);
s2=C12(2,16);
P2=pposition(w2,B2,D2,H2,b2,d2,h2,JC); %For P and R, only e-e or f-f is possible and not e-
f.
```

FIGURE B.1: MATLAB codes used to generate spectroscopic model for the ν_3 mode of CO_2

```
R2=rposition(w2,B2,D2,H2,b2,d2,h2,JD); %Also only transitions from symmetrical
rotational lines are present due to group symmetry.


%Transition C12 01101-01111 f  Note: f refers to the upper sub-level due to l-type doubling
%-----------------------------------
w3=C12(3,3);
B3=C12(3,4);
D3=C12(3,5);
H3=C12(3,6);
b3=C12(3,7);
d3=C12(3,8);
h3=C12(3,9);
l3=C12(3,11);
a13=C12(3,12);
a23=C12(3,13);
a33=C12(3,14);
b13=C12(3,15);
s3=C12(3,16);
P3=pposition(w3,B3,D3,H3,b3,d3,h3,JA);
R3=rposition(w3,B3,D3,H3,b3,d3,h3,JA);
Q2=qposition(w2,B2,D2,H2,b3,d3,h3,JD); % For Q, only e-f or f-e is possible.
Q3=qposition(w3,B3,D3,H3,b2,d2,h2,JA);

%To find the max R value and min P value inorder to define the IR window range
%-------------------------------------------------------------------------------------------------
Pall=[P1 P2 P3 P4 P5 P6 P7 P8 P9 P10 P11 P12 P13 P14 P15 P16 P21 P22 P23 P24 P25 P26
P27 P28 P29 P30];

Pmin=min(Pall)
Rall=[R1 R2 R3 R4 R5 R6 R7 R8 R9 R10 R11 R12 R13 R14 R15 R16 R21 R22 R23 R24
R25 R26 R27 R28 R29 R30];

Rmax=max(Rall)
int=(Rmax-Pmin)/delta
INT=round(int)
points=0:1:INT;
wavenumber=Pmin+(delta*points);

%Transition C12 00001-00011
%---------------------------------------
[HP1,HR1]=honl(JA,JB,0,l1);                    %Honl-London factor for degeneracy
[EP1,ER1]=boltz(B1,JA,JB,0,beta);              %Boltzmann Distribution
[FP1,FR1]=herman(JA,JB,a11,a21,a31);           %Herman-Wallis
Qr1=partition(B1,beta,l1);                  %Partition function
[LP1,LR1]=lorentz(P,JA,JB,0,P1,R1,0,Pmin,delta,points);        %Lorentz line function
[SP1,SR1]=intensity(P1,R1,0,w1,s1,HP1,HR1,0,EP1,ER1,0,FP1,FR1,0,Qr1,beta,mol);
%Intensity of lines

BranchP1=SP1*LP1;                      %Final branch profile after considering line
broadening
BranchR1=SR1*LR1;
BandA=BranchP1+BranchR1;               %Overall band spectrum

figure
```

FIGURE B.2: MATLAB codes used to generate spectroscopic model for the ν_3 mode of CO_2

```
plot(wavenumber,BandA)
xlabel('wavenumber(cm^-1)');
ylabel('Absorption');
title('Absorption Spectrum for C12 BandA');

%Transition C12 01101-01111 e
%----------------------------------------
[HP2,HR2,HQ2]=honl(JC,JD,JD,l2);
[EP2,ER2,EQ2]=boltz(B2,JC,JD,JD,beta);
[FP2,FR2]=herman(JC,JD,a12,a22,a32);
FQ2=1;
Qr2=partition(B2,beta,l2);
[LP2,LR2,LQ2]=lorentz(P,JC,JD,JD,P2,R2,Q2,Pmin,delta,points);
[SP2,SR2,SQ2]=intensity(P2,R2,Q2,w2,s2,HP2,HR2,HQ2,EP2,ER2,EQ2,FP2,FR2,FQ2,Qr2,
beta,mol);
BranchP2=SP2*LP2;
BranchR2=SR2*LR2;
BranchQ2=SQ2*LQ2;

%Transition C12 01101-01111 f
%----------------------------------------
[HP3,HR3,HQ3]=honl(JA,JA,JA,l3);
[EP3,ER3,EQ3]=boltz(B3,JA,JA,JA,beta);
[FP3,FR3]=herman(JA,JA,a13,a23,a33);
FQ3=1;
Qr3=partition(B3,beta,l3);
[LP3,LR3,LQ3]=lorentz(P,JA,JA,JA,P3,R3,Q3,Pmin,delta,points);
[SP3,SR3,SQ3]=intensity(P3,R3,Q3,w3,s3,HP3,HR3,HQ3,EP3,ER3,EQ3,FP3,FR3,FQ3,Qr3,
beta,mol);
BranchP3=SP3*LP3;
BranchR3=SR3*LR3;
BranchQ3=SQ3*LQ3;
BandB=BranchP2+BranchR2+BranchQ2+BranchP3+BranchR3+BranchQ3;
figure
plot(wavenumber,BandB);
xlabel('wavenumber(cm^-1)');
ylabel('Absorption');
title('Absorption Spectrum for C12 Band B');
```

FIGURE B.3: MATLAB codes used to generate spectroscopic model for the ν_3 mode of CO_2

Appendix C

CAD Drawing

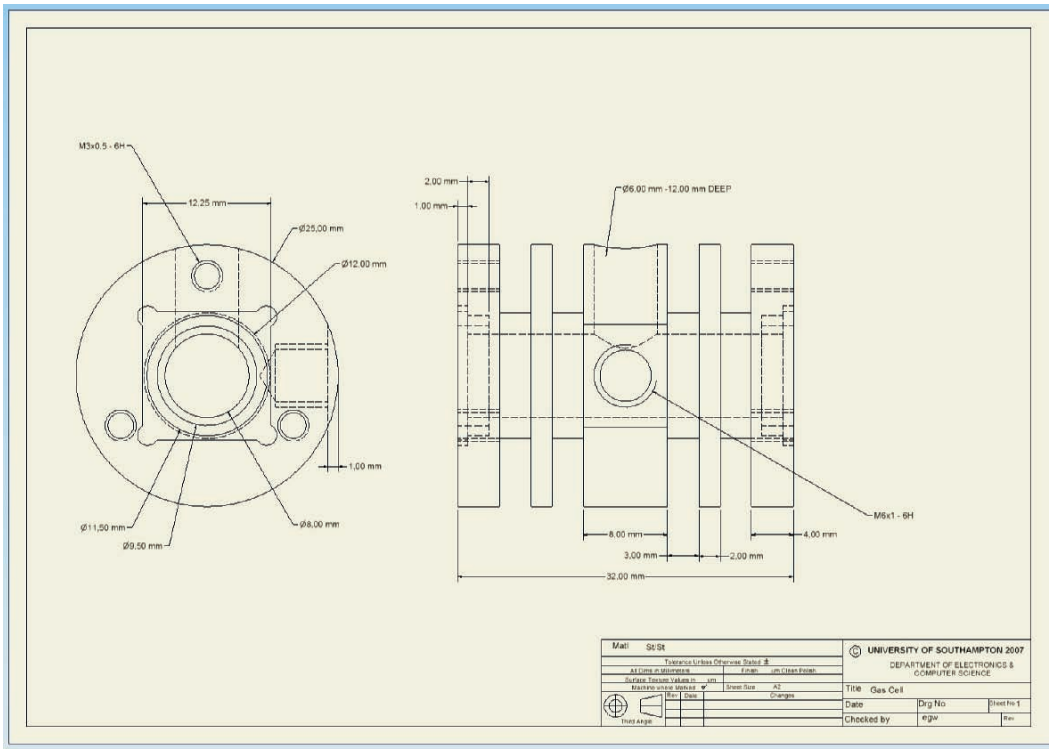

FIGURE C.1: CAD drawing for the ICF cell

Appendix D

Publications

A Kannath and H N Rutt Development of Low Cost Instrumentation for Non-Invasive Detection of Helicobacter Pylori. *Advanced Biomedical and Clinical Diagnostic Systems V*, Vol 6430, Proceedings of SPIE BiOS 2007, San Jose

Bibliography

[1] P. Repond and M. W. Sigrist. Photoacoustic Spectroscopy on Trace Gases with Continuously Tunable CO_2 Laser. *Applied Optics*, 35,No.21:4065–85, 1996.

[2] G. Gagliardi, A. Castrillo, R. Q. Iannone, E. R. T. Kerstel, and L. Gianfrani. High Precision Determination of the $^{13}CO_2/^{12}CO_2$ Isotope Ratio Using a Portable 2.008μm Diode Laser Spectrometer. *Applied Physics B*, 77:119–24, 2003.

[3] http://www.survey.ntua.gr/main/courses/general/sigproc/files/dspguide_book/ch3.pdf, 2009. Last visited 03 August 2009.

[4] P. Bergamaschi, M. Schupp, and G. W. Harris. High Precision Direct Measurements of $^{13}CH_4/^{12}CH_4$ and $^{12}CH_3D/^{12}CH_4$ Ratios in Atmospheric Methane Sources by means of a Long Path Tunable Diode Laser Absorption Spectrometer. *Applied Optics*, 33,No.33:7704–15, 1994.

[5] I. G. Calasso, V. Funtov, and M. W. Sigrist. Analysis of Isotopic CO_2 mixtures by Laser Photoacoustic Spectroscopy. *Applied Optics*, 36,No.15:3212–16, 1997.

[6] P. Ghosh and W. A. Brand. Stable Isotope Ratio Mass Spectrometry in Global Climate Change Research. *Int. J. Mass Spectrometry*, 228:1–33, 2003.

[7] D. F. Ferretti, D. C. Lowe, R. J. Martin, and G. W. Brailsford. A New Gas Chromatograph Isotope Ratio Mass Spectrometry Technique for High Precision N_2O-Free Analysis of $\delta^{13}C$ and $\delta^{18}O$ in Atmospheric CO_2 from Air Samples. *J. Geographical Research*, 105,No.D5:6709–18, 2000.

[8] M. Erdelyi, D. Richter, and F. K. Tittel. $^{13}CO_2/^{12}CO_2$ Isotopic Ratio Measurements using a Difference Frequency based Sensor Operating at 4.35μm. *Appl. Phy. B Laser and Optics*, 75:289–95, 2002.

[9] G. Gagliardi, R. Restieri, G. Casa, and L. Gianfrani. Chemical and Isotopic Analysis using Diode Laser Sectroscopy:Applications to Volcanic Gas Monitoring. *Optics and Lasers in Engineering*, 37:131–42, 2001.

[10] J. F. Becker, T. D. Sauke, and M. Loewenstein. Stable Isotope Analysis using Tunable Diode Laser Spectroscopy. *Applied Optics*, 31,No.12:1921–27, 1992.

[11] P. Stubbs. The Breath of a Drunken Driver. *New Scientist*, 373:71, 1964.

[12] G. Rooth and S. Ostenson. Acetone in Alveolar Air and the Control of Diabetes. *Lancet*, ii:1102–05, 1966.

[13] C. R. Wade and A. M. van Rij. In-vivo Lipid Peroxidation in Man as Measured by the Respiratory Excretion of Ethane, Pentane and Other Low Molecular Weight Hydrocarbons. *Analytical Biochemistry*, 150:1–7, 1985.

[14] C. T. Gregg, J. Y. Hutson, and J. R. Prime. Substantial Replacement of Mammalian Body Carbon with Carbon-13. *Life Science*, 13:775–782, 1973.

[15] G. Preti, L. Clark, B. J. Cowart, R. S. Feldman, L. D. Lowry, E. Weber, and I. M. Young. Non-oral Etiologies of Oral Malodor and Altered Chemosensation. *Journal of Periodontal*, 63:790–96, 1992.

[16] S. Chen, V. Mahadevan, and L. Zieve. Volatile Fatty Acids in the Breath of Patients with Cirrhosis of the Liver. *J. Laboratory Clinical Medicine*, 75:622–27, 1970.

[17] M. Philips, M. Sabas, and J. Greenberg. Increased Pentane and Carbon Disulfide in the Breath of Patients with Schizophrenia. *J. Clinical Pathology*, 46:861–64, 1993.

[18] L. S. Smienhoff, J. F. Burke, J. J. Saukkonen, A. T. Ordinario, and R. Doty. Biochemical Profile of Uremic Breath. *The New England Journal of Medicine*, 297:132–36, 1977.

[19] B. K. Krotoszynski, G. M. Bruneau, and H. J. O'Neill. Measurement of Chemical Inhalation Exposure in Urban Population in the Presence of Endogenous Effluents. *J. Analytical Toxicology*, 3:225–34, 1979.

[20] R. D. Seeley, T. D. Stephens, and P. Tate. *Anatomy and Physiology.* Mosby Year Book, 1992. 2^{nd} edition.

[21] A. D. Schwabe, F. J. Cozzetto, L. R. Benett, and M. M. Mellinkoff. Estimation of Fat Absorption by Monitoring of Expired Radioactive Carbon Dioxide After Feeding a Radioactive Fat. *Gastroenterology*, 42:285, 1962.

[22] M. Wilkinson. Biomedical Comment-Helicobacter Pylori: An Overview. *Brit. J. Biomed Sci.*, 58:59–60, 2001.

[23] V. Pasceri, G. Patti, G. Cammarota, L. Cuoco, G. Gasbarinni, and A. Masseri. Association of Cytoxin Associated Gene A Helicobacter Pylori with Ischemic Heart Disease. *Circulation*, 96:174, 1997.

[24] H. Zhou, K. L. Chan, K. M. Chu, and P. K. H. Tam. Intrafamilial Spread of Helicobacter Pylori: A Prospective Study using Urea Breath Test. *J. Pediatric Surgery*, 35,No.11:1672–75, 2000.

[25] www.helico.com, 2004. The Helicobacter Foundation.

[26] C. D. Mansfield. *An Investigation into the Viability of an Infrared Diagnostic Instrument for Measurement of CO_2 Isotope Ratios in Breath.* PhD thesis, Dept. of Elec. Comp. Sci., Univ of Southampton, 2000.

[27] C. S. Irving, P. D. Klein, P. R. Navratil, and T. W. Boutton. Measurement of $^{13}CO_2/^{12}CO_2$ Abundance by Nondispersive Infrared Heterodyne Ratiometry as an Alternative to Gas Isotope Ratio Mass Spectrometry. *Analytical Chemistry*, 58,No.11:2172–78, 1986.

[28] V. Savarino, G. S. Mela, P. Zentilin, G. Bisso, M. Pivari, C. Mansi, M. R. Mele, C. Bilardi, S. Vigneri, and G. Celle. Comparison of Isotope Ratio Mass Spectrometry and Nondispersive Isotope-Selective Infrared Spectroscopy for ^{13}C Urea Breath Test. *The American Journal of Gastroenterology*, 94,No.5:1203–08, 1999.

[29] S. Koletzko, M. Haisch, I. Seeboth, B. Braden, K. Hengels, B. Koletzko, and P. Hering. Isotope Selective Nondispersive Infrared Spectrometry for Detection of Helicobacter pylori Infection with ^{13}C Urea Breath Test. *The Lancet*, 345:961–62, 1995.

[30] B. Braden, F. Schaffer, W. F. Caspary, and B. Lembcke. Nondispersive Isotope-Selective Infrared Spectroscopy:A New Analytical Method for ^{13}C Urea Breath Tests. *Scan. J. Gastroenterolgy*, 31:442–45, 1996.

[31] P. Repond and M. W. Sigrist. Continuously Tunable High Pressure CO_2 Laser for Spectroscopic Studies on Trace Gases. *IEEE J. Quant. Elec.*, 32,No.9:1549–59, 1996.

[32] D. E. Murnick and B. J. Peer. Laser Based Analysis of Carbon Isotope Ratios. *Science*, 263,No.5149:945–47, 1994.

[33] R. Chaux and B. Lavorel. Relative Line Intensity Measurement in Absorption Spectra Using a Tunable Diode Laser at 1.6μm:Application to the Determination of $^{13}CO_2/^{12}CO_2$ Isotope Ratio. *Applied Physics B*, 72:237–40, 2001.

[34] J. B. McManus, M. S. Zahniser, D. D. Nelson, L. R. Williams, and C. E. Kolb. Infrared Laser Spectrometer with Balanced Absorption for Measurement of Isotopic Ratios of Carbon Gases. *Spectrochimica Acta Part A*, 58:2465–79, 2002.

[35] G. Giubileo, R. Fantoni, L. De Dominicis, M. Giorgi, R. Pulvirenti, and M. Snels. A TDLAS System for the Diagnosis of Helicobacter Pylori Infection in Humans. *Laser Methods in Medicine and Biology*, 11,No.1:154–57, 2000.

[36] E. V. Stepanov. Laser Analysis of the $^{13}C/^{12}C$ Isotope Ratio in CO_2 in Exhaled Air. *Quantum Electronics*, 32,No.11:981–86, 2002.

[37] T. Matsushima, J. Kawanabe, H. Maekawa, S. Saimi, T. Sueta, and Y. Cho. High Sensitivity Isotope Concentration Ratio Measurement CO_2 Infrared Laser System(ii). In *25th International Conference on Infrared and Millimeter Waves Conference Digest, W-D2*, pages 151–52. IEEE, 2000.

[38] T. Matsushima, J. Kawanabe, H. Maekawa, S. Saimi, T. Sueta, and Y. Cho. Trace Level Isotope Concentration Ratio Measurement $^{12}CO_2$-$^{13}CO_2$ Laser System(ii). *IEEE*, pages 66–67, 2000.

[39] A. F. Cutler and P. Toskes. Comparison of ^{13}C Urea Blood Test to ^{13}C Urea Breath Test for the Diagnosis of Helicobacter pylori. *American J. Gastroenterology*, 94,No.4:959–61, 1999.

[40] G. Suto, A. Vincze, F. Pakodi, B. Hunyady, O. Karadi, M. Garamszegi, T. Laszlo, and G. Mozsik. ^{13}C Urea Breath Test is Superior in Sensitivity to Detect Helicobacter pylori Infection than either Antral Histology or Rapid Urease Test. *J. Physiology*, 94:153–56, 2000.

[41] A. F. Cutler, S. Havstad, C. K. Ma, M. J. Blaser, G. I. Perez-Perez, and T. T. Schubert. Accuracy of Invasive and Noninvasive Tests to Diagnose Helicobacter pylori Infection. *Gastroenterology*, 109:136–41, 1995.

[42] A. Slomianski, T. Schubert, and A. F. Cutler. ^{13}C Urea Breath Test to Confirm Eradication of Helicobacter pylori. *American J. Gastroenterology*, 90,No.2:224–26, 1995.

[43] P. D. Klein, H. M. Malaty, R. F. Martin, K. S. Graham, R. M. Genta, and D. Y. Graham. Noninvasive Detection of Helicobacter pylori Infection in Clinical Practice:The ^{13}C Urea Breath Test. *American J. Gastroenterology*, 91,No.4:690–94, 1996.

[44] T. S. Chen, F. Y. Chang, P. C. Chen, T. W. Huang, J. T. Ou, M. H. Tsai, M. S. Wu, and J. T. Lin. Helicobacter Pylori in Peptic Ulcer and Gastritis. *J. Gastroenterology and Hepatology*, 18:1237–43, 2003.

[45] D. Y. Graham, H. M. Malaty, R. A. Cole, R. F. Martin, and P. D. Klein. Simplified ^{13}C Urea Breath Test for Detection of Helicobacter pylori Infection. *American J. Gastroenterology*, 96,No.6:1741–45, 2001.

[46] Y. Urita, Y. Kikuchi, K. Hike, N. Torii, E. Kanda, M. Sasajima, and K. Miki. A Simple Modified 13C-Urea Breath Test:Transnasal Breath Sample Collection Method. *American J. Gastroenterology Supplement*, S55:165, 2002.

[47] F. Mana, H. R. Ham, H. Reynaert, P. Franken, and D. Urbain. ^{13}C-Urea Breath Test using Infrared Spectroscopy:Practical Recommendations. *American J. Gastroenterology*, 95,No.1:316, 2000.

[48] J. P. Gisbert, L. M. Benito, S. Lara, A. Vazquez, I. Jimenez, and J. M. Pajares. C-13 Urea Breath Test for the Diagnosis of Helicobacter Pylori Infection: Are Basal Samples Necessary ? *European J. Gastroenterology and Hepatology*, 12,No.11:1201–05, 2000.

[49] J. P. Gisbert and J. M. Pajares. Review Article: ^{13}c Urea Breath Test in the Diagnosis of Helicobacter Pylori Infection- A Critical Review. *Aliment Pharmacol Ther*, 20:1001–17, 2004.

[50] T. Sekiguchi, M. Nakamura, M. Kato, K. Nishikawa, k. Hokari, T. Sugiyama, and M. Asaka. Immunological Helicobacter Pylori Urease Analyser Based on Ion-Sensitive Field Effect Transistor. *Sensors and Actuators B*, 67:265–69, 2000.

[51] C. D. Mansfield and H. N. Rutt. Development of an Infrared Diagnostic Iinstrument for the Measurement of CO_2 Isotope Ratios in Breath. In *Photonics West*, 1999.

[52] H. N. Rutt, 2003. Private Communication.

[53] L. S. Rothman, D. Jacquemart, A. Barbe, and D. C. Benner et al. The HITRAN 2004 Molecular Spectroscopic Database. *J. Quant. Spectrosc. Radiat. Transfer*, 96,No.2:139–204, 2005.

[54] L. S. Rothman, C. P. Rinsland, A. Goldman, and S. T. Massie et al. The HITRAN Molecular Spectroscopic Database and Hawks (HITRAN Atmospheric Workstation):1996 Edition. *J. Quant. Spectrosc. Radiat. Transfer*, 60:665–710, 1998.

[55] L. S. Rothman, R. R. Gamache, R. H. Tipping, and C. P. Rinsland et al. The HITRAN Molecular Database: Editions of 1991 and 1992. *J. Quant. Spectrosc. Radiat. Transfer*, 48:469–507, 1992.

[56] L. S. Rothman, A. Barbe, D. C. Benner, and L. R. Brown et al. The HITRAN Molecular Spectroscopic Database: Edition of 2000 including updates through 2001. *J. Quant. Spectrosc. Radiat. Transfer*, 82:5–44, 2003.

[57] L. S. Rothman, R. L. Hawkins, R. B. Wattsons, and R. R. Gamache. Energy Levels, Intensities and Linewidths of Atmospheric Carbon Dioxide Bands. *J. Quant. Spectrosc. Radiat. Transfer*, 48:537–66, 1992.

[58] G. Herzberg. *Molecular Spectra and Molecular Structure, Vol II Infrared and Raman Spectra of Polyatomic Molecules*. Van Nostrand Reinhold Company International, USA, 1945. 9^{th} printing.

[59] J. D. Pleil and A. B. Lindstrom. Measurement of Volatile Organic Compounds in Exhaled Breath as Collected in Evacuated Electropolished Canistes. *J. Chromatography B:Biomedical Appl.*, 665:271–79, 1995.

[60] C. D. Mansfield and H. N. Rutt. Evaluation of Multiple Beam Interference Effects in Infrared Gas Spectroscopy. *Meas. Sci. Technol.*, 10:206–210, 1999.

[61] http://www.avbrief.com/briefingservices.html, 2007. Last visited 19 July 2007.

[62] http://fscimage.fishersci.com/msds/76947.htm, 2007. Last visited 25 September 2007.

[63] A. Minakov, J. Morikawa, T. Hashimoto, H. Huth, and C. Schick. Temperature Distribution in a Thin Film Chip Utilised for Advanced Nanocalorimetry. *Meas. Sci. Tec.*, 17:199–207, 2005.

[64] R. Krishnamurti. Some Further Studies on the Transition to Turbulent Convection. *J. Fluid Mech.*, 60,No.2:285–304, 1972.

[65] http://en.wikipedia.org/wiki/Grashof_number, 2008. Last visited 12 January 2008.

[66] http://en.wikipedia.org/wiki/Prandtl_number, 2008. Last visited 12 January 2008.

[67] http://focus.ti.com/docs/toolsw/folders/print/filterpro.html, 2009. Last visited 01 August 2009.